Multi-wavelength study of GRBs detected by Fermi and Swift

Submitted by

You-Dong HU

Thesis Supervisor

Prof. Alberto J. CASTRO-TIRADO
Prof. Bin-Bin ZHANG

Programa de Doctorado en Física y Matemáticas

A thesis submitted to the University of Granada in fulfillment of the requirement for the degree of Doctor of Philosophy

2021-5

Editor: Universidad de Granada. Tesis Doctorales
Autor: You-Dong Hu
ISBN: 978-84-1306-996-8
URI: http://hdl.handle.net/10481/70113

PhD Thesis Examination Committee

TEC Chair:	Prof.
Main Advisor:	Prof.
Co-advisor(s):	None
Internal TEC member 1:	Prof.
Internal TEC member 2:	Prof.
External TEC member 1:	Prof.
External TEC member 2:	Prof.

Declaration

I hereby confirm the following:

- I hereby confirm that the thesis work is original and has not been submitted to any other University or Institution for higher degree purposes.
- I hereby grant University of Granada the permission to reproduce and distribute publicly paper and electronic copies of this thesis document in whole or in part in any medium now known or hereafter created in accordance with Policy on Intellectual Property.
- I have fulfilled all requirements as prescribed by the University and provided 1 copy of my thesis in PDF.
- I have attached all publications and award list related to the thesis (e.g. journal, conference report and patent).
- The thesis does / does not (delete accordingly) contain patentable or confidential information.
- I certify that the thesis has been checked for plagiarism via turnitin/ithenticate. The score is 100%.

Name and signature:

_____

Date:

_____

Abstract

Gamma-ray bursts (GRBs) are the most violent explosions in the Universe. Although they were first discovered over half a century ago, yet many problems remain unsolved. Since the successful launch of GRB dedicated missions such as *Swift* and *Fermi*, multi-wavelength ground-based observations have provided a new approach to better characterize these events, their host galaxies and understand the underlying physics around the newly born compact objects following the GRB itself.

GRB 140629A was a long burst that triggered the *Swift* satellite and many facilities at different wavelengths followed up this event, including the optical (*Swift*/UVOT and various facilities worldwide), infrared (*Spitzer*) and X-rays (*Swift*/XRT). These data were taken between 40 seconds and 3 yr after the burst trigger, which made this burst a good case to investigate the properties of the dominant jet and its host galaxy. The absorption features displayed in the optical spectrum, taken with the 6.0m BTA telescope, confirmed the redshift of this GRB (z = 2.276$\pm$0.001). We found no strong spectral evolution when fitting the spectral energy distribution of the afterglow from the X-rays to optical wavelengths. The hydrogen column density N_H was constrained to be 7.2×10^{21}cm^{-2} along the line of sight. The afterglow in this burst could be explained by a blast wave jet with a long-lasting central engine expanding into a uniform medium in the slow cooling regime. At the end of energy injection, a normal decay phase was observed in both the optical and X-ray bands. An achromatic jet break was also found in the afterglow light curves $\sim$0.4 d after the trigger. We fitted the multi-wavelength data simultaneously with a model (based on numerical simulations) and found that the observations could be explained by a narrow uniform jet in a dense environment with a half-opening angle of 6.7° viewed 3.8° off-axis, implying a total released energy of 1.4×10^{54} erg. Using the redshift and opening angle, we found that GRB 140629A followed both the Ghirlanda and Amati relations. The peak time of the light curve was identified as the onset of the forward shock (181 s after trigger) and we could constrain

the initial Lorentz factor (Γ_0) in the range 82-118. After fitting the host galaxy spectral energy distribution, we found the host to be a low mass, star-forming galaxy with a star formation rate (SFR) of log(SFR) = $1.1^{+0.9}_{-0.4}$ $M_{\odot}yr^{-1}$. We also obtained a value for the neutral hydrogen density N_{HI} by fitting the optical spectrum, from which we derived log$N_{HI} = 21.0 \pm 0.3$, classifying this host as a damped Lyman-alpha system. High ionisation lines (N V,Si IV) were also detected in the optical spectrum. Furthermore, polarisation observations by the MASTER network indicated that this burst was weakly polarised.

GRB 190829A was detected by both *Fermi* and *Swift* but what made a unique event out of it was the detection of very high energy (VHE) gamma-rays by the High-Energy Stereoscopic System telescopes (HESS). The prompt gamma-ray emission displayed two emission episodes separated by a quiescent gap of $\sim$ 40 s. We followed it up with the 10.4 m Gran Telescopio CANARIAS (GTC) and gathered observations of the afterglow of GRB 190829A and its underlying supernova during the following days. We determined the redshift of this event (z = 0.0785$\pm$0.005) and compared GRB 190829A to GRB 180728A, another GRB with similar prompt behaviour at VHE energies, and discussed the implications regarding the underlying physical mechanisms producing these two GRBs. Together with the prompt emission data, the 10.4 m GTC data was used to better understand the emission mechanisms and possible progenitors. In the detailed analysis of the multi-band observations of the afterglow, we found the observational properties of the multi-wavelength afterglow could be explained by the cooling frequency passing between the optical and X-ray bands at the early epoch. A few days after, we saw the transition from the afterglow spectrum to the underlying supernova (dubbed SN 2019oyw) spectrum, which dominated the light curve at later times. Although the prompt emission temporal properties of GRB 190829A and GRB 180728A were similar, the two gamma-ray pulses were different in the spectral domain. We also found that the SN 2019oyw associated with GRB 190829A is powered by Ni decay and could be classified as a Type Ic-BL (broad line) supernova. The spectroscopic and photometric properties of this supernova were consistent with those observed for SN 1998bw (also related to another burst, GRB 980425) but SN 2019oyw evolved much faster than SN 1998 bw.

Besides these above mentioned two long-duration GRBs, we also investigated the prompt emission and the afterglow properties of a sample of short-duration gamma-ray bursts (sGRBs) including GRB 130603B and another eight sGRB events during 2012-2015. They were observed by several multi-wavelength facilities, including the 10.4 m GTC telescope. Prompt emission high energy data of those events were obtained by *INTEGRAL*-SPI-ACS, *Swift*-BAT and *Fermi*-GBM satellites. The prompt emission data by *INTEGRAL* in the 0.1–10 MeV energy range for sGRB 130603B, sGRB 140606A, sGRB 140930B, sGRB 141212A, and sGRB 151228A did not show signs of the extended emission or the precursor activity and their spectral and temporal properties were found to be similar to those seen in case of other short-duration bursts. For sGRB 130603B, our new afterglow photometric data constrained the pre-jet-break temporal decay due to denser temporal coverage. Its afterglow light curve, containing both our new data as well as previously published photometric data, was broadly consistent with the interstellar medium (ISM) afterglow model. Modelling the host galaxies of sGRB 130603B and sGRB 141212A using the LePHARE software supported a scenario where the burst environment was undergoing moderate star formation activity. From the inclusion of our late-time data for the additional eight sGRBs, we were able to place tight constraints on the non-detection of the afterglow, host galaxy or any underlying 'kilonova' emission. Finally, our late-time afterglow observations of the short-duration GRB 170817A (related to the gravitational wave GW 170817) are also discussed and compared with the sub-set of short-duration GRBs.

Resumen

Los estallidos de rayos gamma (GRBs) son los fenómenos más energéticos del Universo que, descubiertos hace más de medio siglo, presentan en la actualidad muchos incógnitas que aún están por resolver. Tras el lanzamiento exitoso de *Swift* y *Fermi*, la observación de los GRBs en múltiples longitudes de onda está proporcionando un nuevo enfoque para poder comprender mejor este fenómeno.

Uno de los GRBs estudiados en este trabajo ha sido GRB 140629A, un estallido de larga duración que detectó el satélite *Swift* y que se pudo observar en diferentes longitudes de onda, obteniéndose un conjunto de datos abundantes que incluye el óptico (por medio de *Swift*/UVOT y de otras instalaciones astronómicas en todo el mundo), infrarrojo (*Spitzer*) y rayos X (*Swift*/XRT). Los datos analizados se tomaron entre 40 segundos y 3 años después del GRB, haciendo de este un caso propicio para poder investigar las propiedades tanto de la emisión colimada como de la de la galaxia anfitriona. A través de las líneas de absorción características presentes en el espectro óptico se derivó el corrimiento al rojo de este GRB (z = 2.276$\pm$0.001). Por otro lado, la evolución de la distribución espectral de energía en el rango del óptico a los rayos X no es significativa. La densidad de columna de hidrógeno N_H se midió en $7.2 \times 10^{21}\mathrm{cm}^{-2}$ a lo largo de la línea de visión. La postluminiscencia observada se puede explicar por medio de la existencia de un chorro colimado resultante de la onda expansiva procedente de un motor central de larga duración, produciéndose la expansión en un medio uniforme y en el régimen de enfriamiento lento. También al final de la fase de inyección de energía, se observa una fase de declive tanto en la banda óptica como en la de rayos X. Igualmente se encuentra una desviación (rotura) de la caída del flujo observado de la postluminiscencia, de manera acromática, en las curvas de luz de la posluminiscencia $\sim$ 0.4 d después del GRB. Ajustamos los datos de las múltiples longitudes de onda de manera

simultáneamente con un modelo basado en una simulación numérica y encontramos que las observaciones pueden explicarse por un chorro uniforme estrecho en un ambiente denso con un ángulo de abertura de 6.7° visto 3.8° fuera de su eje, lo que implica que se liberó una energía total de 1.4×10^{54} erg. Usando el valor del corrimiento al rojo y el ángulo de abertura, encontramos que GRB 140629A obedece las relaciones de Ghirlanda y Amati. Desde el momento del máximo de la curva de luz, identificado como el inicio de la onda de choque que se propaga en el tiempo (181 s después del disparo), el factor de Lorentz inicial (Γ_0) debe situarse en el rango 82-118. Haciendo un ajuste de los valores fotométricos de la galaxia anfitriona, encontramos se trata de una galaxia de baja masa con formación estelar y una tasa de formación estelar de log(SFR)=$1.1^{+0.9}_{-0.4}$ $M_{\odot}yr^{-1}$. Obtenemos un valor de la densidad del hidrógeno neutro N_{HI} ajustando el espectro óptico, $\log N_{HI} = 21.0 \pm 0.3$, clasificando este sistema como un sistema de Lyman-alfa amortiguado. Las líneas de alta ionización (N V, Si IV) también se detectan en el referido espectro. Y las observaciones de polarización realizadas por el telescopio MASTER indican que este estallido es un evento débilmente polarizado.

El segundo evento de los estudiados ha sido GRB 190829A, que fue detectado por *Fermi* y *Swift* y también a rayos-gamma de muy alta energía (VHE) por HESS (Sistema estereoscópico de alta energía). La emisión temprana mostró dos episodios de emisión separados por un intervalo sin actividad alguna con una duración de $\sim$ 40 s. Presentamos las observaciones del 10.4 m Gran Telescopio CANARIAS (GTC) en relación a la post-luminiscencia de GRB 190829A y su supernova subyacente. El corrimiento al rojo de este evento se detectó con z=0.0785$\pm$0.005. También comparamos GRB 190829A con GRB 180728A, un estallido con un comportamiento similar, y discutimos las implicaciones en los mecanismos físicos subyacentes que producen estos dos GRBs. Los datos fotométricos multi-banda junto con la observación espectroscópica de este evento se tomaron con el telescopio GTC de 10.4m. Junto con los datos de la emisión inicial, los datos del GTC se utilizan para comprender los mecanismos de emisión y el posible progenitor. En el análisis detallado de las observaciones multibanda del resplandor, encontramos que este evento es consistente con el paso de la frecuencia de enfriamiento entre las bandas ópticas y de rayos X en épocas tempranas. Luego estudiamos la supernova subyacente 2019oyw, que domina las fases más tardías. Aunque las propiedades temporales de emisión rápida de

GRB 190829A y GRB 180728A son similares, los dos pulsos de rayos-gamma son diferentes en el dominio espectral. Encontramos que SN 2019oyw, asociada con GRB 190829A se puede explicar por la desintegración de Ni y ha sido clasificada como una supernova de Tipo Ic-BL. Las propiedades espectroscópicas y fotométricas de esta supernova son consistentes con las observadas para SN 1998bw (asociada a GRB 980425), pero mostrando una evolución más rápida. Además de los dos GRBs de larga duración reseñados anteriormente, también investigamos la emisión rápida y las propiedades de la postluminiscencia del estallido de rayos gamma de corta duración GRB 130603B así como de otros 8 eventos GRB de corta duración, detectados durante el periodo 2012-2015, y observados por varias instalaciones en diferentes longitudes de onda, incluyendo el telescopio GTC de 10.4 m de diámetro. Los satélites *INTEGRAL* (SPI-ACS), *Swift* (BAT) and *Fermi* (GBM) obtuvieron datos de alta energía de dichos GRBs. Los datos de emisión temprana por *INTEGRAL* en el rango de energía de 0,1 a 10 MeV para sGRB 130603B, sGRB 140606A, sGRB 140930B, sGRB 141212A y sGRB 151228A no muestran ningún indicio de la emisión extendida o la actividad precursora y sus propiedades espectrales y temporales son similares a los que se ven en el caso de otros GRBs de corta duración. Para sGRB 130603B, nuestros nuevos datos fotométricos en relación a la posluminiscencia restringen el decaimiento temporal previo al desvío en la curva de luz producida por la expasión del chorro, gracias a haber dispuesto de una cobertura temporal más completa. La curva de luz de la postluminiscencia, que contiene tanto nuestros datos fotométricos nuevos como los publicados anteriormente, es consistente con el modelo de post-luminiscencia atravesando un medio de tipo interestelar (ISM). El modelado de las galaxias anfitrionas de sGRB 130603B y sGRB 141212A, utilizando el software LePHARE, respalda un escenario en el que el entorno de la explosión en la galaxia huésped está experimentando una actividad de formación estelar moderada. A partir de la inclusión de nuestros datos para los otros 8 GRBs de corta duración anteriormente referidos, podemos imponer restricciones estrictas a la no detección de la postluminiscencia, la galaxia anfitriona o cualquier emisión de kilonova subyacente. Nuestras observaciones tardías en el tiempo, de la post-luminiscencia de sGRB 170817A / GW170817 también se discuten y comparan con el subconjunto de GRBs de corta duración.

Acknowledgements

It is lucky to have a PhD study experience in southern Spain in my life where I met much talent with kindness and enthusiasm. Here I would like to acknowledge all those who have provided supports and helps in the PhD studying and this Thesis writing. Without their kind support and guidance, this thesis would be not possible.

First of all, I would like to extend the sincere gratitude to my supervisor, Prof. Alberto J. Castro-Tirado. His selfless guidance helped me to present this thesis (finally!). His broad scientific interest and distinguished foresight permanently remove my doubts during the different research steps. Besides, he also provided much help in my daily life. His hard-working habit and the impression that he never seemed to sleep also inspired positivism during these years.

I owe many thanks to Prof. Bin-bin Zhang as co-supervisor of this thesis, an excellent researcher in the gamma-ray burst research field, who kindly kept the door open for any problem in astronomy or computer science at any time. I also thank Dr. Samantha Oates, a former post-doc in our ARAE group who taught many of us about optical data analysis. I hope she has a good life with her husband Andy Fenney and her new baby Toby back to England. I am also grateful to Prof. Shashi Pandey, a great theoretical scientist and a collaborator, who answered many questions in this study to improve the final result. He also helped me in different aspects, so this project progressed more smoothly.

I also want to express heartfelt thanks to all of the ARAE research group members at IAA-CSIC. To Juan Carlos Tello, who kindly shared information and answered my endless questions, some of them probably stupid ones. Wishing he will have a good life with his wife Sandra Ocando and his son Daniel (I do not forget the expression "Oh, my God"). To Ronan Cunniffe for his brilliant computer technology skills making our life easier regarding his support on laptop's management and server access. I hope he will have a great time at Czech Rep. with the new job he took there. To Emilio Fernández, for his hard

work on the BOOTES network telescope management supporting our observation smoothly and continually and kindly sharing our fascinating talks on the local culture. I also hope he will have a good life with his family and the extensive olive fields. Soomin Jeong, a post-doc from Korea with a similar cultural background, taught me a lot at the start of this research. I hope she will have a good life after her married (and got a baby!) back to Korea. To Martin Jelinek, Ruben Sánchez-Ramírez, Irene Carrasco and Adrián Ayala for the good discussions I had with all them. Finally, also in memory of Javier Gorosabel, who was a great scientist and provided many valuable suggestions when I just arrived in Granada. Pity that he left us so suddenly. I hope he will be fine in Heavens.

I would like to thank all friends whom I met at IAA-CSIC. To the activities organizers Michael Jones, Estefanía C. López and Matilde Fernández for their professional hiking plans, free cars, 'Queimada' from Galicia and other celebrations for festivals. To my lunch companions, Naím, Jesus Muñoz, Antonio, Fran, Ny, Manuel Lampón, Javier, Jesús Escobar, Estela, Pablo Santos, Antonio, Christina, Jaime Perea and Ascensión del Olmo for their freely talk and sharing a handmade cake that makes the lunch to be the best relax time and first Spanish slang learning, "Por yaqui", and from their enthusiasm to help me washing the dishes. Mainly thanks Manuel Lampón, who proposal a five-minute Spanish time, which improved my language capability. To my office mate Raúl Carballo who helped me find the apartment and other living things. Some of them already moved to a new job place, and I hope they get a good time there. To student manager María who kept tracing my PhD progress. To Toalá, Alejandro, Alex, Alicia, Katarzyna, Sara and Mariel, for their valuable help. To Josefa Masegosa, who helped to provide documents for the university from the institute. To Chinese post-docs, Xuan Fang, Hui Dong, Dongshuai Li, and the old China hand Rubén García for their help when I first came to Spain and sharing free cars during the summer vacation. I especially appreciate Hui's wife Yuan Yuan, her lovely son Tan-tan and their two fat cats, Antonio and Ela. Those two cute and lazy cats also accompanied me for half a year. To Dongshuai's husband Tao Liu, who showed very professional skills in photography. To the research visitors, Xiao-yan Li, Yu-Feng Fan, Mary Loli, Margarita, Anqi Li, Maria Caballero-Garcia (now in our ARAE team, back to Spain), Juan Luís, Esma Zouaoui and Amina Leghmouche for their helpful discussions. And to the security personnel who work at the main entrance, who came for opening

the entrance gate for me many times.

I owe deeply indebted to all the professors from the university and IAA regarding the Físymat astronomy classes: Dr. Iván Agudo, Dr. Rainer Schoedel, Prof. Enrique P. Jiménez, Dr. Martín Guerrero, Dr. José Francisco Gómez Rivero, Dr. Guillem Anglada, Prof. Antonio Alberdi, Prof. Eduardo Battaner, Prof. Inma Domínguez, Dr. Almudena Zurita, Prof. Carlos A. Abia, Dr. Jorge Jiménez et al. Their broad knowledge and excellent teaching activities helped me to expand the scientific horizon and also provided helpful advice in this research. And many, many thanks to the coordinator of the doctorate program Físymat, Prof. Juan Soler, who helped patiently in the registration process every year.

Next, the acknowledgement goes to my friends in La Mayora, where the BOOTES-2 station is located in the wonderful agriculture research institute IHSM "La Mayora" belonging to both CSIC and Málaga University at Algarrobo-Costa. I stayed there for several months. To the manager Antonio Cordón for his help with documents and the fire accident treatment. To the hiking organizers, Carmen and Jorge L. Cabrera, who make a detailed trip plan and drove me to the starting place. To my kindly neighbours Juan M. Losada, his wife Nuria Clamor and their lovely daughter, for their kind invitation to join their party which made life more exciting while I was in La Mayora. To the cats' breeder Dr. Rafael F. Muñoz, who kindly provide food for those wild cats living in the IHSM "La Mayora" UMA-CSIC agriculture institute. To Francisco R. Ruiz, who always was driven a white pickup truck with white hair, his selflessness made the heavy luggage carry on easier. Thanks to those students and visitors working on the fruit plants, Irene, Lidia, Fabio, Eszter, Mercedes, and Alicia, who introduced me to their laboratories and taught me the seasonal fruit secrets.

Particular thanks go to Chinese friends in Spain. To Quan, Ruiting, Yingqiang, Weijia, Yue male, Xiaoxuan, Jialin, Yiyi, Jingxuan, Simin, Bin, Yue female, Luyi, Meng, Rui, Wenmin et al. for their selfless help on language translation, entertainment and leisure activities. All of that makes me feel delighted and relax with them.

I know there still have many names forgotten in the previous paragraphs, which also contributed to either this research or my residence. Thanks here for them also.

Finally, extended profound gratefulness goes to my family for their most

robust backing and supports. My health situation is always their top concern, and their condition is always good, which should be a white lie. Encouragement from married sister and brother-in-law wipes out those worries all through these years. Their support implies immeasurable contributions and sacrifices for this study, which is the power source for pushing every step forward. Thanks to them, loving them is always sincere.

Contents

List of Figures

List of Tables

Moonlight
Flapping the Mediterranean under the Hot Gates
Ursa Minor
Point the home at Palos de la Frontera
Sun
Shines on a falling apple
Universe
White the cloud upon Havel

.

—-A spoon of Milk Way dedicated to my family.

Chapter 1

Introduction. Gamma-ray bursts

Gamma-ray bursts (GRBs) are the most violent and catastrophic explosions in the Universe, which involve the extreme processes of stellar evolution, such as the final collapse of the massive stars or the merger of compact binary stars. A typical GRB releases a total of energy $10^{48} \sim 10^{52}$ erg in several seconds, which is even greater than the sum of the energy emitted by hundreds of suns in their lifetimes. Since the first GRB detected by the *Vela* satellites in 1967 (Klebesadel, Strong, and Olson, 1973), more than half a century ago, several generations of instruments have been built in order to shed light in this scientific field. Due to their high energy release, and relativistic effects, GRBs have became one of the most active laboratories to test the different theoretical models. Typically, the average observed event rate of GRBs is about 1∼2 per day, with are randomly located in the sky (Paciesas et al., 1999).

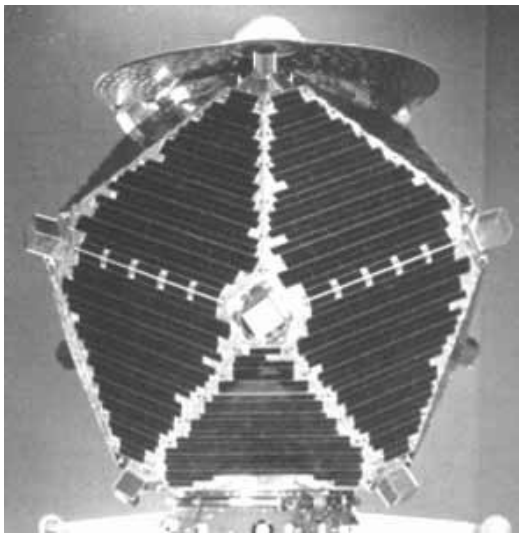

FIGURE 1.1: One of the *Vela* satellites[1].

Historical introduction

Missions

Capturing this elf (sort to speak) starts in the 1960s after the URSS and USA signed the nuclear-bang treaty. The Partial Test Bang Treaty (1963) included a comprehensive set of prohibitions on participating in any nuclear weapon activities. In order to check whether the URSS abided by the treaty, an American satellite named *Vela*[1] (see Figure 1.1) was designed to detect the γ-ray radiation of possible nuclear weapon experiments developed by URSS. Finally, six pairs of satellites were successfully launched between 1963 and 1965. On the 2nd July 1967 at 14:19UT (Strong and Klebesadel, 1976), several *Vela* satellites recorded a double peaked signal, shown in Figure 1.2. This initially caused some tension between the two countries, but following some careful analysis proved the signal to be unrelated to any nuclear experiment on the Earth. Nevertheless, these data remained classified until the scientists could access them in 1973 (Klebesadel, Strong, and Olson, 1973) publishing the list of another 15 similar events recorded by *Vela*. Since then, these events of astrophysical origin were named Gamma-Ray Bursts (GRBs).

In the following two decades, several instruments were able to detect new GRBs (*Konus, Ginga*, *Granat*-WATCH, etc.) (Mazets et al., 1981; Murakami et al., 1989; Castro-Tirado et al., 1994), but their origin remained an impenetrable mystery: where do the GRBs arise from? That led to the Great Debate in 1995 between Bohdan Paczynski (Cosmological viewpoint, Paczynski, 1995) and Donald Lamb (Galactic viewpoint, Lamb, 1995). This situation started to change thanks to the large number of GRB detections achieved in the 1990s and the instrument BATSE on-board the *CGRO*, followed by *BeppoSAX*, which had the capability of a high time resolution and precise localization.

The *Compton Gamma Ray Observatory (CGRO)* was designed as a gamma-ray satellite, being part of the NASA 'Great Observatories' series. It included four main instruments: BATSE (Burst and Transient Source Experiment), OSSE (Oriented Scintillation Spectrometer Experiment), COMPTEL (Imagining Compton Telescope) and EGRET (Energetic Gamma Ray Experiment Telescope), which could cover the energy range from 30 keV to 30 GeV (see Figure 1.3, Gehrels,

[1] https://space.skyrocket.de/doc_sdat/vela.htm

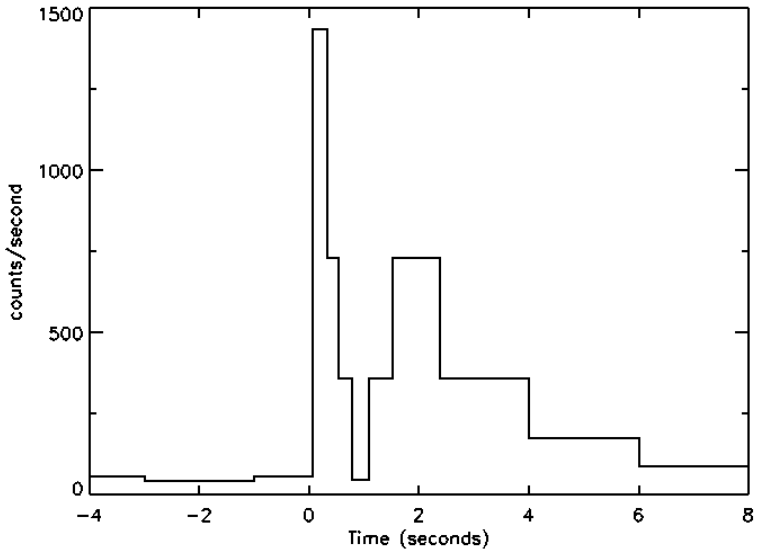

FIGURE 1.2: First GRB light curve recorded by *Vela* (Strong and Klebesadel, 1976).

Chipman, and Kniffen, 1993). Certainly, BATSE was the most fantastic experiment among them regarding GRB research, consisting of 8 modules that pointed to different sky directions (Fishman et al., 1994). Each module equipped with a 2000 cm^2 Large Area Detector and a Spectroscopy Detector (both made of scintillator crystals), which were optimized for directional response and energy resolution respectively. With their high sensitivity, BATSE could record a GRB at a time resolution of 100 ms. Hence, the 8 detectors could cover the entire sky (except they are blocked by the Earth) in order to monitor any incoming GRB and locate it with an uncertainty of few degrees. During its nine-year lifetime, BATSE detected 2704 GRBs (Kaneko et al., 2006) as well as other variety of other astrophysical phenomena, such as Soft Gamma-ray Repeaters (SGRs), Solar Flares and new phenomena such as Terrestrial Gamma-ray Flashes (TGFs). One of the main results achieved by BATSE was the finding of two types of GRBs based on the bimodal duration distribution (Kouveliotou et al., 1993). Furthermore, the distribution of GRBs in the sky being isotropic (Paciesas et al., 1999) confirmed the early *Konus* findings (Mazets et al., 1981) also provided a piece of indirect evidence that GRBs were located at cosmological distances

(details in the following section).

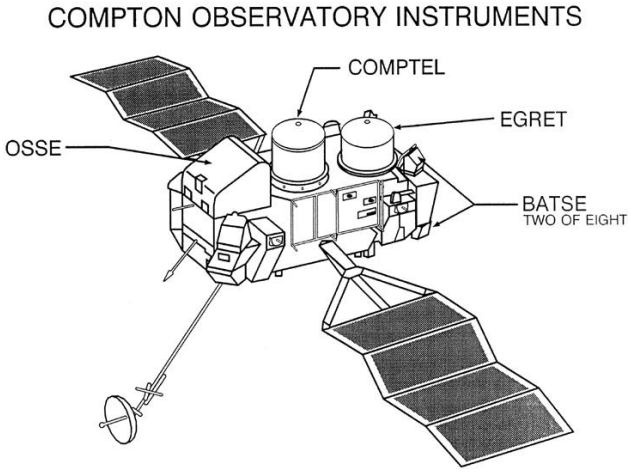

FIGURE 1.3: The *CGRO* satellite marked with its payloads (McConnell, 2017).

Although BATSE could locate hundreds of GRBs on a yearly basis in the 1990s, the error regions were far too large for ground-based telescopes to conduct follow-up observations. Then an outstanding satellite for GRB research was launched in the meantime. In 1996, the it BeppoSAX (Satellite Italiano per Astronomia X) was successfully put in orbit. It was an Italian-Dutch satellite whose scientific goal was performing spectroscopic and time variability studies of cosmic X-ray sources. Moreover, its accurate position capability would allow the prompt identification of new sources in the sky paving the way for multi-wavelength follow-up observations on GRBs. Three instruments were placed in this satellite: the Gamma-Ray Burst Monitor (GRBM), the Wide Field Camera (WFC, 2 units) and four Narrow Field Instruments (NFI), working at 60-600keV, 2-30 keV and 0.1-120 keV, respectively (see Figure 1.4, Boella et al., 1997). In order to promptly localize a GRB, the observing strategy was optimized thanks to the cooperation between two instruments: GRBM and WFC. The GRBM consisted of four 1136 cm^2 CsI scintillator slabs and covered nearly 4π field of view, thus being able to triggering on GRBs, but without providing an accurate localization. However, the WFC was position sensitive and equipped with a coded mask ($40^\circ \times 40^\circ$ field of view) could provide the source position information with few arcmin accuracy (Frontera et al., 2009). Since the WFC could not provide the source positions in flight, once GRBM triggered a new GRB, the scientist-on-duty had to check whether the WFC image revealed

any uncatalogued X-ray source at the same burst time recorded by the GRBM. This was done once the data were downloaded after each Malindi passage, and then they could distribute to ground-based observers the newly GRB position with an error box of just several arcminutes. Even if there was only a 10% probability that GRBs detected by the GRBM could fall within the WFC field-of-view (FOV), *BeppoSAX* managed to observe 1082 GRBs on its 6 yr lifetime. time (Frontera et al., 2009).

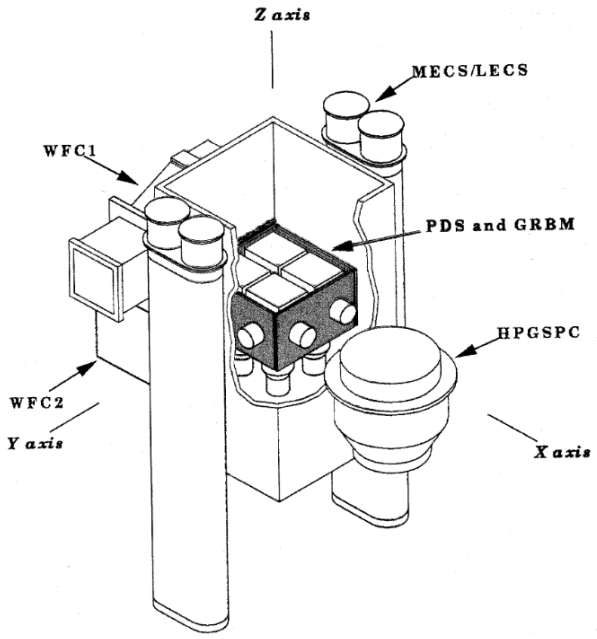

FIGURE 1.4: Payloads on *BeppoSAX* statellite (Frontera et al., 2009).

On 02:58 UT Feb. 28, 1997, the *BeppoSAX*/WFC pinpointed an event, GRB 970228 (Costa et al., 1997), within a 3′ error region. This small localization uncertainty led to the first detection of its X-ray counterpart (the so-called afterglow) a few hours after (see Figure 1.5) when the *BeppoSAX*/NFI pointed to that direction of the sky. Then van Paradijs et al., 1997 used the 4.2 m William Herschel Telescope at La Palma to identify the optical afterglow 1.9 days post-trigger (see Figure 1.6). Since a spectroscopy observation was lacking, its distance could not be determined. Nevertheless, just a couple of months later, another event, dubbed GRB 970508, triggered *BeppoSAX* on May 8, 1997, at 21:42 UT, and this time, a radio counterpart was first detected by the Very Large Array (VLA) (Frail et al., 1997), besides an accompanying optical counterpart. Its

redshift was then determined by absorption lines from Keck spectroscopy, $z = 0.835$ (Metzger et al., 1997), which provided the first direct evidence for GRBs being at cosmological distances.

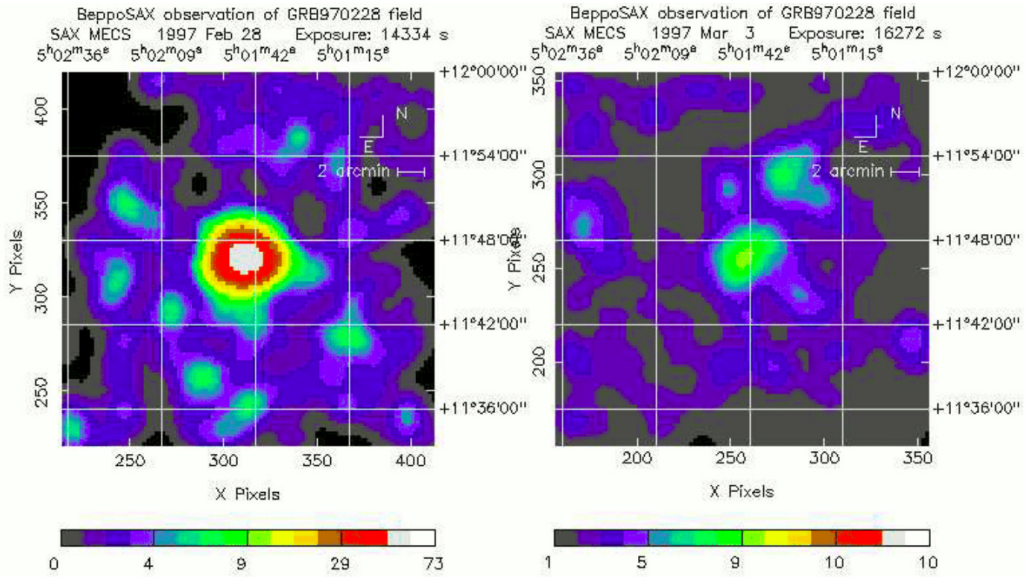

FIGURE 1.5: The first GRB X-ray afterglow (for GRB 970228) recorded by *BeppoSAX* a few hours after (Costa et al., 1997).

Following the successful European *BeppoSAX* mission, a complementary mission named *High Energy Transient Explorer (HETE)* developed in the US was launched a few years later, with participation (besides the US) of Japan, France, and the Netherlands. It was designed to have three independent modules: the Soft X-ray Cameras (SXC), a Wide-field X-ray Monitor (WXM) and the French Gamma Telescope (FREGATE), which altogether covered the energy range from 0.5 keV to 400 keV, see Figure 1.7 (Shirasaki et al., 2003). In order to pinpoint the GRB, the three modules had to work independently and drive other instruments, i.e. if there was one trigger detected by any one of those three detectors, the other two instruments had to collect data at a higher temporal and spectral resolution mode in the direction of the triggered instrument. With the improvement of the detector technology at that time, *HETE*, could localize the transient position with a 10" accuracy and quickly spread the position information to the ground-based observers for prompt follow-ups. Unfortunately, *HETE-1*, the first satellite of this program, first launch failed due to technical reasons in 1996. We had to wait until 2000 when *HETE-2* was successfully launched, i.e. four years after *BeppoSAX*. *HETE-2* managed to achieve some breakthrough

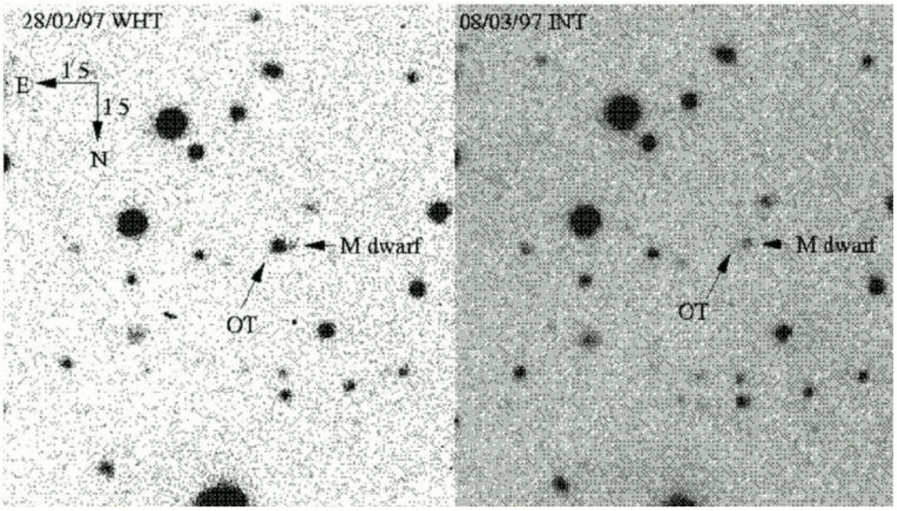

FIGURE 1.6: The first GRB optical afterglow (for GRB 970228) observed by the 4.2 m WHT (van Paradijs et al., 1997).

discoveries during its lifetime, when around 250 GRBs were detected during its eight years operation (Pélangeon et al., 2008). These include the first GRB and supernova (SN) association event (Hjorth et al., 2003), the first optical afterglow of a short-duration burst (Fox et al., 2005), and insight into the optically dark bursts (Nakagawa and Hete-2 Collaboration, 2009).

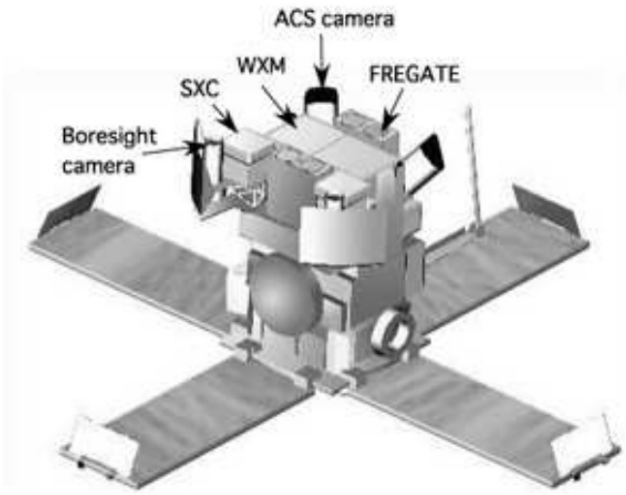

FIGURE 1.7: The *HETE − 2* satellite and its payload (Shirasaki et al., 2003).

In 2002, the *INTErnational Gamma-Ray Astrophysics Laboratory (INTEGRAL)*

was launched, becoming at the time the most sensitive MeV gamma-ray detector in space and the first space observatory which could simultaneously observe a given target in gamma-rays, X-rays and optical. The European Space Agency (ESA) led the design, which aimed at providing spectroscopy and imaging of the most energetic astrophysical sources. The payload included two gamma-ray detectors with coded aperture masks: the Spectrometer on it INTEGRAL (SPI; 20 keV - 8 MeV) and the Imager on Board the *INTEGRAL* Satellite (IBIS; 15 keV - 10 MeV), one X-ray detector: the Joint European X-ray Monitor (JEM-X; 3 - 35 keV), and an optical instrument: the Optical Monitoring Camera (OMC; 500-850 nm), see Figure 1.8 (Winkler et al., 2003). Any GRBs within the IBIS field of view could be localized during the ground-based analysis once the *INTEGRAL* soft gamma-ray imager (ISGRI) data was processed by the *INTEGRAL* Burst Alert System (IBAS) with an average delay of only 10 s. A coincident method used to locate the burst in two different ways, whose first triggering mechanism was the search of significant excess in the accumulated overall count rate against the average background, whereas the second one was based on the comparison of continuous images with varying integration times from 10 s to 100 s in order to detect the new source. Thus, any GRB location could be achieved with a typical uncertainty radius of 3 arcmin in a few tens of seconds after the GRB. Since 2002, *INTEGRAL* has already observed ∼140 GRBs[2] so far and its operation has been extended until the end of 2022.

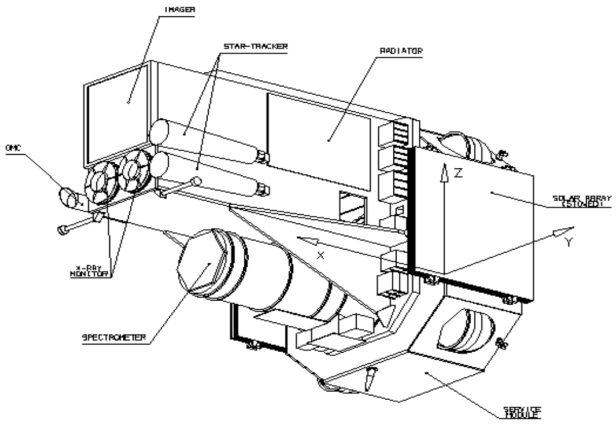

FIGURE 1.8: *INTEGRAL* satellite and its payloads (Dean et al., 2003).

[2] http://ibas.iasf-milano.inaf.it/

Following the experience with the above-mentioned satellites, it was realised the importance of the rapid localisation and the capability of distributing this information as soon as possible in order to get high-quality GRBs multi-wavelength follow-up observations. Hence, the next milestone satellite in the GRB research field was the *Swift* Gamma-Ray Burst Mission (dubbed nowadays the *Neil Gehrels Swift Observatory*, name after Neil Gehrels, the Principal Investigator, who passed away in 2017). *Swift* was designed to focus on GRB science gathering multi-wavelength observations, covering from optical to gamma-ray. This medium-size mission contained three main instruments: the Burst Alert Telescope (BAT; Barthelmy et al., (2005)), the X-ray Telescope (XRT; Burrows et al., (2005)) and the Ultraviolet Optical Telescope (UVOT; Roming et al., (2005)), see Figure 1.9[3]. BAT consisted of a wide field of view camera with a coded aperture mask used for source localisation of photons at an energy range of 15-150 keV. Besides, the XRT was a 23.6 arcmin FOV imaging spectrometer optimised to detect the soft X-ray photons in the 0.2 - 10 keV range, and the UVOT is a modified Ritchey-Chrétien telescope which was designed to follow up optical afterglows in 7 bands, i.e. $uvw2, uvm2, uvw1, u, b, v, white$, and two grisms which covered the 170-650 nm range (Gehrels et al., 2004). A great improvement over previous missions was the localisation strategy. Once a burst was detected with BAT, the software on-board calculates the GRB preliminary position with < 4 arcmin accuracy, which will be provided to ground-based facilities, with some of them (automated/robotic telescopes) pointed to the GRB location within a minute or so. On this manner, *Swift* can autonomously slew to this position. Hence, within 20-70 s, the GRB position will be covered by the two narrow field instruments XRT and UVOT. Then, a more precise position can be provided once the X-ray (optical) afterglow is detected. With its outstanding capability of rapid source localisation to arcsec accuracy and quick data dissemination, *Swift* has detected already more than 1600 GRBs[4] and provided a complete study of this phenomenon which has prompted the GRB science development since 2004. It is expected to last at least a few more years providing exciting GRB science, such as the one I will describe in the following sections.

As *Swift* was conceived as a rapid-response multi-wavelength mission whose

[3] https://i0.wp.com/www.esascosas.com/wp-content/uploads/2016/10/SWIFT3.jpg

[4] https://swift.gsfc.nasa.gov/archive/grb_table/quickview/

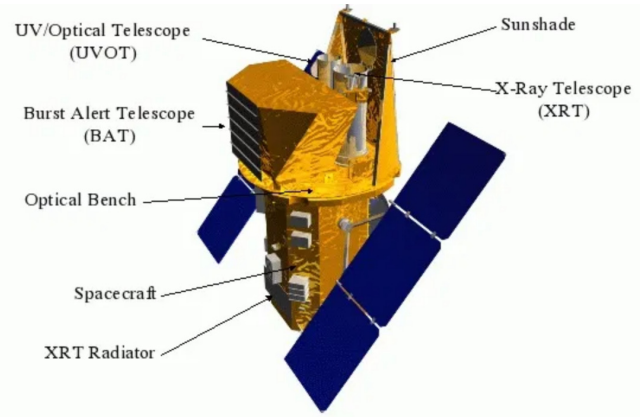

FIGURE 1.9: The *Swift* satellite and its payload[4].

upper energy band was limited to 150 keV (Barthelmy et al., 2005), it has not the capability to detect GRB high-energy photons at higher energies (hundreds of keV or in the MeV range). In order to cover this gap and to observe the high-energy Universe following the *CGRO*, the *Fermi Gamma-ray Space Telescope (FGST)*, formerly named the *Gamma-Ray Large Area Space Telescope (GLAST)*, and launched in 2008. Its payload consisted of two main instruments: the Large Area Telescope (LAT) and the Gamma-ray Burst Monitor (GBM) (von Kienlin et al., 2020). LAT is an imaging gamma-ray telescope for recording photons between 20 MeV - 300 GeV within its FOV, covering 20% of the sky (Atwood et al., 2009). At the same time, GBM can cover the whole sky with 12 sodium iodide detectors (NaI) and two bismuth germanate detectors (BGO) which are active in the 8 keV-1 MeV and 0.2 - 40 MeV bands respectively (Meegan et al., 2009). Those detectors are distributed in different locations in order to point to different sky regions to detect GRBs from any incoming direction to avoid being blocked by the Earth (see Figure 1.10). Although *Fermi* is capable of detecting higher energies GRB, its localization accuracy is not as good as *Swift*. However, the synergy between *Swift* and *Fermi* extend the GRBs' observation wavelength from the optical range to even GeV energies, which has opened a new window in this field.

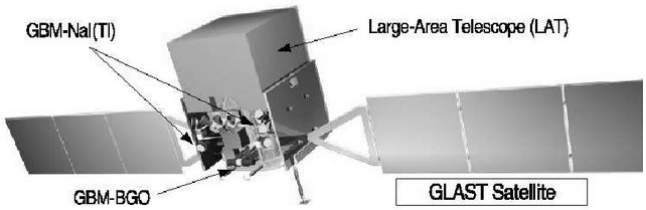

FIGURE 1.10: The *Fermi* satellite and its payload (von Kienlin et al., 2004).

Satellite Networks

The InterPlanetary Network (IPN)[5] was conceived in order to locate any GRB (or SGR) detected with several spacecraft. It was proposed that missions with very eccentric orbits or even planetary missions could be equipped with gamma-ray detectors. The idea came in the early times (1970s) when the method of considering the different arrival times from the GRB event to different satellites was proposed (i.e. 'triangulation') in order to significantly improve the location in the sky of those events. Using each pair of spacecraft, the arrival time difference in each pair provides a single annulus. When combining different pairs of spacecraft, several annuli are obtained and their overlap indicates the actual burst direction (see Figure 1.11 upper panel, Hurley et al., 2013). Within 24-48 h after the event, this position can be distributed to the astronomical community in order to take follow-up observations. So far, 32 satellites have contributed to the IPN, with the Third IPN being the one which is operational nowadays, following the launch of *Ulysses* in 1990 (Hurley et al., 2003), including another six missions: *Odyssey*, *RHESSI*, *Swift*, *Konus*-Wind, *INTEGRAL*SPI-ACS and *Fermi* (Hurley et al., 2016) that all together can provide a position at arcmin accuracy level. See, for example, GRB 200415A (see Figure 1.11 bottom panel, Svinkin et al., 2020).

On the other side, technological development nowadays makes the spaceborne GRB missions calculate the GRB position in real-time. Hence, the Gamma-ray Burst Coordinates Network (GCN)[6] was first built to rapidly distribute that positional information automatically. It started with the BATSE coordinate distribution network (BACODINE), which aimed at observing the prompt GRB emission at other wavelengths while the GRB is still going on (Barthelmy et

[5] http://www.ssl.berkeley.edu/ipn3/index.html
[6] https://gcn.gsfc.nasa.gov/

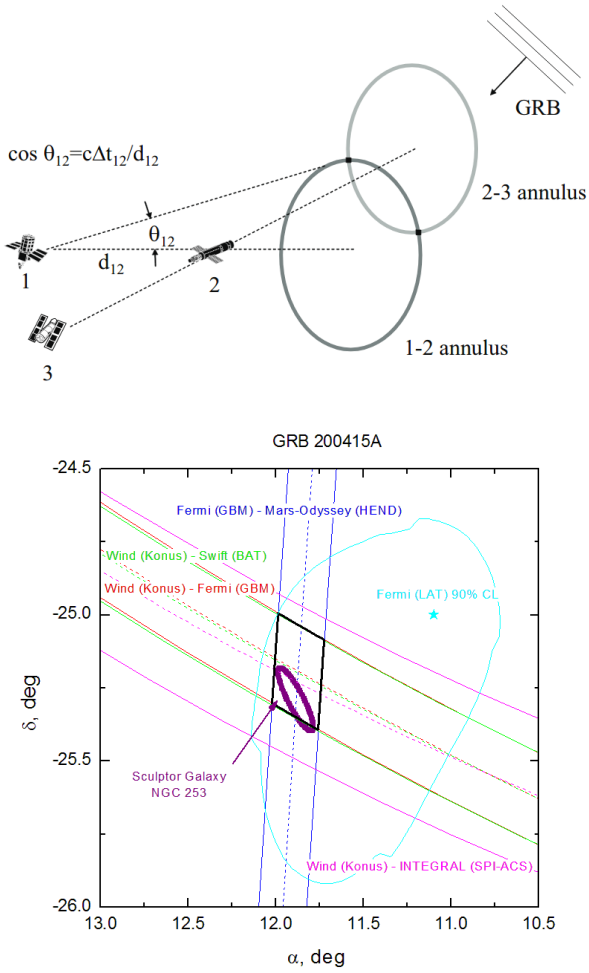

FIGURE 1.11: The triangulation technique used in the IPN network (upper panel, Hurley et al., 2013) and its location of GRB 200415A (bottom panel, Svinkin et al., 2020).

al., 1995; Barthelmy et al., 1998b). Nowadays, it has already become the most powerful way for automatically receiving and distributing information in order to distribute essential information (position, preliminary light curve, etc.) and ongoing ground-based observations that can be reported by any observer in the world (Barthelmy, 2008). This has helped greatly to extend the astronomical community in order to properly plan any follow-up observations (see Figure 1.12). Moreover, with the newer multi-messager detectors, such as the gravitational interferometer LIGO/Vigo and the neutrino detectors (IceCube,

ANTARES) alerts joining this network for distribution of alerts, new opportunities have been given, not serving only to the GRB community but also offering relevant information for new transients. Thus, the network now has been renamed: Transient Astronomy Network (TAN).

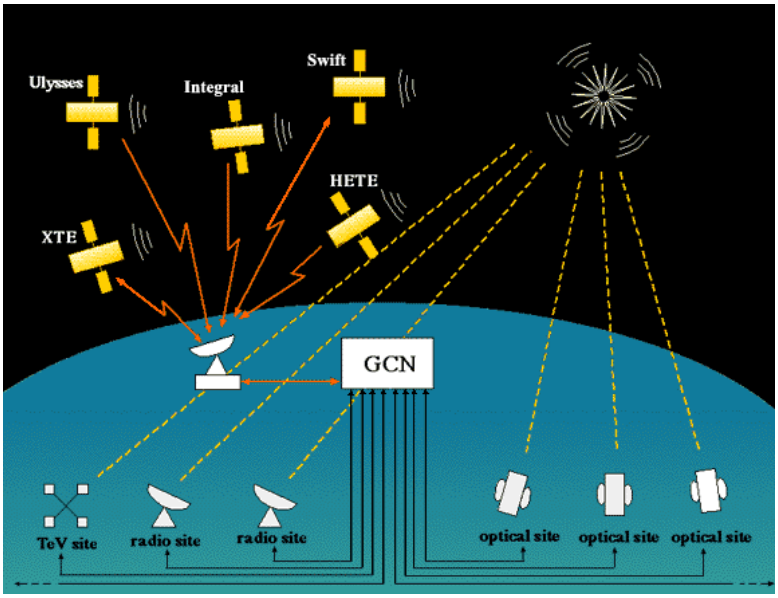

FIGURE 1.12: The Gamma-ray Coordinates Network (GCN) modus operandi[6].

Therefore we can consider these two different approaches regarding the gathering of GRB multi-wavelength data. The first one is installing multi-band detectors on the same satellite, and the second one is to distribute the detection information to the multi-wavelength follow-up observers as soon as possible. In the former case, the given satellite has to focus in the high energy range (hard X-rays or gamma-rays) in order to pinpoint the GRB itself, such as *Vela* and *CGRO*/BATSE. A second step was to include as payload lower-energy instruments, such as *BeppoSAX* did in the 1990s, followed by *INTEGRAL* and *Swift*, or even extend the higher energies to the GeV range (e.g. *Fermi*). In addition to the above-mentioned satellites, many missions have the capability of detecting GRBs even if they are not their main goals, such as *AGILE*, *AstroSat* and *HXMT*. Recently, the Korean UFFO experiment onboard the Russian *Lomonosov* satellite (launched in 2016) (Park et al., 2018) was a very interesting concept although no GRBs could be recorded due to a technical failure, and *GECAM* (using state-of-the-art scintillators) was just launched at the end of 2020 (Li et

al., 2020). The future is promising, with the advent of *SVOM* (a French-Chinese collaboration to be launched in 2022) (Yu et al., 2020) and *THESEUS* (an ESA M5 candidate mission, to be launched in 2032) (Amati et al., 2018). Their contributions will greatly increase our knowledge in GRB science due to the simultaneously multi-wavelength observations of GRBs from the bursting phase to the late afterglow.

Multi-messenger results

After accumulating multi-wavelength observations for more than half a century, provided by the above-mentioned missions and ground-based follow-up facilities, a rich database is now available. Here we will review the most outstanding results achieved so far in the following four subsections.

Electromagnetic counterparts

The observational results in the electromagnetic (EM) domain were achieved thanks to the available mature technology in all fields, spanning radio, near-infrared (NIR), optical, ultraviolet (UV), X-rays and gamma-rays.

Light curves

The prompt emission of GRBs is defined as the emission observed during the gamma-/hard X-rays phase, whose photons are the ones triggering the space instrumentation leading to multi-wavelength follow-up observations.

Thus, GRB light curves represent the count rates/photons recorded by the high energy detectors as a function of time. Each of the recorded events shows different variability patterns, meaning that each light curve is different from the rest. As it is shown in Figure 1.13, the light curves can be classified into four different categories Pe'er, 2015:

- single-peak events (e.g. GRB 910711),
- a smoothed light curve composed with several peaks (e.g. GRB 920221),
- separated multi-collisions (e.g. GRB 930131A),
- and irregular peaks (e.g. GRB 991216)

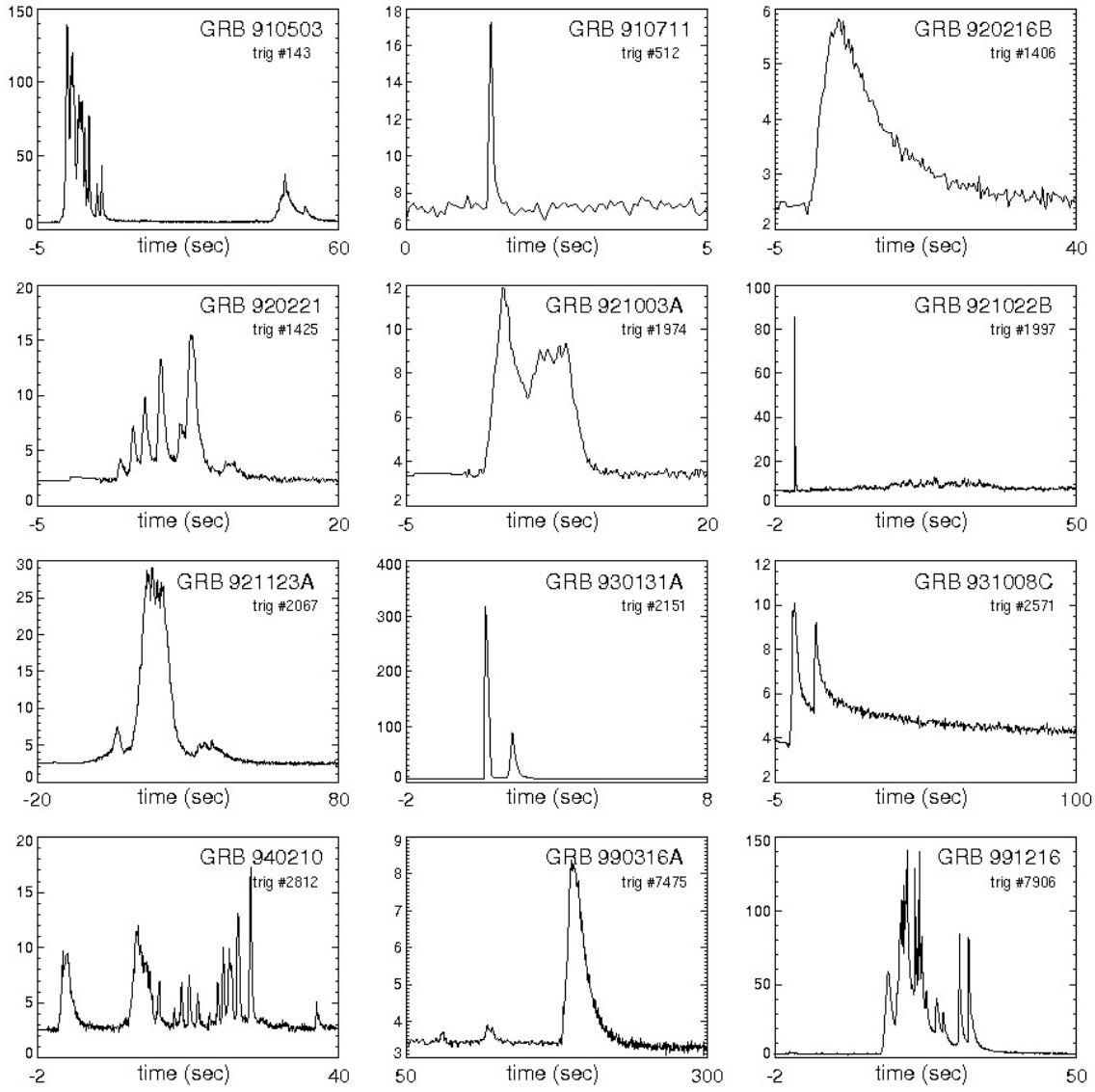

FIGURE 1.13: A sample of highly variable GRB light curves, taken from the BATSE GRB catalogue (Pe'er, 2015).

Generally, GRBs show during their prompt different overlapping episodes within a wide range of timescales. Some events can be split into several pulses, such as GRB 931031A, whose single pulse shows striking similarities with GRB 920216B, a fast rise and exponential decay (FRED) event (Fishman et al., 1994). There are also bursts that show separated pulses but with a small spike appearing before the main burst like GRB 990316A, where the initial spike can be considered a 'precursor' (Murakami et al., 1991). About 10% GRBs show such a feature and in the context of the theoretical models, it is proposed that

the precursor is the signature of the ejecta when the envelope of the supernova progenitor is being broken by the developing jet, showing a thermal spectrum, while the spectral analysis shows that the precursor is not too different from the main burst early phase (Hu et al., 2014). Another GRB class is the one showing the main burst being followed up by a softer, extended tail even longer than the main phase, which is dubbed 'extended emission' (Norris and Bonnell, 2006) as shown in GRB 921022B. But its soft spectrum is clearly different from the main burst (harder spectrum). The power spectrum density (PSD) analysis of GRBs found no evidence of quasi-periodic oscillations (QPOs) and the PSD can be fitted by power-law with an index of ∼-5/3 (Beloborodov, Stern, and Svensson, 2000), see Figure 1.14. Thanks to the high temporal resolution achieved by BATSE, the minimum light curve timescale of ~ 1 ms is derived, which represents the fast variability even in a short-duration burst (Walker, Schaefer, and Fenimore, 2000). This timescale can be used to constrain the size of the radiation-emitting region. Assuming a Lorentz factor (Γ) of $\Gamma \sim 100$ considering the relativistic effects, this implies an emitting region size with a radius $R < \Gamma^2 c\Delta_t = 3\times10^6$ km which indicates the GRB is originated from a stellar-size compact object, such as a stellar black hole.

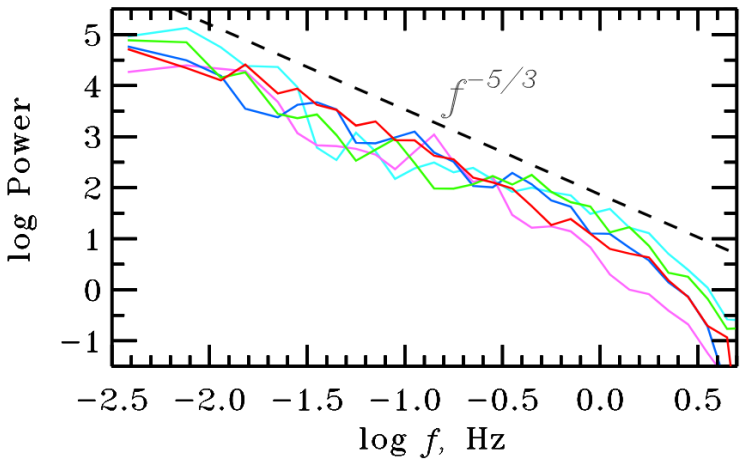

FIGURE 1.14: Power density spectrum for 5 brightest GRBs detected by BATSE with duration longer than 100 s (Beloborodov, 2002).

Duration distribution

The GRB duration is usually quantified as T_{50} (or T_{90}), which means the time interval over which 25% to 75% (or 5% to 95%) of the counts are gathered by the high-energy detector. Kouveliotou et al., (1993) used data from the BATSE 1B Catalogue covering the 25-350 keV energy band to study the statistical distributions of bursts as a function of T_{90} and found that it showed a bimodal distribution with a clear separation at ∼2 s, which also was confirmed later on by the BATSE 4B dataset (see Figure 1.15 left panel)[7]. This distribution pointed out the existence of two type of GRBs: short-duration GRB (sGRB, T_{90} <2 s) $vs.$ long-duration GRB (lGRB, T_{90} >2 s). And when using the available hardness ratio (HR) information, the T_{90}-HR diagram shows that the long-duration bursts are softer than the short-duration bursts (see Figure 1.15 right panel, Fishman, 1999), which is evidence of their different origin.

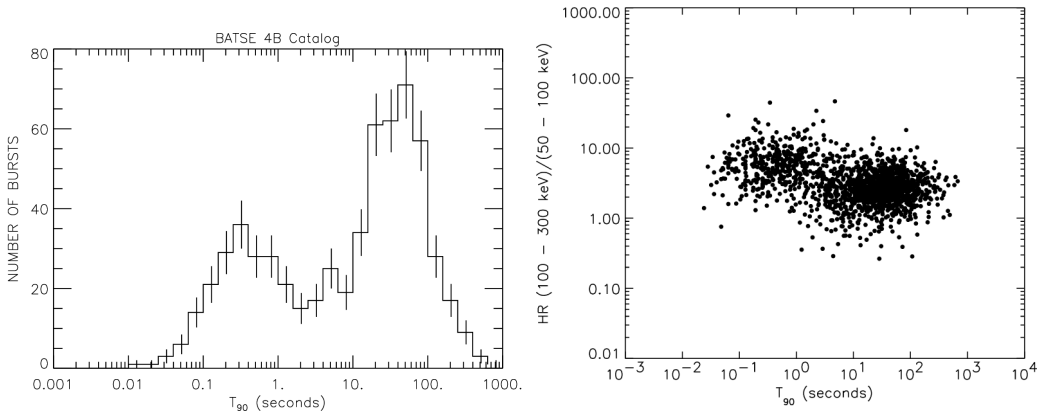

FIGURE 1.15: T_{90} distributions (left panel)[7] and T_{90}-HR diagram (right panel) for the events given in the BATSE 4B Catalogue (Fishman, 1999).

Besides the above-mentioned bimodal distribution of GRBs, Horváth, (1998) used the BATSE 3B Catalogue and found that the data can be fitted by a 3 Gaussian function model which indicates that the third class of events may exist which are called 'intermediate' GRBs. This trimodal distribution is being reinforced when considering *RHESSI* and *BeppoSAX* data. Nevertheless, it was found that the duration distribution can be affected by the given instruments and their different energy bands (Qin et al., 2013). From the latest statistical

[7] https://gammaray.nsstc.nasa.gov/batse/grb/duration/

studies using both the *Swift* and *Fermi* catalogues, it was found that the duration distribution is still in agreement with the bimodal distribution of short- and long-duration GRBs (Lien et al., 2016; von Kienlin et al., 2020) both with T_{50} or T_{90}.

Of course, there are outliers that not really fit into this typical classification, such as GRB 101225A (Campana et al., 2011; Thöne et al., 2011) and GRB 111209A (Greiner et al., 2015b) which both have durations $> 10^3$ s. Another event, GRB 110328A, showed long-duration emission even up to months and finally it was identified as a tidal disruption event (unrelated to classical GRBs) which was renamed to 'Swift J16444 9.3+573451' (Zauderer et al., 2011; Burrows et al., 2011). These exceptional cases indicate that the short-hard/long-soft classification is not sufficient for considering all GRBs, which supports that a subclass of 'super-long' GRBs exists, that could have a different astrophysical origin.

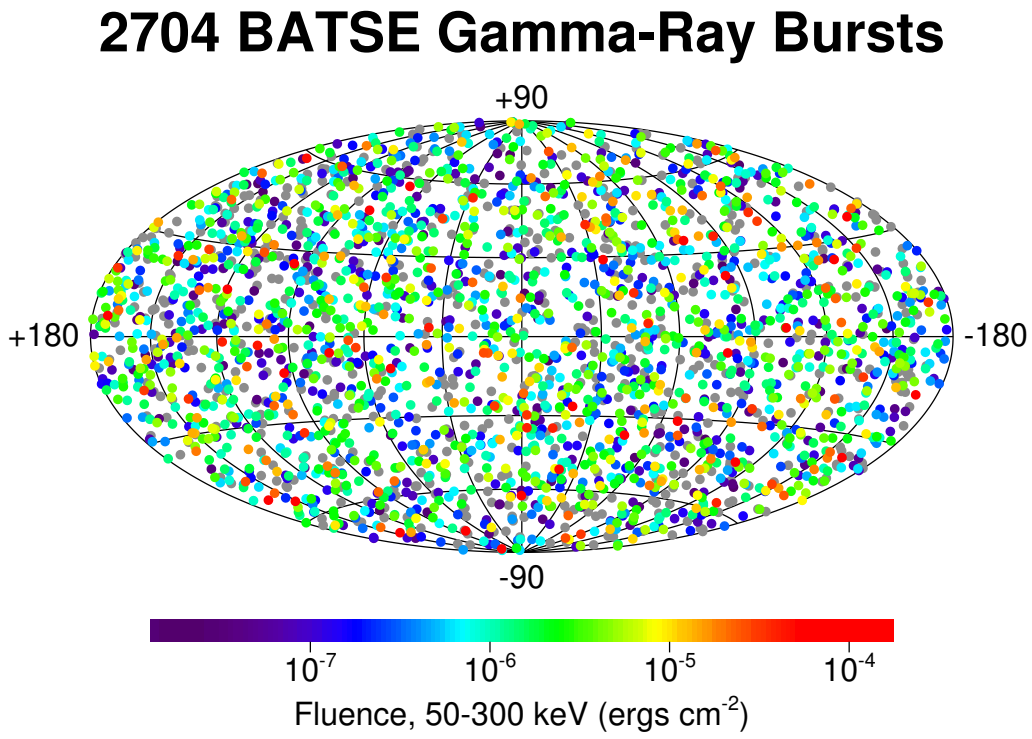

FIGURE 1.16: The isotropic angular distribution of GRBs in BATSE 4B Catalogue[8].

Angular distribution

The origin of GRBs was unknown for three decades due to the lack of distance information which made it challenging to constrain the released energy range for such a source that outshines (for few seconds) the rest of the Universe in the gamma-ray domain. In the 1980s, the different theoretical models (more than 100 at that time!) could be grouped into two different classes, according to the distance scales assumed for each model: those dealing with GRBs happening in our own galaxy (the Milky Way) or those considering GRBs at cosmological distances. In the mid-1990s, there was no consensus, as it was crystal clear once the great debate in 1995 took place (Paczynski, 1995; Lamb, 1995). If the bursts' origin was related to neutron stars in the Milky Way, then GRB distribution on the celestial sphere should be concentrated along and near the plane of the Milky Way (as projected onto the celestial sphere). However, after the first years of $CGRO$ operation, the detected GRBs skymap showed clear evidence of an isotropic distribution of bursts which also occurs randomly around the Universe (Paciesas et al., 1999). On top of that, it was found that there was no concentration around the Andromeda Galaxy or our Local Group of galaxies, being the isotropic distribution the one shown in Figure 1.16[8], reinforcing the idea of an extragalactic population of events. Today, much more than a decade of *Swift*'s and *Fermi*'s operations, the isotropic distribution of events, either short or long-durations, is still consistent with the BATSE findings (see Figure in Lien et al. 2016; von Kienlin et al. 2020).

Afterglow

After the prompt emission ceases, the 'afterglow' can be observed in all wavelengths from X-ray to radio. As it was above mentioned, the $BeppoSAX$ detection in 1997 of the first X-ray afterglow initiated the so-called 'Afterglow Era'. While theoreticians already predicted the afterglow appearance before the initial discovery (Mészáros and Rees, 1997), with the increase of the existing GRB samples, it is found that the afterglow light curves can be fitted by several multi-segment broken power-law along with the flux decay in a given observation band.

[8] https://gammaray.nsstc.nasa.gov/batse/grb/skymap/

- **X-ray afterglow** Although the first X-ray afterglow discovered by *BeppoSAX* for GRB 970228A (Costa et al., 1997), a larger sample of X-ray afterglows was only provided by *Swift*/XRT about 1-2 yr after the *Swift* launch. Thanks to *Swift*'s capability of fast-slewing, almost 96% BAT detected GRB's X-ray afterglow could be recorded by XRT (Burrows et al., 2008). After performing the corresponding statistical studies for this large sample, a canonical light curve is found which can represent most of the GRBs' X-ray afterglows. It exhibits a multi power-law segments behaviour as shown in Figure 1.17 which consists of five components: a steep decay phase, a shallow decay phase, a normal decay phase, a late steepening phase and eventually, X-ray flares (Zhang et al., 2006).

  The first X-ray afterglow segment is the steep decay phase, which is smoothly connected with the prompt emission and presents a sharp decay with a typical temporal index between -3 and -10 until 100-1000 s after the burst. In some cases, this first segment is same times found simultaneously following with the last prompt emission pulse for some long bursts. Therefore, the steep decay is believed to be the tail of prompt emission and shows a robust spectral evolution. After taking an appropriate starting point for the GRB T_0 time, its origin was proposed to be the curvature effect of radiation from the high latitude regions of the jet (Kumar and Piran, 2000; Liang et al., 2006).

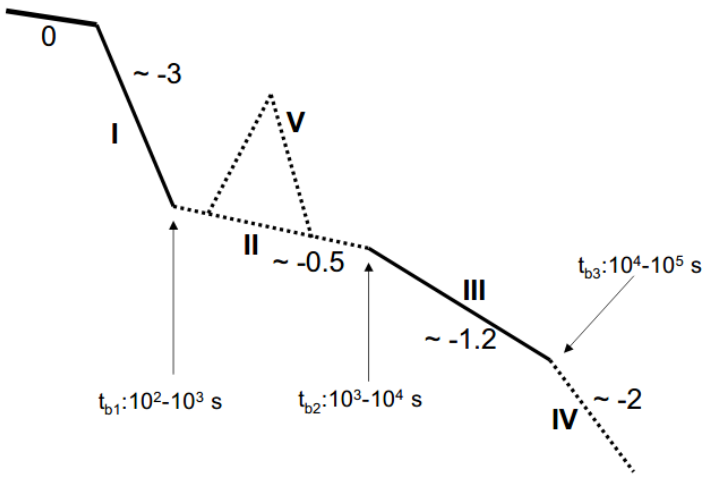

FIGURE 1.17: The GRB canonical X-ray light curve (Zhang et al., 2006).

The second X-ray afterglow segment is the shallow decay phase, which is the so-called 'plateau' sometimes since its flat temporal index ranges between 0 and -0.5. Typically, it flattens until 10000 s after the burst and no spectral evolution is found during this phase. Consequently, there are two different models about its origin depending on the next segment in the light curve. If a normal decay component connected to the shallow decay phase shows a temporal decay index of $\sim$-1, that is consistent with the scenario of continuous energy injection in the standard external shock model (Rees and Mészáros, 1998; Zhang and Yan, 2011) i.e. an external plateau. In contrast, the internal plateau is suitable for the situation that the normal decay shows a very sharp power-law decay index which could reach up to -9, such as in the case of GRB 070110 (Troja et al., 2007; Lyons et al., 2010), in which a long-lasting central engine is needed to provide direct energy injection and produce such an internal plateau, for example, a millisecond magnetar as the central engine (Troja et al., 2007).

The third X-ray segment is the normal decay phase, typically with a slop index of -1.2, that will continue until the end of afterglow. It can be interpreted well by the standard external forward shock model (Sari, Piran, and Narayan, 1998).

The next connected segment is the jet break, which is not detected in all GRBs. And there is no evidence for its existence in some GRBs even up to months post-trigger. In most cases, a decay shape with an index of -2 is detected as predicted by the theoretical model. It is mainly a geometric effect, occurring around the time the opening angle of the jet is of order the inverse of the jet Lorentz factor, with the light curve displaying a characteristic break because at that time, the observer starts to see the edge of the jet, so the decay of the light curve becomes faster than it would if the GRB were a spherical outflow. This was first seen in GRB 990123 (discussed below). See also Wang et al., 2018; Rhoads, 1999.

The last component that may show up is the X-ray flare, which shows a rapid rise and fast decay, superimposed on the light curve. Only less than half of GRBs displays this signature, but it can be detected more than once in some particular cases. This flaring structure can increase the basal flux brightness up to 6 orders of magnitude and its fluence (the flux integrated

over the time) being about 1-10% of the fluence from the prompt emission, also showing strong spectral evolution(Zhang, Lü, and Liang, 2016). Similar temporal and spectral properties between X-ray flares and the prompt emission support its origin being related to the late time central engine activity.

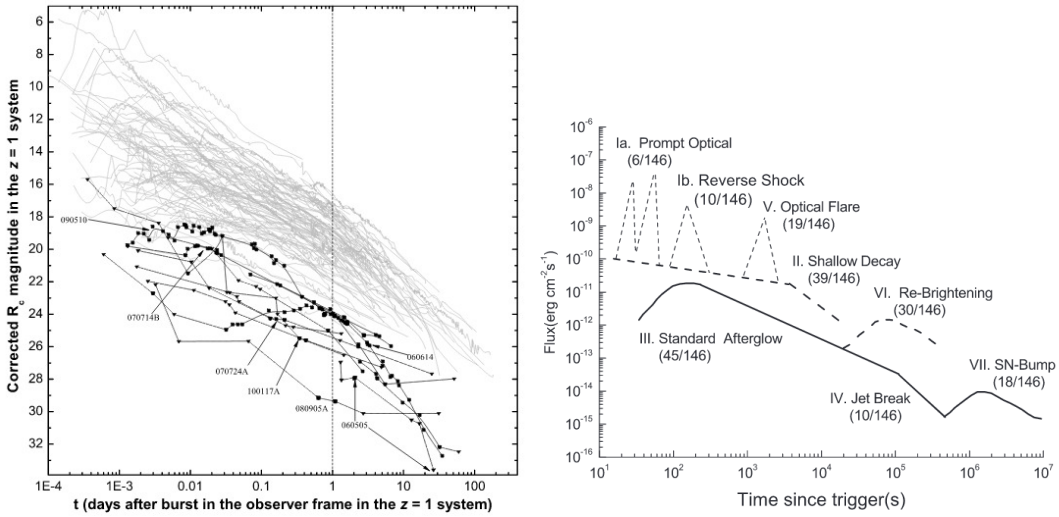

FIGURE 1.18: Left panel: Optical afterglow samples (Kann et al., 2011). Right panel: The canonical optical light curve (Li et al., 2012).

- **Optical afterglow** Since the first optical afterglow detected for GRB 970228A, optical afterglows have been discovered for many GRBs so far. However, prior to *Swift*, the burst location was only accessible several hours post-trigger, and the optical ground-based facilities could only record the late-time light curves, which just displayed the power-law decay. Occasionally, a broken power-law light curve was detected, which provided evidence of jet breaks in the optical band, such as GRB 990510 (Kuulkers et al., 2000) and an early optical decay detected with sharp decay, which could be explained by a reverse shock such as GRB 990123 (Castro-Tirado et al., 1999b; Akerlof et al., 2000). Overall, the optical afterglow detection rate was found to be lower than X-ray because soon it became clear that some events had no optical counterparts in spite of deep searches (such as GRB 970111 (Gorosabel et al., 1998) and GRB 970828 (Groot et al., 1998)) and the term 'dark GRB' was coined, meaning events that are intrinsically dark in the optical band (Berger et al., 2002). In *Swift* and *Fermi* era, more

comprehensive light curves were observed, including prompt emission to late times (even a supernova -like bump for low redshift events). A global view of the optical light curve of a large sample of GRBs is shown in Figure 1.18 left panel (Kann et al., 2011) in which the light curve is corrected to a common rest-frame at redshift $z = 1$. The different components found in systematic optical light curves are shown in Figure 1.18 right panel, which displays a much more complex structure than it is seen in X-ray, i.e. the prompt optical emission, the reverse shock component, the shallow decay segment, the standard afterglow component, the jet break structure, the optical flare, the re-brightening component and the supernova (SN) bump for the nearby events (Li et al., 2012). In the standard external forward shock model scenario, both the optical and X-ray components are originated from the same synchrotron emitting region, which leads to an achromatic light curve in those two bands. This means that the jet break and the energy injection breaks should be detected simultaneously in optical and X-ray light curves. Hence, optical afterglows share some common features seen in X-ray afterglows, including the standard afterglow component, the shallow decay phase, the jet break and the optical flare. But there are some exceptions, such as GRB 050319 (Panaitescu et al., 2006; Huang et al., 2007). However, most bursts still show a roughly achromatic light curve in optical and X-ray bands, implying that the external shock model can be used to explain most of the observed afterglow.

In addition to the light curve, optical spectroscopy observations following up some GRB alerts are essential in order to measure their properties, including the redshift z obtained from the absorption lines, from which the distance is determined. As in the case of GRB 970508, $z = 0.835$ (Metzger et al., 1997), it led to confirm the cosmological origin of GRBs. To date, the most distant GRB confirmed by spectroscopy is GRB 090423, at $z = 8.2$ (Salvaterra et al., 2009) and the nearest one is GRB 980425, at $z = 0.008$ (Galama et al., 1998). The furthermost event is GRB 090429B, for which only a photometric redshift ($z = 9.4$) could be determined (Cucchiara et al., 2011).

- **Radio afterglow** Radio afterglow is the most long-lasting part of GRB afterglow, which can be detected even up to ~ 1000 d post-trigger. However,

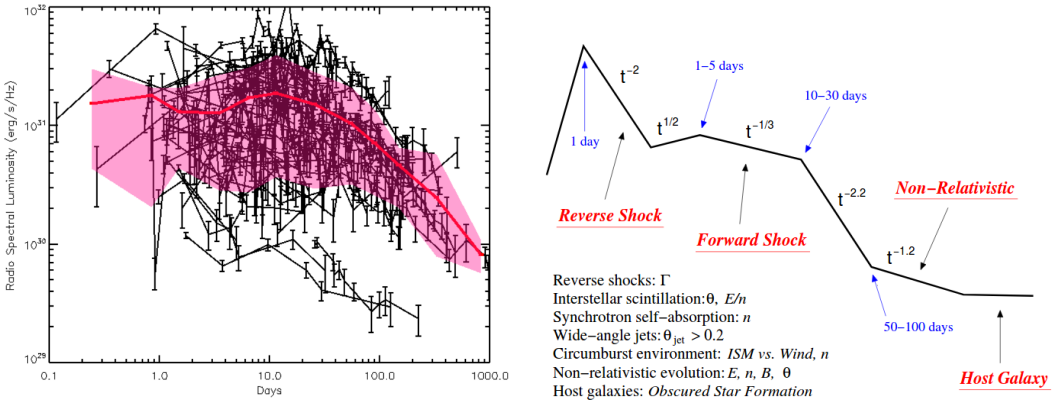

FIGURE 1.19: Left panel: GRB radio afterglow light curves at 8.5 GHz and their median light curve (Chandra and Frail, 2012). Right panel: Schematic radio light curve (Frail, 2003).

limited by the radio telescope time available, only 31% of GRBs have detected radio afterglows, and this situation did not change even after *Swift* was launched. A sample of 304 GRB radio afterglow light curves (at 8.5 GHz) has been collected and shown in Figure 1.19 left panel (Chandra and Frail, 2012). The red line is the median light curve, and the pink shaded area shows the 75% confidence region. It was found that the radio afterglow initially rises to reach a peak around 3-6 d after trigger with a median luminosity of 10^{31}erg s^{-1} Hz^{-1} for a typical long-duration burst. Following the external shock model, a schematic radio light curve is shown in Figure 1.19 right panel, which consists of several power-law segments. The light curve evolves from a relativistic to a non-relativistic regime with several breaks and shows a similar temporal index and jet break structure as in other wavelengths, but showing a slower evolution and spanning a longer timescale. This can also be seen in the median light curve shown in Figure 1.19 left panel. Remarkably, the early reverse shock component in the radio band can be detected in some bright GRBs, such as GRB 130427A (Anderson et al., 2014).

Spectrum at high energies

Most gamma-ray bursts show a non-thermal continuum radiation spectrum during the prompt emission which can be well fitted by a phenomenological model called 'Band' function (Band et al., 1993). This Band function is a

smoothly transited broken power-law model which can be described as:

$$N(E) = \begin{cases} A(\frac{E}{100keV})^{\alpha} exp(-\frac{E}{E_0}) & E < (\alpha - \beta)E_0 \\ A[\frac{(\alpha-\beta)E_0}{100keV}]^{(\alpha-\beta)} exp(\beta - \alpha)(\frac{E}{100keV})^{\beta} & E \geq (\alpha - \beta)E_0 \end{cases} \tag{1.1}$$

where A is a constant, α is the low energy spectral index, β is the high energy spectral index and E_0 is the break energy. Hence, the peak energy E_p in the energy spectrum is given by $E_p = E_0(2 + \alpha)$. See Figure 1.20 for Band function fitted GRB 990123 data (Briggs et al., 1999). From the BATSE GRB observations, the typical indexes are $\alpha \sim -1$ and $\beta \sim -2.25$, later confirmed by the *Fermi* results. The peak energy E_p typical value is 250 keV, but it can range from a few keV to several MeV (Axelsson et al., 2012; Campana et al., 2006).

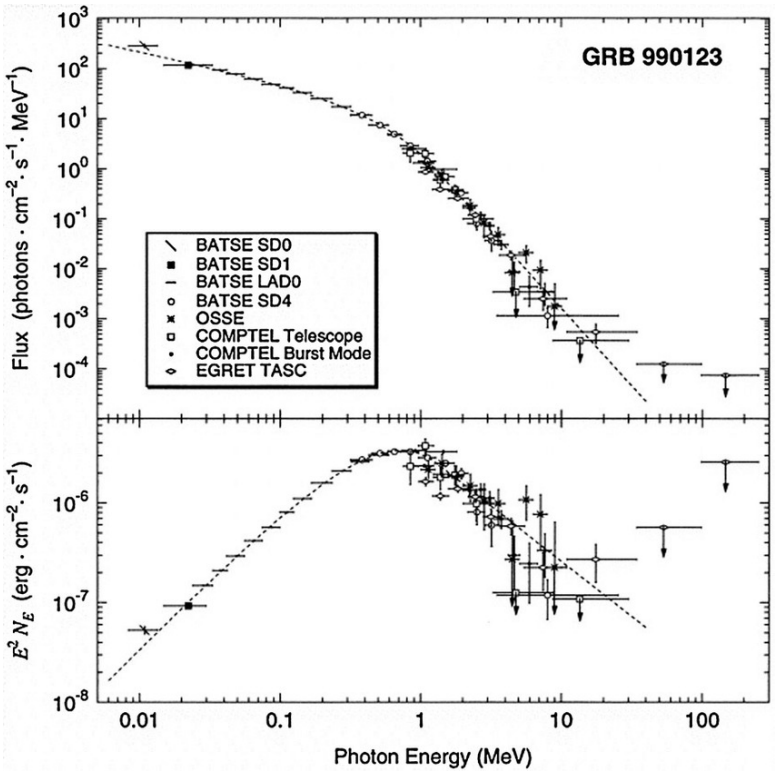

FIGURE 1.20: The GRB 990123 high-energy spectrum fitted with a Band function (Briggs et al., 1999).

Some GRBs spectra can also be described by a cut-off power-law function as shown below:

$$N(E) = A(\frac{E}{100keV})^{\alpha} exp(-\frac{E}{E_c}) \tag{1.2}$$

where E_c is the cut-off energy. It is clear that the cut-off power-law model just contains the first segment of the Band function.

Nevertheless, the Band function lacks physical explanation and there several extra components that may add more complexity to the GRB spectrum. Thus, a thermal component is predicted by the fireball model, which will be produced at the photosphere when the relativistic outflow will turn optically thin (Ryde, 2005; Pe'er and Ryde, 2011). However, it is not seen in most GRBs and just be found in several cases, such as GRB 090902B (see Figure 1.21 right top panel). Although a narrow Band function can describe this particular bump, it can be better fitted by a blackbody model in the time-resolved spectra (Zhang et al., 2011). Besides, an extra non-thermal power-law component may show up, as found in GRB 090510 (see Figure 1.21 left top panel), which shows a spectrum that can be fitted by a Band function with extra power-law component (Ackermann et al., 2010). This power-law component also appears in GRB 090902B and it extends several orders of magnitude from the keV to the GeV range with the same spectral index, which indicates that a high-energy peak should arise in a higher band (maybe in the TeV range). Furthermore, the GRB 090926A spectra revealed an extra component (see Figure 1.21 left bottom panel), which exhibits a high-energy cut-off (Ackermann et al., 2011). Therefore, the GRB prompt emission spectrum can be composed of three components: the Band function component, a thermal component and an extra power-law component extending to higher energies (at least up to the GeV range). Typically, a GRB spectrum will be dominated by one component or a combination of the above mentioned three components, as shown in Figure 1.21 right bottom panel.

The high energy emission is not only observed during the prompt emission but also in the afterglow phase. For example, for a handful of GRBs emission above 100 MeV was detected by $CGRO$/EGRET, such as a 18 GeV photon from GRB 940217, detected 1.5 h post burst (Hurley et al., 1994). After $Fermi$ was launched, more events were recorded within the GeV regime, such as GRB 130427A and GRB 090510. It is found that the GeV emission was always delayed regarding the sub-MeV emission (Abdo et al., 2009a; Abdo et al., 2009b) and lasted longer than the MeV emission in most cases. Moreover, a hard spectral component was detected in GRB 130427A during prompt emission which continued during the afterglow phase (Ackermann et al., 2014). Both of them

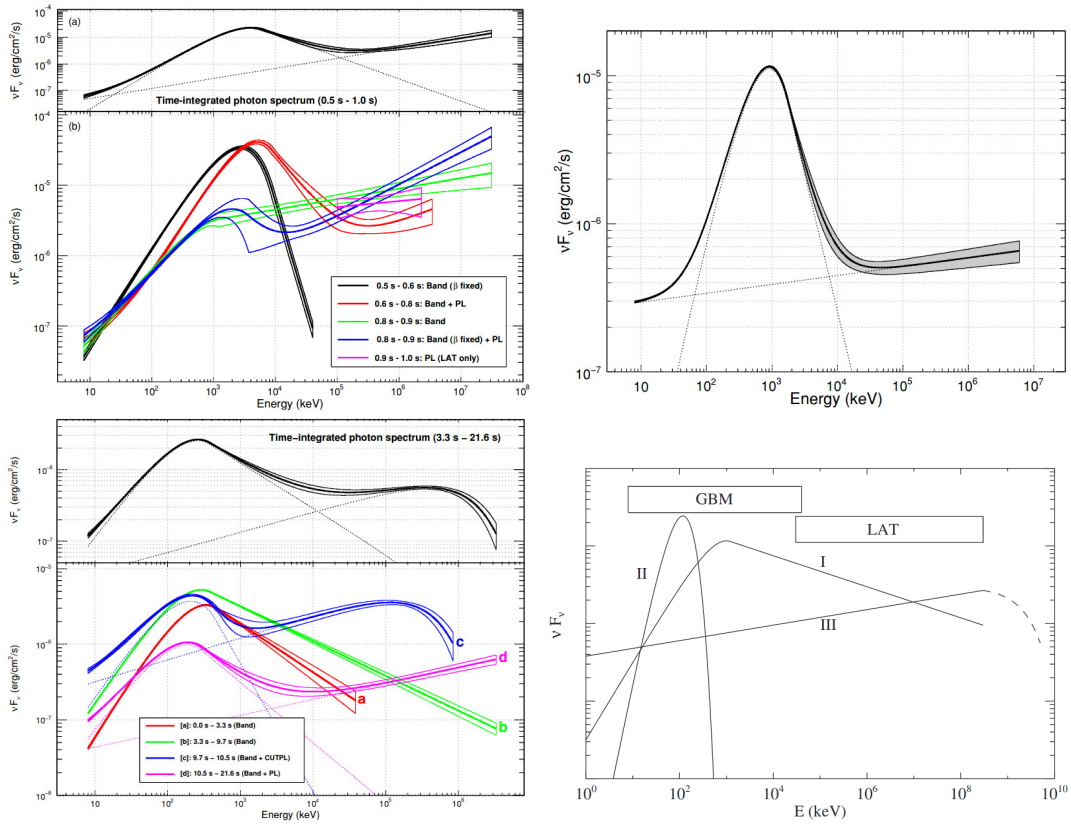

FIGURE 1.21: Left top panel: GRB 090510 spectrum (Ackermann et al., 2010); Right top panel: GRB 090902B spectrum (Abdo et al., 2009a); Left bottom panel: GRB 090926A spectrum (Ackermann et al., 2011) Right bottom panel: possible components in GRB spectra (Zhang et al., 2011)

proved that an extra emission component exists during the afterglow (at least in a few cases). On 14 Jan 2019, an extraordinary event, GRB 190114C, was detected by the MAGIC telescope at very high energies (VHE) in the TeV gamma-ray domain (details about this event will be described in the following section). This detection shows the GRB 190114C afterglow spectrum had a two-peak structure (see Figure 1.22), with the first peak corresponding to the synchrotron emission and the second peak due to inverse Compton processes (MAGIC Collaboration et al., 2019a).

Another topic on GRB spectra is spectral evolution, which evolves rapidly with time in the prompt emission phase. Different arrival times from photons are expected depending on the sampled frequency, known as the 'spectral lag'. Usually, the high-frequency photons will arrive earlier and the pulse will be

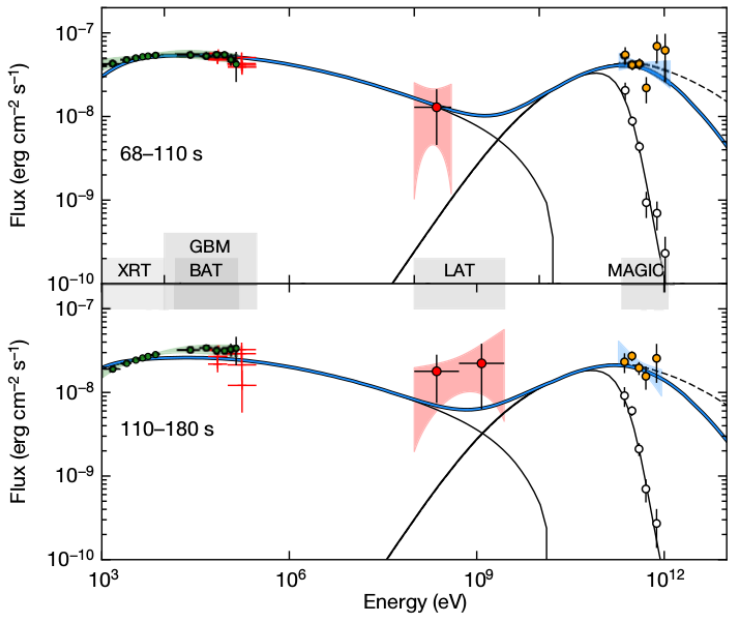

FIGURE 1.22: The GRB 190114C spectrum (MAGIC Collaboration et al., 2019a)

narrower (Norris, Marani, and Bonnell, 2000). Besides, the peak energy of the observed spectrum, E_p, can be an indicator of the spectral evolution and two different patterns have been found: 'hard to soft' and 'flux tracking' (Norris et al., 1986; Lu et al., 2012). Furthermore, the analysis of time-resolved spectra can provide more information about the burst evolution, such as GRB 160625B, a burst displaying three pulses during the prompt emission. The spectra of the first two pulses exhibited a transition from thermal to non-thermal and this supports the scenario in which a transition from a fireball to a Poynting-flux dominated jet was observed (Zhang et al., 2018b).

Empirical correlations

GRBs have been detected at a variety of distance scales, with the measured redshifts spanning from $z = 0.008$ to $z = 9.4$. Other astrophysical objects have not been detected at such high redshifts. For instance, the SNe Ia, considered standard candles, have been observed up to $z = 2.26$ (Rodney et al., 2015). Hence, GRBs are almost an order of magnitude further away than the SNe Ia standard candles and can be observed even at distances much higher than any other cosmic object. Theoretically, their afterglow can be detected even up to

$z \sim 20$, which makes GRBs a unique tool to investigate the early Universe (Ciardi and Loeb, 2000; Gou et al., 2004). Subsequently, several empirical correlations been found, which are based on observational results and they can be used to constrain the intrinsic burst properties and even the cosmological parameters (Dainotti, Del Vecchio, and Tarnopolski, 2016).

Here are the most relevant correlations observed in different GRB samples:

- The Amati relation ($E_{p,z} \sim E_{iso}$) (Amati et al., 2002; Amati, 2006; Amati et al., 2008; Amati, Frontera, and Guidorzi, 2009; Amati and Della Valle, 2013): It is found that the redshift corrected peak energy(E_p) in the νF_ν spectra and the total isotropic energy emitted during the burst(E_{iso}) satisfies an exponential relation:

$$\frac{E_{p,z}}{100keV} = K(\frac{E_{iso}}{10^{52}erg})^m \tag{1.3}$$

  where, $K \sim 95$ and $m \approx 1/2$, see dot-dashed line in Figure 1.23 left panel.

- The Ghirlanda relation ($E_{p,z} \sim E_r$) (Ghirlanda, Ghisellini, and Lazzati, 2004): The peak energy and the total energy corrected by beaming satisfies a tighter relation described as:

$$\frac{E_{p,z}}{100keV} \simeq 4.8(\frac{E_r}{10^{51}erg})^{0.7} \tag{1.4}$$

  where E_r is the beaming corrected energy and $E_r = (1 - cos(\theta_{jet}))E_{iso}$, see solid line in Figure 1.23 left panel.

- The Yonetoku relation ($E_{p,z} \sim L_{r,iso}$) (Yonetoku et al., 2004; Ghirlanda, Nava, and Ghisellini, 2010): In the standard synchrotron emission model, $E_{p,z}$ should be a function of $L_{r,iso}$ (Zhang and Mészáros, 2002a; Lloyd, Petrosian, and Mallozzi, 2000) and this relation is confirmed with the relation between $E_{p,z}$ and the peak luminosity $L_{r,p,iso}$ (see Figure 1.23 middle panel) is shown as:

$$\frac{E_{p,z}}{100keV} \simeq 1.8(\frac{L_{r,p,iso}}{10^{52}ergs^{-1}})^{0.52} \tag{1.5}$$

- The Liang-Zhang relation (Liang and Zhang, 2005): A three parameters correlation was found between the peak energy, the isotropic energy and

the break time in optical light curves $t_{b,z}$. It can be given as

$$\frac{E_{p,z}}{100keV} \simeq 1.09(\frac{E_{r,iso}}{10^{52}erg})^{0.52}(\frac{t_{b,z}}{day})^{0.64} \tag{1.6}$$

which is consistent with the Ghirlanda relation if $t_{b,z}$ is taken as the jet break time, see Figure 1.23 right panel.

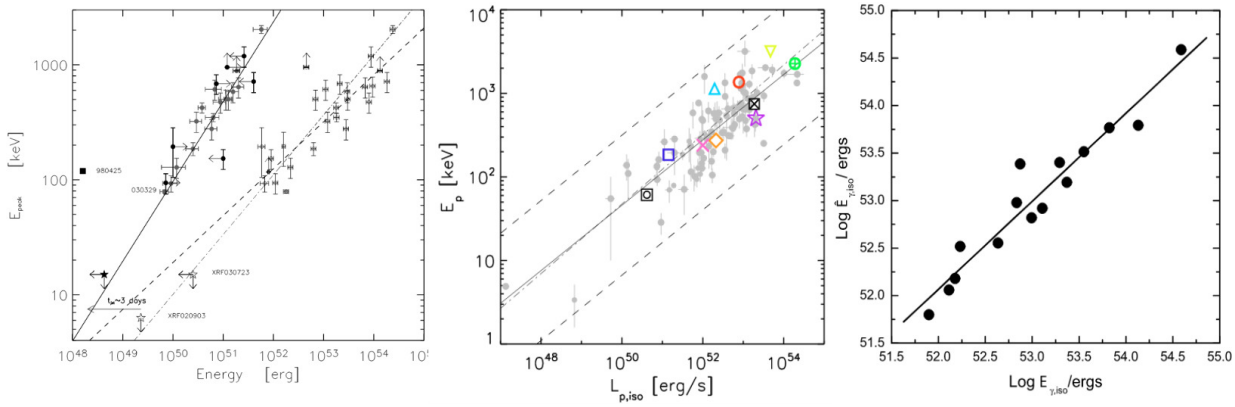

FIGURE 1.23: Empirical correlations of GRBs. Left panel: Amati relation (dot-dashed line) and Ghirlanda relation (solid line) (Ghirlanda, Ghisellini, and Lazzati, 2004); Middle panel: Yonetoku relation (Ghirlanda, Nava, and Ghisellini, 2010); Right panel: Liang-Zhang relation (Liang and Zhang, 2005).

Apart from those correlations found in the GRB sample, there is a relation that includes other astrophysical objects as well. The $P_{jet} \sim L_{iso}$ relation, Nemmen et al., (2012) used $f_b E_{iso,k}(1+z)/T_{90}$ to estimate the jet power, where f_b is the beaming factor $f_b = 1 - cos\theta$ and $E_{iso,k}$ is the kinetic energy evaluated from the radio and X-ray luminosity. Meantime, the isotropic luminosity can be derived through $L_{iso} = E_{iso}(1+z)/T_{90}$. This relation was first found in the active galactic nucleus (AGN) and microquasars, which can be extended to the GRB sample (see Figure 1.24) since the AGN standard model drew a picture in which there is a supermassive black hole accretion in a galaxy centre able to produce a disk and load a jet structure from the poles (Netzer, 2015). The consistency with the GRB sample implies that GRBs should share a similar jet formation as in AGNs powered by supermassive black holes in the centre of these active galaxies, i.e. in GRBs there is a stellar black hole in the centre able to form a jet through accreting materials around.

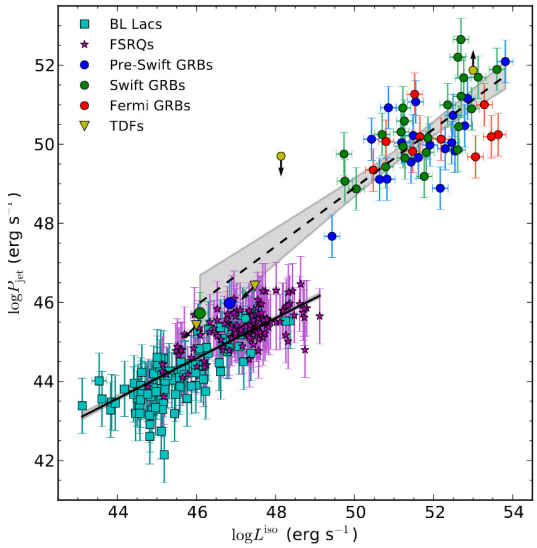

FIGURE 1.24: The Power-Luminosity relation between different size of black holes (Nemmen et al., 2012).

LGRB-SN connection

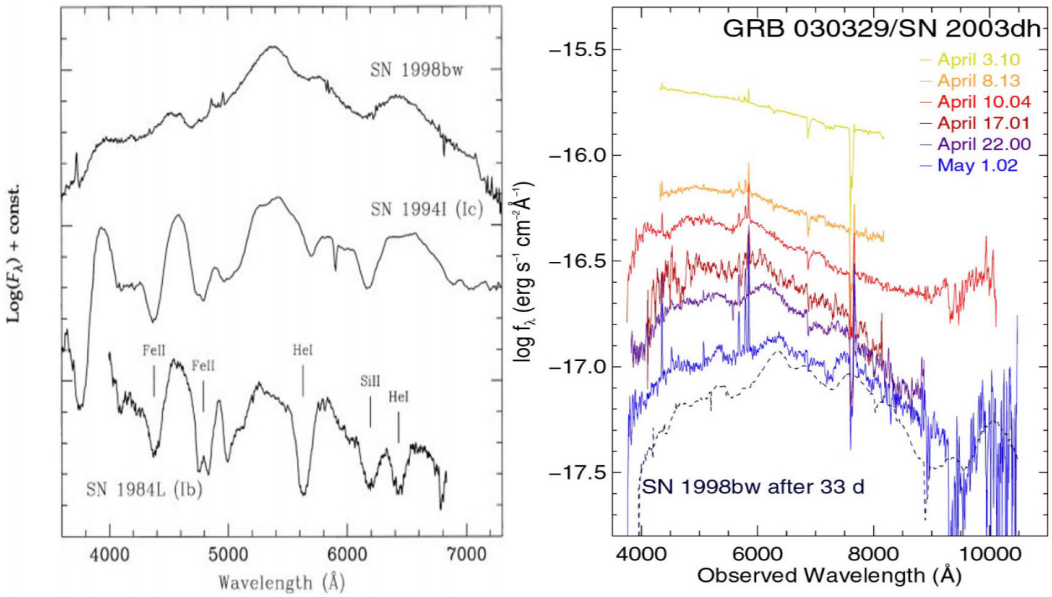

FIGURE 1.25: GRB-SNe connection. Left panel: The GRB 980425/SN 1998bw spectroscopy (Galama et al., 1998); Right panel: The GRB 030329/SN 2003dh spectroscopic evolution (Hjorth et al., 2003).

One year after the first afterglow was discovered, *BeppoSAX* triggered on

26 March 1998 for GRB 980326, a burst for which a supernova (SN) was proposed in order to explain the bump seen in the optical light curve 3 weeks later (Castro-Tirado and Gorosabel, 1999). And about one month later, on 25 April, $BeppoSAX$ also recorded an extraordinary long-duration burst, which showed a single peak on its gamma-ray light curve. Moreover, it was classified as a low luminosity burst whose total isotropic equivalent energy was just $10^{45}erg$ with no optical afterglow detected. However, a rising supernova was found in the local galaxy ESO 184-G82 at a distance of $\sim 35Mpc$, which is located in the error region of GRB 980425. Spectroscopy of this particular event was taken during the following nights, and a series of spectra do not show hydrogen and helium emission lines but other broad lines instead were observed, which looked pretty much similar to those ones found in type Ic supernova (see Figure 1.25 left panel, Galama et al., 1998). Five years later, $HETE-2$ detected another particular event, GRB 030329, an extremely bright and long-duration burst at a redshift of z=0.17 with the isotropic energy of $\sim 10^{52}erg$ (Hjorth et al., 2003). In the coming weeks, the spectroscopy of this high luminosity event revealed a spectral transition from a pure power-law into a spectrum similar to the observation from GRB 980425, i.e. a type Ic supernova spectrum, see Figure 1.25 right panel. Hence, it became the first direct evidence of the association between long-duration GRBs type I supernovae (lGRB-SNe). Normally the lGRB-SNe events share similar spectra, but not identical, as it happens in all type Ic SNe with broad lines, including OI, Ca II, Si II and Fe II. On average, their velocity width is at the order of ten thousands of kms^{-1} (Cano et al., 2017). However, most GRBs occurred at higher redshift, which limits the detection rate of the lGRB-SNe events. Therefore, a light curve that contains a re-brightening bump due to the SNe becomes another tool to identify lGRB-SNe events. Generally, the optical light curve from a lGRB-SNe event will have three components: the GRB afterglow, which is usually a power-law component usually, the SNe re-brightening component, which should happen about 15 days after the burst went off and the contribution from its host galaxy, see Figure 1.26. As of today, there more than 30 GRBs found to be associated with supernovae using those two methods. After extracting the contributions from both the afterglow and the host galaxy, a statistical analysis of GRB-associated SNe show that their average kinetic energy is $E_K \simeq 2.5 \times 10^{52}erg$, an ejecta mass of $M_{ej} = 6M_{sun}$, a nickel mass of $M_{Ni} \simeq 0.4M_{sun}$, an ejecta velocity at peak light

of $v \simeq 20000 kms^{-1}$ and a peak bolometric luminosity of $L_p = 10^{43} ergs^{-1}$. And the time it reaches the bolometric light peak, $t_p \simeq 13d$ (Cano et al., 2017). Nowadays, the concept of long GRB origin from the massive star death is widely accepted.

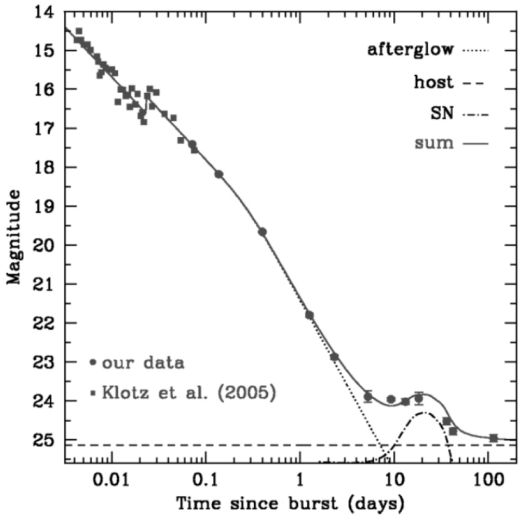

FIGURE 1.26: s
Late time rebrightening in late-time the light curve of GRB 050525A (Della Valle et al., 2006b).

There also a few long-duration events without a clear SNe detection that challenges this scenario. They are GRB 060614 and GRB 060505 (Fynbo et al., 2006). They were both long-duration events at a short distance (z=0.125 and z=0.089 respectively) from which an expected supernova component would have been recorded, but finally, there is no further evidence of SNe neither on their spectral nor in their light curves. These two cases imply that a different mechanism should be considered.

Host galaxy

The accurate localization of GRBs first obtained by means of the GRB prompt gamma-ray emission and better refined once the afterglow is detected, allows pinpointing their host galaxies, where the GRB progenitor was born, revealing the burst environment and the progenitor. For the first optical afterglow ever reported, for the long-duration GRB 970228, an underlying 'nebulosity' was first found at the burst location place (Sahu et al., 1997), but it was doubtful whether this GRB was related to it (and the nature of this 'nebulosity') until the first GRB

absorption redshift was confirmed for GRB 970508. In this way, the nebulosity was believed to be the underlying GRB host galaxy at a redshift 0.695 (Bloom, Djorgovski, and Kulkarni, 2001). In the cases of short-duration bursts, the first host galaxy was first detected only when *Swift* pointed to GRB 050509B and an elliptical galaxy at a redshift of 0.225 was identified as its host (Gehrels et al., 2005).

After about two decades of gathering observations of host galaxies, a number of properties have been found for the above mentioned two types of GRBs. Usually, GRBs host galaxies have a magnitude of about 25 mag on average and some faint galaxy can even get to 29 mag or even fainter. For long-duration GRBs, most host galaxies are blue, actively star-forming galaxies with low metallicity (Le Floc'h et al., 2006; Chary, Becklin, and Armus, 2002; Chary, Berger, and Cowie, 2007; Fynbo et al., 2008; Savaglio, Glazebrook, and Le Borgne, 2009; Bloom, Kulkarni, and Djorgovski, 2002; Bloom et al., 1998; Christensen, Hjorth, and Gorosabel, 2004; Fruchter et al., 2006; Blanchard, Berger, and Fong, 2016). Most of them are irregular galaxies, but spiral galaxies have also been found in a few cases. Long-duration GRBs are often located in the bright regions in their hosts, which traces the star-forming region in the galaxies (Fruchter et al., 2006). For short-duration GRBs, they are found in various types of galaxies, including both late-type and early-type (20%) galaxies with a wide span of star formation rates (Gehrels, Ramirez-Ruiz, and Fox, 2009; Berger, 2014), but they are often found in the faint regions of theirs hosts and do not appear to trace star formation (Fong, Berger, and Fox, 2010). Generally, the long-duration bursts are more concentrated towards the host galaxy cores, while the short-duration bursts are found in the outskirts. A study based on the $Hubble Space Telescope (HST)$ observation (see Figure 1.27) also support this point and it was found that short-duration GRBs are located at around 5 kpc offset with respect to the galaxy centres, which is about five times larger than the offset seen in the long-duration GRB sample (Fong, Berger, and Fox, 2010) which is also confirmed in statistical studies (Berger, 2014; Li, Zhang, and Lü, 2016). Furthermore, the redshift distribution of GRBs shows a median value of $z \simeq 0.48$ for the short-duration GRB population, which is substantially lower than the value found in the long GRBs sample, which a median $z \simeq 2$ (see Fong et al., 2013; Berger, 2014. In the case of long-duration GRBs, it is accepted they can be good tracers of star formation in the early Universe by assuming the GRB rate as an approximation of

star formation rate over cosmic time (Greiner et al., 2015a; Robertson and Ellis, 2012; Yüksel et al., 2008).

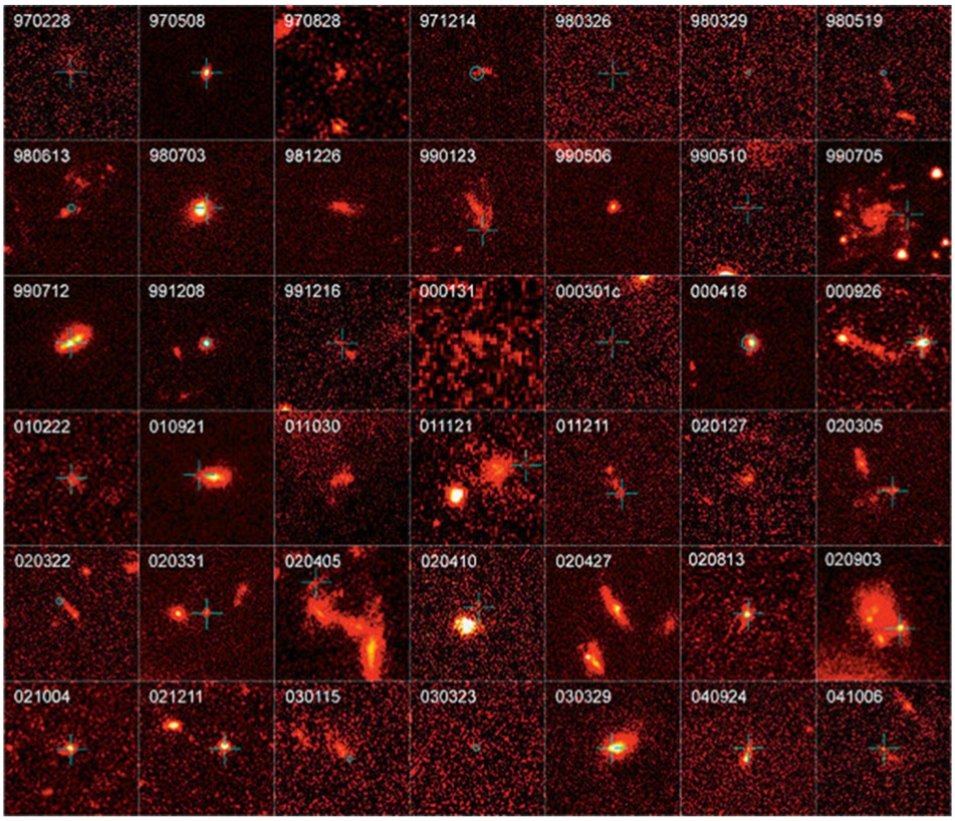

FIGURE 1.27: A sample of GRB host galaxies taken by HST (Fruchter et al., 2006).

Savaglio, Glazebrook, and Le Borgne, (2009) investigated the GRB host galaxy environment by means of optical and near-infrared photometry as well as conducting a spectroscopy analysis of the GRB sample whose redshift spanned from 0.0087 to 6.3. It was found that GRB hosts are small star-forming galaxies with a mean stellar mass $M_* \sim 10^{9.3} M_\odot$, which is consistent with the Large Magellanic Cloud (a satellite of the Milky Way) in a sample range of $10^{8.5} - 10^{10.3} M_\odot$. However, the mean star formation rate $SFR = 2.5 M_\odot yr^{-1}$ and the median specific star formation rate $SSFR \sim 0.8 Gyr^{-1}$ are all higher than the corresponding values in the Large Magellanic Cloud. In the case of the sub-sample of short-duration GRBs, the mean stellar mass spans a wide range, between of $10^{8.7} M_\odot \sim 10^{11.0} M_\odot$ and SSFRs lie in the range $0.006 \sim 6 Gyr^{-1}$, which is limited by the sample size. The host galaxy stellar mass lies in the range

$10^{9.5} \sim 10^{12.1} M_{\odot}$ whose median value $M_{*} \sim 10^{10.0} M_{\odot}$ means that the short-duration GRB host galaxies are typically more massive than the ones hosting long-duration GRBs. The short-duration GRB hosts also span a wider range of metallicities ($12 + log(O/H) \simeq 8.5 \sim 9.2 Z_{\odot}$) with its median value being $8.8 Z_{\odot}$, which is higher than the mean value obtained in the long-duration GRB sample ($12 + log(O/H) \simeq 8.3 Z_{\odot}$ (Leibler and Berger, 2010)). The metallicity can be directly measured from spectroscopy, being found that the metallicity is substantially lower than the solar value suggesting that a cut-off does exist in the metallicity around $1/3$ $Z_{\odot}$. However, this result is thought to be biased since only optical afterglows confirmed host galaxies were used for this study. An unbiased sample compiled by using a series of observational restrictions and imposing a fluence limit $> 10^{-6} ergcm^{-2}$, was the basis of the Swift Gamma-Ray Burst Host Galaxy Legacy Survey (SHOALS) result (Perley et al., 2016a) which was used to derive that the threshold for GRB production should be drawn at the solar level.

Although the GRB-SN Ic connection is widely accepted, their host properties are set apart since long-duration GRBs are more concentrated on the very bright region of their host than are the core-collapse supernovae, which indicates the long-duration GRB population is massive star related. Additionally, GRB hosts are fainter and appear more of irregular galaxy types than the SNe host galaxies (Fruchter et al., 2006). On the contrary, the short-duration GRBs are located far from the core of their host galaxies, the usual location for the old stellar population, which indicates that the progenitors of at least some short-duration GRBs have moved far away from the original birthplaces, this being consistent with short-duration GRBs related to a compact object (neutron star) binary merger model. Overall, the host galaxy observational differences, such as star formation rate, stellar mass and location offset, are significantly different for each class of GRBs.

Gravitational Waves observation and the short-duration GRB - Binary Neutron Star association

According to Einstein's general theory of relativity, massive objects create gravitational fields, producing curvature of space-time. Either an accelerated object or a rotating (non-symmetrical) object or a collapsing (non-symmetrical)

massive object will induce gravitational waves, which propagates with the speed of light. Massive stars become the most interesting object in the Universe, particularly due to their late evolution which are related to the birth of compact objects, such as black holes and neutron stars. As the result of the massive stars death, the compact object and its companion become the ideal natural environment to search for new physics related to many types of cataclysmic phenomena, such as GRBs. In those extreme processes, such as super-massive star collapse or binary black hole (BBH), binary neutron star (BNS) and black hole - neutron star (BHNS) mergers, most of the energy is released through electromagnetic radiation. Meanwhile, some energy propagated in the form of gravitational waves (GW), which contains specific information about the collapse or merger origin. Hence, the GW signal becomes a new probe to investigate the characteristics of the GW emitting source (e.g. initial, mass, orbit, distance, etc.) (Schutz, 1999).

The GW detectors were first designed in the 1960s by using large cylinders of aluminium that vibrated in response to a passing wave, with their sensitivity approaching $10^{-15} \sim 10^{-17}$. Due to its strong noise accompanying the GW signal, they did not detect any GW signal (Ricci and Brillet, 1997), but it paved the way for future GW detectors. The following generation of GW detectors used the laser interferometry method, which monitors the relative motion of freely hanging mirrors (Harry and LIGO Scientific Collaboration, 2010). In the $21^{\rm st}$ century, two km-size interferometers were built and improved the sensitivity up to 10^{-22} which finally made the detection of GWs possible: the Laser Interferometer Gravitational-wave Observatory (LIGO, Livingston and Hanford at America) consists of two four km arms. The Virgo interferometer (Virgo, Pisa at Italy) consists of two three km arms. Besides, some detectors were designed, such as the GEO600 at Hildersheim, Germany, with two 600 m arms, but the noise level prevented any GW detection.

Although the existence of GWs has been proved indirectly through the orbital decay in the first discovered binary pulsar system (Hulse and Taylor, 1975), the first direct detection of GWs event was achieved by LIGO on $14^{\rm th}$ September 2015, during the first observing scientific run (O1) soon after detectors first operation. The GW was confirmed to be produced by two $\sim$30 solar mass black holes merging at a distance of 410^{+160}_{-180} Mpc (Abbott et al., 2016b). This discovery of the first GW signal led Rainer Weiss, Kip Thorne and Barry Barish to be

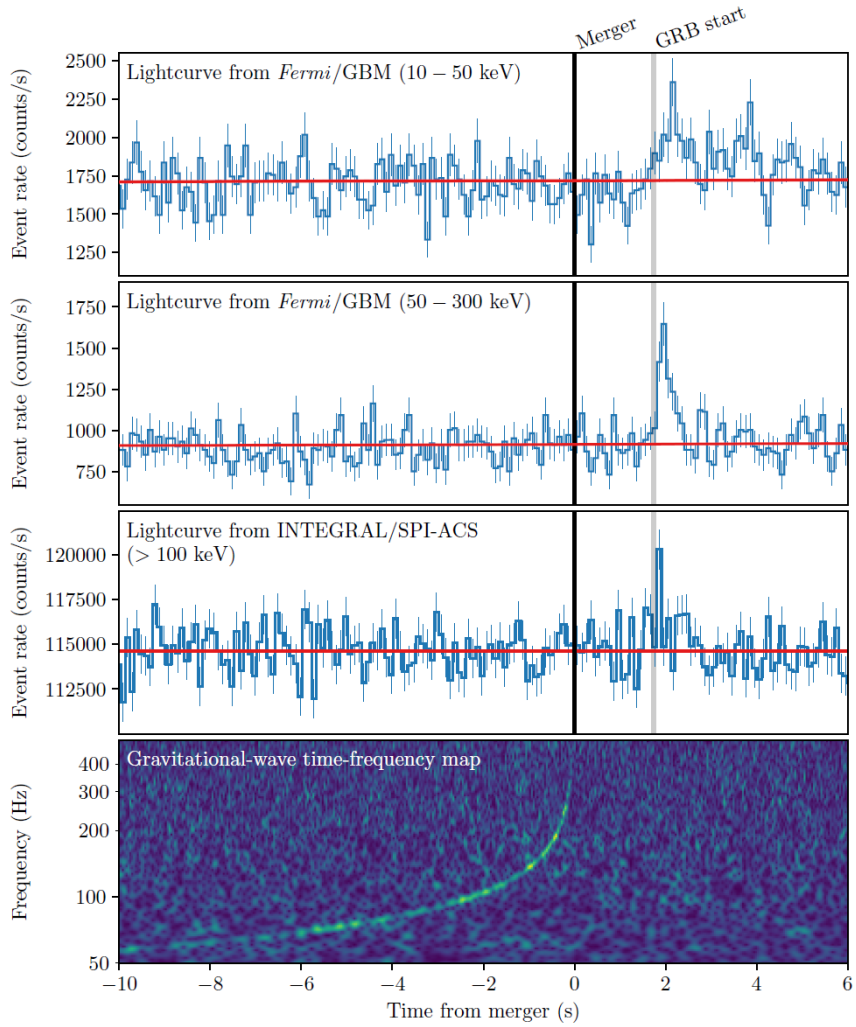

FIGURE 1.28: The GRB 170817/GW 170817 as detected by LIGO/Virgo, *Fermi* and *INTEGRAL* (Abbott et al., 2017a).

awarded the Physics Nobel Prize in 2016.

Nearly two years later, another crucial breakthrough took place. On 17^{th} August 2017 at 12:41:04UT, LIGO/Virgo detected the first signal from the merger of a binary neutron star system (GW 170817) with a total mass of 2.82 $M_{\odot}$ (Abbott et al., 2017b). And just 1.74s after the merger time, both the *Fermi* and *INTEGRAL* satellites detected a short-duration burst (GRB 170817A) with $T_{90} \sim 2s$ (see Figure 1.28, Abbott et al., 2017b). Thanks to this accompanying GRB, the position of the source was significantly improved to ~ 30 square degrees with a distance estimate from the modelling of the GW signal, of $\sim 40Mpc$. This limited the number of candidate host galaxies in the error region allotting to

make the counterpart search efficient as only ~ 100 galaxies have to be imaged looking for an optical transient source around them. Finally, 11 h after the GW arrival time, the Swope telescope in Chile identified a new, blue object in the outskirts of the galaxy NGC 4993, with this source being confirmed by several other teams, with the new source being named AT 2017gfo (originally SSS 17a) (Abbott et al., 2017c). After several weeks of subsequent observations by many facilities worldwide, it was found that this object evolved rapidly from blue to red, with spectroscopic features (a double blackbody (BB) of different temperatures) being distinct from any other SNe, being classified as a kilonova. The early blue BB component is believed to be caused by the material in which light r-process elements are being produced, whereas the red BB component is due to the higher opacity in synthesising higher elements (in the Periodic Table) such as lanthanides.

Indeed the first kilonova was found 4 years earlier, following another short-duration event, GRB 130603B, but at a much higher distance ($z = 0.356$ (Tanvir et al., 2013). The GRB 130603B optical afterglow was very bright at early times and then rapidly decayed. The near-IR magnitude showed an excess by a factor of about 25, thus matching the predictions for an underlying kilonova in the context of r-process opacities. Thus, the detections of the GW170817 and the short-duration GRB 170817A are considered the strongest evidence to confirm the hypothesis that binary NS mergers do produce GWs and accompanying short-duration GRBs.

Neutrino observations

The detection of neutrinos as part of multi-messengers would be another important piece of information in order to understand high-energy events better since these elementary electrically neutral particles have been detected arising from some nearby astrophysical sources (discussed below). Nevertheless, neutrinos only interact through the weak force, making of them particles very difficult to be detected. Nowadays, most neutrino detectors focus on tracing the Cherenkov radiation photons, which are produced when a neutrino passes the medium with speed faster than the phase velocity of photons in it.

In order to enhance the detection capability, the detector needs to contain as much medium as possible. This is the case of the IceCube observatory on

Antarctica, which is the largest neutrino detector by now. It consists of 86 strings, and each connecting 60 digital optical modules, which are distributed in the Antarctic ice within one square kilometre area evenly, i.e. a km^3 cubic of ice as its volume. This design made it possible for IceCube to detect incoming events with energy in the range from 0.1 TeV to beyond 1 EeV (Karle and IceCube Collaboration, 2009). A similar design is also employed in the ANTARES (Astronomy with a Neutrino Telescope and Abyss environmental RESearch) project, which is located in the Mediterranean Sea and makes use of seawater as the interaction medium.

In 2013, IceCube found extraterrestrial neutrinos in several multiple detections, but their reliable origin could not be confirmed. Apart from the solar neutrinos, astrophysical neutrinos were only identified in two cases so far. The first detection took place in 1987, when neutrinos from SN 1987A in the Large Magellanic Cloud were captured by the Kamiokande experiment in Japan, after the neutrinos crossing the Earth (as the SN 1987A sky location was not reachable from Japanese skies) (Hirata et al., 1987). The second detection of astrophysical neutrinos was in the direction of the flaring active galactic nucleus AGN TXS 0506+056, a BL Lac object (IceCube Collaboration et al., 2018b; IceCube Collaboration et al., 2018a), a discovery achieved by IceCube. So far, no neutrinos have been found related to very distant GRBs, but GRB relativistic jets are thought to be one possible accelerator of high energy neutrinos through pr interaction (Biehl et al., 2017).

Cosmic Rays observations

Cosmic rays (CRs) were first found in 1912 when Viktor Hess observed an excess in the density of ionized particles at high altitude with a balloon experiment. Today we know that cosmic rays can achieve energies as high as 10^{21} eV and that they constantly collide with other nuclei on the Earth's atmosphere (Lorenz and Wagner, 2012). Very high energy gamma-rays constitute a small part of the CRs composition and they can travel from the central engine to the observer without any change on its trajectory, unlike other CR components (charged particles) that are deflected by interstellar magnetic fields which will change their path and makes tracing their origin impossible. As we already know, GRBs are the most energetic γ ray explosions in the Universe and very

high energy photons have been already observed by *Fermi*/LAT up to several GeV. The existence of an extra power-law component in the GRB prompt emission spectrum can be extrapolated to even higher energies beyond the range of the *Fermi* satellite (Ackermann et al., 2010; Ackermann et al., 2014). And even MAGIC and H.E.S.S. have detected a handful of GRBs in the TeV range (see below). This provides strong evidence that GRBs could be one possible factory of such high energy CRs.

Limited by the satellite detector's effective area and low fluxes, the direct detection of the very high energy γ-rays from the space is challenging. Nevertheless, when high energy gamma-ray impinges on the atmosphere, it can interact with molecules and produce secondary particles that undergo further interactions with air nuclei, called extensive air showers (EASs) that ground-based detectors could record. Hence, a feasible way is to use these ground-based detections to reproduce the EASs in the atmosphere accurately. Since some of the particles produced in the shower can archive a speed faster than the speed of photons in the atmosphere, then Cherenkov light will be produced, which can be collected using Imaging Atmospheric Cherenkov Telescopes (IACTs) (Lorenz and Wagner, 2012; Di Sciascio, 2019).

The Major Atmospheric Gamma Imaging Cherenkov Telescopes (MAGIC) and the High Energy Stereoscopic System (H.E.S.S.) have been built according to this aforementioned principle. Another popular method used for detecting these high energy particles is the Water Cherenkov Detectors (WCDs) (Lorenz and Wagner, 2012; Di Sciascio, 2019) which used a similar idea to that implemented in the neutrino detection. This kind of telescope normally consists of several neatly arranged water tanks equipped with photomultiplier tubes to capture the UV Cherenkov light when high energy particles pass the water at a higher speed than the light speed in the water. This has been used in both the High-Altitude Water Cherenkov Observatory (HAWC) and the Pierre Auger Cosmic Ray Observatory in Argentina. However, there was no detection confirmed related to GRBs through the Water Cherenkov Detectors method until now.

Regarding the detection of GRBs in the very high energy (VHE) gamma-rays, on 14^{th} Jan 2019, the MAGIC telescope, a system of two 17 m diameter imaging array Cherenkov telescopes, followed up the *Swift* trigger for the long-duration GRB 190114C as soon as 57s after the prompt emission started (MAGIC

Collaboration et al., 2019a). VHE gamma-rays from this burst were detected in both MAGIC telescopes and its TeV light curve combined with other wavelength results are shown in Figure 1.29, which is already corrected for the attenuation by the extragalactic background light in the $0.3 - 1$ TeV energy range. The VHE emission was observable until ∼40 min after the trigger, which is much longer than the gamma-ray prompt emission as recorded by *Swift*. It was the first time that a GRB was observed covering a frequency range that spans more than 17 orders of magnitude and providing a good opportunity to investigate the GRB spectrum across this large frequency range. The temporal and spectral analysis proved that its afterglow started 25 s after the trigger. Hence, the afterglow emission produced these VHE gamma-rays. The multi-wavelength spectrum displayed a two-peak structure (see Figure 1.22), where the TeV observations constrain the second peak. This result supports the fact that the synchrotron radiation and the synchrotron self-Compton (SSC) process drive the GRB afterglow. The TeV peak can also explain the non-detection of a cut-off in some bright GRBs observed in the past, such as GRB 130427A (Zhang, 2019).

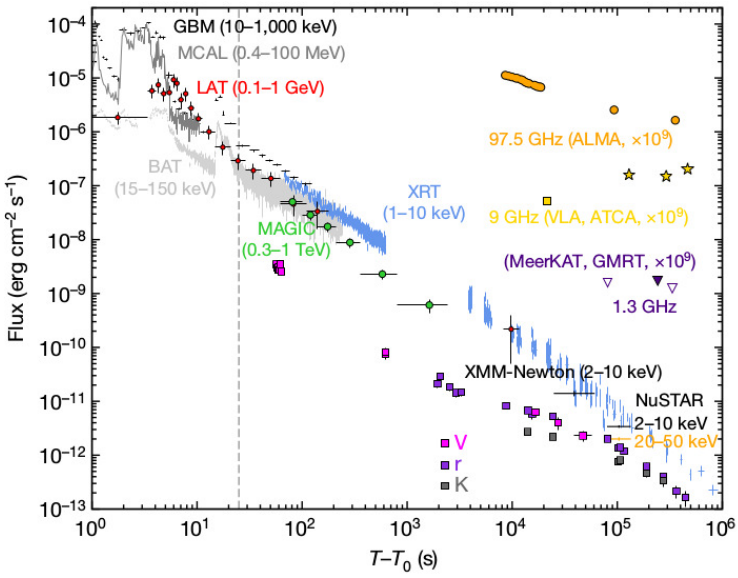

FIGURE 1.29: Multi-wavelength light curve of GRB 190114C (MAGIC Collaboration et al., 2019a), TeV light curve (green points).

Furthermore, a second GRB was detected in this VHE range, thanks to H.E.S.S. on 20^{th} July 2018, when the long-duration GRB 180720B (Abdalla et

al., 2019) was followed-up. This burst was first triggered by *Fermi*/GBM, and a few seconds later *Swift*/BAT found this event too. The GRB 180720B prompt emission was extremely bright and *Fermi*/LAT detected 5 GeV photons at 142 s post burst, but no further high energy emission was detected after 700 s. Ten hours later, this source fell into the FOV of H.E.S.S. and a 2 h long observation was executed. A new point-like VHE gamma-ray source was found at the GRB position in the $100 - 440$ GeV energy range. This late afterglow detection at energies > 100 GeV suggested that exotic particle-acceleration mechanisms did exist, which supports the existence of the SSC component (Zhang, 2019).

Related Theoretical Model

The Fireball model

As described in previous sections, long-duration GRBs are associated to energetic SNe produced during massive star collapses, whereas short-duration GRBs are associated to kilonovae, which are produced by binary NS mergers, indicating the different progenitors for these two types of GRBs, i.e. massive star collapse and compact binary mergers (Zhang and Mészáros, 2004; Kumar and Zhang, 2015). In order to explain the observational properties, many theoretical models have been proposed, but most of those models can only describe partial features. Nowadays, the most popular model is the so-called 'fireball model' (Piran, 1999), which is based on the prompt emission properties without considering the uncertainty of the central engine energy mechanism.

There are three key ingredients for a GRB production regarding the prompt emission: i) the total emitted energy, ii) the timescale, and iii) the spectrum.

Regarding the total energy, as a cosmological event, the typical fluences of GRB are $10^{-4} \sim 10^{-7}$ erg cm^{-2} in the gamma-ray band, which indicates a total isotropic emission is $\sim 10^{52}$ erg (when relativistic beaming is taken into account) that is at a similar level of the energy released by energetic SNe (Paciesas et al., 1999).

Regarding timescales, this is related to the physical scales on which the event occurs and reflects the time taken by the light to travel across the system. In GRBs light curves, the prompt emission varies on millisecond timescales and constrains the size of the central engine to $c\Delta(t) < 10^6 m$, even smaller than the

size of the Sun (Mészáros, 2006), which indicates that GRB do have a stellar size centre engine.

Regarding the spectrum, a smoothed connected power-law model and a given peak energy were observed in most GRBs' prompt emission phases, the 'Band function' (Briggs et al., 1999). When the short duration is taken into account, such an amount of energy released in such a small radiation region will lead to the compactness problem (Piran, 1999; Cheng and Lu, 2001): the high energy density at the radiation place will improve the efficiency of the pair production, making them optically thick for those γ rays with E_γ >1 MeV, and instead, a thermal spectrum should be observed, which is against the observational results. The relativistic effect has mitigated this problem (Paczynski, 1986; Piran, 1999). Thus, the expanding fireball is created at a speed of v whose Lorentz factor $\Gamma = 1/\sqrt{1 - v/c}$ will provide a moving size of the fireball dilated to Γ^2 times larger. Subsequently, the density decreases and the pair production is reduced as well. Moreover, the photons towards the observer will be blue-shifted, suggesting that most photons have energy $E_\gamma < 1$ MeV in the rest frame, which further reduces the optical depth since pair production efficiency decrease. However, the photons produced by pair annihilation will be thermal in an optically thin fireball that contradicts the observed non-thermal spectrum. So the fireball must contain baryons that could carry the bulk of the fireball energy, conversed from thermal energy to its kinetic energy (Piran, 1999). Since typical GRB Lorentz factors are > 100, the amount of baryonic matter is constrained by the relativistic effect, which should be $< 10^{-5}$ $M_\odot$ (Cheng and Lu, 2001).

Briefly, the fireball evolution, as described in Zhang and Mészáros, (2004), starts with a hot fireball arising from the compact central engine at an initial radius $\sim 10^7$cm, with photons and pairs being in equilibrium, while baryons are essentially at rest. The central engine will eject energy constantly and the fireball expands adiabatically. Hence, the bulk Lorentz factor increases linearly with the radius until reaching the maximum Γ_0. Meanwhile, baryons will be accelerated by the radiation pressure. Once the fireball acceleration is over, it will maintain at a constant Γ_0 value until it expands to the photospheric radius (r_{ph}) at which both the photon number density and the typical photon energy significantly drop. Although much of the initial energy is converted to kinetic energy, some energy will be radiated away as emission with a quasi-thermal

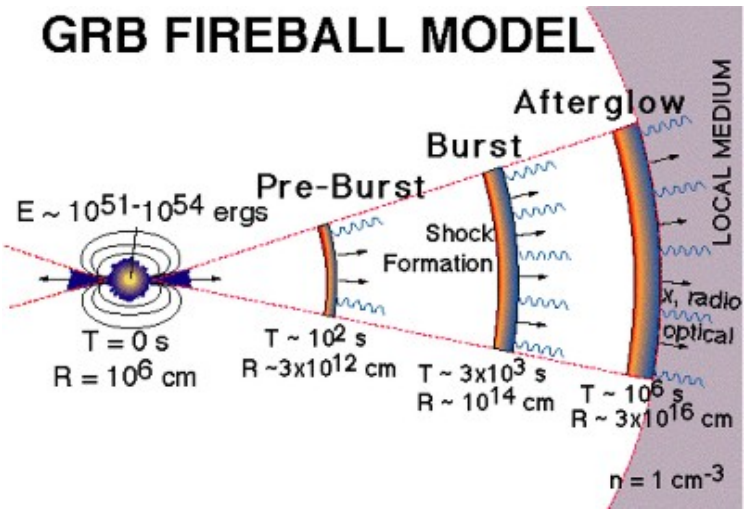

FIGURE 1.30: The different phases of the fireball in the context of the standard model (Dar, 2006).

spectrum. Since the central engine mechanism is launching matter in an inhomogeneous way, a relativistic jet comprised of expanding shells (each with a different Lorentz factor) will be produced and these shells will collide with each other catching up with previous shells, producing the so-called 'internal' shocks that happen at a typical internal shock radius (r_{is}). Then, the shells will keep spreading and interacting with the interstellar medium (ISM), which will decelerate the fireball and then a strong external shock will be formed and will propagate into the medium. Hence, the external shock radius (r_{es}) is also called deceleration radius. When the fireball first interacts with the medium, a reverse shock could be produced and propagate in the opposite direction. Generally, the first detectable electromagnetic signal from the fireball is the quasi-thermal radiation from the r_{ph}. The internal shocks at r_{is} will produce the prompt emission (mainly gamma-rays) and the radiation from external shock or reverse shock at r_{es} should be the domain of the afterglow phase (mainly from X-rays to radio). Due to involving baryonic matter, the thermal energy of the fireball is converted into kinetic energy of the baryons before becoming optical thin. After the shocks appear, the burst emission mainly accelerates the electrons using energy converted kinetic energy to non-thermal radiation, including synchrotron emission and inverse Compton scattering. Those typical radii can be calculated

with the following formulae:

$$\begin{aligned} r_{ph} &\simeq (L_0\sigma_T/4\pi m_p c^3\eta^3) \sim 4\times10^{12}L_{\gamma,52}\eta_{2.5}^{-3}[cm] \\ r_{is} &\simeq \Gamma^2 ct_v \sim 3\times10^{13}\eta_{2.5}^2 t_{v,-2}[cm] \\ r_{es} &\simeq (3E_0/4\pi n_{ext}m_p c^2\eta^2)^{1/3} \sim 2\times10^{17}(E_{53}/n_0)^{1/2}\eta_2^{2/3}[cm] \end{aligned} \tag{1.7}$$

where $E_0, L_0, \eta, \Gamma, n_{est}, t_v$ are the burst total energy, luminosity, initial dimensionless entropy, coasting bulk Lorentz factor, external density and intrinsic time variability respectively (Zhang and Mészáros, 2004; Mészáros, 2006; Dai, Daigne, and Mészáros, 2017). A schematic diagram of the fireball evolution with internal and external shocks is shown in Figure **??**.

Spectrum and light curve resulting from the model

In most observed GRBs, their prompt emission is of non-thermal origin and so is the afterglow emission (Band et al., 1993; Pe'er, 2015; Zhang, Lü, and Liang, 2016). The synchrotron emission is the most natural mechanism for non-thermal emission and is thought to be the primary emitting mechanism during the internal and external shocks process. Synchrotron emission is produced by relativistic electrons spiralling in magnetic fields.

Two main assumptions are adopted in this scenario: i) the accelerated electrons by shocks satisfies a power-law distribution, and ii) the total electron energy and the magnetic energy density behind the shock are both a fraction of internal energy (Sari, Piran, and Narayan, 1998), which will follow:

$$\begin{aligned} &N(\gamma_e)d\gamma_e \propto \gamma_e^{-p}d\gamma_e, \gamma_e > \gamma_m \\ &\gamma_m = \epsilon_e\left(\tfrac{p-2}{p-1}\right)\tfrac{m_p}{m_e}\gamma \\ &B = (32\pi m_p\epsilon_B n)^{1/3}\gamma c \end{aligned} \tag{1.8}$$

where γ, γ_e, γ_m, p, ϵ_e, ϵ_B, m_p, m_e, B and n are the bulk Lorentz factor, electron Lorentz factor, the minimum Lorentz factor, power-law spectral index, proton mass, electron mass, total electron energy fraction, the fraction of energy stored in the magnetic field, magnetic field strength and particle density respectively. Those micro-physical parameters p, ϵ_e, ϵ_B whose value can be fitted from the observed data (Wijers and Galama, 1999; Paciesas et al., 1999; Zhang

and Mészáros, 2004). A third assumption is that in the observer frame, the electrons accelerated through synchrotron emission will achieve a radiation power and characteristic frequency, which are given as:

$$P(\gamma_e) = \frac{4}{3}\sigma_T c\gamma^2\gamma_e^2\frac{B^2}{8\pi} \tag{1.9}$$

$$v(\gamma_e) = \gamma\gamma_e^2\frac{q_e B}{2\pi m_e c} \tag{1.10}$$

where σ_T, q_e are the Thompson cross-section and the charge of an electron. Thus, the peak power occurs at $v(\gamma_e)$ (Sari, Piran, and Narayan, 1998; Zhang and Mészáros, 2004).

Consequently, the spectrum is constrained by three characteristic frequencies which are: i) v_a: the synchrotron self-absorption frequency, ii) v_m: the characteristic synchrotron frequency, and iii) v_c: the cooling frequency. At frequencies below v_a, those photons will be re-absorbed by the synchrotron-emitting electrons. The characteristic synchrotron frequency corresponds to the typical frequency of electrons which are characterized by the minimum Lorentz factor of the electron distribution. The cooling synchrotron frequency marks when above this frequency, cooling by synchrotron radiation becomes significant.

Hence, the synchrotron spectrum can be described with a four-segment broken power law (Sari, Piran, and Narayan, 1998; Zhang and Mészáros, 2004; Mészáros, 2006). Since v_a only becomes significant at the low frequencies, the spectrum, therefore, can be divided into two types, depending on the order of v_m and v_c. For the case of '$v_m > v_c$', i.e. the so-called fast cooling case, the spectrum is given by:

$$F(v) = \begin{cases} (v_a/v_c)^{1/3}(v/v_a)^2 F_{v,max} & v_a > v \\ (v/v_c)^{1/3} F_{v,max} & v_c > v \geq v_a \\ (v/v_c)^{-1/2} F_{v,max} & v_m > v \geq v_c \\ (v_m/v_c)^{-1/2}(v/v_m)^{-p/2} F_{v,max} & v \geq v_m. \end{cases} \tag{1.11}$$

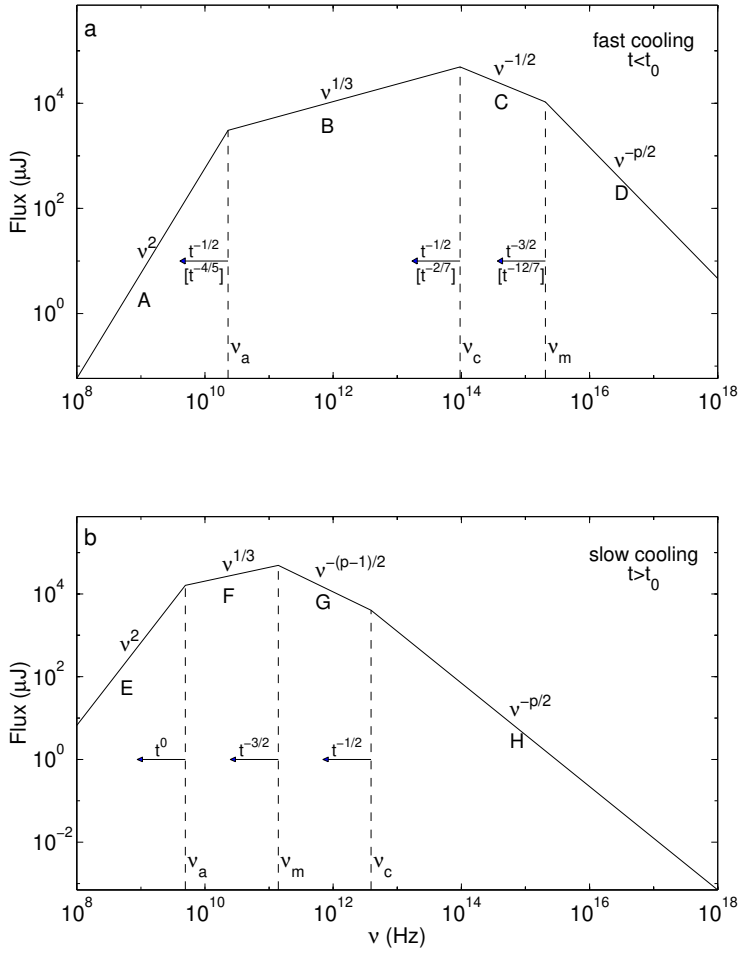

FIGURE 1.31: Top panel: Predicted spectrum of a GRB in the fast cooling case. Bottom panel: Predicted spectrum of a GRB in the slow cooling case (Sari, Piran, and Narayan, 1998).

For the case of '$v_m < v_c$', which is called slow cooling case, the spectrum is given by:

$$F(v) = \begin{cases} (v_a/v_m)^{1/3}(v/v_a)^2 F_{v,max} & v_a > v \\ (v/v_m)^{1/3} F_{v,max} & v_m > v \geq v_a \\ (v/v_m)^{-(p-1)/2} F_{v,max} & v_c > v \geq v_m \\ (v_c/v_m)^{-(p-1)/2}(v/v_c)^{-p/2} F_{v,max} & v \geq v_c. \end{cases} \tag{1.12}$$

In the above-mentioned equations, $F(v)$ is the flux at a given frequency and $F_{v,max}$ is the peak flux, which is the flux at $v = v_c$ in the fast cooling and the

flux at $v = v_m$ in the slow cooling. A typical spectrum of these two cases can be found in Figure 1.30 (Sari, Piran, and Narayan, 1998).

In order to get the light curve produced by synchrotron emission, the location of the typical frequencies with respect to the given observational band is needed. Besides, the temporal flux evolution is also affected by the spectral index p, the circumburst environment, the viewing angle of the observer and the hydrodynamical evolution of the shock (radiative or adiabatic) (Sari, Piran, and Narayan, 1998; Zhang and Mészáros, 2004). Minimizing the complication and considering the simplest model, we assume that it is an isotropic fireball with impulsive injection in a constant interstellar medium which will expand adiabatically and the spectral index $p > 2$ will not evolve with time (Sari, Piran, and Narayan, 1998). Under such assumption, the Lorentz factor of the fireball will evolve with radius r and observer's time t, implying $\Gamma \propto r^{-3/2} \propto t^{-3/8}, r \propto t^{1/4}$. Subsequently, the evolution of those typical frequencies and the peak flux can be quantified by the burst properties and the micro-physics parameters, which can be given as follows (Zhang and Mészáros, 2004):

$$\begin{aligned} v_m &= (6 \times 10^{15} Hz)(1+z)^{1/2} E_{52}^{1/2} \epsilon_e^2 \epsilon_B^{1/2} (t/1day)^{-3/2} \\ v_c &= (9 \times 10^{12} Hz)(1+z)^{-1/2} E_{52}^{-1/2} \epsilon_B^{-3/2} n^{-1} (t/1day)^{-1/2} \\ v_a &= (2 \times 10^{9} Hz)(1+z)^{-1} E_{52}^{1/5} \epsilon_e^{-1} \epsilon_B^{1/5} n^{3/5} \\ F_{v,m} &= (20 mJy)(1+z) \epsilon_B^{1/2} n^{1/2} E_{52} d_{L,28}^{-2} \end{aligned} \tag{1.13}$$

where E_{52}, $d_{L,28}$, n are the isotropic energy of the GRB in units of 10^{52} erg, the luminosity distance $d_L = 10^{28} d_{L,28}$ and the particle density of circum-burst medium in units of cm^{-3}. The predictions of the light curve are shown in Figure 1.31. We can find that $v_m \propto t^{-3/2}$ and $v_c \propto t^{-1/2}$ which means that v_m evolves faster than v_c and a transition from fast cooling to slow cooling will happen when $v_m = v_c$ which corresponds to the t_0 in Figure 1.31. In addition to this, t_m and t_c describe when the v_m and v_c pass across the observing frequency (Sari, Piran, and Narayan, 1998).

As above mentioned, the afterglow light curve consist of a series of power-law components and then the flux at any time from any frequency can be described by:

$$F_v(v,t) = t^{-\alpha} v^{-\beta} \tag{1.14}$$

where α and β are the temporal slopes and spectral index respectively.

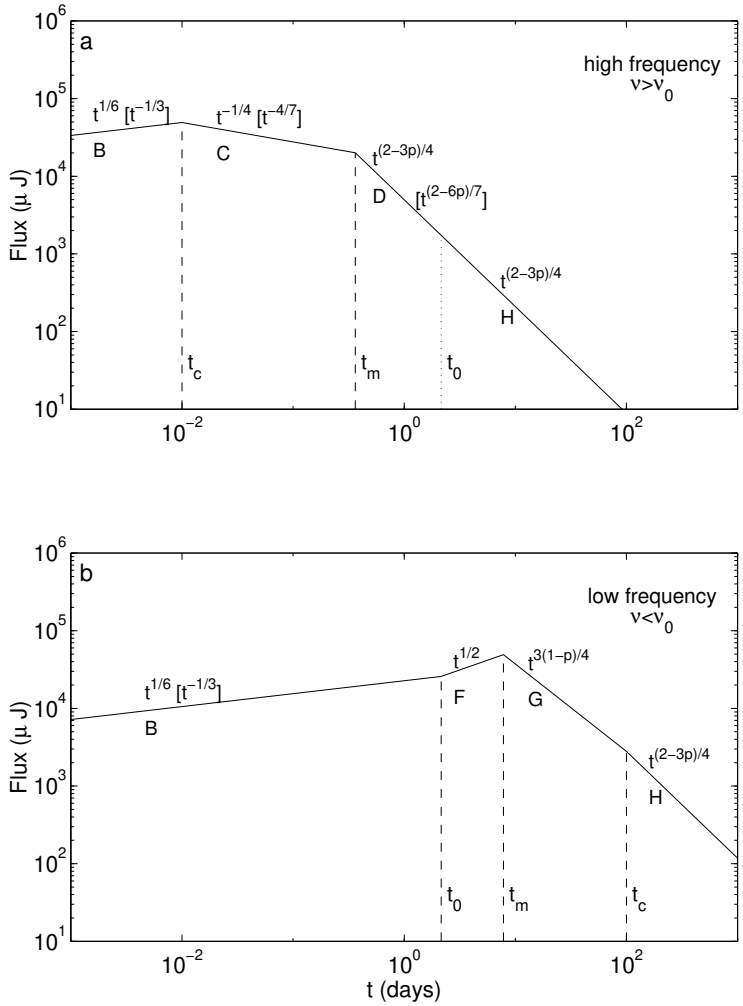

FIGURE 1.32: Top panel: Predicted light curve of GRBs at high frequencies. Bottom panel: Predicted light curve of GRBs at low frequencies (Sari, Piran, and Narayan, 1998).

We need to be aware that the basic fireball model is presented here, without having considered additional ingredients into account, such as the energy injection (Zhang et al., 2006) and the stellar wind type for the circum-burst medium (Chevalier and Li, 1999), etc. These temporal and spectral relations are known as the closure relations (Mészáros and Rees, 1997; Zhang et al., 2006; Racusin et al., 2009; Gao et al., 2013).

We shall be aware that for this simplest fireball model, a spherical expansion of the GRB is assumed, but those observed achromatic breaks in many afterglow light curves support the outflow should be beamed into a jet with an opening angle of θ (Rhoads, 1999; Sari, Piran, and Halpern, 1999). Thus, the

relativistic outflow in the jet moves with bulk Lorentz factor Γ and the beamed opening angle is Γ^{-1}. In the beginning, $\Gamma > \theta^{-1}$, and the observed blastwave still satisfy the isotropic fireball prediction. With the decrease of Lorentz factor until $\Gamma = \theta^{-1}$, the edge part of the jet will be observable and the jet begins to expand sideways, which will show a steepening break in the light curve, the so-called jet break (Panaitescu and Mészáros, 1999). Since it is a geometric effect, the achromatic break can be well explained in this way.

Outline of this PhD Thesis

Motivation and goals

Since the successful launch of *Swift*, *INTEGRAL* and *Fermi*, their sensitivity and rapid location capability have dramatically improved the number of GRBs detected so far. And from the ground, new facilities, including larger diameter telescopes and robotic telescopes networks are essential to complement the data gathered by the space-borne instruments providing a great data sample to better understand the most energetic events in the Universe.

The following three objectives were envisaged:

- First objective: a study of a long-duration event in order to constrain the jet geometry.
- Second objective: a study of a very-high gamma-ray event to characterize its associated supernova.
- Third objective: a study of a sample of short-duration events to find signatures of related kilonovae such as the one found for the burst related to the gravitational-wave alert GW 170817.

Methodology

This investigation makes use of multi-wavelength data which have been analysed according to the theoretical modelling. Our GRB follow-up observations were taken by means of our target-of-opportunity (ToO) programs approved at many observatories worldwide, ranging between optical and radio wavelengths, making use of the BOOTES and MASTER Networks, the 1.5m

telescope at Observatorio de Sierra Nevada (OSN), the 2.2m telescope at Calar Alto Observatory (CAHA), the 10.4m Gran Telescopio Canarias (GTC) and the IRAM facilities at mm wavelengths (30m Pico Veleta and NOEMA). Thus, the data we have used are composed by: i) Our own observational program data, which provides the basic photometric and spectroscopy results, ii) Space-borne data, including *INTEGRAL*, *Fermi* and *Swift*, available from open access archives, which also play an important role, being downloaded and analysed following the standard way as suggested on their official websites, and iii) Other data, for completeness, reported by other groups in the published literature.

Regarding the multi-wavelength data analysis process, specific software is used for the corresponding bands, such as Heasoft, 3ML for X-ray, gamma-ray, IRAF for optical and CASA for radio. Xspec and LePHARE packages are used for broad-band spectral fitting. The drawing software also becomes inevitable in improving data visualisation, such as QtiPlot. A Monte Carlo simulation python script utilised for uncertainty estimation. Standard afterglow theory and closure relationships are used in examining the afterglow data.

Finally, a model based on numerical simulations following the standard theoretical fireball model is also applied to derive the micro-physics related parameters.

Contents

In chapter 1, a brief introduction presents a short history of the development of GRB detectors. Then I focus on different wavelength observational results and the basic fireball model for gamma-ray bursts.

In chapter 2, and in order to accomplish the above mentioned 1st objective, a long-duration burst, GRB 140629A, is presented in different wavelengths, which includes X-ray, optical and near-infrared bands. With the simulation of the multi-wavelength afterglow and a chromatic light curve, we constrained the properties of the launched jet. The host galaxy of this event was also discussed with the analysis result from GTC and *Spitzer* observation.

In chapter 3, and in order to accomplish the above mentioned 2nd objective, a very high energy gamma-ray burst, GRB 190829A, was analysed using *Fermi* and optical data. This result was also compared with another similar

case, GRB 180720B, in order to discover its properties and compare the related supernova.

In chapter 4, and in order to accomplish the above mentioned 3rd objective, our multi-wavelength data on GRB 130603B was used to focus on the light curve and spectrum of the afterglow. We also study its host galaxy. To broaden the properties on sGRB, we discuss the results of prompt emission and multi-band afterglow observations of the other eight sGRBs we observed during 2012-2015. In addition to this, the sGRB 170817A/GW170817 late time GTC observation was presented and compared the observed properties with the subset of those sGRBs discussed.

Finally, a brief review of the enlightenment of this work, as well as a hint for future research, is presented in the last chapter.

An additional note: All errors in this thesis are providing with 1σ significance unless other stated. The cosmological parameters adopted in this work are the following ones: Hubble constant H_0 = 70 km s^{-1}. Density parameters $\Omega_\Lambda = 0.73$ and $\Omega_\mathrm{m} = 0.27$ (Jarosik et al., 2011).

Chapter 2

The long-duration burst GRB 140629A and its jet properties

In this chapter, we present observations of GRB 140629A, a GRB observed ∼40 s after the trigger (Yurkov et al., 2014) as a consequence of the rapid dissemination of alerts from space to ground-based telescopes. This allowed us to obtain rich multi-wavelength data from the early to late epoch (∼ 4 d), making this object a good case for constraining the jet properties and the host environment. We present multi-wavelength observations performed by *Swift*, *Konus*-WIND, *Spitzer*, and various ground-based facilities worldwide as well as results of our modelling from the jet and its properties.

Introduction

As the most energetic explosion in the Universe, GRB normally release $10^{48}-10^{54}$ ergs (if considered isotropic) typically within a few seconds in gamma rays; but these explosions have been observed up to a few hours in some instances (Zhang et al., 2014; Greiner et al., 2015b), which were divided into two classes depending on their duration: long (>2 s) and short (≤2 s) (Kouveliotou et al., 1993), the progenitors of which are thought to be the collapse of massive stars or the merger of two compact objects (Zhang and Mészáros, 2004; Kumar and Zhang, 2015), respectively. In the final stages of merger or collapse, a highly collimated ejecta is released, which has a typical opening angle $\theta_{jet} = 5°$-$10°$ (Racusin et al., 2009; Zhang et al., 2015). An internal dissipation process within the jet is thought to produce prompt gamma-ray emission (Rees and Meszaros, 1994; Kobayashi, Piran, and Sari, 1997; Daigne and Mochkovitch, 1998; Maxham and Zhang, 2009; Hu et al., 2014), while a longer-lived, multi-wavelength

afterglow is expected to be produced as the jet ploughs into the circumstellar medium (of constant density or a stellar-wind-like density; Mészáros and Rees, 1997; Sari and Piran, 1997). The relativistic effect implies that emission from the jet is beamed into a cone of half-opening angle $1/\Gamma_0$ (Rhoads, 1997; Piran, 2004; Granot, 2007; Liang et al., 2008; van Eerten and MacFadyen, 2013), where Γ_0 is the initial Lorentz factor of the jet, typically of a value of several hundred (Piran, 1999). The beamed geometry leaves a clear signature on the afterglow light curve, manifesting itself as an achromatic break known as a jet break, occurring simultaneously at all frequencies, days to weeks after the burst (Sari, Piran, and Halpern, 1999; Rhoads, 1999). This jet break, resulting in a steeper decay index, occurs when Γ_0 has decreased to $1/\theta_{jet}$. The shallower decay index, observed prior to the jet break, is maintained owing to the observer receiving emission from an increasing proportion of the jet as Γ decreases (Zhang et al., 2006). Once the observer sees the entire jet, the jet break is observed. The geometry and angular size of the jet directly affect measurements of the GRB energy and event rate. The isotropic energy should therefore be corrected by the collimation correction factor, f_b=(1-$\cos\theta_{jet}$), which solves the energy budget problem (Bloom, Frail, and Kulkarni, 2003; Frail et al., 2001; Friedman and Bloom, 2005; Kocevski and Butler, 2008; Racusin et al., 2009). Hence, the detection of a jet break in the afterglow light curve is an important diagnosis for constraining the outflow geometry and burst energetics. Although the determination of the jet opening angle from the observed break in the afterglow light curves depends on the model (e.g. assumed jet structure, radiation efficiency, and circumburst matter density profile; Sari, Piran, and Halpern, 1999; Frail et al., 2001).

Much of our current understanding of GRB jets has been built upon observational data. Generations of facilities, including the *CGRO*, *Beppo-SAX*, *HETE-2*, *Konus*-WIND, *INTEGRAL* (Meegan et al., 1992; Aptekar et al., 1995; Costa et al., 1997; Ricker et al., 2003; Rau et al., 2005) have been used to study such catastrophic events since they were first detected almost half a century ago. In particular, the *Neil Gehrels Swift Observatory*, a multi-wavelength observatory, has made great contributions to the understanding of the GRB phenomenon since its launch in 2004 (Gehrels et al., 2004). Three instruments onboard collaborated to observe events from hard X-ray to optical with BAT, XRT and UVOT. X-ray emission has even been observed in one case for several years after the

trigger (De Pasquale et al., 2016). In addition to UVOT, early IR/optical follow-up is also possible with ground-based robotic telescopes such as MASTER-net (Lipunov et al., 2010) and BOOTES (Castro-Tirado et al., 1999a). The MASTER-net (Mobile Astronomical System of Telescope-Robots) includes eight observatories located in Russian, South Africa, Spain (Canarias), and Argentina: MASTER-Amur, MASTER-Tunka, MASTER-Ural, MASTER-Kislovodsk, MASTER-Tavrida, MASTER-SAAO, MASTER-IAC, and MASTER-OAFA. MASTER-net began operating in full mode in 2010 (Lipunov et al., 2004; Lipunov et al., 2010; Kornilov et al., 2012; Gorbovskoy et al., 2013b). Each MASTER-II telescope contains a twin-tube aperture system with a total field of view of 8 square degrees with a photometer in the Johnson-Cousins system and polarising filters that were manufactured using linear conducting nanostructure technology (Kornilov et al., 2012; Gorbovskoy et al., 2013b; Kornilov et al., 2012; Ahn et al., 2005). The Burst Observer and Optical Transient Exploring System (BOOTES[1]) has been part of the effort to follow-up GRBs since 1998 (Castro-Tirado et al., 1999a; Castro-Tirado et al., 2012a). Each BOOTES station has a Ritchey-Chretien 60 cm aperture fast-slewing telescope, which covers a $10' \times 10'$ field of view and is equipped with clear, Sloan g r i, and WFCAM/VISTA Z and Y filters. Each system operates autonomously. Swapping from a pre-planned target list to active observations of GRBs is accomplished by switching the filters, focussing, and pointing the telescope to the event coordinates received from the Gamma-ray Coordinates Network (GCN; Barthelmy et al., 1998a). Thanks to the capability to react autonomously and to slew promptly, the robotic telescope has increased optical samples, particularly during the early epoch immediately following a GRB trigger. Therefore, those favourable conditions make GRB 140629A followed-up with several different bands facilities to be a good case to check its properties with multi-wavelength data.

Observations and data reduction

High-energy observations

The *Swift*/BAT triggered and located GRB 140629A on June 29, 2014 at 14:17:30 UT (T_0) (Lien et al., 2014; Evans et al., 2009). The BAT light curve is

[1] http://bootes.iaa.es

multiply-peaked with a duration T_{90}=42±14.3 s (see Figure 2.1) and exhibited a peak count rate of $\sim$ 2000 counts/s in the 15-350 keV range at $\sim$ 0 s after the trigger. The time-averaged spectrum from T_0-7.53 to 56.47 s was fitted by a simple power-law model with a photon index 1.86 ± 0.11 (Cummings et al., 2014b). The prompt emission light curve from BAT is shown in Figure 2.1. GRB 140629A triggered the S2 detector of the *Konus*-WIND GRB spectrometer at 14:17:30:00 UT in waiting mode (Golenetskii et al., 2014a). This instrument observed a double-peaked light curve [2]. A power-law with an exponential cut-off is the best fit model to the time integrated spectrum with parameters α = 1.42 ± 0.54 and E_p = 86 ± 17 keV. The spectrum resulted in a fluence of $3.4(\pm 0.5) \times 10^{-6}$ erg/cm^2 in the 20-10000 keV energy range. The isotropic energy release in rest frame is $E_{r,iso} = 4.4 \times 10^{52}$erg (Golenetskii et al., 2014a).

The *Swift*/XRT began observing the field 94.2 s after the BAT trigger and found a bright, fading uncatalogued X-ray source. An astrometrically corrected X-ray position was reported of RA(J2000)=$16^h35^m54.52^s$, Dec(J2000)=+$41°52'36.8''$ with an uncertainty of $1.7''$ (90% confidence radius; Evans et al., 2014). The initial XRT spectral analysis resulted in a power-law photon index of 1.98 ± 0.10 and a column density of 5.2 $(+2.2, -2.0) \times 10^{20}$ cm^{-2} (90 % confidence), in excess of the galactic value at 3.5σ (9.3 $\times 10^{19}$ cm^{-2}; Osborne et al., 2014).

Optical observations

MASTER

Three stations of MASTER-net observed GRB 140629A: MASTER-Amur (in Blagoveschensk), MASTER-Tunka (near Baykal Lake), and MASTER-Kislovodsk (Yurkov et al., 2014; Gorbovskoy et al., 2014a). The MASTER II robotic telescope in Blagoveschensk pointed to GRB 140629A 33 s after the BAT trigger time (T_0) and 15 s after notice time at 14:18:03.19 UT, June 29 (Yurkov et al., 2014) and was the first ground-based telescope to observe the burst. The first two MASTER observations were obtained during the gamma-ray emission. A transient object of brightness 14.26±0.06 mag was detected. Unfortunately, observations at Blagoveschensk were carried out in only one of the two tubes of the twin-tube aperture system as a result of technical disrepair. Observations at this location

[2] http://www.ioffe.rssi.ru/LEA/GRBs/GRB140629A/

lasted until ∼800 s after the trigger and finished when weather conditions became unsuitable. During this time, ten images with increasing exposure from 10 s to 120 s were obtained.

The MASTER II robotic telescope in Tunka pointed to GRB 140629A 78 s after T_0 on June 29, 2014,14:18:48.10 UT, during the evening twilight sky (the Sun was about five degrees below the horizon). For this reason, the first few images are overexposed. Nevertheless, the object is visible at the 4σ level in one polarisation at 14:36:16 UT (1060 s after trigger) with 3 min exposure during the evening sky observations. Following this, a small pause in observations was made for focussing. The observations were restarted in Tunka at 15:01:25 in the R and V filters. From 15:31:52 (∼2600 s after trigger), observations were performed with two mutually perpendicular polarisers. Observations continued until dawn at 18:51:36 UT (∼4.5 h after trigger).

MASTER II in Kislovodsk pointed to GRB 140629A approximately 3.2 h after T_0, which was when the weather conditions first became suitable after sunset. A total of about 40 good frames each of 180 s exposure were obtained in white light (C) and R filters. The optical transient is not detected in individual images but is visible in summed images. Frames were grouped into three sets, added together, and processed.

Swift/**UVOT**

Following the detection by *Swift*/BAT and XRT, the UVOT began settled observations 101.15 s after the BAT trigger and detected a fading candidate consistent with the XRT error circle (Breeveld and Lien, 2014). A series of images was taken with v, b, u, $uvw1$, $uvm2$, $uvw2$, and $white$ filters. The source was detected in all filters, except $uvm2$ and $uvw2$.

BOOTES

The 60 cm robotic telescope BOOTES-2/TELMA, in La Mayora, Malaga, Spain (Castro-Tirado et al., 2012a) automatically responded to the GRB alert as soon as its position was observable. Observations started on June 29, 22:19:47.227 UT, ∼8 hrs after the *Swift*/BAT trigger, in the clear and Sloan-i band filters, with exposure of 60 s. The source was observed until 2014-06-30 03:46:32.804 UT,

∼13.5 hrs after the burst. The clear exposures were smeared and were thus discarded. For the i-band exposures, the object was faint and not visible in the single frames, but it was detectable in stacked images.

OSN

At the Sierra Nevada mountain range (Granada, Spain), the 1.5 m telescope of Sierra Nevada Observatory (OSN)[3] pointed to the source at 2014-06-29 21:06:27.23 UT ∼6.82 hrs after trigger. The GRB field was also observed on June 30 and July 3. A series of images were obtained in Johnson-Cousins broadband filters: R filter with 300 s exposure and V, I filters with 600 s exposure.

BTA

The optical counterpart of GRB 140629A was also observed with the 6 m Big Telescope Alt-azimuth (BTA) of SAO-RAS (Caucasus Mountains, Russia) on June 29, starting 4.1 hrs after the detection of the burst by *Swift* (Lien et al., 2014; Yurkov et al., 2014). Observations of the field were carried out with the Scorpio-I optical reducer (Afanasiev and Moiseev, 2005) set in the BTA primary focus. Long-slit spectroscopy was also taken with the grism VPHG440, covering 4000 to 9800 Å. A 43.6 min spectral observation was obtained. The particular configuration of the device in combination with the 1″ slit achieves a resolution of full width at half maximum (FWHM)=13 Å.

GTC

The 10.4 m Gran Telescopio CANARIAS[4] (GTC, Canary Islands, Spain) obtained several images with the Optical System for Imaging and low-Resolution Integrated Spectroscopy (OSIRIS) camera (Cepa et al., 2000) on Feb. 27, 2015 and Feb. 7, 2017, ∼8 months and 2.7 yr after the burst respectively in order to detect the host galaxy. Eight images were obtained in the first epoch with Sloan-g, r, i filters. Four images were taken with the Sloan-i filters of 90 s exposure, three images were taken with the Sloan-g filter of 140 s exposure, and one 90 s exposure was taken with the Sloan-r filter. In the second epoch, 22 images were obtained: seven images each in the Sloan-g and Sloan-r filters with 150 s

[3] http://www.osn.iaa.es/
[4] http://www.gtc.iac.es

exposure and 120 s exposure, respectively, and eight images with 90 s exposure in Sloan-i band.

Infrared observations

The *Spitzer* Space Telescope (SST) also observed the source with the InfraRed Array Camera (IRAC) instrument at a wavelength of 3.6 μm (Perley et al., 2016a; Perley et al., 2016b). The total exposure time is two h. The data were downloaded from the *Spitzer* data archive center[5]. The source was observed on June 6, 2015, $\sim$1 yr after the trigger.

Data analysis and results

Photometry

The final photometry for the MASTER telescopes was extracted using the IRAF[6] package (Tody, 1993). The MASTER observations were taken with the polariser R, V, and C bands (P0, P45, P90, V, R, C at Fig.1). The C filter is white light corresponding to 0.2B+0.8R. The polarisation observations were taken with orientations 0°, 45°, and 90° to the celestial equator. Automatic astrometric and photometric calibrations were performed with a method common to all MASTER observatories (Kornilov et al., 2012; Gorbovskoy et al., 2013b). For these data, a robust 'centroid' algorithm was used to determine the background level. This algorithm allows us to exclude the influence of nearby objects. The data were corrected for the fluctuations with atmospheric opacity using the Astrokit programme (Burdanov, Krushinsky, and Popov, 2014), which implements a slightly modified algorithm to that described in Everett and Howell, (2001). This programme conducts differential photometry using an ensemble of stars that are close to an object. The details of the photometry calibration can be found in Gorbovskoy et al., (2012). For the polarisation observations, stars with zero polarisation are required for the channel calibration. We assume the polarisation of light from stars in the field of view is small. This can be checked

[5] http://sha.ipac.caltech.edu/applications/Spitzer/SHA/

[6] IRAF is distributed by the National Optical Astronomy Observatory, which is operated by the Association of Universities for Research in Astronomy, Inc. under a cooperative agreement with the National Science Foundation. http://ast.noao.edu/data/software

using Serkowski law (Serkowski, Mathewson, and Ford, 1975). The difference in magnitudes between two polariser orientations averaged for all reference stars gives the correction that takes into account different channel responses.

Swift/UVOT sky images were downloaded from the *Swift* science data centre[7] and the magnitudes were extracted following standard UVOT procedure (Poole et al., 2008). In this work, a 3σ upper limit is given when its signal to noise is <3. For individual filters after 2000 s, the data are binned with $(\delta t)/t$ = 0.2 to improve the signal to noise.

In order to obtain the instrumental magnitudes for the other instruments, point spread function (PSF) photometry was applied with the DAOPHOT tool in the IRAF package. Photometric magnitudes from the OSN were calibrated with the nearby reference stars in USNO-B1, GSC2.3 catalogue (Monet et al., 2003; Lasker et al., 2008). For the GTC, magnitudes were calibrated with the standard star STD_PG1323-086D.

The observation log of GRB 140629A is given in Table 2.1 and the photometry for all filters and polarisations is presented in Table 2.4. All magnitudes are presented in the Vega system except the GTC host galaxy observations, which are calibrated using the AB system. The final magnitude errors include the systematic error from the reference star calibration. The magnitudes in the table are not corrected for galactic extinction owing to the reddening of E(B-V) = 0.01 in the direction of the burst (Schlegel, Finkbeiner, and Davis, 1998). For clarity, the afterglow light curves are shown in Figure 2.1.

Temporal properties of the afterglow: An empirical fit

In this section, we fitted the light curves in X-ray and optical band with the empirical multi-segment smooth broken power-law models (Beuermann et al., 1999; Jóhannesson, Björnsson, and Gudmundsson, 2006; Molinari et al., 2007).

The X-ray light curve (0.3-10 keV) was obtained from the UK Swift Science Data Centre at the University of Leicester (Evans et al., 2009). As shown in Figure 2.2, the GRB 140629A X-ray light curve appears to show a canonical structure. An initial shallow decay is followed by a normal decay and then a steep decay (Zhang et al., 2006). To ensure two breaks are required, we first attempted to fit the light curve with a single broken power-law. This resulted in a poor fit

[7] http://www.swift.ac.uk

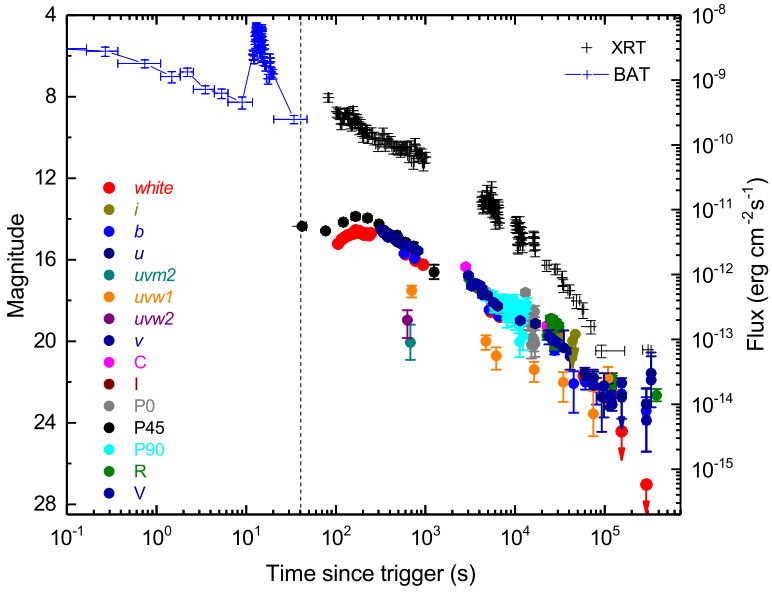

FIGURE 2.1: X-ray and optical light curves for GRB 140629A. Observations from both BAT and XRT are given with blue crosses and black crosses, respectively. The BAT data are normalised to the same energy range as XRT. The optical data are shown with circles. The vertical dash line indicates the end of the prompt emission, given by T_{90}.

TABLE 2.1: Observation log of GRB 140629A.

t_{start}	t_{end}	Filters
MASTER		
2014 Jun 29 14:18:03	Jun 29 21:58:09	C,V,R
Swift/UVOT		
2014 Jun 29 14:19:10	Jul 03 09:33:28	*white,u,v,b* *uvw1,uvw2* *uvm2*
BOOTES		
2014 Jun 29 22:19:47	Jun 30 03:47:33	*i*
OSN		
2014 Jun 29 21:06:27	Jun 29 22:54:33	V,I,R
2014 Jun 30 22:20:55	Jul 01 00:19:09	V,I,R
2014 Jul 03 22:52:42	Jul 04 00:16:30	R
GTC		
2015 Feb 27 06:03:20	Feb 27 06:23:50	*u,g,r,i*
2017 Feb 06 04:43:04	Feb 06 05:36:08	*u,g,r,i*
Spitzer		
2015 Jun 05 16:48:20	Jun 05 19:00:48	3.6*um*

with a reduced chi-square (χ^2)= 1.32 $(110$ $d.o.f.)$, and a corresponding null hypothesis probability of only 0.01%. We then tested a smooth broken power law, which showed an improvement, giving a reduced $\chi^2 = 1.10$ $(110$ $d.o.f.)$. For this model the best-fitting parameters are $\alpha_1 = 0.84 \pm 0.02$, $\alpha_2 = 1.87 \pm 0.08$ with a break time $(8.8 \pm 1.3) \times 10^3$ s. We then tried a smooth double broken power-law model. This again improved the fit giving a reduced $\chi^2/d.o.f.$= 0.99/108. According to the Akaike information criterion (Akaike, 1974; Liddle, 2007, AIC), the smooth double broken power-law model gives a lower AIC value in comparison to the smooth broken power law, suggesting the second break is required. This is also confirmed by the F-test, which suggests the second break is statistically required at more than 3σ confidence. We can also check the need for an additional break using a Monte Carlo simulation. We create 10000 synthetic light curves by randomly selecting, for each data point of the observed light curve, a new flux and flux error using a Gaussian function for which the mean and standard deviation is equal to the original observed flux and flux error. Each of the synthetic light curves is then fitted with both a broken power law and a double broken power law. From the resulting distribution of the change in reduced χ^2, we find that 98.2% of the simulated light curves have a change in reduced χ^2 that is equal to or greater than that obtained for the observed X-ray light curve. The Monte Carlo simulation thus suggests that the double break power law is preferred over the broken power-law model at the 2σ confidence level. We do not identify any X-ray flares in the light curve.

For the optical data, we normalised the observations in the different filters to the Johnson-R band using the period between 3000 s and 30000 s, during which the light curves appear to decay in the same fashion (Oates et al., 2007). The resulting light curve is shown in Figure 2.2. We exclude data prior to 70 s from our analysis since the data are likely contaminated by the prompt emission. When fitting the optical data, we tested both a smooth double broken and a smooth triple broken power-law against the data. The reduced χ^2 changed from 1.53 (d.o.f = 123) to 1.38 (d.o.f=121) with the addition of third break. The smooth triple broken power-law model is preferred according to the F-test, which provides a chance probability of 0.0008. We also used the Monte Carlo method, which we used to determine the significance of improvement of an additional break in the X-ray light curve, on the optical data. The synthetic light curves in optical are fitted with both a double broken and a triple broken

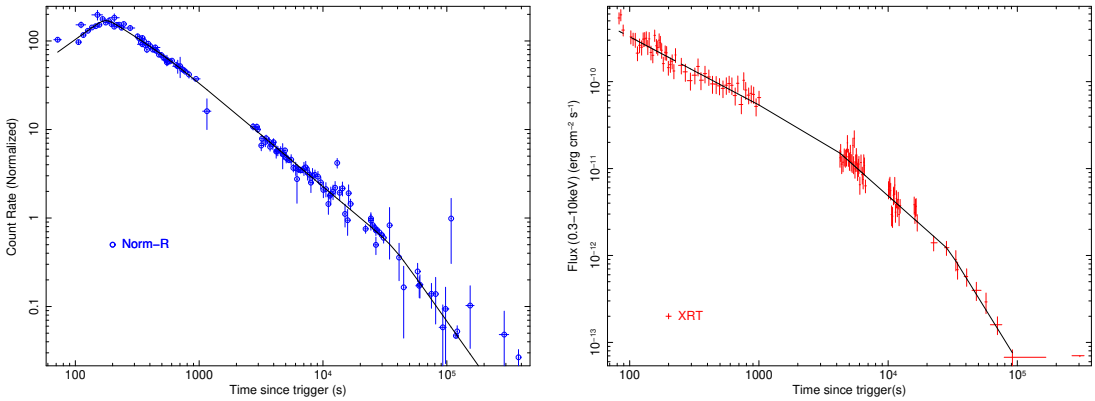

FIGURE 2.2: Fitting of the X-ray and optical GRB 140629A data. The normalised optical data are shown on the top panel with blue circles. The X-ray data are plotted on the bottom panel with red crosses. The black lines indicate the fitting results.

power-law model. In the resulting distribution of the change in reduced χ^2, we find that 99.9% of the simulated light curves have a change in reduced χ^2 that is equal or greater than that obtained from the observed light curve. Thus the Monte Carlo simulation suggests the triple break power law is preferred over the double break power law at 3σ confidence level. The values of the best fitting parameters for the optical and X-ray light curves are shown in Table 2.2 and the temporal fits are shown in Figure 2.2.

Spectral analysis

Optical spectroscopy

The optical spectrum observed by the 6 m BTA telescope, given in Figure 2.3, shows multiple absorption lines that we identify as Lyman-α (Ly-α) absorption, Al III (1854.72Å , 1862.78Å), C IV (1548.20Å , 1550.77Å), C II (1334.53Å), N V (1238.81Å , 1242.80Å) Fe II (1608.45Å), Mg II (2803.53Å , 2796.35Å), Si II (1260.42Å , 1304Å , 1526.72Å), Si IV (1393.76Å , 1402.77Å), and Al II (1670.79Å). All these absorption features can be attributed to a single intergalactic cloud at a common redshift z= 2.276 $\pm$0.001. This measurement is consistent with and refines previous determinations (Moskvitin et al., 2014a; D'Avanzo et al., 2014b; Xin et al., 2018) of the redshift of the GRB and its host galaxy. Both random and systematic errors are included in the uncertainty of the redshift. There are a few absorption features probably due to intervening systems in the line of sight, but we are not able to identify nor determine their redshift. In addition, we do not

TABLE 2.2: Results of the best fit model to the X-ray and optical afterglows of GRB 140629A.

Optical		X-ray	
Para	Value[a]	Para	Value[a]
$\alpha_{o,1}$	$-0.72^{+0.15}_{-0.33}$		
t_{o,b_1}	$176.85^{+3.48}_{-3.22}$		
$\alpha_{o,2}$	$0.91^{+0.03}_{-0.04}$	$\alpha_{x,1}$	$0.78^{+0.04}_{-0.04}$
t_{o,b_2}	$638.69^{+126.31}_{-105.89}$	t_{x,b_1}	$3428.52^{+1167.48}_{-808.52}$
$\alpha_{o,3}$	$1.17^{+0.01}_{-0.01}$	$\alpha_{x,2}$	$1.33^{+0.09}_{-0.07}$
t_{o,b_3}	$36164.96^{+7895.06}_{-5064.96}$	t_{x,b_2}	$31179.38^{+12470.62}_{-6560.38}$
$\alpha_{o,4}$	$1.97^{+0.18}_{-0.10}$	$\alpha_{x,3}$	$2.46^{+0.49}_{-0.24}$
$\chi^2/d.o.f.$	1.38/121	$\chi^2/d.o.f.$	0.99/108

[a] The break times are given in seconds.

find any obvious strong emission lines in our spectrum. The absorption lines associated with the host galaxy at z=2.276 are identified on the spectrum provided in Fig 2.3.

We measured the equivalent widths (EW) of the detected absorption features (see Table 2.3). We found that the C IV line has a rest-frame EW value of 4.11. This makes it the strongest absorption feature in the spectrum, confirming the identifications made by de Ugarte Postigo et al., (2012b) and Xin et al., (2018). The EWs of the high ionisation species are higher than average, as compared to the results of de Ugarte Postigo et al., (2012b), while the low ionisation species show no peculiarities. This implies the line of sight has a stronger ionisation absorption than is typically found for GRBs. We are also able to derive the EW ratio of C IV/C II=2.72 ± 0.15, which is consistent with the result of Xin et al., (2018), but higher than the median value found for GRBs in de Ugarte Postigo et al., (2012b). We find the ratio of Al III/Al II=1.44 ± 0.09 and the ratio of Si IV/Si II= 5.1, which are both higher than the median values found for GRBs de Ugarte Postigo et al., (2012b). Using the ratios of C IV/C II and Si IV/Si II, we find this GRB to be consistent with the highly ionised tail of the distribution of ionisation ratios of carbon and silicon; see Fig.11 in de Ugarte Postigo et al., (2012b).

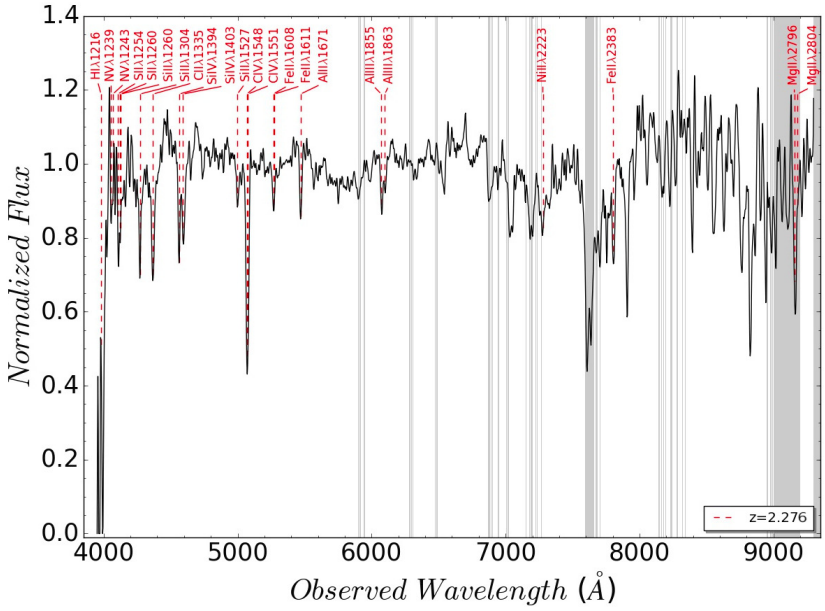

FIGURE 2.3: Overall view of the optical spectrum from BTA, obtained ∼4.1 hr after the GRB 140629A trigger. These metal lines of the absorption system in the GRB host galaxy are labelled in red, showing the corresponding transitions. The wavelength range with strong telluric absorption features are indicated by grey vertical lines.

TABLE 2.3: Spectroscopic information for the GRB 140629A.

Wave (Å)	Rest EW (Å)	Feature	z
4057.8	0.95 ± 0.12	N Vλ1238.8	2.27553
4071.2	0.51 ± 0.07	N Vλ1242.8	2.27581
4127.5	< 0.48	S IIλ1259.52 + Si IIλ1260.42	–
4272.5	2.01 ± 0.11	O Iλ1302.170 + Si IIλ1304.4	–
4289.5	0.66 ± 0.06	Si IIλ1309.3	2.27622
4374.9	1.51 ± 0.08	C IIλ1334.5 + C II*λ1335.7	–
4584.6	2.96 ± 0.11	Si IVλ1393.8+1402.8	–
5007.2	0.58 ± 0.08	Si IIλ1526.71	–
5077.4	4.11 ± 0.07	C IVλ1548.2+1550.8	–
5275.9	0.84 ± 0.06	Fe IIλ1608.4+1611.2	–
5474.7	1.01 ± 0.05	Al IIλ1670.8	2.27672
6085.6	1.45 ± 0.06	Al IIIλ1854.7+1862.8	–
7809.7	1.59 ± 0.16	Fe IIλ2383.8	2.27616
9161.8	2.66 ± 0.13	Mg IIλ2796.4+2803.5	–

Afterglow spectral analysis

As reported above, our temporal analysis of the X-ray light curve shows it to be best fitted by a double broken power-law that has two breaks at ∼3000 s and ∼30000 s. For each X-ray segment, we extracted an X-ray spectrum from the *Swift*/XRT GRB spectrum repository[8] (Evans et al., 2009). We fit each spectrum with a power-law and two photoelectric absorption components: one for our Galaxy and the other for the host galaxy of the burst. The fitting results are shown in Table 2.4. The spectral indices of the three spectra are consistent with each other at 1σ confidence. Therefore, the spectral slope does not show any evidence for evolution across the three X-ray light curve segments.

In order to constrain the spectral properties of the optical and the X-ray afterglow, we produced spectral energy distributions (SEDs) at ∼775 s and ∼9350 s after the trigger, respectively. The joint SEDs (see Figure 2.4) were fit using Xspec 12.9.0 in the HEAsoft package (Arnaud, 1996). We fit both a power-law and a broken power-law model to each of the SEDs, including components for dust and photoelectric absorption for both our Galaxy and the GRB host galaxy. We expect the synchrotron cooling frequency to be the cause of the spectral break in the broken power-law model therefore we fixed the difference in the two spectral indices to be $\Delta\beta$ =0.5. For the extinction in our Galaxy, we fixed the dust component to have an $E_{B-V} = 0.0067$ (Schlegel, Finkbeiner, and Davis, 1998) and used the Milky Way (MW) extinction curve. We fixed the hydrogen column density of the MW to be $9.3\times\ 10^{19}\mathrm{cm}^{-2}$ (Kalberla et al., 2005; Osborne et al., 2014). The fitting results are listed in Table 2.5. We tested three extinction laws for the GRB host galaxy: R_V=3.08, R_V=2.93 and R_V=3.16 for the MW, Small Magellanic Cloud (SMC), and Large Magellanic Cloud (LMC), respectively.

In the SED obtained at 775s, we consider the power-law to be the best model since the F-test indicates that the broken power-law model does not provide a significant improvement. Of the extinction models, the MW model provides the best chi-square of the three extinction models, but the reduced χ^2 is similar for all three scenarios. For the SED at 9350s (see Fig 2.4), we find that the SMC model gives a better fit compared to the other two extinction models for both the power-law and broken power-law models. Again for this SED, the F-test indicates that the broken power-law model does not improve the fit

[8] http://www.swift.ac.uk/xrt_spectra/

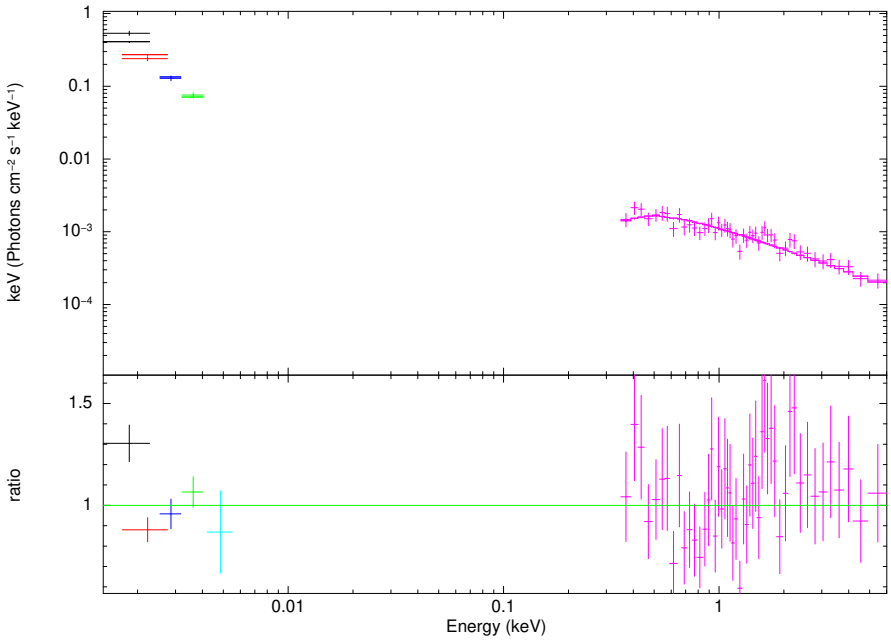

FIGURE 2.4: Optical and X-ray SED in time interval of 9350s fitted with the SMCxBKP model.

TABLE 2.4: Spectral analysis of the X-ray light curve of the GRB 140629A afterglow fitted with three segments.

Segment	Time interval (s)	Photon index	N_H (10^{21}cm^{-2})
1	$100 - 3 \times 10^3$	$1.86^{+0.14}_{-0.13}$	$6.9^{+4.4}_{-4.0}$
2	$3 \times 10^3 - 3 \times 10^4$	$1.93^{+0.11}_{-0.11}$	$7.1^{+3.6}_{-3.3}$
3	$3 \times 10^4 - 10^5$	$1.91^{+0.36}_{-0.33}$	$7.0^{+12.5}_{-7.0}$

compared to the single power-law model. The AIC supports this conclusion, as the AIC value increases for the broken power-law model compared to the power-law model. While there is no strong preference for a particular extinction law for the 775 s, the 9350 s SED clearly indicates the SMC extinction law is the best model. This is consistent with the preference for an SMC extinction law found for a large number of GRBs (Schady et al., 2010). We therefore assume this model during the further investigation of this GRB. Comparing the SMC power-law models of both SEDs, we find the parameters from the 775 s and 9350 s SEDs are consistent at 3σ confidence level and that the N_H values are consistent at 1σ confidence with the best fit values determined from the X-ray spectrum.

TABLE 2.5: Fit results for the GRB 140629A afterglow SEDs.

Model[a]	R-chi. /D.O.F	E_{B-V} (mag)	N_H (10^{21}cm^{-2})	Photon index
775s				
MW×POW	0.94/27	$0.131^{+0.017}_{-0.017}$	$3.30^{+2.24}_{-2.02}$	$1.948^{+0.026}_{-0.026}$
LMC×POW	1.02/27	$0.108^{+0.013}_{-0.013}$	$3.69^{+2.27}_{-2.04}$	$1.963^{+0.027}_{-0.027}$
SMC×POW	1.05/27	$0.085^{+0.011}_{-0.011}$	$3.40^{+2.24}_{-2.02}$	$1.952^{+0.025}_{-0.026}$
MW×BKP	0.94/26	$0.160^{+0.006}_{-0.006}$	$6.23^{+2.13}_{-1.90}$	$1.563^{+0.010}_{-0.010}$
LMC×BKP	0.99/26	$0.125^{+0.005}_{-0.005}$	$4.67^{+2.05}_{-1.84}$	$1.502^{+0.010}_{-0.010}$
SMC×BKP	1.02/26	$0.098^{+0.004}_{-0.004}$	$4.35^{+2.04}_{-1.83}$	$1.489^{+0.010}_{-0.010}$
9350s				
MW×POW	1.92/50	$0.135^{+0.017}_{-0.017}$	$6.52^{+2.01}_{-1.86}$	$2.020^{+0.024}_{-0.024}$
LMC×POW	1.44/50	$0.122^{+0.013}_{-0.013}$	$7.51^{+2.05}_{-1.89}$	$2.052^{+0.023}_{-0.023}$
SMC×POW	1.25/50	$0.083^{+0.010}_{-0.009}$	$7.20^{+2.01}_{-1.85}$	$2.039^{+0.020}_{-0.020}$
MW×BKP	1.95/49	$0.135^{+0.017}_{-0.017}$	$6.52^{+2.01}_{-1.86}$	$2.020^{+0.024}_{-0.024}$
LMC×BKP	1.47/49	$0.122^{+0.013}_{-0.013}$	$7.51^{+2.05}_{-1.89}$	$2.053^{+0.023}_{-0.023}$
SMC×BKP	1.28/49	$0.085^{+0.010}_{-0.009}$	$7.16^{+2.01}_{-1.85}$	$2.040^{+0.020}_{-0.020}$

[a] MW is Milky Way extinction model. LMC is Large Magellanic Cloud extinction model; SMC is Small Magellanic Cloud extinction model; POW is power-law model; and BKP is broken power-law model.

Host galaxy SED fitting

In order to study the GRB host galaxy, late time observations were taken by 10.4 m GTC at two separate epochs. An object was found within the XRT and UVOT error circles in the second epoch, 2.7 yr after the trigger (as shown in Figure 2.5). *Spitzer* also observed the field ~ 1 yr after the burst in the infrared in the 3.6 μm band. By this time, the afterglow contribution is negligible.

The brightness of the host galaxy is 24.94±0.24 mag in the Sloan-r band, which is within the brightness distribution for GRB host galaxies (see Fig. 2. in Guziy et al., (2005)). It is slightly fainter than the reference $M_r^\star$ galaxy at the same distance, where $M_r^\star$ is the r-band absolute magnitude, considering $M_r^\star = -20.29 + 5log(H_0/100)$ (Lin et al., 1996) and adopting an Einstein-de Sitter Universe model where the spectrum of the $M_r^\star$ galaxy was assumed to be a power-law with an index of 2.

The four photometric magnitudes for the host galaxy were fit with a set of galaxy templates based on the models from Bruzual and Charlot, (2003) at a fixed redshift (Castro-Tirado et al., 2007; Krühler et al., 2011) using the LePhare package (v.2.2; Arnouts et al. 1999; Ilbert et al. 2006). As shown in Figure 2.6,

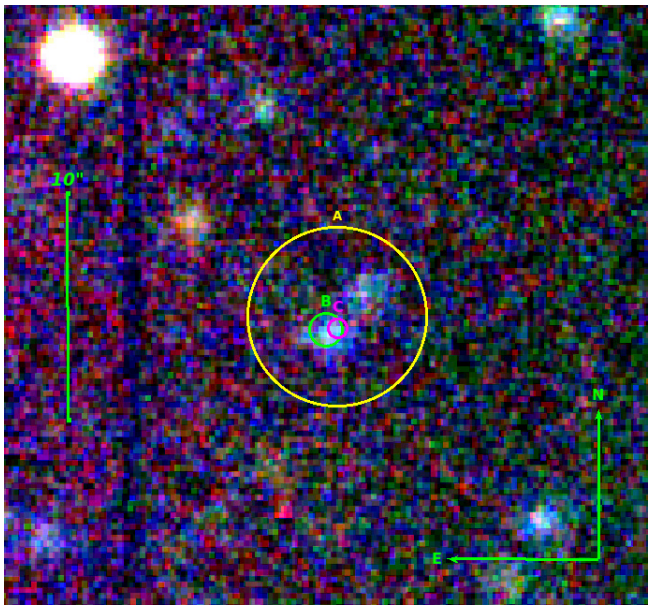

FIGURE 2.5: Sloan gri-bands false colour image of the field of GRB 140629A taken with the 10.4 m GTC on July 2, 2017. Circle A (yellow dash circle) represents the 4 arcsec radius error circle of the XRT. The circle B (green circle) and C (pink circle) represent the UVOT observation in 0.74 arcsec and 0.42 arcsec, respectively (Lien et al., 2014; Breeveld and Lien, 2014). The host galaxy is clearly found at the burst location. North is up and east to the left.

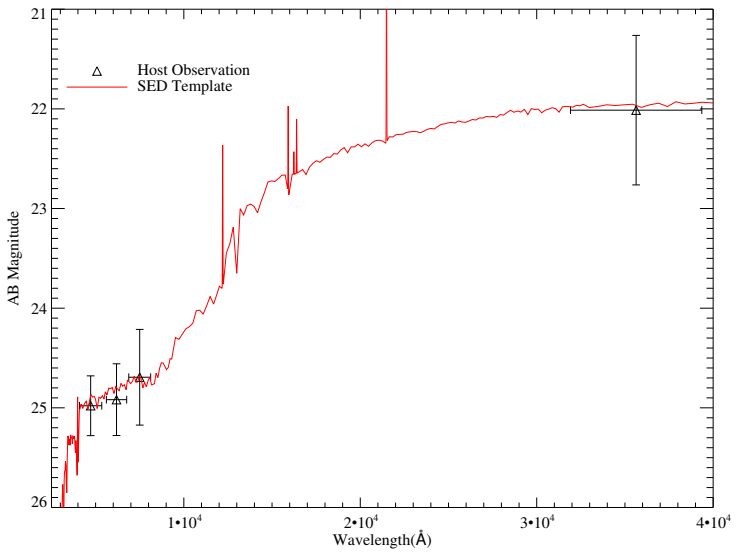

FIGURE 2.6: GRB 140629A host galaxy observations overlaid with the best fit host galaxy template.

the optical SED is reproduced best (reduced χ^2/dof=0.1/3) by a template of a galaxy with a starburst age of $1.14^{+1.03}_{-0.35}$ Gyr and a mass of $\log(M_*/M_\odot) = 8.3^{+0.9}_{-0.4}$, which is lower but consistent within errors with $10^{9.3} M_\odot$, i.e. the average value of GRB hosts (Savaglio, Glazebrook, and Le Borgne, 2009). The absolute bolometric magnitude of the host galaxy is -22.49 mag and the star formation rate (SFR) is $\log(\mathrm{SFR})=1.1^{+0.9}_{-0.4}$ $M_\odot$ yr^{-1}, which is determined from the UV luminosity of the rest-frame SED (Kennicutt, 1998). The specific star formation rate (SSFR) for this burst is $\log(\mathrm{SSFR})=-7.5^{+0.6}_{-1.3}$ yr^{-1}.

Polarisation

According to our observations with the MASTER network, GRB 140629A reached maximum optical brightness ∼150 s after the burst with 13.8 mag in white light, measured using the polariser, after which it decays as a power-law. The difference between the signals obtained in the two polarisers for the time interval from 4463 s to 11596 s were computed as $Q = \frac{I_1 - I_2}{I_1 + I_2}$. It was found that the dimensionless time-averaged Stokes parameter is $Q = 2.5 \pm 2.6\%$. For the derived uncertainty of 2.6%, the 1σ upper limit for the degree of linear polarisation P is about 18% (see Fig. 14 of Gorbovskoy et al., (2012): the value of P = 18% matches 1σ probability $L = 100\% - 68\% = 32\%$ for the curve corresponding to a relative accuracy 2.6%). At the same time, a non-evolving, weak polarisation result was obtained by Hiroshima one-shot wide-field polarimeter(HOWPol) at the Kanata telescope. They found P $\sim 2\%$ between ~ 70 to ~ 1200 s in the burst frame (Fig.10 in Gorbovskoy et al., (2016)). Our upper limit is consistent with their result.

Discussion

We have studied the optical and X-ray afterglow of GRB 140629A. There is no strong evidence for spectral evolution, with the spectral indices consistent within 3σ. The optical light curve begins with an initial rise, which decays thereafter with two breaks. The X-ray light curve decays from the start of observations and also decays with two breaks. A weak polarisation signal was found in the afterglow observations and we were able to obtain information on

the host by fitting the host galaxy SED. In the following subsections, we examine the closure relations between the temporal and spectral indices. Then we use the data to test the jet structure to determine a plausible scenario to explain this burst. Finally, we explore the properties of the host.

Closure relationship in optical and X-ray data

The closure relations are a set of equations that relate observational parameters, namely the spectral and temporal indices, with the microphysical parameters, for example, p (the electron energy spectral index), υ_m (the characteristic synchrotron frequency of the electrons at the minimum injection energy) and υ_c (the cooling frequency). Typically, the closure relations are used to determine the location of the observing bands relative to the synchrotron frequencies, υ_m and υ_c, and also the environment in which the burst occurs (Sari, Piran, and Narayan, 1998; Sari and Piran, 1999; Piran, 2004; Zhang and Mészáros, 2004; Zhang et al., 2006).

For GRB 140629A, we examined the three segments of the X-ray light curve. Spectral evolution is not observed across these segments. We first examined the second segment since this is expected to be consistent with the normal decay phase. After the first break at $\sim$ 3000 s, the light curve becomes steeper with $\alpha_{x,2} = 1.33^{+0.09}_{-0.07}$. This slope is typical of the normal decay phase ($\sim$1.1-1.5; Zhang et al., (2006)). The spectral slope for this segment is $\beta_{X,2} = 0.93^{+0.11}_{-0.11}$. During this phase, the temporal index and spectral index are consistent with the closure relation $\alpha = 3\beta/2$, which is for electrons that are slow cooling within the range $\upsilon_m < \upsilon_x < \upsilon_c$ without energy injection in a uniform circumstellar medium. The first segment decays with $\alpha_{x,1} = 0.78^{+0.04}_{-0.04}$ until 3430 s and the spectral index is $\beta_{X,1} = 0.86^{+0.14}_{-0.13}$. We first tested a simple non-injected model and found that neither $\alpha = 3\beta/2$, $\alpha = (3\beta + 1)/2$ and $\alpha = (1 - \beta)/2$ agree with the theoretic prediction (>3 σ). Only the relation $\alpha = (3\beta - 1)/2$ in the $\upsilon_x > \upsilon_c$ case can fit the indices at 1σ. However, comparing the best fit closure relations between the first and second segments implies there must be a spectral break between the two segments which is not observed. We therefore examined more complex closure relations that include energy injection. It is assumed that the luminosity evolves as $L(t) = L_0(t/t_b)^{-q}$, where q is the luminosity index affected by the energy injection (Zhang et al., 2006). The relation satisfied is

$\alpha = (q-1) + (2+q)\beta/2$. This is for a constant density medium with slow cooling electrons, where $\upsilon_m < \upsilon_x < \upsilon_c$. This relation requires $q = 0.59 \pm 0.05$. This relation can also be used in the case $\upsilon < \upsilon_m$, but we can able to rule this out since the observed slope is 3σ away from the predicted slope. Therefore, the change between the first two segments most likely signals the end of additional energy injection, after which the afterglow enters the normal decay phase. The origin of the shallow decay phase (plateau) is also an issue that has been debated. The plateau may be categorised as having an internal or external origin, depending on the behaviour of the temporal index of the next light curve segment. The internal plateau is followed by a steep decay whose index is larger than 3, even as large as 10. This plateau is a result of the internal dissipation of a millisecond magnetar as it spins down (Liang, Zhang, and Zhang, 2007; Troja et al., 2007; Yi et al., 2014). In this case, when the energy injection ceases, a sharp drop in the light curve is observed. The decay index following an external origin for the plateau is typically smaller than 3 and is well explained by energy injection into the external shocks from either slower travelling shells that are received later or by a long-lived central engine (Dai and Lu, 1998; Zhang and Mészáros, 2001; Tang et al., 2019). For GRB 140629A, the plateau is followed by a normal decay with a slope of 1.33, indicating that it has an external origin. The change in slope across the second break at ∼30000s is $\Delta\alpha \sim 1.1$. We immediately ruled out several potential interpretations for this break, including the transition of the cooling frequency across the band that predicts a $\Delta\alpha \sim 0.25$ (Sari, Piran, and Narayan, 1998); an energy injection from refreshed shocks; a long-lasting central engine that predicts a $\Delta\alpha \sim 0.7$ (Rees and Mészáros, 1998; Sari and Mészáros, 2000; Zhang and Mészáros, 2002b), or an external density change, which in order to achieve such a large change in alpha, the density would have to decrease by a factor larger than 10^3 (Nakar and Granot, 2007; Fong et al., 2012). Therefore, this observed break can only be explained by the jet geometry, for example a jet break. The light curve after the jet break should follow t^{-p}. For the third segment, the best fitting closure relation is for a spreading jet with slow cooling, where $\upsilon_m < \upsilon_x < \upsilon_c$ is consistent with the previous segments. Using the spectral index for X-ray segment 3, we found a temporal slope of -2.82 ± 0.35, which is consistent with the observed temporal slope at 1.1 sigma.

For the optical afterglow, we excluded data before 70 s from the fitting process as they were observed during the prompt emission phase and thus may be

dominated by the tail of the prompt emission. The best fit to the rest of the optical data required four segments. The first segment is an initial rise that peaks at 180 s. This is likely to be the onset of the afterglow and is discussed in more detail in Sect. 2.3.4. In that section, we focus on the decay segments. After the peak, a slope of $\alpha_{o,2} = 0.91^{+0.03}_{-0.04}$ can be explained by the scenario of energy injection in a slow cooling interstellar medium (ISM) model with $\upsilon_m < \upsilon_o < \upsilon_c$. We obtained a value of $q = 0.73 \pm 0.04$, which is consistent with that derived from the X-ray energy injected decay segment at 2σ confidence level. Furthermore, the next segment with a temporal index of $\alpha_{o,3} = 1.17^{+0.01}_{-0.01}$ is in agreement with the $\alpha = 3\beta/2$ at 3σ confidence level, which also suggests that the afterglow ceases to be energy injected and enters the normal decay phase in which electrons are slow cooling in a uniform medium. Other explanations are ruled out because the temporal indices derived using the spectral indices and the other closure relations are inconsistent with the measured values at >3σ. The last optical decay segment breaks to a steeper decay at a time (∼30000s) consistent, at 1σ, with the jet break in the X-ray light curve. The optical decay slope for this segment is shallower than -2.82 ± 0.35 derived using the X-ray spectral index, but is consistent within 3σ confidence level. As the jet break is a geometric effect, it should have an achromatic break time and the same post-break decay index at all frequencies. For GRB 140629A, the break is achromatic in time, but the slopes of the post-break power-law components are only marginally consistent; the decay index of the X-ray light curve is steeper than that in the optical. This has also been found for other GRBs such as GRB 050730 and GRB 051109A (Panaitescu, 2007).

Overall, our analysis of the optical and X-ray light curves draws a consistent picture. The light curves are both produced by the blast wave jet impinging on the constant density circumstellar medium in the slow cooling regime, where $\upsilon_m < \upsilon_o < \upsilon_x < \upsilon_c$. A long-lasting central engine is still active after the prompt emission has vanished, which when it ceases, causes the light curve to enter the normal decay phase. At ∼30000 s, an achromatic break is observed in the optical and X-ray light curves, which can be attributed to the jet break. The same process in both bands supports the X-ray radiation and the optical radiation originating from a single component outflow.

Physical model

Following Zhang et al., (2015), we fitted the multi-wavelength data with a model based on numerical simulations to obtain further information about the jet. This process is based on a 2D relativistic hydrodynamics (RHD) simulation, which assumes a jet with a top-hat Blandford-McKee profile (Blandford and McKee, 1976) that decelerates into a constant density medium. An ISM-type medium can be assumed as it has been found to explain the observations of most GRB afterglows (Panaitescu and Kumar, 2001; Racusin et al., 2009; Schulze et al., 2011) and is consistent with our analysis of GRB 140629A, as discussed in the previous section. Other assumptions of the model include that the radiation and dynamics of the collimated relativistic blast wave are assumed to be separate, and that the fraction of energy contained within the magnetic field at the front of the blast wave is low. The RHD simulation is performed with a relativistic adaptive mesh that employs a high-resolution adaptive mesh refinement (AMR) algorithm (Zhang and MacFadyen, 2006). This algorithm calculates the radiation transfer at a given observer time, angle, and distance along a line of sight (van Eerten, van der Horst, and MacFadyen, 2012; van Eerten and MacFadyen, 2013). The numerical model takes into account all the factors that can affect the shape of a jet break: (i) lateral expansion, (ii) edge effects, and (iii) off-axis effects. By fitting such a model to the optical and X-ray light curves, we are able to constrain some key physical parameters of the jet.

Because the data before the onset of the afterglow are still dominated by the prompt emission, we only model the data after 180 s. We corrected the optical data for extinction from the MW (Schlafly and Finkbeiner, 2011; Schlegel, Finkbeiner, and Davis, 1998) and the host galaxy, assuming the best fit host extinction law from the SED fitting (SMC) (for details see the previous section, Pei, 1992; Schady et al., 2007; Schady et al., 2010). We then converted the extinction corrected light curves to flux density at the central wavelength of the corresponding filter. For the X-ray light curve, the galactic and host neutral hydrogen absorption was also corrected to get the intrinsic flux density at 1 keV.

The numerical modelling calculates the flux density at any frequency and observer time. The Markov Chain Monte Carlo method is used to determine the best parameter values (i.e. the smallest χ^2 value) (Laskar et al., 2016; Sánchez-Ramírez et al., 2017). The parameters determined include the total energy $E_{tot,iso,53}$,

TABLE 2.6: Best fit parameters of the numerical simulation to the multi-wavelength afterglow.

Modelling fitting			
Parameters	Value	Err (-)	Err (+)
θ_{jet}	0.1171	0.0002	0.0061
$\log\ E_{tot,iso,53}$	1.1414	0.6226	0.0675
$\log\ n$	4.6106	0.5047	0.1875
p	2.0263	0.0008	0.0039
$\log\ \epsilon_B$	-5.6730	0.1616	0.5201
$\log\ \epsilon_e$	-0.9974	0.1347	0.5294
$\theta_{obs}/\theta_{jet}$	0.5713	0.0163	0.0048

the fraction of shock energy given to the electrons ϵ_e, the fraction of shock energy given to the magnetic fields ϵ_B, the density of the medium n, the electron energy index p, the jet opening angle θ_{jet} and the observed angle θ_{obs}. The starting ranges for each parameter are $\theta_{jet} \in$ [0.045,0.5], $E_{tot,iso,53} \in [10^{-10},10^{3}]$, $n \in [10^{-5},10^{5}]$, $p \in [2,4]$, $\epsilon_B \in [10^{-10},1]$, $\epsilon_e \in [10^{-10},1]$, and $\theta_{obs}/\theta_{jet} \in$ [0,1]. For more details, see Zhang et al., (2015).

With these settings, the resulting best-fit parameters and their uncertainties are listed in Table 2.6. The uncertainty on the parameters is calculated at the 68% confidence level in the local mode region. The best fit to each light curve for the different wavelengths is shown in Figure 2.7 and the parameter distribution is given in Figure 2.13. In this case, the numerical model finds a solution with best fit parameters of $\theta_{jet} \sim 6.7^{\circ}$ and $\theta_{obs} \sim 3.8^{\circ}$, giving a total energy release of 1.4×10^{54}erg. Since the modelling focuses on the effects of the jet break and based on a 2D RHD simulation, the energy injection is not taken into account, but the fit can still roughly describe most of the data. Furthermore, the analytic approach ($p = 2.8 \pm 0.3$) and the simulation both have p values that agree at 3σ. We find the opening angle to be typical of GRBs (Zhang et al., 2015; Racusin et al., 2009). The relative off-axis angle, $\theta_{obs}/\theta_{jet} = 0.57$, is also consistent with the distribution, which peaks at 0.8, given in Zhang et al., 2015. We also obtained a high circumstellar density value that suggests this burst originated in a dense environment. In addition, our value for $\log\ \epsilon_B$ ~-5.7 is consistent with the modelling result from (Xin et al., 2018).

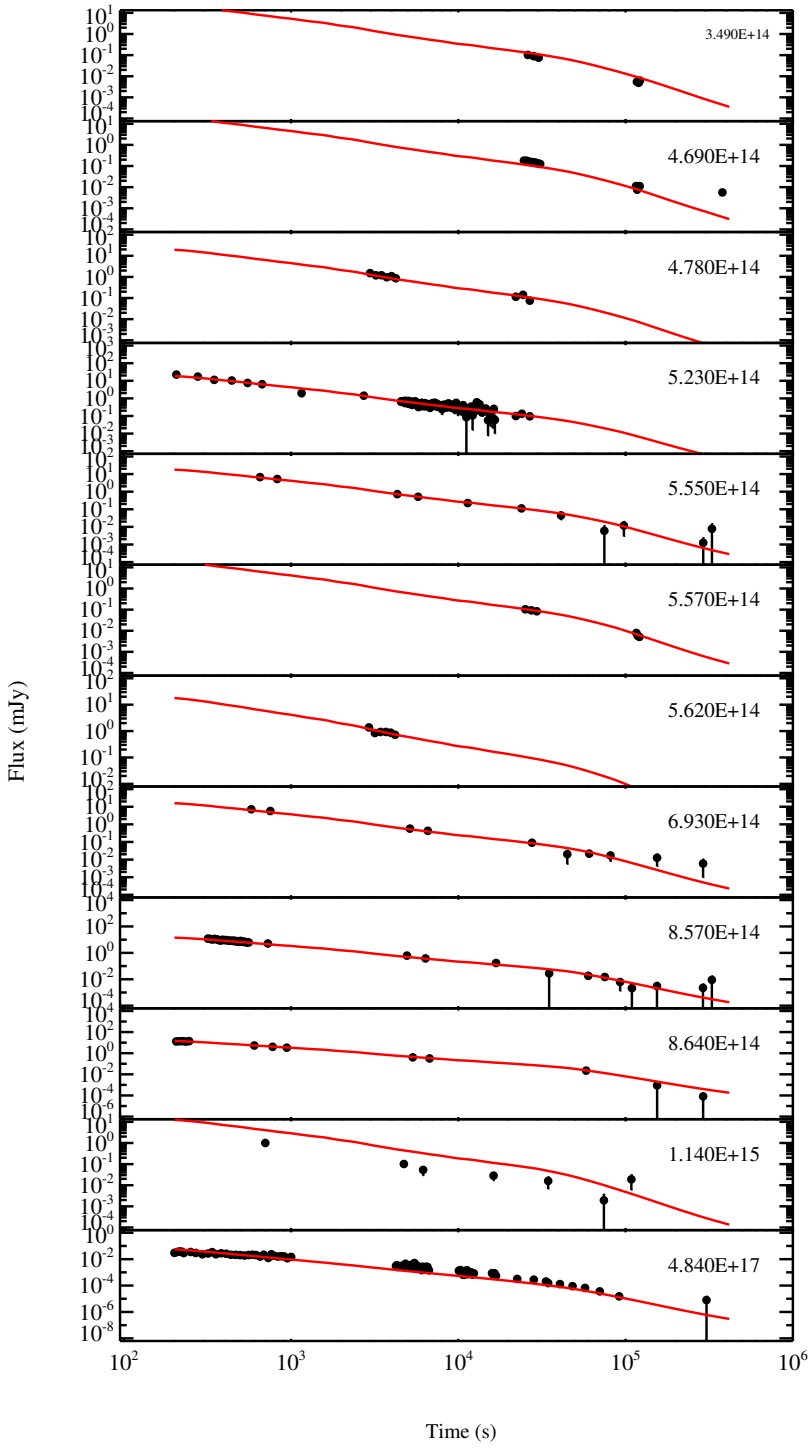

FIGURE 2.7: Best fit model determined from the numerical simulations overlaid on the observations at different wavelengths. The corresponding frequency is shown on the right corner in each panel in unit of Hz. The x-axis is the time since trigger in units of seconds. The observed flux density of each instrument is indicated on the y-axis in units of mJy. All data were corrected for MW and host galaxy absorption and extinction effects before modelling. Red solid lines represent the modelled light curves.

Jet angle and empirical relation

The $E_{r,iso}$ is the energy in γ-rays calculated assuming that the emission is isotropic. The collimation corrected energy is calculated following

$$E_\gamma \;=\; E_{\gamma,\mathrm{iso}} f_\mathrm{b} = E_{\gamma,\mathrm{iso}} \left(1 - \cos\theta_\mathrm{j}\right), \tag{2.1}$$

where f_b is the collimation correction factor. For GRB 140629A, from the high-energy emission, we determined the isotropic rest-frame energy to be $E_{\gamma,\mathrm{iso}} = 4.4 \times 10^{52}$ erg and the observed E_{peak}= 86 ± 17 keV. The peak of the energy spectrum in the rest frame is $E_{p,rest}$=$E_{peak} \times (1 + z)$= 281 ± 55 keV. The $E_{\gamma,\mathrm{iso}}$ and $E_{p,rest}$ of this burst lie within the distribution of Amati correlation as shown in Figure 2.8 (Amati et al., 2002; Amati et al., 2008; Amati, Frontera, and Guidorzi, 2009; Nava et al., 2012).

From the numerical modelling, we obtained a jet opening angle, $\theta_{jet} = 6.7°$. The collimation corrected energy is $E_\gamma = 3.0(\pm0.3) \times 10^{50}$erg. Together with $E_{p,rest}$, this burst is also consistent with the Ghirlanda relation (Ghirlanda, Ghisellini, and Lazzati, 2004; Ghirlanda et al., 2007) also shown in Figure 2.8. GRB 140629A is denoted with a red point on both these empirical relations. The bootstrap method is used to estimate their errors. We also tested the relation between $E_{\gamma,\mathrm{iso}}$, $E_{p,rest}$ and $t_{b,rest}$ (the jet break time) known as Liang-Zhang relation (Liang and Zhang, 2005), but GRB 140629A is inconsistent with this correlation, shown in Figure 2.9. It is unclear why this GRB appears to be an outlier of the Liang-Zhang relation; it could be due to selection effects relating to the GRB prompt emission.

Early optical rise

Both MASTER and UVOT observed a peak at ∼180 s (see Figure 2.1). There are several explanations for this rise based on physical mechanisms and geometric scenarios, which include the passage of the peak synchrotron frequency through the observing band, the reverse shock, decreasing extinction with time, an off-axis jet, two-component outflows, and the onset of the forward shock in the case of an isotropic outflow (Oates et al., (2009)). We discuss each of these options in turn.

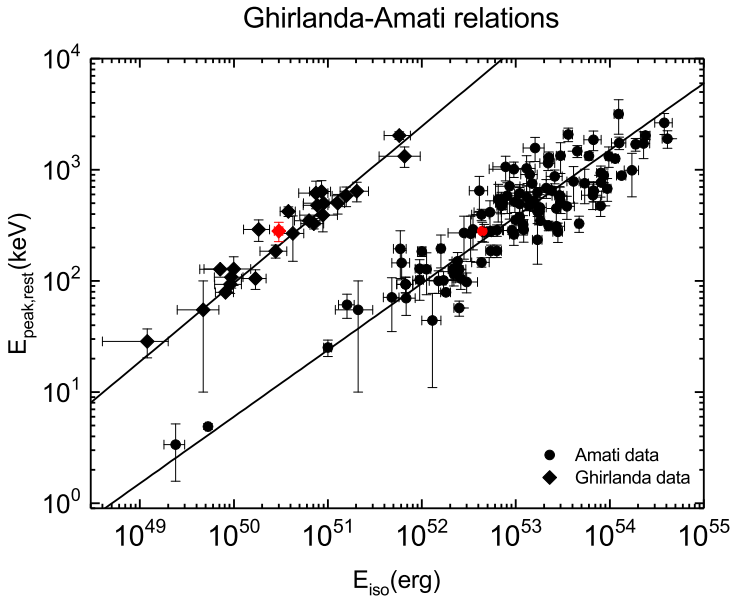

FIGURE 2.8: Location of GRB 140629A (red point) with the Ghirlanda (black prism) and Amati relation (black circle) derived from other typical GRBs (data from Ghirlanda et al., 2007; Amati et al., 2008; Amati, Frontera, and Guidorzi, 2009). The two straight lines indicate the two empirical relations.

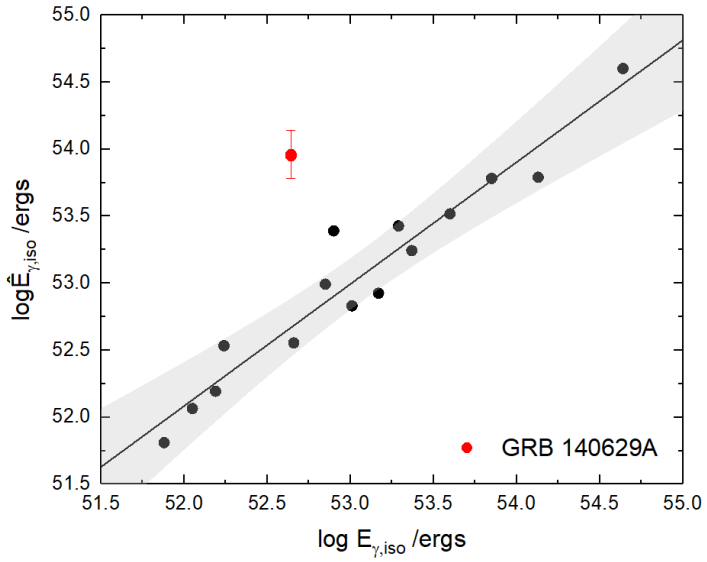

FIGURE 2.9: Location of GRB 140629A (red point) with the Liang-Zhang relation (black circle) derived from other typical GRBs (data from Liang and Zhang, 2005). $\hat{E}_{\gamma,iso}$ represents the calculated energy with the Liang-Zhang relation. The straight line indicates the empirical relations and the grey zone corresponds to the 3σ confidence level.

TABLE 2.7: Fitting result from the first optical bump in two filters.

Ins.	Slope1	Peak time	Slope2
MASTER	$-0.87^{+0.16}_{-0.15}$	$170.0^{+13.6}_{-11.8}$	$1.09^{+0.12}_{-0.13}$
UVOT	$-1.01^{+0.10}_{-0.10}$	$179.9^{+3.4}_{-3.0}$	$0.94^{+0.03}_{-0.02}$

The peak synchrotron frequency of the forward shock $\nu_{m,f}$ is expected to cross from blue to red frequencies, producing a chromatic peak which evolves at $t^{2/3}$. If the peak were due to the crossing of $\nu_{m,f}$ across the optical bands, the spectrum after peak is expected to be consistent with $\nu^{-(p-1)/2}$ for $\nu_m < \nu < \nu_c$ (Sari, Piran, and Narayan, 1998). The effective frequency of the MASTER clear filter and the UVOT white filter are 5746 and 3469 respectively (Poole et al., 2008; Kornilov et al., 2012), thus the MASTER clear filter is the redder filter. Using the central wavelengths of the white and clear filters converted to frequency and assuming p=2, we predicted the peak in the bluer filter should appear 54 s earlier than the peak in the redder filter. We therefore selected the optical data from the MASTER clear filter and UVOT white filter between 90 s and 600 s and fit with a smooth broken power-law model. The results are shown in Table 2.7. The measured difference between the peak times of the two filters is only 9 s and are the same within a 1σ confidence level. This is inconsistent with the predicted peak time difference by 4σ. This therefore makes it unlikely that the passage of $\nu_{m,f}$ is the cause of the peak in the optical filters.

For the reverse shock model, we just considered the constant density medium as this is consistent with the results of Sect. 2.3.1. In this case, when the peak synchrotron frequency of the reverse shock $\nu_{m,r}$ is lower than the optical wavelength, $\nu_{m,r} < \nu_{opt}$, the light curve is expected to decay after the peak with $\alpha = (3p+1)/4$ (Zhang, Kobayashi, and Mészáros, 2003) with $p \sim 2$ in this case, $\alpha \sim -1.75$. On the contrary, if $\nu_{m,r} > \nu_{opt}$, then the temporal index after the peak should be $\alpha \sim -0.5$, which is followed by a decay of $\alpha = (3p+1)/4$. The slope after the early optical peak is inconsistent (>3σ confidence) with both these scenarios for GRB 140629A.

Another option to produce the rise could be dust destruction. An initially high level of dust could cause optical extinction, as this dust is destroyed by the radiation from the GRB, a chromatic peak is produced with different rise indices for the different filters (Klotz et al., 2008). As dust affects the bluest filters more strongly, the redder filters rise less steeply compared to the blue

filters. While the redder MASTER filter has a shallower rise compared to the bluer UVOT filter, the slopes are consistent within 1σ and we do not consider this to be a likely cause of the optical rise.

In the forward shock model, a peak is observed when the jet ploughs into the external medium. It is expected to produce an achromatic rise with $\alpha \sim 1$ in the thick shell case with a constant density medium (Sari and Piran, 1999; Granot et al., 2002). This is consistent with the rising slopes given in Table 6. We can exclude more complex jet geometry, such as off-axis viewing and two-component outflows. If the observer's viewing angle is larger than the half-opening angle of the jet, a rise is produced when the Lorentz factor Γ decrease to $(\theta_{obs} - \theta)^{-1}$ (Granot et al., 2002; Granot, Ramirez-Ruiz, and Perna, 2005). However, the modelling result shows that the observer angle is smaller than the half-opening angle, thus this explanation can be excluded. Also, the two-component outflow can be ruled out because we find that the afterglow can be explained by a single component outflow in Sect. 2.3.1. Thus, the achromatic peak and consistent slope make the forward shock the most likely option for GRB 140629A early optical bump.

Initial bulk Lorentz factor

The initial Lorentz factor (Γ_0) is an important parameter describing the initial parameters of the jet. A common way to estimate the initial Lorentz factor is to use the peak time of the early afterglow light curve. The peak time determines the deceleration time of the external forward shock and occurs when roughly half of the blast wave jet energy is transferred to the surrounding medium, as predicted in the blast wave jet model (Sari, Piran, and Halpern, 1999; Kobayashi and Zhang, 2007). At this point, the Lorentz factor is half that of the Γ_0. For a constant density medium, the initial Lorentz factor can be expressed as

$$\Gamma_0 = 2.0 \left[\frac{3E_{\gamma,\mathrm{iso}}(1+z)^3}{32\pi n m_{\mathrm{p}} c^5 \eta_\gamma t_{\mathrm{p}}^3} \right]^{1/8}, \tag{2.2}$$

where z is the redshift, n is the density of the external medium, m_p is the proton mass, c is the speed of light, η_γ is the radiation efficiency, and t_p is the peak time of the afterglow onset bump (Sari, Piran, and Halpern, 1999; Liang et al., 2010). In the optical data, we found the early onset bump peaks at ∼180

s after the trigger. Using the parameters, n and η_γ, obtained from the modelling, the initial Lorentz factor for GRB 140629A is $\Gamma_0 = 118 \pm 5$. Lü et al., (2012) corrected the coefficient to 1.4 by integration of blastwave dynamics before the deceleration time. Using the revised equation, we obtained a Lorentz factor of $\Gamma_0 = 82 \pm 4$, which is lower than the value of 315 obtained by (Xin et al., 2018). We likely got such different results because the parameters η_γ and n obtained from our modelling are one or two magnitudes higher than those used by Xin et al., (2018). For GRB 140629A, the radiative efficiency, defined as η_γ=$E_{\gamma,\rm iso}/(E_{\gamma,\rm iso}$+$E_{\rm K,iso})$=$E_{\gamma,\rm iso}/E_{tot,iso}$, is 3.1%; this is within the radiative efficiency distribution for long GRBs (see figure 10 in Racusin et al., 2011).

Properties of the optical polarisation

The optical polarisation of GRBs provides additional clues to determine the structure and radiation mechanisms of the jet (Covino et al., 2004; Granot and Ramirez-Ruiz, 2010). Most GRB polarisation observations have been taken during the afterglow as the prompt emission is short-lived. Both linear and circular polarisations have been found at optical wavelengths (Covino et al., 1999; Wiersema et al., 2014). In our observation of 140629A, we find an upper limit of $P < 18\%$, which is consistent with the result from HOWPol (Gorbovskoy et al., 2016). Such a low degree of linear polarisation implies this burst is weakly polarised. This is considered to be confirmation that the dominant afterglow emission mechanism is synchrotron radiation. Moreover, the polarisation measurement suggests an average dust-to-gas ratio in the GRB host galaxy along the line of sight lower than our Galaxy (Klose et al., 2004), which is consistent with our findings in Sect. 2.3.7. It has been proposed that the polarisation light curves have varied trends for various jet structures, especially at the jet break time (Rossi et al., 2004; Granot and Ramirez-Ruiz, 2010). However, our polarisation observations were taken before the jet break and therefore we cannot use them to constrain the jet models for this burst.

Properties of the host galaxy and environment

The optical to X-ray SED at 9350 s gives the N_H along the line of sight as 7.2×10^{21}cm^{-2}, which is higher than that of our Galaxy (N_H^{MW}=$9.3\times\ 10^{19}$cm^{-2}) by two orders of magnitude. In addition, the intrinsic E_{B-V} is 0.083 $\pm$ 0.009,

which is also one order of magnitude higher than that of our Galaxy. Therefore, the dust-gas ratio along the line of sight to GRB 140629A is $N_H/A_V = 2.96 \times 10^{22}\text{cm}^{-2}$. This is lower than that of our Galaxy by one order of magnitude and is slightly lower than the mean value of $3.3 \times 10^{22}\text{cm}^{-2}$ for the SMC extinction model from Schady et al. 2010. This burst does not show any distinct feature in comparison with the other typical GRBs in the $N_H - A_V$ plane (see Figure 9 in Littlejohns et al., 2015).

The best fit of the host galaxy SED suggests the host galaxy has a SFR of log(SFR)=$1.1^{+0.9}_{-0.4}$ $M_\odot$ yr^{-1}. Compared to other GRB host galaxies, the SFR is higher than the median value 2.5$M_\odot$ yr^{-1} (Savaglio, Glazebrook, and Le Borgne, 2009), but within 2σ of the distribution. The host galaxy is consistent with the SFR and stellar mass correlation for star-forming galaxies, known as the star formation main sequence (Daddi et al., 2007), while it is at the edge of the distribution in the GRB sample shown in Figure 2.10 (Savaglio, Glazebrook, and Le Borgne, 2009). This may indicate the mass of this galaxy is lower than other semi-SFR galaxies, although the errors are fairly large. The specific SFR is higher than the average value of 0.8Gyr^{-1}, but it follows the correlation between the SSFRs and the stellar mass (Christensen, Hjorth, and Gorosabel, 2004; Savaglio, Glazebrook, and Le Borgne, 2009), as shown in Figure 2.11. The growth timescale in this case is lower than the Hubble time (Savaglio, Glazebrook, and Le Borgne, 2009) at the burst distance, which suggests the galaxy is in a bursty mode.

Damped Lyman-alpha (DLA; Wolfe et al., 1986; Wolfe, Gawiser, and Prochaska, 2005) systems trace the bulk of neutral hydrogen available for star formation processes and are usually found in the lines of sight towards quasars (QSOs; Noterdaeme et al., 2012; Sánchez-Ramírez et al., 2016) and GRBs (Fynbo et al., 2009; Thöne et al., 2013). Since GRBs are produced in star-forming regions, their sight-lines probe their surrounding neutral environments within a few hundred parsecs of the sites of the bursts (Vreeswijk et al., 2013; D'Elia et al., 2014b). Hence, burst afterglow absorption spectroscopy at z $\geq$1.8 (for which the Lyman-alpha absorption line is red-shifted out of the atmospheric blue cut-off) provides a unique tool to investigate the amount of metals produced by the vicinal star formation process. At a redshift of 2.276, GRB 140629A is therefore located at a suitable distance from which we were able to obtain the constituents of the GRB environment.

In order to investigate the neutral hydrogen content at the redshift of the host galaxy, we fitted the red damping wing of the Lyman-alpha absorption with the Voigt profile using the same prescription and tools described in Sánchez-Ramírez et al., (2016), obtaining a column density value of log N_{HI}=21.0±0.3, as shown in Figure 2.12. The large error in the fit mostly comes from the uncertainties in the continuum determination due to the low S/N at the blue end of the spectra. In particular, the neutral hydrogen column density is the characteristic indicator with which to distinguish if the host galaxy is a DLA system, by definition of $N_{HI} \geq 2 \times 10^{20}$cm^{-2}(Wolfe, Gawiser, and Prochaska, 2005). Therefore, the associated absorption system is technically classified as a DLA.

The measured column density is lower than the peak value $N_{HI} = 10^{21.5}$cm^{-2} found in the GRB-DLAs distribution (Fynbo et al., 2009), but is still higher than the mean value of QSO-DLAs. Compared to other GRB-DLAs, this one does not show any properties distinct to the sample of bursts in Figure 4 of Toy et al., (2016). This value is unusual in the QSO-DLA sample, but frequently observed in GRB sight-lines, suggesting once more that both samples are drawn from distinct populations.

In addition, we also identified strong high-ionisation lines, such as C IV, Si IV, and N V, which are present at the redshift of the absorber. In a previous analysis, it was found that the EWs of the GRB absorption feature are, on average, 2.5 times larger than those in QSO-DLAs (de Ugarte Postigo et al., 2012b). As shown in Table 2.3, those features in GRB 140629A are still consistent and even have an excess on the high-ionisation lines, which is at least six times larger than the median value from the QSO sample. Therefore, this burst also provides evidence for EWs in GRB-DLA systems being larger than those in QSO-DLAs. That may imply that GRBs are produced inside the most luminous regions of star-forming galaxies and that the light from the burst has to interact with much more host galaxy material. The N V lines can be used to trace collisionally ionised gas near long GRBs, since N^{3+} has a high ionisation potential that makes the production of N^{4+} difficult. The cold N V lines indicate that the GRB progenitor occurred within a dense environment $n \geq 10^3$cm^{-2} (Prochaska et al., 2008) within the photo-ionisation scenario. This indirectly supports the dense medium found through numerical modelling of GRB 140629A. Nevertheless, we can constrain neither the distance of the N V absorption to the progenitor nor the metal abundance owing to the low signal-to-noise ratio and

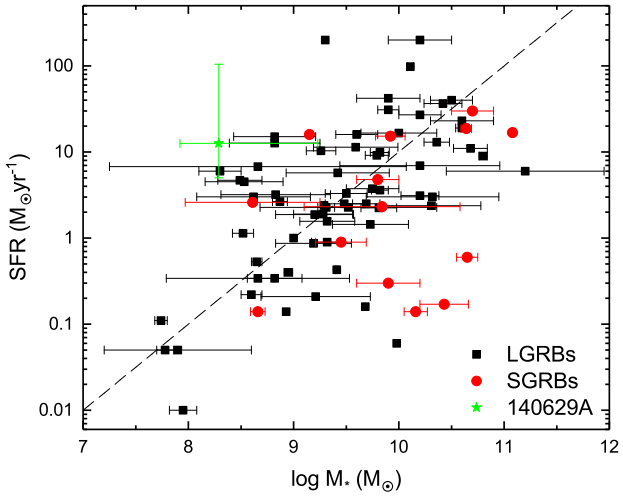

FIGURE 2.10: Plot of SFR vs. stellar mass for a sample of GRB hosts, inferred from template fitting to their photometric SEDs. The host of GRB 140629A is shown by a green star. Black squares and red dots represent the long burst and short burst hosts with SFRs measured from GHostS from 1997 to 2014 (Savaglio, Glazebrook, and Le Borgne, 2006; Savaglio, Glazebrook, and Le Borgne, 2009). The dashed line indicates a constant specific SFR of 1 Gyr^{-1}.

resolution of the spectrum.

Conclusions

Thanks to the rapid response of several robotic telescopes and continuous follow-up by larger facilities that make it possible to present multi-wavelength photometric and spectroscopic observations of the long duration GRB 140629A, providing a unique dataset on which to test models for this GRB. A detailed analysis of this burst was carried out to uncover the jet and host galaxy properties. This analysis is based on the data obtained by MASTER net, OSN, BOOTES, GTC, and BTA, as well as the public data from *Swift* and *Spitzer*. Optical spectroscopy obtained with BTA shows absorption features at a redshift of z=2.276 ± 0.001 for this burst.

The signals in two orthogonal polarisations, measured by the MASTER telescope of GRB 140629A, set an upper limit of 18% at 1σ confidence level which implies that it is a weakly polarised burst and that synchrotron radiation dominates the afterglow emission. Using the closure relations, we found that the afterglow in X-ray and optical bands can be well explained by a long-lasting

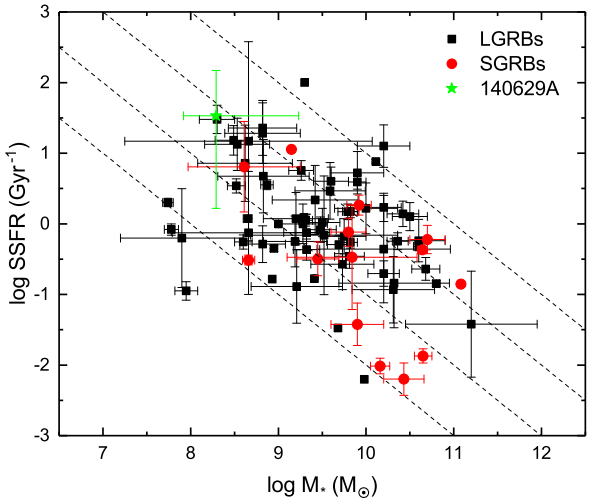

FIGURE 2.11: Plot of specific SFR vs. stellar mass for a sample of GRB hosts, inferred from template fitting to their photometric SEDs. The host of GRB 140629A is shown by a green star. Black dots indicate burst hosts with SFRs measured from GHostS from 1997 to 2014 (Savaglio, Glazebrook, and Le Borgne, 2006; Savaglio, Glazebrook, and Le Borgne, 2009). The dashed lines indicate the constant specific SFR of 0.1, 1, 10, and 100 Gyr^{-1} from left to right.

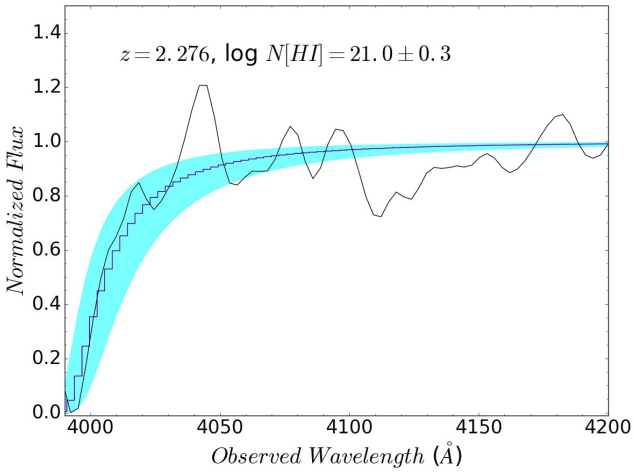

FIGURE 2.12: Voigt profile fit to the DLA in the spectrum of GRB 140629A. The figure shows the data (black solid line) and the best fit damped profile (blue solid line) with its 1σ confidence interval (cyan area).

central engine that produces continued energy injection at the beginning. After the end of energy injection, the normal decay phase is observed in both bands. The scenario in which a blast wave jet expands in a constant density ISM with slow cooling electrons, in the range $\upsilon_m < \upsilon_o < \upsilon_x < \upsilon_c$, can describe this burst well during the phases with and without energy injection. We identify the final X-ray break at 31000 s as a jet break. This break is achromatic and is observed in the optical at the same time and has break times consistent at 1σ. The afterglow is well explained by a single component outflow.

We also attempted to model the broadband data with a blast wave jet model based on the prescription of Zhang et al., (2015). The modelled result shows that this burst has a total energy release of 1.4×10^{54}ergs with an opening angle of 6.7° viewed 3.8° off-axis. In addition, a high circumstellar density is obtained from modelling and is also inferred indirectly from the identification of a high ionisation line (N V).

After correcting for redshift and the opening angle, for GRB 140629A, we find the peak energy in the rest frame and collimation-corrected energy are consistent with the Ghirlanda and Amati relations but not with the Liang-Zhang relation. The optical light curve displays a peak, which we identified as the afterglow onset produced by the forward shock which is the Γ_0 indicator. The onset is found at 181 s and indicates an initial Lorentz factor of 82-118.

Based on analysis of the host galaxy photometry, a low mass galaxy template with a SFR of log(SFR)=$1.1^{+0.9}_{-0.4}$ $M_{\odot}$ yr^{-1} at an age of $1.14^{+1.03}_{-0.35}$Gyr is obtained. This result implies the host galaxy is consistent with the star formation main sequence in a star-forming galaxy. Fitting the spectroscopy at 4000 with a Voigt profile, a neutral hydrogen density $\log N_{HI} = 21.0 \pm 0.3$ derived indicates that we detect a DLA system in the GRB host galaxy.

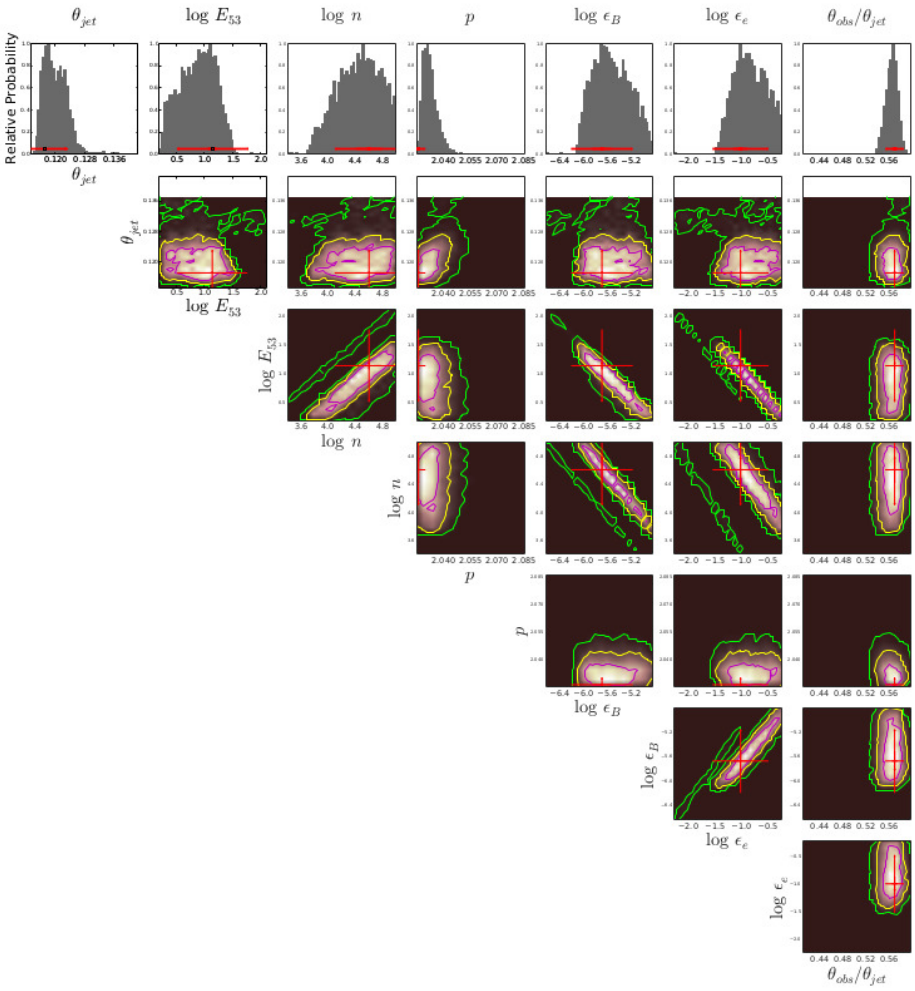

FIGURE 2.13: Triangle plot of the MCMC fitting to our simulation-based model. It shows the posterior distribution and the correlation between the parameters.

TABLE 2.8: Photometric observations at the GRB 140629A field at optical wavelengths. No correction for galactic extinction is applied.

Ins.	Band	T-T_0 (s)	Exp(s)	Mag	Err
UVOT	v	643	10	15.30	0.09
UVOT	v	817	10	15.57	0.10
UVOT	v	4219	100	17.72	0.14
UVOT	v	5654	100	18.10	0.14
UVOT	v	10933	453	18.99	0.10
UVOT	v	23772	93	19.75	0.40
UVOT	v	40923	205	20.74	0.65
UVOT	v	74215	454	>22.2	nan
UVOT	v	91482	6229	22.19	1.54
UVOT	v	142800	11769	>22.1	nan
UVOT	v	265545	25697	>23.9	nan
UVOT	v	328350	54	>21.9	nan
UVOT	b	569	10	15.70	0.06
UVOT	b	742	10	15.94	0.07
UVOT	b	5039	100	18.45	0.08
UVOT	b	6474	100	18.76	0.10
UVOT	b	27297	281	20.45	0.20
UVOT	b	44612	233	22.08	1.43
UVOT	b	56976	3651	22.00	0.38
UVOT	b	80901	364	22.26	0.85
UVOT	b	142563	11702	22.59	1.21
UVOT	b	264961	25578	23.41	2.01
UVOT	b	328171	42	>21.5	nan
UVOT	u	313	5	14.52	0.08
UVOT	u	323	5	14.57	0.08
UVOT	u	333	5	14.69	0.08
UVOT	u	343	5	14.56	0.08
UVOT	u	353	5	14.65	0.08
UVOT	u	363	5	14.77	0.08
UVOT	u	373	5	14.89	0.09
UVOT	u	383	5	14.72	0.08

Continuation of Table

Ins.	Band	T-T_0 (s)	Exp(s)	Mag	Err
UVOT	u	393	5	14.81	0.08
UVOT	u	403	5	14.77	0.08
UVOT	u	413	5	14.86	0.09
UVOT	u	423	5	14.92	0.09
UVOT	u	433	5	14.89	0.09
UVOT	u	443	5	14.96	0.09
UVOT	u	453	5	14.90	0.09
UVOT	u	463	5	15.05	0.09
UVOT	u	473	5	15.01	0.09
UVOT	u	483	5	15.13	0.10
UVOT	u	493	5	14.94	0.09
UVOT	u	503	5	15.07	0.09
UVOT	u	513	5	15.14	0.10
UVOT	u	523	5	15.12	0.10
UVOT	u	533	5	15.20	0.10
UVOT	u	543	5	15.25	0.10
UVOT	u	553	5	15.23	0.10
UVOT	u	717	10	15.44	0.08
UVOT	u	4834	100	17.74	0.08
UVOT	u	6269	100	18.27	0.10
UVOT	u	16707	116	19.13	0.15
UVOT	u	34925	6	>20.3	nan
UVOT	u	56063	3776	21.56	0.34
UVOT	u	69374	5761	21.79	0.41
UVOT	u	86665	6117	22.73	1.72
UVOT	u	108800	305	>23.1	nan
UVOT	u	142443	11665	>22.7	nan
UVOT	u	264669	25515	>23.1	nan
UVOT	u	328082	42	>21.6	nan
UVOT	$white$	101	5	15.21	0.05
UVOT	$white$	111	5	15.01	0.05
UVOT	$white$	121	5	14.89	0.05
UVOT	$white$	131	5	14.80	0.05

Continuation of Table

Ins.	Band	T-T_0 (s)	Exp(s)	Mag	Err
UVOT	$white$	141	5	14.76	0.05
UVOT	$white$	151	5	14.72	0.05
UVOT	$white$	161	5	14.56	0.05
UVOT	$white$	171	5	14.66	0.05
UVOT	$white$	181	5	14.61	0.05
UVOT	$white$	191	5	14.70	0.05
UVOT	$white$	201	5	14.77	0.05
UVOT	$white$	211	5	14.72	0.05
UVOT	$white$	221	5	14.72	0.05
UVOT	$white$	231	5	14.80	0.05
UVOT	$white$	241	5	14.70	0.05
UVOT	$white$	593	10	15.74	0.04
UVOT	$white$	767	10	16.05	0.05
UVOT	$white$	868	75	16.25	0.03
UVOT	$white$	5244	100	18.54	0.05
UVOT	$white$	6678	57	18.80	0.08
UVOT	$white$	57887	225	21.69	0.29
UVOT	$white$	142681	11739	>24.4	nan
UVOT	$white$	265252	25641	>27.0	nan
UVOT	$white$	328259	42	>21.5	nan
UVOT	$uvw1$	692	10	17.52	0.33
UVOT	$uvw1$	4629	100	20.01	0.41
UVOT	$uvw1$	6064	100	20.71	0.68
UVOT	$uvw1$	15801	450	21.39	0.60
UVOT	$uvw1$	34019	450	22.02	0.96
UVOT	$uvw1$	51655	5523	>21.8	nan
UVOT	$uvw1$	68467	5757	>23.6	nan
UVOT	$uvw1$	85759	5610	>21.7	nan
UVOT	$uvw1$	107894	450	21.83	1.27
UVOT	$uvm2$	677	10	20.05	0.86
UVOT	$uvw2$	628	10	18.96	0.89
OSN	V	24852	600	19.83	0.11
OSN	V	27020	600	19.96	0.11

Continuation of Table

Ins.	Band	T-T_0 (s)	Exp(s)	Mag	Err
OSN	V	29186	600	20.07	0.11
OSN	V	115713	600	22.63	0.19
OSN	V	117851	600	22.97	0.22
OSN	V	120677	600	23.11	0.30
OSN	I	25781	600	18.99	0.20
OSN	I	27944	600	19.14	0.20
OSN	I	29931	600	19.33	0.20
OSN	I	116628	600	22.17	0.35
OSN	I	119433	600	22.29	0.33
OSN	I	121592	600	22.03	0.46
OSN	R	24537	300	18.89	0.15
OSN	R	25469	300	18.89	0.15
OSN	R	26393	300	19.03	0.15
OSN	R	26706	300	19.04	0.15
OSN	R	27632	300	19.06	0.15
OSN	R	28557	300	19.09	0.15
OSN	R	28871	300	19.17	0.15
OSN	R	29798	300	19.22	0.15
OSN	R	30723	300	19.28	0.15
OSN	R	115404	300	21.89	0.27
OSN	R	116320	300	21.97	0.26
OSN	R	117235	300	22.32	0.34
OSN	R	117543	2798	21.94	0.20
OSN	R	120369	2130	21.90	0.22
OSN	R	376511	5329	22.65	0.27
BOOTES	i	28937	1200	19.57	0.18
BOOTES	i	30413	1800	19.74	0.18
BOOTES	i	32305	1800	19.94	0.21
BOOTES	i	34310	1800	20.17	0.24
BOOTES	i	40041	2100	20.51	0.30
BOOTES	i	42288	2700	>19.97	nan
BOOTES	i	45521	2640	>19.65	nan
GTC	Sloan-g	2.1×10^7	140×3	>24.7	nan

Continuation of Table					
Ins.	Band	T-T_0 (s)	Exp(s)	Mag	Err
GTC	Sloan-r	2.1×10^7	90	>24.3	nan
GTC	Sloan-i	2.1×10^7	90×4	>24.6	nan
GTC	Sloan-g	8.2×10^7	150×7	25.01	0.20
GTC	Sloan-r	8.2×10^7	120×7	24.94	0.24
GTC	Sloan-i	8.2×10^7	90×8	24.71	0.32
Spitzer	3.6μm	2.9×10^7	100×72	22.01	1.00
MASTER-net					
Amur	P\	37	10	14.26	0.06
Amur	P\	72	10	14.48	0.06
Amur	P\	111	20	14.06	0.08
Amur	P\	151	30	13.78	0.13
Amur	P\	206	40	13.86	0.11
Amur	P\	277	50	14.15	0.07
Amur	P\	348	60	14.61	0.06
Amur	P\	443	80	14.70	0.07
Amur	P\	550	100	15.05	0.13
Amur	P\	672	120	15.23	0.17
Tunka	P\	1156	180	16.50	0.35[a]
Tunka	C	2725	180	16.85	0.09
Tunka	V	2924	180	17.06	0.08
Tunka	R	2968	180	16.62	0.08
Tunka	V	3172	180	17.59	0.13
Tunka	R	3218	180	16.88	0.09
Tunka	V	3426	180	17.49	0.12
Tunka	R	3471	180	16.87	0.09
Tunka	V	3691	180	17.49	0.12
Tunka	R	3737	180	17.11	0.11
Tunka	V	3941	180	17.56	0.13
Tunka	R	3987	180	16.98	0.10
Tunka	V	4188	180	17.76	0.16
Tunka	R	4233	180	17.23	0.12
Tunka	P-	4553	180	17.87	0.23
Tunka	P|	4553	180	17.55	0.14

Continuation of Table

Ins.	Band	T-T_0 (s)	Exp(s)	Mag	Err
Tunka	P|	4803	180	17.72	0.15
Tunka	P-	4803	180	17.79	0.22
Tunka	P-	5046	180	17.81	0.22
Tunka	P|	5047	180	17.84	0.17
Tunka	P-	5287	180	17.92	0.24
Tunka	P|	5289	180	17.98	0.19
Tunka	P|	5531	180	17.90	0.17
Tunka	P-	5533	180	17.87	0.23
Tunka	P-	5778	180	18.38	0.32
Tunka	P|	5778	180	18.29	0.23
Tunka	P|	6023	180	18.16	0.21
Tunka	P-	6025	180	18.08	0.27
Tunka	P|	6289	180	18.19	0.21
Tunka	P-	6293	180	18.13	0.28
Tunka	P-	6534	180	18.25	0.30
Tunka	P|	6534	180	18.18	0.21
Tunka	P-	6775	180	18.34	0.31
Tunka	P|	6777	180	18.41	0.25
Tunka	P|	7016	180	18.15	0.21
Tunka	P-	7019	180	18.12	0.27
Tunka	P-	7257	180	18.07	0.27
Tunka	P|	7258	180	18.13	0.21
Tunka	P-	7505	180	18.25	0.30
Tunka	P|	7507	180	18.25	0.22
Tunka	P|	7748	180	18.26	0.22
Tunka	P-	7748	180	18.45	0.34
Tunka	P-	7990	180	18.99	0.45
Tunka	P|	7991	180	18.33	0.24
Tunka	P-	8233	180	18.34	0.31
Tunka	P|	8234	180	18.34	0.24
Tunka	P|	8490	180	18.37	0.24
Tunka	P-	8491	180	18.59	0.36
Tunka	P-	8733	180	18.16	0.28

Continuation of Table

Ins.	Band	T-T_0 (s)	Exp(s)	Mag	Err
Tunka	P|	8734	180	18.23	0.22
Tunka	P-	8976	180	18.30	0.31
Tunka	P|	8977	180	18.35	0.24
Tunka	P-	9228	180	18.43	0.33
Tunka	P|	9229	180	18.40	0.25
Tunka	P|	9471	180	18.50	0.26
Tunka	P-	9471	180	18.93	0.43
Tunka	P-	9711	180	18.09	0.27
Tunka	P|	9716	180	18.59	0.28
Tunka	P|	9952	180	18.58	0.28
Tunka	P-	9953	180	19.08	0.47
Tunka	P-	10189	180	18.70	0.38
Tunka	P|	10191	180	18.78	0.31
Tunka	P-	10431	180	19.07	0.47
Tunka	P|	10432	180	18.68	0.30
Tunka	P-	10682	180	18.42	0.33
Tunka	P|	10684	180	18.75	0.31
Tunka	P-	10923	180	19.21	0.50
Tunka	P|	10924	180	18.86	0.33
Tunka	P|	11175	180	18.79	0.32
Tunka	P-	11176	180	20.13	0.75
Tunka	P-	11431	180	18.87	0.42
Tunka	P|	11431	180	18.50	0.26
Tunka	P-	11686	180	19.18	0.49
Tunka	P|	11688	180	19.09	0.38
Tunka	P-	11933	180	18.62	0.37
Tunka	P|	11934	180	18.45	0.26
Tunka	P-	12173	180	19.88	0.67
Tunka	P|	12175	180	18.57	0.28
Tunka	P-	12412	180	18.61	0.37
Tunka	P|	12413	180	18.67	0.29
Tunka	P-	12652	180	18.51	0.35
Tunka	P|	12654	180	18.82	0.32

Continuation of Table					
Ins.	Band	T-T_0 (s)	Exp(s)	Mag	Err
Tunka	P|	12905	180	17.61	0.14
Tunka	P|	13152	180	18.32	0.23
Tunka	P-	13394	180	18.29	0.31
Tunka	P|	13396	180	18.70	0.30
Tunka	P|	13638	180	18.87	0.33
Tunka	P|	13882	180	19.07	0.37
Tunka	P|	14119	180	18.78	0.32
Tunka	P|	14347	180	18.73	0.31
Tunka	P|	14586	180	18.50	0.26
Tunka	P|	14819	180	18.91	0.34
Tunka	P|	15059	180	20.17	0.68
Tunka	P|	15301	180	19.06	0.37
Tunka	P|	15550	180	19.81	0.56
Tunka	P|	15799	180	18.97	0.35
Tunka	P|	16057	180	19.91	0.59
Tunka	P|	16302	180	18.54	0.27
Tunka	P|	16553	180	20.11	0.66
Kislovodsk	C	22078	1080[b]	19.74	0.13
Kislovodsk	R	22078	1080[c]	19.42	0.22
Kislovodsk	C	23985	1980[d]	19.42	0.13
Kislovodsk	R	24382	1800[e]	19.19	0.22
Kislovodsk	C	26759	1620[f]	19.78	0.13
Kislovodsk	R	26759	2160[g]	19.88	0.22
End of Table					

Optical data from different telescopes. (Col. 1) Telescopes' name. (Col. 2) Filter used for observation. (Col. 3) The time interval between the middle of exposure and trigger time. (Col. 4) Exposure time of observation. (Col. 5) Photometry data for GRB 140629A. (Col. 6) Error of the photometry data. For the UVOT observations, after 2000 s the exposure corresponds to the bin width rather than the exposure of individual images (see Sect. 2.2.1). Photometry data for GRB 140629A by MASTER in the polarisers and R,V, C bands. The designation C indicates white light that approximately corresponds to 0.2B+0.8R. The designation P|, P\, P- indicate

polarisers orientated at 0°, 45°, 90° to the celestial equator, respectively. The absolute fluxes can be obtained using zero points from http://master.sai.msu.ru/calibration/. All magnitudes are in Vega system except the GTC data. [a]: Evening sky observation. [b]: Coadd 6 frames. [c]: Coadd 6 frames. [d]: Coadd 11 frames. [e]: Coadd 10 frames. [f]: Coadd 9 frames. [g]: Coadd 12 frames.

Chapter 3

The very high energy long-duration GRB 190829A

In this chapter, we focus on a particularly long-duration burst, GRB 190829A, in which very high energy (VHE) gamma-ray photons were detected and a late supernova association was also found. Therefore, it prompted us to investigate its properties by observing it in different bands and comparing it with other events. For the prompt emission, we compared the properties of GRB 190829A to those of GRB 180728A, using data from *Fermi* and *Swift*. During the afterglow, we combined *Swift* observations and discussed the late time photometric and spectroscopic observational results of GRB 190829A/SN 2019oyw taken with the 10.4m GTC telescope and their comparison with other well-studied GRB/SN association events.

Introduction

Multi-wavelength observations of nearby (redshift $z \leq 0.2$) long-duration GRBs and their association with Type Ic supernovae with broad lines (Type Ic-BL SNe) have revolutionized our understanding in the explosion mechanisms and environments of massive stars across the electromagnetic spectrum (Woosley, 1993; Hjorth and Bloom, 2012). Some of these nearby GRBs also belong to the class of low-intermediate luminosity GRBs and ultra long-duration GRBs, outliers, which have revealed crucial observational evidence to distinguish between potential powering mechanisms and progenitors (Georgy et al., 2009; Dessart et al., 2017). As underlying supernova features are faint and diluted by their host galaxies, 8-10m class optical-NIR facilities play a vital role to extract information (Pandey, 2013; Cano et al., 2014). So far, there are only

handful of nearby GRBs, having associated Ic-BL SNe: GRB 980425/SN 1998bw ($z = 0.00867$; Galama et al., 1999), GRB 030329/SN 2003dh ($z = 0.16867$; Stanek et al., 2003), GRB 031203/SN 2003lw ($z = 0.10536$; Malesani et al., 2004), GRB 060218/SN 2006aj ($z = 0.03342$; Mirabal et al., 2006), GRB 100316D/SN 2010bh ($z = 0.0592$; Chornock et al., 2010), GRB 130702A/SN 2013dx ($z = 0.145$; D'Elia et al., 2015), GRB 171205A/SN 2017iuk ($z = 0.0368$; Izzo et al., 2019) and GRB 180728A/SN 2018fip ($z = 0.117$; Izzo et al., 2018).

GRB 190829A belongs to a subclass of long bursts whose prompt emission light curves show double episodes: the first being a fainter, harder pulse (a precursor), and the second, following a quiescent phase, being a significantly brighter and softer main pulse (Chand et al., 2020; Coppin, de Vries, and van Eijndhoven, 2020). These events provide a unique opportunity to probe deeper into the nature of the central engine of GRBs (Hu et al., 2014; Chand et al., 2020; Fraija et al., 2020) emitting even at very high energy (VHE; de Naurois and H. E. S. S. Collaboration, 2019; Sahu and Fortín, 2020). The proximity of GRB 190829A also provided the opportunity to discover the underlying SN (Bolmer, Greiner, and Chen, 2019; Lipunov et al., 2019a; Perley and Cockeram, 2019; Terreran et al., 2019), posing the natural question of whether such double-episodic prompt emission GRBs have a particular connection with progenitor models invoking SN features (Woosley and Bloom, 2006; Davies et al., 2007). In the *Fermi* era, Lan et al., 2018 studied a large sample (101) of such GRBs. Among these, there are only 11 bursts with known redshifts. In this sample, GRB 180728A is the nearest burst ($z = 0.117$) also found to be associated with SN 2018fip (Izzo et al., 2018; Selsing et al., 2018; Wang et al., 2019) and exhibiting remarkable similarity with the properties of GRB 190829A. Therefore, observed prompt emission properties with a significant quiescent temporal gap at *Swift*/BAT and *Fermi*/GBM frequencies for these two nearby and SN-connected GRBs prompted us to perform a joint prompt emission analysis using a sophisticated tool, the Multi-Mission Maximum Likelihood framework (3ML[1]) to explore their prompt spectral properties systematically.

VHE photons from GRB 190829A were detected by the High Energy Stereoscopic System (H.E.S.S.; de Naurois and H. E. S. S. Collaboration, 2019) making this burst the nearest to be seen at these high frequencies. Many ground-based telescopes searched for the counterparts soon after the *Swift* and *Fermi*

[1]https://github.com/threeML/threeML

gamma-ray detection and follow-up observations at other wavelengths were reported. Using the 10.4m Gran Telescopio CANARIAS (GTC, Canary Islands, Spain) optical-NIR observations, a redshift z = 0.0785 $\pm$ 0.005 was reported (Valeev et al., 2019), thus triggering larger facilities to follow-up the event and later reporting the re-brightening of the underlying transient AT 2019oyw/SN 2019oyw (Lipunov et al., 2019b; Terreran et al., 2019; Volnova et al., 2019; de Ugarte Postigo et al., 2019). The late time afterglow observations at radio frequencies were also reported by Chandra and et al., 2019, Laskar et al., 2019, and Rhodes et al., 2020.

Prompt emission properties: GRB 190829A and GRB 180728A

The *Fermi* satellite first triggered on GRB 190829A on 29 August 2019 at 19:55:53 UT (T_0, Fermi GBM Team, 2019). After 51 s, the Burst Alert Telescope (BAT) on board *Swift* also triggered and located this event at 19:56:44 UT with a duration of T_{90} = 58.2 $\pm$ 8.9 s (Dichiara et al., 2019; Lien et al., 2019). Both *Fermi*/GBM and *Swift*/BAT reported the temporal behaviour of this GRB as having a double-peaked structure. Konus-*Wind* also detected two emission episodes in the waiting mode with a total duration of $\sim$ 61.8 s. The time-integrated spectrum of the first episode using Konus-*Wind* data in the 20 keV to 2 MeV range was best described using a power-law with an exponential cut-off model with $E_p = 579^{+2282}_{-281}$ keV and a spectral slope index of $\alpha = -1.33^{+0.30}_{-0.23}$ (Tsvetkova et al., 2019). The X-ray telescope (XRT) on board *Swift* began observing the field 97.3 s after the BAT trigger and found a bright, fading uncatalogued X-ray source and continued to monitor it until four months after the trigger. The astrometrically corrected X-ray position is RA(J2000)=$02^h\ 58^m\ 10.57^s$, Dec(J2000)=$-08^\circ\ 57'30.1''$ with an uncertainty of $1.8''$ (90% confidence radius; Evans et al., 2019).

Observations by the Gamma-ray Burst Monitor (GBM, Meegan et al., 2009) on board the *Fermi* satellite were obtained from the GBM archive[2] and analysed using the 3ML software. We used data from three of the twelve sodium iodide (NaI) detectors with the strongest detections and one of the two bismuth

[2] https://heasarc.gsfc.nasa.gov/W3Browse/fermi/fermigbrst.html

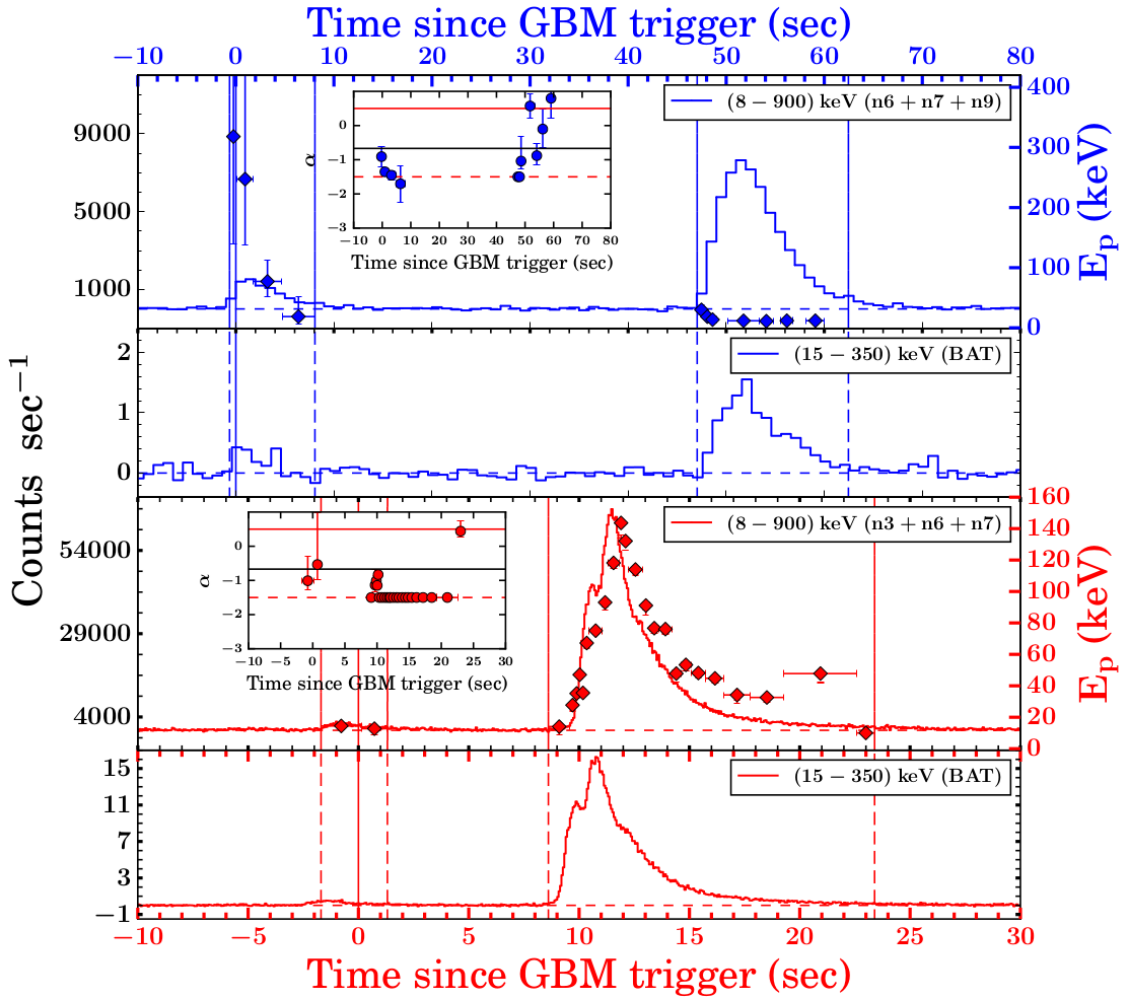

FIGURE 3.1: Prompt emission light curves of GRB 190829A (blue) and GRB 180728A (red). The two upper panels show the gamma-ray light curves of GRB 190829A (1 s bins) whereas the two bottom panels show the gamma-ray light curves of GRB 180728A (64 ms bins). The energy channels are given in the legend. Solid blue and red vertical lines represent the *Fermi* trigger times. The red and blue dashed vertical lines indicate the time interval used for the joint time-averaged spectral analysis for each episode of the two bursts. The peak energy evolution of the first episode of GRB 190829A shows a trend from hard to soft whereas the second episode is disordered. The behaviour of this second episode is contrary to the E_p behaviour observed for GRB 180728A which tracks intensity. The insets for GRB 190829A (blue) and GRB 180728A (red) show the evolution of the low-energy spectral index (α) with the red-dashed and the black-solid lines representing the synchrotron fast cooling spectral index ($-3/2$) and the line of death of synchrotron emission ($-2/3$), respectively. Interestingly, α in the case of GRB 190829A seems to overshoot the synchrotron limits in later bins whereas, for GRB 180728A, α remains within the synchrotron limit throughout its evolution.

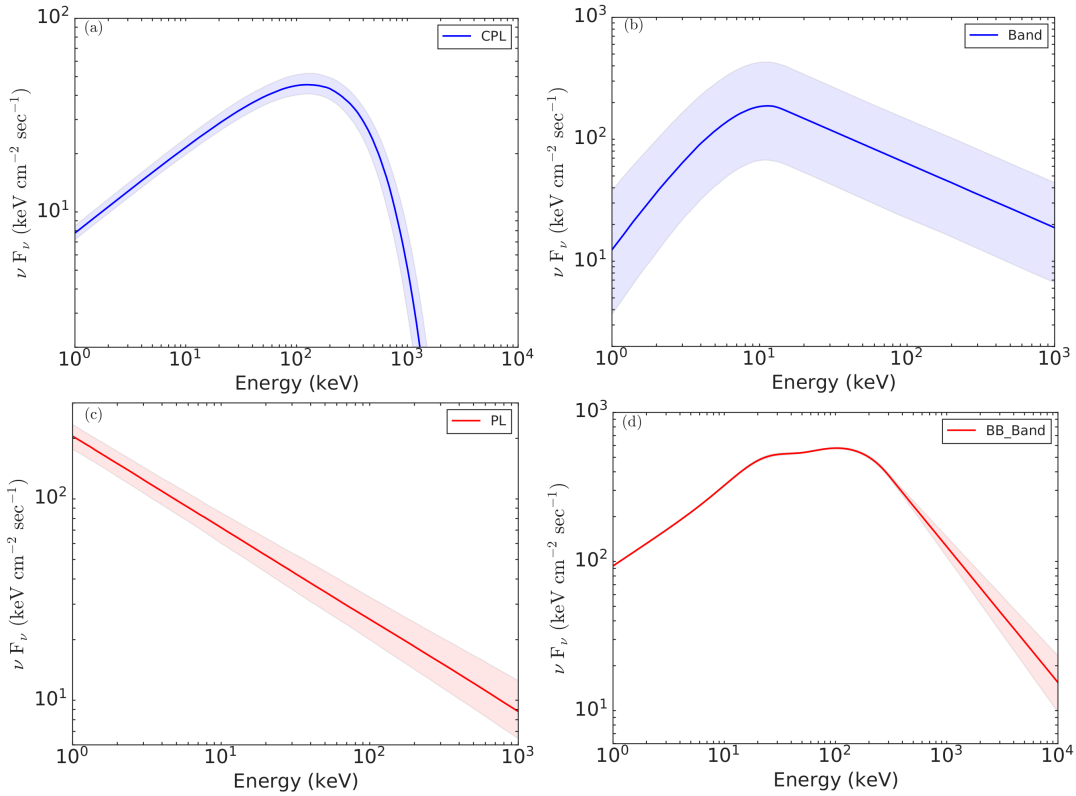

FIGURE 3.2: Best-fit time-integrated energy spectra of GRB 190829A (blue) and GRB 180728A (red) in model space using joint spectral analysis with different combinations of detectors (see Table 3.1). (a) The first pulse of GRB 190829A is modelled with a Cut-off power-law model. (b) The second pulse of GRB 190829A is best described with a Band function. (c) The first pulse of GRB 180728A is modelled with a Power-law model. (d) The second pulse of GRB 180728A is described by a combination of Band and BB functions. The shaded regions mark the 1σ contour for the corresponding best fit model.

TABLE 3.1: Comparison between different models used for the episode-wise time-averaged joint spectral analysis of *Fermi*-GBM and *Swift*/BAT data of GRB 180728A and GRB 190829A. In the model column, the best-fit model is marked with a star. The PL, CPL, and BB correspond to the power-law, cut-off power law and blackbody models, respectively.

			GRB 180728A		
E	Time (s)	Model	Log(Likelihood)	AIC[a]	BIC[b]
1	-1.70 - 1.31	PL*	1475.81	2961.76	2981.78
		CPL	1475.81	2963.82	2987.81
		Band	1471.44	2957.15	2985.11
		PL+BB	1475.81	2965.89	2993.85
		CPL+BB	1487.62	2985.39	3005.41
		Band+BB	1471.24	2960.92	2996.77
2	8.61 - 23.39	PL	4358.70	8729.56	8755.10
		CPL	3395.31	6804.84	6834.60
		Band	3472.00	6960.27	6994.25
		PL+BB	3877.83	7771.93	7805.91
		CPL+BB	3347.10	6712.54	6750.74
		Band+BB*	3273.44	6567.31	6609.71
			GRB 190829A		
1	-0.64 - 8.06	PL	2268.45	4549.07	4574.61
		CPL*	2261.82	4537.84	4567.62
		Band	2262.13	4540.54	4574.54
		PL+BB	2264.48	4545.24	4579.24
		CPL+BB	2261.43	4541.21	4579.43
		Band+BB	unconstrained	unconstrained	unconstrained
2	47.04 - 62.46	PL	2182.14	4374.42	4394.47
		CPL	2175.54	4363.29	4387.31
		Band*	2147.17	4308.61	4336.60
		PL+BB	2150.16	4314.60	4342.59
		CPL+BB	2148.33	4313.02	4344.97
		Band+BB	2142.71	4303.85	4339.75

[a] Akaike information criterion, [b] Bayesian information criterion.

germanate (BGO) detectors with the best detection (if available). We used the data from *Fermi* along with *Swift*/BAT data to examine the temporal and spectral prompt emission properties of GRB 190829A and GRB 180728A. These two nearby GRBs show similar temporal behaviour consisting of two episodes: a weak precursor and a main burst, separated by a quiescent gap. This rarely observed temporal behaviour prompted us to compare the two. To perform the time-averaged and time-resolved spectral analysis, we reduced the time-tagged event (TTE) mode data of GBM using the gtburst[3] software as they have high time precision in all 128 energy channels. We retrieved the *Swift*/BAT light curve and spectrum following the standard procedure[4], and fitted spectrum with the Band function (Band et al., 1993) and various other models (Black-body, Cut-off Power law, and Power law or their combinations) based upon the model fit, residuals of the data, and their parameters. The results based on the analysis described above are presented in Figures 3.1 and 3.2, and the values are provided in Table 3.1. The episodes are identified with the Bayesian Blocks method (Scargle, 1998).

For GRB 190829A, the time-averaged spectrum of the precursor (first episode) is best described as a power-law with an exponential high-energy cutoff function having a photon index of $-1.56^{+0.07}_{-0.08}$, and a cutoff energy corresponding to the peak energy, E_p = $123.51^{+56.14}_{-31.61}$ keV. On the contrary, the main episode is best fit by a Band function with E_p = $11.23^{+0.30}_{-0.32}$ keV, low-energy spectral index (α) = -0.23 $^{+0.26}_{-0.24}$ and high-energy spectral index (β) = $-2.53^{+0.01}_{-0.01}$, consistent with Lesage et al., 2019. However, in the case of GRB 180728A, the precursor episode is best described by a power-law with photon index equal to $-2.45^{+0.04}_{-0.05}$ whereas the main episode is best described with band+ black-body component with E_p = $102.70^{+2.12}_{-2.00}$ keV, α = -1.50 $^{+0.01}_{-0.01}$, β = $-2.91^{+0.12}_{-0.12}$ and the temperature (kT) = $5.61^{+0.09}_{-0.10}$ keV.

[3] https://fermi.gsfc.nasa.gov/ssc/data/analysis/scitools/gtburst.html

[4] https://www.swift.ac.uk/analysis/bat/index.php

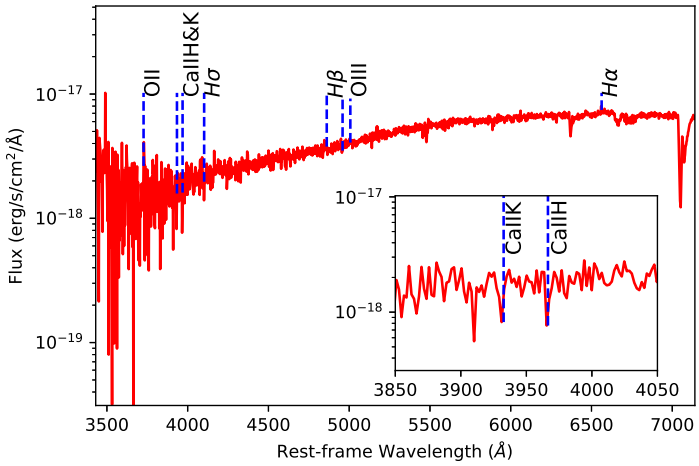

FIGURE 3.3: Optical spectrum from the 10.4 m GTC in the range $3,500-7,000$ Å, which provides the redshift of GRB 190829A. The CaII lines are shown in absorption (see Inset) and the emission lines of the underlying host galaxy are found at the same redshift.

10.4m GTC spectroscopic observations of its associated SN 2019oyw

Spectroscopic observations of GRB 190829A were triggered at the 10.4 m GTC (+OSIRIS) soon after the burst and a set of spectroscopic observations were acquired (see Table 3.2). We obtained optical spectroscopy covering the range 3,700-10,000 Å from 0.32 to 4.09 d post-burst (in the rest-frame), in order to monitor the optical evolution of its associated SN 2019oyw ; see Table 3.2. To improve the signal-to-noise ratio (S/N), the spectra at nearby epochs and their respective phases were averaged. In the following sections, the redshift determination and spectral analysis of the underlying supernova, along with the comparison to other similar nearby events, are described.

Redshift determination:

The Ca H & K absorption lines doublet (3933.664 and 3968.470 Å) were identified in the observed spectrum (see Figure 3.3) which allowed us to determine the redshift z = 0.0785 $\pm$ 0.0005 (Valeev et al., 2019). Emission lines (O III, Hα, Hβ) of the underlying galaxy are also visible at the same redshift, thus supporting the physical association between GRB 190829A and the SDSS

galaxy J025810.28-085719.2, as first proposed by Dichiara et al., 2019. In order to achieve the maximum spectral resolution at bluer wavelengths, we used the R1000B (and especially the R2500U) grisms on 30 Aug. 2019, in order to constrain the redshift.

Spectroscopic evolution of GRB 190829A/SN 2019oyw

The upper panel of Figure 3.4 shows the spectral evolution. Multiple spectra observed at similar epochs were co-added to improve the signal-to-noise ratio. All the spectra have been de-reddened for the Galactic and host extinction values (Schlafly and Finkbeiner, 2011; Chand et al., 2020) and also shifted to the rest-frame wavelength. Because of poor signal-to-noise, the smoothing of spectra has been done using the Savitzky–Golay method by fitting the second-order polynomial function for each λ in the range $\lambda - \lambda/50 < \lambda < \lambda + \lambda/50$, as described by Quimby et al., 2018. All the spectra have been flux calibrated by scaling them to the observed photometric flux density values (shown with black circles in Figure 3.4) whenever possible.

As shown in Figure 3.4, the first two spectra (at 0.32 and 1.29 days post-burst) are featureless and typical of those expected from GRB afterglows, but a transition from the afterglow (AG) to the underlying supernova (SN) is clearly illustrated with broad lines as emerging features in the later (after $\sim$ 2.23 days) optical spectra of GRB 190829A/SN 2019oyw indicating high velocities already at this stage. The spectrum at 0.32 days shows a power-law behaviour, whereas the spectra at 1.29, 2.23, and 4.09 days appear to deviate from the power-law and can be constrained with the black-body function implying black-body temperatures (T_{BB}) of $\sim$ 5100, $\sim$ 4660, and $\sim$ 4575 K, respectively (shown with cyan colour in the upper panel of Figure 3.4). The clear atmospheric features are indicated with green arrows in the spectrum taken at 4.09 days. The associated SN 2019oyw spectrum at 4.09 days appears to have Si II (λ 6355 Å) and Ca II NIR (λ 8498 Å, 8542 Å, and 8662 Å) spectral features (blue arrows) at higher velocities, typical of those seen Type Ic-BL SNe.

In the bottom panel of Figure 3.4, the spectrum of SN 2019oyw taken at $\sim$ 4.09 d is compared with other GRB/SNe spectra: SN 1998bw (Patat et al. 2001), SN 2006aj (Pian et al. 2006), and SN 2010bh (Bufano et al. 2012). For comparison, all the spectra were normalised, de-reddened (Galactic + host) and shifted to the

TABLE 3.2: GRB 190829A/SN 2019oyw spectroscopic observation log taken with the 10.4m GTC.

MJD	Phase (days)	Range (Å)	Detector	Exp time (s)
58725.120411	0.293	5100-10000	OSIRIS+R1000R	600
58725.127789	0.301	3630-7500	OSIRIS+R1000B	600
58725.180198	0.375	3440-4610	OSIRIS+R2500U	1200X2
58725.216805	0.393	3630-7500	OSIRIS+R1000B	1200
58726.202041	1.387	3630-7500	OSIRIS+R1000B	900x2
58726.223595	1.397	5100-10000	OSIRIS+R1000R	600
58727.230284	2.405	3630-7500	OSIRIS+R1000B	900
58727.241158	2.414	5100-10000	OSIRIS+R1000R	600
58729.228917	4.407	3630-7500	OSIRIS+R1000B	750x2
58729.246993	4.420	5100-10000	OSIRIS+R1000R	600

rest-frame wavelength. It is apparent that the observed broad spectral features for GRB 190829A/SN 2019oyw are similar to those observed in the other SNe. The spectrum of SN 2019oyw taken at $\sim$ 4.09 d bears a close resemblance to the spectrum of SN 1998bw taken at 7 d. This time difference between the spectra of the two SNe indicates that SN 2019oyw evolved faster than SN 1998bw.

10.4 m GTC Photometric Observations of GRB 190829A /SN 2019oyw

Photometric observations of GRB 190829A/SN 2019oyw obtained by the 10.4 m GTC telescope show that this GRB lies in the outskirts of the host; see Figure 3.5. Multi-band optical photometry observations obtained for GRB 190829A /SN 2019oyw were measured using aperture photometry through standard procedures after image subtraction. A model for the light profile of the galaxy was determined in order to estimate the contribution from the host assuming a symmetric light distribution, and we subtracted this model from the images containing the GRB/SN in order to obtain accurate photometric measurements. The photometry was calibrated against a number of stars from the SDSS catalogue (Alam et al., 2015) in the field of view. These calibration stars were

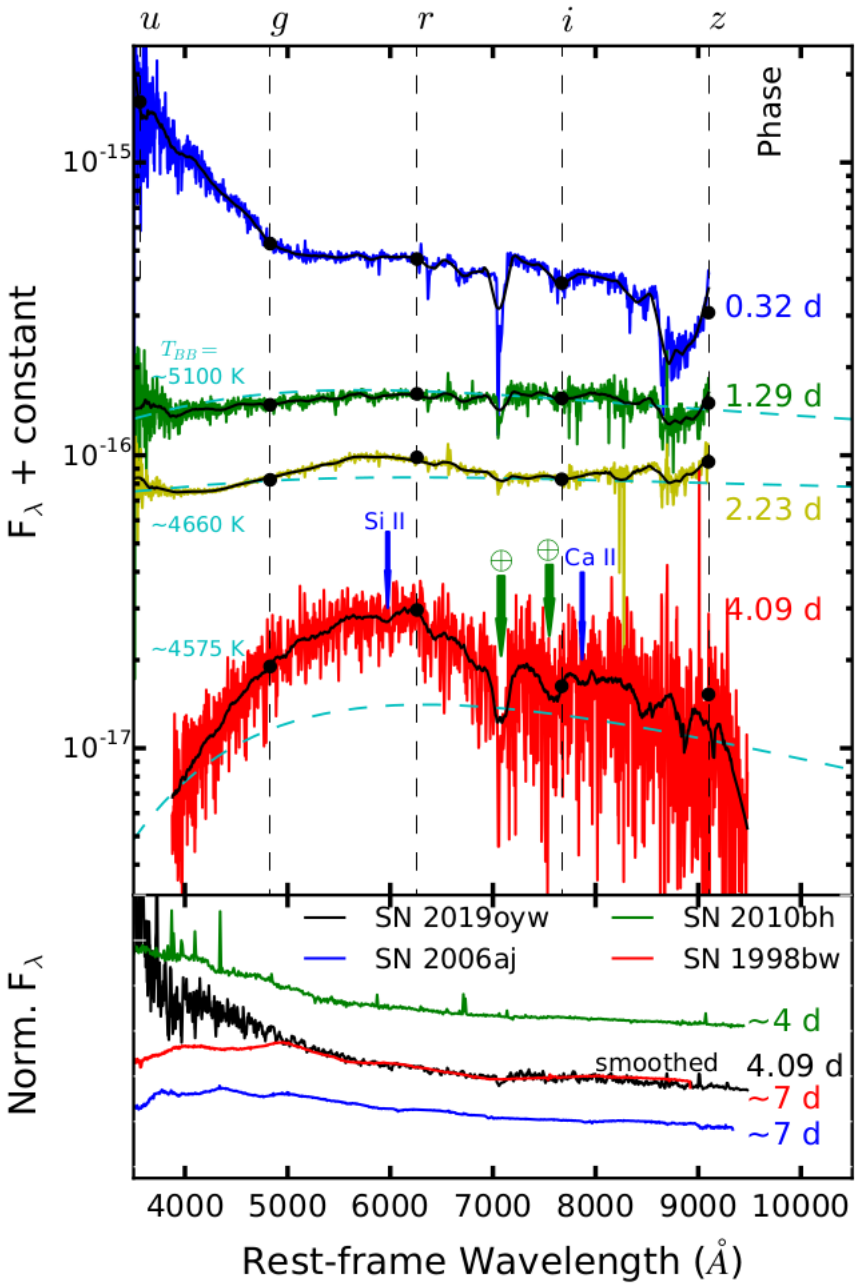

FIGURE 3.4: Spectroscopic evolution of GRB 190829A/SN 2019oyw from 0.32 to 4.09 d after the burst. The flux density as a function of the rest-frame wavelength is plotted after correcting spectra for Galactic and host extinctions. All the spectra presented in the upper panel have been corrected for grism losses and scaled to the observed photometric flux density values shown with black circles, wherever possible. Atmospheric features are indicated with green arrows in the spectrum at 4.09 d. The emission lines: Si II (λ 6355 Å) and Ca II NIR (λ 8498 Å, 8542 Å, and 8662 Å) are indicated by blue arrows. For clarity, random offsets in the Y-axis are applied to the smoothed spectra. An unusual bluer excess in the early spectrum taken at 0.32 d deviating from the overall power-law nature is also noticeable. In the bottom panel, we display the spectrum of SN 2019oyw taken at $\sim$ 4.09 d (in black, smoothed) along with other GRB/SNe spectra: SN 1998bw (red), SN 2006aj (blue), and SN 2010bh (green).

TABLE 3.3: Optical photometric data of GRB 190829A/SN 2019oyw in SDSS *u*, *g*, *r*, *i*, and *z*-bands obtained using the 10.4m GTC.

MJD	Phase[a] (days)	Exp time (s)	Filter	mag (AB)[b] (mag)	error (mag)
58725.195050	0.365	120	*u*	21.77	0.05
58726.186209	1.381	120x4	*u*	>22.83	–
58727.204482	2.377	120x5	*u*	>23.28	–
58728.229954	3.400	120	*u*	>23.65	–
58729.203136	4.376	120x5	*u*	>23.64	–
58725.196904	0.367	60	*g*	21.08	0.05
58726.184475	1.382	120x2	*g*	23.56	0.05
58727.212898	2.385	120x3	*g*	25.04	0.04
58728.231701	3.403	120x3	*g*	23.95	0.06
58729.211539	4.383	120x3	*g*	24.64	0.09
58725.198025	0.368	30	*r*	19.68	0.01
58726.191965	1.364	60x2	*r*	21.75	0.06
58727.224253	2.396	180	*r*	22.60	0.03
58728.236767	3.407	120	*r*	22.94	0.03
58729.222909	4.394	60x2	*r*	22.59	0.06
58725.115196	0.287	10x3	*i*	18.40	0.02
58725.176400	0.354	50	*i*	18.79	0.01
58726.183430	1.382	60x2	*i*	20.73	0.05
58727.217984	2.388	120	*i*	22.34	0.06
58728.238499	3.409	120	*i*	22.30	0.02
58729.216606	4.387	120	*i*	22.15	0.08
58732.158872	7.331	30x3	*i*	22.00	0.04
58736.180631	11.35	30x2	*i*	21.08	0.03
58739.131398	14.30	30x2	*i*	20.76	0.09
58754.138870	29.31	60x2	*i*	21.23	0.02
58765.162492	40.33	60	*i*	22.48	0.01
58725.199912	0.370	30	*z*	18.17	0.02
58726.177119	1.347	30	*z*	19.93	0.00
58727.219749	2.390	45x3	*z*	20.70	0.01
58728.240237	3.411	45x3	*z*	20.44	0.04
58729.218345	4.389	45x3	*z*	21.31	0.05

[a] Time after the burst, [b] Galactic extinction corrected.

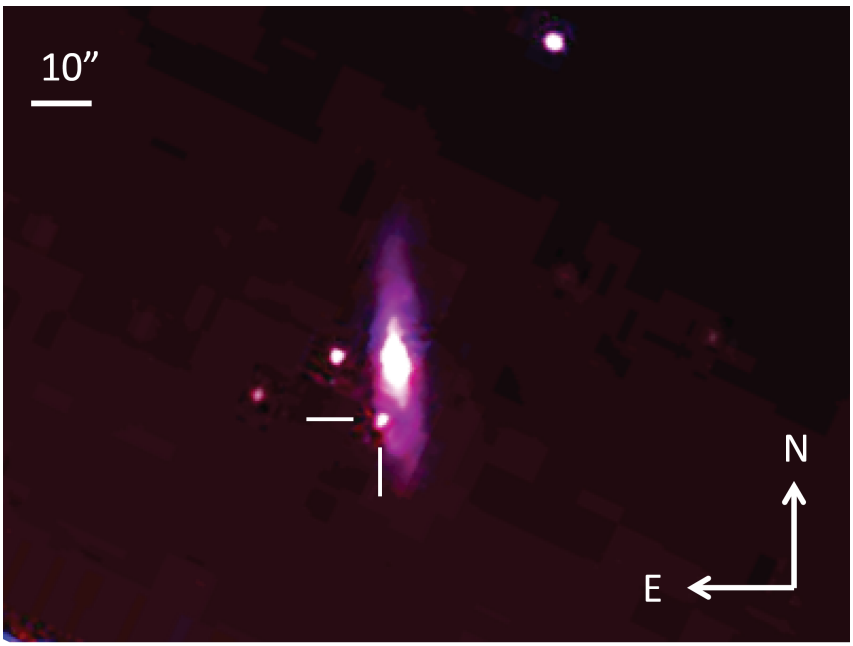

FIGURE 3.5: Sloan *gri*-band false colour image of the field of GRB 190829A taken with the 10.4 m GTC on 29 August 2019. Two perpendicular lines indicate the afterglow position. The associated host galaxy, J025810.28-085719.2, is clearly seen. North is up and east to the left.

specifically chosen because they are isolated, not saturated, and are in a constant background. The derived AB magnitudes in SDSS ($ugriz$) filters for the afterglow/SN 2019oyw are provided in Table 3.3.

The optical photometric observations of GRB 190829A/SN 2019oyw spanning from 0.29 to 40.33 d after the trigger are shown in Figure 3.6 along with the XRT light curves (at 10 keV) in the observer frame. The magnitudes have been corrected for Galactic as well as the host galaxy extinction using E(B-V) = 0.049 mag and 1.04 mag, respectively. The host-galaxy extinction is adopted from the best-fit model of Chand et al., 2020 obtained for the Small Magellanic Cloud (SMC) extinction law. The plotted *ugriz* light curves of GRB 190829A/SN 2019oyw are contributions of the AG and the associated SN, whereas the constant flux contribution from the host galaxy has already been removed using the template subtraction technique. Late-time *i*-band (in black) data (up to ~ 40 d after the burst) for GRB 190829A/SN 2019oyw clearly show the expected SN signature with a late-time bump peaking at ~ 20 d. The light curves in the g, r, i, and z-filters up to ~ 2.3 d post burst were individually fitted with a single power-law model. The temporal flux decay indices in each of the four filters

were determined to be $\alpha_g = 1.77 \pm 0.08$, $\alpha_{\rm r} = 1.45 \pm 0.01$, $\alpha_{\rm i} = 1.53 \pm 0.13$, and $\alpha_{\rm z} = 1.25 \pm 0.01$. To extract the afterglow contribution from the entire *i*-band GTC dataset, we used the flux temporal decay index determined in the i filter measured up to $\sim$ 2.3 d post burst. We also use the value of $\alpha_{\rm i}$ for subsequent analysis as this value is close to the average value of the decay indices obtained using all four individual filters.

Light curve evolution

Using the temporal decay indices determined in Sect. 3.4, we extrapolated the AG contribution up to $\sim$ 41 d (see Figure 3.6, cyan dashed line) and subtracted it from the *i*-band light curve to obtain the light curve of the associated SN (in lime green). SN 2019oyw appears to emerge at very early phases (from $\sim$ 3 d) and reaches peak magnitude at $\sim$ 20 d. The X-ray light curve (at 10 keV) shows a late-time bump at $\sim$ 20 d, contemporaneous with the SN bump (see Figure 3.6 (in red)); however, we do not see any blackbody evolution at the four epochs of the joint spectral energy distributions (SEDs; see Figure 3.7). Interestingly, such late time XRT bumps at 10 keV were also observed in the cases of GRB 171205A (Izzo et al., 2019) and GRB 180728A (Wang et al., 2019; Rueda et al., 2020). Based on observations, the progenitors and powering mechanisms for these nearby rare events are constrained to the plausible models such as 'Collapsar' (Woosley, 1993) and the binary-driven hypernova model (Ruffini et al., 2001; Ruffini et al., 2016). A separate detailed investigation is underway to obtain a detailed understanding of this subclass of nearby bursts, namely GRB 171205A/SN 2017iuk, GRB 180728A/SN 2018fip, and GRB 190829A/SN 2019oyw, with noticeable late-time X-ray bumps (at 10 keV) along with the evolution of the XRT photon indices ($\Gamma_{\rm XRT}$).

SED evolution of GRB 190829A

Near-simultaneous optical and X-ray SEDs were constructed at four different epochs covering the afterglow decay phase and the peak of SN 2019oyw; see times indicated by cyan shaded bands in Figure 3.6. The SEDs at XRT frequencies were collected from the *Swift*-XRT page[5] and modelled using XSPEC to determine the spectral indices. The 10.4 m GTC extinction corrected SEDs

[5] https://www.swift.ac.uk/xrt_spectra/

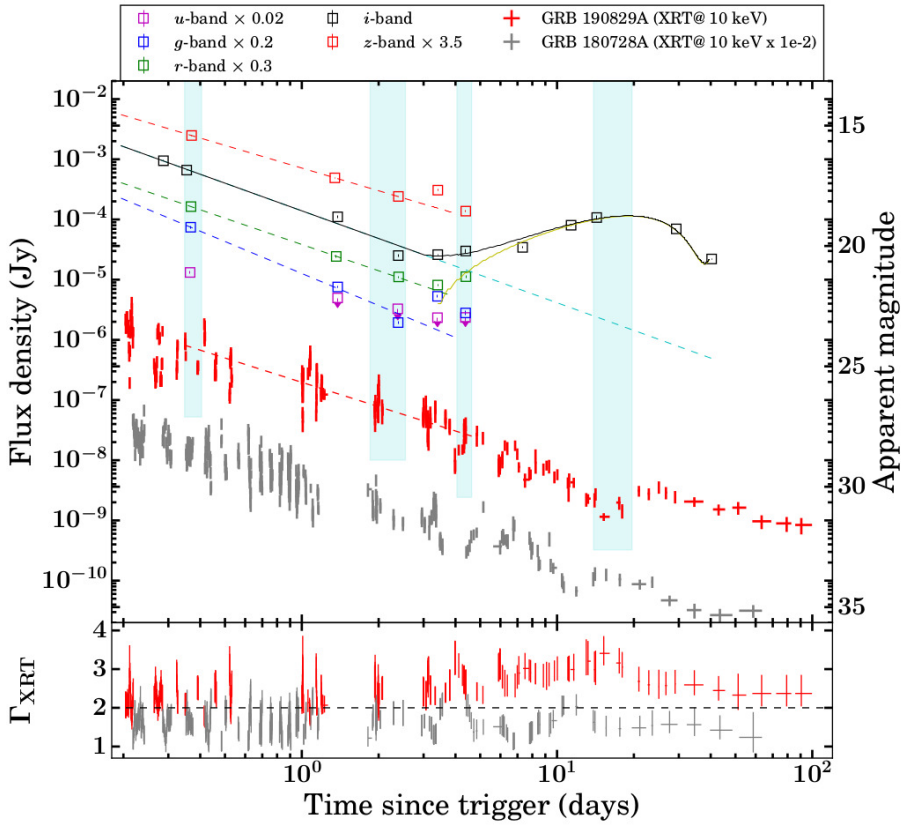

FIGURE 3.6: 10.4 m GTC multi-band optical light curves (in flux density) of GRB 190829A/SN 2019oyw between 0.32 and 40.3 d post burst. The data are corrected for Galactic and host extinction, as discussed above. The *i*-band light curve of SN 2019oyw peaks around 20 d after the burst which appears to match with the late-time bump in the 10 keV *Swift*/XRT light curve (in red). The shaded vertical bars (in cyan) show the four epochs used to create the SED of the GRB 190829A afterglow. For comparison, the X-ray light curve (at 10 keV) of GRB 180728A (in grey) is also plotted; it has similar temporal features (including temporal decay indices, light-curve variability, late-time bump) to the X-ray light curve of GRB 190829A. The bottom panel shows the evolution of the XRT photon indices ($\Gamma_{\rm XRT}$) of the two GRBs discussed. The horizontal black dashed line shows $\Gamma_{\rm XRT}$ equal to 2. The evolution of $\Gamma_{\rm XRT}$ indicates late-time softening during the 'SN phase', and demands a detailed investigation using a larger subset of such events.

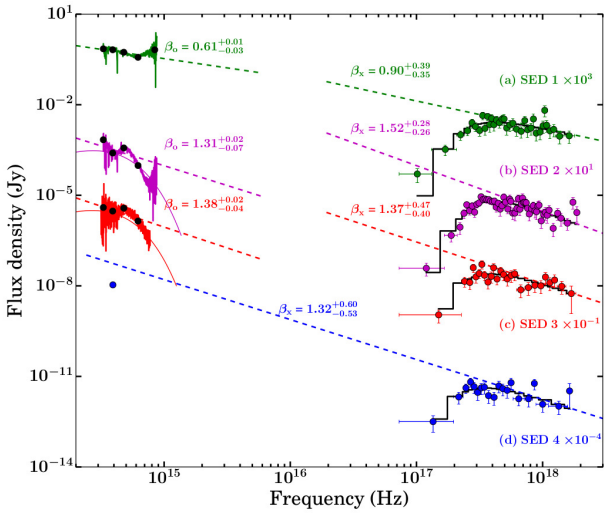

FIGURE 3.7: Spectral energy distributions of the GRB 190829A afterglow using the optical-XRT data. (a) SED at $\sim$ 0.37 days (green), (b) SED at $\sim$ 2.2 days (magenta), (c) SED at $\sim$ 4.34 days (red), and (d) SED at $\sim$ 14.3 days (close to the i-band peak) showing the absence of thermal emission at XRT frequencies. In (b) and (c) optical SEDs, fitted BB contributions are also plotted in respective colours as described in section 3.3.2. The derived values of the spectral indices are tabulated in Table 3.4.

were fitted using a single power-law model as discussed above. The X-ray temporal decay index using data taken at 10 keV was found to be $\alpha_{\rm x-ray} \sim 1.34^{+0.06}_{-0.06}$ between $\sim 3 \times 10^4$ and $\sim 4 \times 10^5$ s. This temporal index was used along with those estimated at optical frequencies $\alpha_{\rm opt}$ to study the evolution of the SEDs. The details of the four epochs of SEDs and their corresponding indices for the different segments of optical and X-ray data (SED 1- SED 4) are listed in Table 3.4. We used the closure relations $\alpha_{\rm opt} - \beta_{\rm opt}$, $\alpha_{\rm x-ray} - \beta_{\rm x-ray}$ (Sari, Piran, and Narayan, 1998; Gompertz, Fruchter, and Pe'er, 2018) to constrain the model and location of the cooling-break frequency (ν_c). Considering adiabatic cooling without energy injection from the central engine and a slow cooling case for an interstellar matter (ISM)-like environment as suggested by Chand et al., 2020 and Fraija et al., 2020, there are three possible scenarios from optical to X-ray frequencies (Gompertz, Fruchter, and Pe'er, 2018):

(i) $\nu_{\rm c} < \nu_{\rm opt} < \nu_{\rm x-ray}$; in this case it is

$$\begin{aligned} \alpha_{\rm opt} = \alpha_{\rm x-ray} = \frac{3p-2}{4}; \\ \beta_{\rm opt} = \beta_{\rm x-ray} = \frac{p}{2} \end{aligned} \tag{3.1}$$

(ii) $\nu_{\rm opt} < \nu_{\rm c} < \nu_{\rm x-ray}$; in this case it is

$$\begin{aligned} \alpha_{\rm opt} = \frac{3(p-1)}{4}; \alpha_{\rm x-ray} = \frac{3p-2}{4}; \\ \beta_{\rm opt} = \frac{p-1}{2}; \beta_{\rm x-ray} = \frac{p}{2} \end{aligned} \tag{3.2}$$

(iii) $\nu_{\rm opt} < \nu_{\rm x-ray} < \nu_{\rm c}$; in this case it is

$$\begin{aligned} \alpha_{\rm opt} = \alpha_{\rm x-ray} = \frac{3(p-1)}{4}; \\ \beta_{\rm opt} = \beta_{\rm x-ray} = \frac{p-1}{2}. \end{aligned} \tag{3.3}$$

We calculated the electron distribution index (p) for each scenario mentioned above using the calculated value of $\alpha_{\rm opt,x-ray}$ and $\beta_{\rm opt,x-ray}$. For SED 1, we find that the afterglow can be described with the $\nu_{\rm opt} < \nu_{\rm c} < \nu_{\rm x-ray}$ spectral regime. Later on, for SED 2, SED 3, and SED 4, $\nu_{\rm c}$, the spectral index decreases consistent with $\nu_{\rm c}$ having crossed the optical/X-ray band, and indicating that at these epochs we are now in the $\nu_{\rm c} < \nu_{\rm opt} < \nu_{\rm x-ray}$ spectral regime.

SN 2019oyw properties and comparisons

The extracted light curve of SN 2019oyw in absolute magnitudes (in black) is plotted in the rest-frame, see Figure 3.8. The absolute magnitudes are calculated from de-reddened apparent magnitudes and also corrected for cosmological expansion (Hogg et al., 2002) to get the rest-frame magnitudes, as described in Kumar et al., 2020. The *i*-band light-curve evolution of SN 2019oyw (see Figure 3.8, black solid line) is compared with other well studied low-redshift GRB-SNe such as SN 1998bw (in red; Galama et al., 1999), SN 2006aj (in blue; Bianco et al., 2014), and SN 2010bh (in green; Cano et al., 2011) after correcting for Galactic as well as host galaxy extinction using values taken from Cano, 2013 and references therein.

TABLE 3.4: Best fit optical and X-ray spectral indices of SEDs at different epochs and the spectral regime that best describes them. p is the mean value of the electron distribution indices calculated from the observed values of $\alpha_{\rm opt}/\alpha_{\rm x-ray}$ and $\beta_{\rm opt}/\beta_{\rm x-ray}$ of the best-descriptive spectral regimes.

SED	Time interval (s)	$\beta_{\rm opt}$	$\beta_{\rm x-ray}$	p (Spectral regime)
1	3-3.5 $\times$ 10^4	$0.61^{+0.01}_{-0.03}$	$0.90^{+0.39}_{-0.35}$	2.33 ± 0.38 ($\nu_{\rm opt} < \nu_{\rm c} < \nu_{\rm x-ray}$)
2	1.6-2.2 $\times$ 10^5	$1.31^{+0.02}_{-0.07}$	$1.52^{+0.28}_{-0.26}$	2.65 ± 0.23 ($\nu_{\rm c} < \nu_{\rm opt} < \nu_{\rm x-ray}$)
3	3.5-4.0 $\times$ 10^5	$1.38^{+0.02}_{-0.04}$	$1.37^{+0.47}_{-0.40}$	2.61 ± 0.14 ($\nu_{\rm c} < \nu_{\rm opt} < \nu_{\rm x-ray}$)
4	1.2-1.7 $\times$ 10^6	-	$1.32^{+0.60}_{-0.53}$	2.54 ± 0.09 ($\nu_{\rm c} < \nu_{\rm opt} < \nu_{\rm x-ray}$)

Light curves of the four SNe connected to GRBs (see Figure 3.8) are fitted with low-order polynomials to estimate the peak absolute magnitudes ($\rm M_i$) and the times taken by the SNe to rise and fall by 1 mag from the peak ($\rm t_{rise}^{\Delta 1mag}$ and $\rm t_{fall}^{\Delta 1mag}$, respectively). The peak magnitude of SN 2019oyw is $\rm M_i = -19.04 \pm 0.01$ mag, which is brighter than SN 2006aj ($\rm M_i = -18.36 \pm 0.13$ mag) and SN 2010bh ($\rm M_i = -18.58 \pm 0.08$ mag), and more similar to the peak absolute magnitude of SN 1998bw ($\rm M_i \sim -18.95$ mag).The calculated value of $\rm t_{fall}^{\Delta 1mag}$ for SN 2019oyw is found to be 13.32$\pm$0.04 d, which is lower in comparison to those estimated for other GRB-SNe, namely SN 1998bw ($\sim$ 24.8 d), SN 2006aj ($\sim$ 20.3 d), and SN 2010bh ($\sim$ 17.1 d). This indicates a steeper post-peak decay rate for SN 2019oyw, as can also be inferred from the faster spectral evolution in Sect. 3.3.2. Examining the value of $\rm t_{rise}^{\Delta 1mag}$ for SN 2019oyw (9.67 $\pm$ 0.02 d), we find it to be most similar to SN 2006aj ($\sim$ 8.80 d) and SN 2010bh ($\sim$ 9.0 d), whereas it is lower in comparison to that observed in the case of SN 1998bw ($\sim$ 13.3 d). We also estimate the value of the ejected nickel mass ($\rm M_{Ni}$) as $0.5 \pm 0.1\,\rm M_\odot$ for GRB 190829A/SN 2019oyw using the relation between $\rm M_{peak}$ and $\rm M_{Ni}$ given by Lyman et al., 2016. The discussed light curves of the four GRB-SNe have also been compared with the ^{56}Ni –> ^{56}Co theoretical decay curve. SN 2019oyw appears to be consistent with this decay curve (shown with a black dotted line) soon after the peak. As studied by Wheeler, Johnson, and Clocchiatti, 2015; see also Cano,

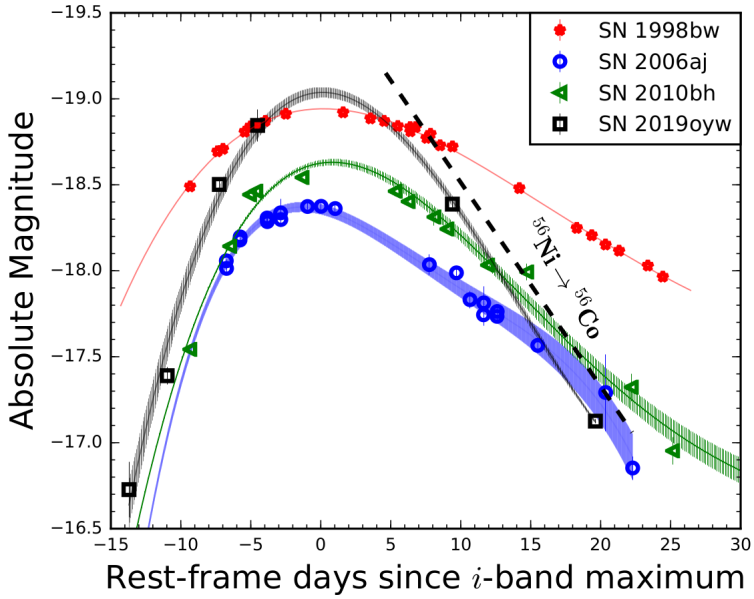

FIGURE 3.8: i-band light curve of SN 2019oyw presented along with three other well-studied GRB-SN events: SN 1998bw, SN 2006aj, and SN 2010bh. Light curves for the given SNe have been de-reddened (Galactic + Host absorption) and also magnitude values and phase have been shifted to the rest-frame. The constrained value of the peak brightness of SN 2019oyw is close to that estimated in the case of SN 1998bw. SN 2019oyw exhibits a post-peak decay rate close to that expected for the radioactive decay of ^{56}Ni –> ^{56}Co (black dotted line). The shaded region marks the 1σ contour for the corresponding best-fit light curve.

2013, we can estimate the ejecta mass ($\mathrm{M_{ej}}$) and kinetic energy ($\mathrm{E_k}$) of the SN using the photospheric velocity near the peak and rise time (see equations 1 and 3 of Wheeler, Johnson, and Clocchiatti 2015). SN 2019oyw exhibits a rise time ($\mathrm{t_r}$, i.e. the time taken from the GRB detection to the SN peak time in the i-band) of 19.19 $\pm$ 0.25 days. We are unable to estimate the photospheric velocity ($\mathrm{v_{ph}}$) for SN 2019oyw due to the absence of late-time spectral coverage. Therefore, we used the average value of photospheric velocity ($\sim 20,000 \pm 2500$ km $\mathrm{s^{-1}}$) of GRB/XRF-SNe estimated by Cano, 2013. For SN 2019oyw, using $\mathrm{t_r}$ and $\mathrm{v_{ph}}$ we obtain $\mathrm{M_{ej}}$ 5.67 $\pm$ 0.72 $\mathrm{M_\odot}$ and $\mathrm{E_k}$ (13.55 $\pm$ 5.08) $\times$ 10^{51} erg. For this analysis, the fiducial optical opacity κ = 0.1 $\mathrm{cm^2\ g^{-1}}$ and the fiducial gamma-ray opacity κ_γ = 0.03 $\mathrm{cm^2\ g^{-1}}$ are adopted as suggested by Wheeler, Johnson, and Clocchiatti, 2015. The estimated values of $\mathrm{M_{Ni}}$, $\mathrm{M_{ej}}$ and $\mathrm{E_k}$ for SN 2019oyw are in close agreement with those estimated for SN 1998bw by Nakamura et al., 2001. For

SN 2019oyw, the $\mathrm{E_k}/\mathrm{M_{ej}}$ is also highly consistent with the values estimated by Lyman et al., 2016, Cano et al., 2017.

Results and Discussion

The prompt emission light curve of GRB 190829A, consisting of two emission episodes separated by a quiescent gap, is found to be similar to that exhibited by another nearby GRB 180728A. A time-averaged and time-resolved spectral analysis of the double-episode prompt emission using *Swift*/BAT and *Fermi*/GBM data for GRB 190829A and GRB 180728A reveals diverse $\mathrm{E_p}$ and α evolution posing a challenge to the proposed progenitor models. For GRB 190829A, the low-energy spectral index (α) overshoots the synchrotron limits in later time bins, which poses a problem for synchrotron models, whereas for GRB 180728A the evolution of α remains within the synchrotron limit.

We also present 10.4 m GTC spectroscopy (0.32 to 4.09 d post burst, in the rest-frame) and the redshift determination for GRB 190829A, a VHE-detected GRB. Our spectrum taken as early as 0.32 d shows a featureless power-law behaviour as expected for GRB afterglows, whereas the spectrum taken at a later epoch (4.09 d post burst) shows the type Ic-BL broad absorption features (Si II and Ca II NIR lines) indicative of higher velocity outflows as reported by de Ugarte Postigo et al., 2019. Thermal evolution of the spectra at three later epochs shows decreasing photospheric temperatures from $\sim$5100 to 4575 K, typical of those observed in other similar SNe (Cano et al., 2017). Spectroscopically, around 4.09 d post burst, the underlying SN closely resembles GRB 980425/SN 1998bw.

The host-subtracted 10.4 m GTC $ugriz$ band photometry was used to construct the light curves from 0.27 to 37.99 rest-frame days after the burst. These clearly show a power-law decay nature typical of that observed in GRB afterglows until $\sim$ 2.3 d post burst. Using 10.4 m GTC multi-band optical data along with the XRT data, we were able to constrain the evolution of ν_c (between 0.32 to 4.09 d post-burst) and determine the electron energy index p, assuming the afterglow follows the model predictions in the case of an ISM-like ambient medium. However, photometrically, apart from showing a typical afterglow

decay at early epochs, a deviation from the power-law decay is clearly seen in all filters with a clear signature of a re-brightening peaking around $\sim$ 20 d post burst in the i-band. The peak brightness ($M_i \sim$ -19.04 mag) of SN 2019oyw confirms the SN as being one of the brightest GRBs/SNe and similar to SN 1998bw in terms of other estimated parameters such as M_{Ni}, M_{ej}, and E_k. While the values of M_{ej} and E_k are higher than usual, their ratio is closer to those seen in other type Ibc-BL SNe and GRB/SNe events (Lyman et al., 2016; Cano et al., 2017). The low value of $t_{fall}^{\Delta 1mag}$ and the post-peak decay rate are indicative of ^{56}Ni as a possible powering source for SN 2019oyw.

It is also notable that Wang et al., 2019 attempted to explain the nature of the prompt emission of GRB 180728A in terms of the type II binary-driven hypernova (BdHN II) model (Rueda et al., 2020) for the observed underlying SN as an alternative to the 'Collapsar' model (Woosley, 1993; Hjorth and Bloom, 2012). In the near future, with more observations of events of this kind, it would be very interesting to decipher whether or not such nearby GRBs, with two emission episodes in their prompt emission phase, have underlying SN features.

Chapter 4

A sample of short-duration GRBs in the 2012-2015 time interval

In this chapter, we present results based on prompt emission data from *INTEGRAL*, *Swift*, and *Fermi*, and on multi-wavelength afterglow follow-up observations of nine short GRBs, in particular GRB 130603B. The data were gathered by several optical and NIR ground-based telescopes, including the 10.4 m GTC. Observations of these nine bursts, including GRB 170817A, were collected during 2012-2018 as part of a large multi-wavelength collaboration. The analysis of the new data for the subset of sGRBs mainly focused on constraining prompt emission, afterglow and host galaxy properties and adding value towards known physics behind these cosmic explosions. We also attempt to compare the observed properties of the sGRB subset with a new class of less-studied but associated events, the 'Kilonovae'.

Introduction

Short-duration gamma-ray bursts (sGRBs) were originally classified using the $Konus$ catalogue (Mazets et al., 1981) that preceded the wider realization that sGRBs likely are binary compact mergers (Narayan, Paczynski, and Piran, 1992; Nakar, 2007) based on various observed properties like duration, fluence etc. as described in Kouveliotou et al., (1993) and Bromberg et al., (2013). During the era of the Neil Gehrels Swift Observatory, arcsec X-ray Telescope (XRT) localizations enabled the discovery of the first afterglow of sGRB 050509B (Castro-Tirado et al., 2005; Gehrels et al., 2005) and subsequently other observed features like extended emission (EE) at Swift Burst Alert Telescope (BAT) energies, temporally extended variable X-ray emission suggesting late time central

engine activity due to either merger of two neutron stars (NS–NS) or a neutron star and a stellar-mass black hole (NS–BH) as possible progenitors (Eichler et al., 1989; Narayan, Paczynski, and Piran, 1992; Usov, 1992; Zhang and Mészáros, 2001; Troja et al., 2007; Rowlinson et al., 2013; D'Avanzo et al., 2014a; Gibson et al., 2017; Desai, Metzger, and Foucart, 2019). The physical nature of the EE, observed in some of the sGRBs, is not yet resolved. It could be connected with the beginning of the afterglow phase (Minaev, Pozanenko, and Loznikov, 2010), the activity of a magnetar, formed during merger process Metzger, Piro, and Quataert, (2008) or viewing angle effects (Barkov and Pozanenko, 2011). The prompt emission properties of sGRBs: such as relatively harder spectra (higher E_{peak}) and nearly zero spectral lag (Gehrels et al., 2006; Zhang et al., 2009); discriminate sGRBs from long GRBs (lGRBs). sGRBs have also been speculated as a potential key to understand gravitational wave (GW) sources and the nucleosynthesis of elements over the history of the Universe(Berger, 2014; Kumar and Zhang, 2015; Abbott et al., 2017b; Abbott et al., 2017c).

More than 90 afterglows of sGRBs have been detected at various wavelengths exhibiting diverse properties (Lee and Ramirez-Ruiz, 2007; Gehrels, Ramirez-Ruiz, and Fox, 2009; Berger, 2014). Afterglows of sGRBs are in general less luminous, less energetic and favour typically lower circumburst densities than those seen in the case of lGRBs (Kann et al., 2011; Nicuesa Guelbenzu et al., 2012; Berger, 2014). Despite intensive efforts, this leads to a lower detection rate for sGRBs: $\sim$ 75 per cent in X-rays, $\sim$ 33 per cent in optical-NIR and only a handful in the radio (Berger, 2014). In comparison to long ones, sGRBs are observed to occur at over a lower and narrower redshift range (z $\sim$ 0.1 - 1.5) and both early and late-type galaxies have been identified as hosts (Fong et al., 2013). Afterglow observations of sGRBs also indicate that these bursts have a range of jet-opening angles (Burrows et al., 2006; Kann et al., 2011; Nicuesa Guelbenzu et al., 2012; Fong et al., 2013; Zhang et al., 2015; Troja et al., 2016; Lamb and Kobayashi, 2018; Margutti et al., 2018) and have systematically larger radial offsets from the host galaxies (Fong et al., 2013; Tunnicliffe et al., 2014) in turn supporting compact binary merger as possible progenitors (Bloom, Kulkarni, and Djorgovski, 2002; Zhang, Liang, and Zhang, 2007; Troja et al., 2008; Zhang et al., 2009; Salvaterra et al., 2010). Optical afterglows of sGRBs are generally fainter in comparison to those observed in the case of lGRBs, implying the need for fast and deep afterglow observations using moderate- to large-size

telescopes.

Study of sGRBs now extends beyond understanding just about their explosion mechanisms, progenitors and environments. These explosions are now key to improve our understanding of multi-messenger astronomy and to search for new compact binary mergers as GW sources. It has been proposed that during the compact binary merger process, radioactive decay of heavy elements could give rise to a supernova-like feature, termed 'macronovae' or 'kilonovae' (Li and Paczyński, 1998; Kulkarni, 2005; Hotokezaka et al., 2013; Kasen, Fernández, and Metzger, 2015) having a component of thermal emission caused by radioactive decay of elements through r-process nucleosynthesis. So far, tentative 'kilonova' like signatures have been identified in only a few cases including sGRB 050709 (Jin et al., 2016), sGRB 060614 (Yang et al., 2015), sGRB 080503A (Perley et al., 2009), sGRB 130603B (Hotokezaka et al., 2013; Tanvir et al., 2013), sGRB 150101B (Fong et al., 2016; Troja et al., 2018), sGRB 160821B (Kasliwal et al., 2017) and sGRB 170817A/GW170817/AT 2017gfo (Abbott et al., 2017b; Abbott et al., 2017c). Discovery of the ground-breaking event called sGRB 170817A/GW170817/AT 2017gfo has opened new windows in the understanding of GWs: their electromagnetic counterparts (Abbott et al., 2017c; Albert et al., 2017), and their likely contribution to heavy element nucleosynthesis in the nearby Universe (Lattimer and Schramm, 1974; Piran, Nakar, and Rosswog, 2013; Pian et al., 2017).

Multi-wavelength observations of a larger sample of nearby sGRBs and 'kilonovae' features like GW170817/sGRB 170817A/AT 2017gfo are crucial to establish whether compact binary mergers are the progenitors (Kasen, Fernández, and Metzger, 2015) for all such events (Abbott et al., 2017b; Abbott et al., 2017c) and to put a constraint on the electromagnetic counterparts and number density of GW sources in the near future (Li and Paczyński, 1998; Shibata and Taniguchi, 2011; Loeb, 2016).

sGRB 130603B multi-wavelength observations

sGRB 130603B was discovered on 2013 June 3 at 15:49:14 UT by *Swift*-BAT (Barthelmy et al., 2013; Melandri et al., 2013), and by $Konus-Wind$ (Golenetskii et al., 2013). The γ-ray light-curve of GRB 130603B consists of a single group of pulses with a duration of T_{90} = 0.18$\pm$0.02 s (15–350 keV; Barthelmy et al. 2013).

The $Konus - Wind$ fluence of the burst is (6.6±0.7)$\times 10^{-6}$ erg cm^{-2} (20 to 10^4 keV), with a peak energy of 660±100 keV (Golenetskii et al., 2013). The reported measured value of $E_{iso,\gamma} \sim 2.1 \times 10^{51}$ erg, places the burst well above the E_{peak}-E_{iso} locus for long GRBs in the Amati diagram (Amati et al., 2008). Such behaviour is often observed for short bursts (Minaev and Pozanenko, 2020).

sGRB 130603B shows negligible spectral lag (Norris et al., 2013), typical for short bursts. Many authors (e.g. Hakkila and Preece, 2014; Minaev et al., 2014) have found a strong correlation between pulse duration and spectral lag: longer pulses have larger lags. The correlation is similar for both sGRBs and lGRBs. As sGRBs typically consist of shorter pulses than long ones, they have less significant spectral lags in general. GRB light curves often consist of several pulses including highly overlapping ones: spectral and temporal properties of individual pulses maybe not adequately resolved (Chernenko, 2011). By performing spectral lag analysis via the superposition of several overlapping pulses, one can obtain an unpredictable result because each pulse has unique spectral and temporal properties (Minaev et al., 2014). As a result, one can find negligible or negative lag under certain conditions even if each pulse has a positive (but unique) lag (Minaev et al., 2014). sGRB 130603B consists of several very short and overlapped pulses, so its negligible spectral lag may be connected with the short duration of pulses while performing spectral lag analysis for superposition of several pulses.

SPI-ACS *INTEGRAL* Observations

sGRB 130603B was also triggered by the INTEGRAL Burst Alert System (IBAS) system operating with spectrometer for *INTEGRAL*-anticoincidence system (SPI-ACS) (Figure 4.1). It has a very high effective area (up to 0.3 m^2) in energy range $>$ 100 keV and a stable background at timescales of hundreds of seconds (Minaev, Pozanenko, and Loznikov, 2010), which makes SPI-ACS a suitable instrument to study light curves of short hard GRBs and especially to search for weak signals from their precursors and EE components. The off-axis angle of sGRB 130603B to the SPI-ACS axis is 103 degrees, which is almost optimal for detection, making sGRB 130603B one of the brightest short bursts ever registered by SPI-ACS. Nevertheless, we do not find statistically significant EE in the SPI-ACS data (Inset in Figure 4.1, in terms of peak flux at 50 ms time

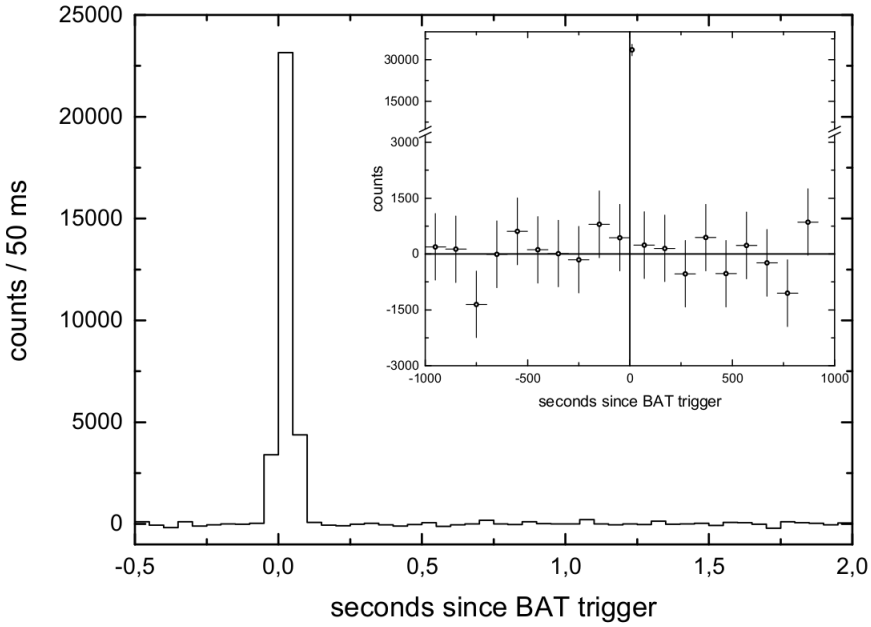

FIGURE 4.1: Background subtracted light curve of sGRB 130603B of *INTEGRAL* SPI-ACS in the energy range 0.1-10 MeV with 50 ms time resolution. The x-axis shows time since BAT trigger. Inset: light curve with time resolution of 100 s.

scale), which is in agreement with results obtained from *Swift*-BAT in the softer energy range of 15-150 keV (Norris et al., 2013). There is also no evidence for a precursor in SPI-ACS data during timescales from 0.01s up to 5s, in agreement with the previous results (Troja, Rosswog, and Gehrels, 2010; Minaev and Pozanenko, 2017; Minaev, Pozanenko, and Molkov, 2018).

In Viganò and Mereghetti, (2009), it was shown that one SPI-ACS count corresponds on average to $\sim 10^{-10}$ erg cm^{-2} in the (75, 1000) keV range, for directions orthogonal to the satellite pointing axis. Using the conversion factor, we can roughly estimate the flux values in the (75, 1000) keV range for GRBs observed by SPI-ACS. The fluence estimation of sGRB 130603B in SPI-ACS is $\sim$ 31000 counts or S$\sim 3.1 \times 10^{-6}$ erg cm^{-2} in the (75, 1000) keV range, which is in agreement with *Konus*-WIND observations (Golenetskii et al., 2013). At a time scale of 50 s, the upper limit on EE activity for sGRB 130603B is $\sim$ 7100 counts (S$_{EE} < 7\times10^{-7}$ erg cm^{-2}) at the 3σ significance level, the corresponding upper limit on precursor activity at a time scale of 1s, is $\sim$ 1000 counts (S$_{Pre} <$ 10^{-7} erg cm^{-2}), both are in the (75, 1000) keV range.

Optical-NIR photometric Observations

As a part of this collaboration, photometric observations of the optical-IR afterglow and the host galaxy were performed using several facilities worldwide, including 1.0 m telescope at the Tubitak National Observatory (Antalya, Turkey); the 1.5 m telescope at Observatorio de Sierra Nevada (Granada, Spain); the AS-32 0.7 m telescope at Abastumani Astrophysical Observatory Georgia; the Reionization And Transients Infra-Red RATIR camera at the 1.5 m telescope of the San Pedro Martir observatory; the 2.0 m Liverpool telescope at La Palma; AZT-22 1.5 m at the Maidanak observatory Uzbekistan; the Centro Astronómico Hispano-Alemán (CAHA) 3.5 m located in Almeria (Spain); the 3.6 m Devasthal Optical Telescope (DOT) at Aryabhatta Research Institute of Observational Sciences (ARIES) Nainital, India and with the 10.4 m Gran Telescopio Canarias (GTC) at La Palma (Spain). Our observations by the 1.0 m telescope at the Tubitak, starting $\sim$ 0.122d after the burst, are the earliest reported ground-based observations so far for sGRB 130603B. All optical-NIR data were processed using DAOPHOT software of NOAO's IRAF package. The photometry was performed in comparison to nearby standard stars and image subtraction was applied whenever it was required to subtract the host galaxy contribution as explained in Alard and Lupton, (1998). The unfiltered observations made with the AbAO AS-32 telescope have been considered equivalent to r-band as the quantum efficiency of the detector is at a maximum around r-band frequencies. The final AB magnitudes of the afterglow and the host galaxy in different pass-bands as a part of the present analysis are listed in Table 4.1.

Spectroscopic Observations

A spectroscopic redshift at the location of the afterglow was obtained by several groups including Xu et al., (2013), Foley et al., (2013), de Ugarte Postigo et al., (2013) and Cucchiara, Perley, and Cenko, (2013). As a part of the present study, spectroscopic observations were performed to measure the redshift of sGRB 130603B independently and are reported in Sanchez-Ramirez et al., (2013).

We obtained optical spectra with the GTC(+OSIRIS) starting at 23:58 h. Observations consisted of two 450 s exposures, one with each of the R1000B and R500R grisms, using a slit of width 1.2 arcsec. Data reduction was performed using standard routines from the IRAF. The afterglow spectrum shows Ca II in

TABLE 4.1: Broad-band optical-IR photometric observations of the GRB 130603B afterglow and its host galaxy (h) presented in the AB-magnitude system. The values are not corrected for extinction and are tabulated in order of time in days (d) since the burst. The quoted values of limiting magnitude are 3σ.

t-t0,mid (d)	exp (s)	Afterglow/ Host magnitudes	pass-band	Telescopes
0.1222	150×10	20.15±0.17	R_c	Tubitak 1.0 m
0.1959	300×10	21.37±0.25	$clear$	AS-32 0.7 m
0.2024	300×4	21.10±0.27	I_c	OSN 1.5 m
0.3360	50	21.29±0.02	i	GTC 10.4 m
0.5196	3020.0	22.12±0.81	Y	RATIR 1.5 m
0.5196	3020.0	20.37±0.28	H	RATIR 1.5 m
0.5347	2818.0	21.64±0.34	Z	RATIR 1.5 m
0.5347	2818.0	20.94±0.38	J	RATIR 1.5 m
0.5405	6960.0	22.30±0.20	r	RATIR 1.5 m
0.5405	6960.0	21.98±0.20	i	RATIR 1.5 m
1.1141	150×2+200×8	21.34±0.50	R_c	Tubitak 1.0 m
1.1160	180×14	$>$ 22.64	$clear$	AS-32 0.7 m
2.0937	180×10	$>$ 22.92	R_c	Maidanak 1.5 m
2.1489	200×5	$>$ 21.14	R_c	Tubitak 1.0 m
2.2803	300×5	20.69±0.15 (h)	I_c	OSN 1.5 m
5.1143	180×23	$>$ 22.56	$clear$	AS-32 0.7 m
16.2691	300×10	20.69±0.06 (h)	i	LT 2.0 m
19.2650	60×15	19.69±0.13 (h)	K_s	CAHA 3.5 m
19.2323	60×15	20.06±0.09 (h)	J	CAHA 3.5 m
19.2481	60×15	19.68±0.13 (h)	H	CAHA 3.5 m
19.2155	60×15	20.11±0.07 (h)	Z	CAHA 3.5 m
32.2411	50×4	22.01±0.03 (h)	g	GTC 10.4 m
32.2471	50×4	20.97±0.01 (h)	r	GTC 10.4 m
32.2511	50×4	20.65±0.02 (h)	i	GTC 10.4 m
35.5168	469.8	20.88±0.41 (h)	Y	RATIR 1.5 m
35.5168	469.8	20.84±0.30 (h)	H	RATIR 1.5 m
35.5168	335.6	20.39±0.19 (h)	Z	RATIR 1.5 m
35.5168	335.6	20.49±0.43 (h)	J	RATIR 1.5 m
35.5162	960.0	21.26±0.12 (h)	r	RATIR 1.5 m
35.5162	960.0	20.79±0.09 (h)	i	RATIR 1.5 m
1387.84	300.0×2	22.13±0.05 (h)	B	3.6 m DOT
1387.86	300.0×2	20.72±0.02 (h)	R_c	3.6 m DOT

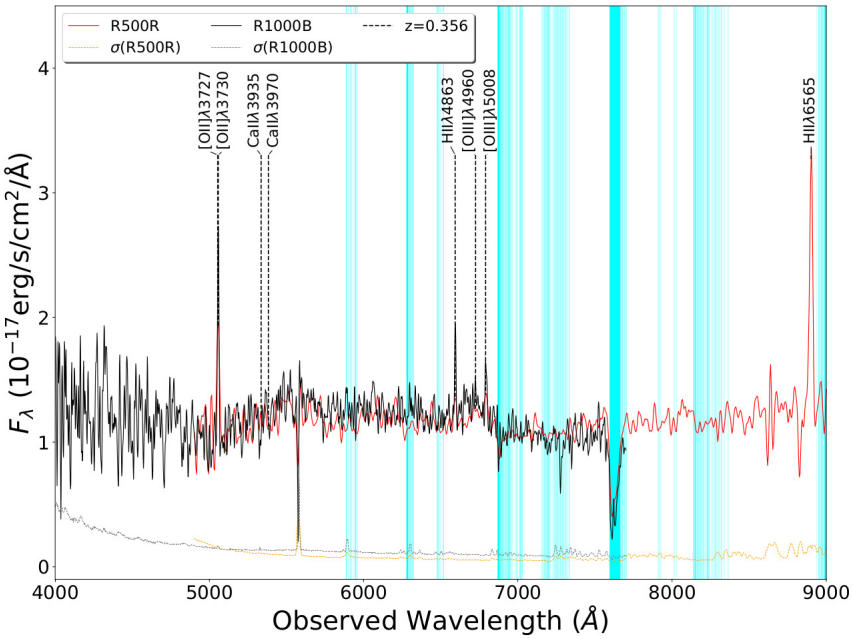

FIGURE 4.2: Spectroscopic observations of the sGRB 130603B at the location of the afterglow taken by the 10.4 m GTC (+OSIRIS) using grisms R1000B and R500R starting $\sim$ 8 hrs after the burst (Sanchez-Ramirez et al., 2013). Telluric absorption bands are marked as cyan.

absorption, and we detect a significant contribution from the underlying host galaxy (e.g. [OII], [OIII], H-β and H-α emission lines about 1" offset), together implying a redshift of z = 0.356$\pm$0.002, consistent with the values provided by de Ugarte Postigo et al., (2013) and Foley et al., (2013). The reduced spectrum obtained at the location of the afterglow along with the lines identified is shown in Figure 4.2. Using our redshift value and the fluence published by Golenetskii et al., (2013), the isotropic-equivalent gamma-ray energy is $E_{iso,\gamma} \sim 2.1 \times 10^{51}$ erg (20 to 10^4 keV, rest-frame).

mm-wavelength Observations

The afterglow of sGRB 130603B was observed with the Plateau de Bure Interferometer (Guilloteau et al., 1992), one of the largest observatories in the Northern Hemisphere operating at millimetre wavelengths (1, 2 and 3 mm). Observations were performed in a four-antenna extended configuration for the first epoch whereas a five-antenna configuration on the consecutive dates as listed in Table 4.2. The data reduction was done with the standard CLIC and

TABLE 4.2: Millimetre wave observations of the sGRB 130603B, sGRB 140606A, sGRB 140622A and sGRB 140903A (1-σ upper limits) afterglows as observed by Plateau de Bure Interferometer (PdBI) and centimetre wave observations using RT-22 in Crimea.

Start time	end time	center t-t0(d)	frequency (GHz)	Flux center (mJy)	Telescopes
sGRB 130603B					
2013 June 03.844	03.926	03.901	86.743	+0.051±0.120	PdBI
2013 June 04.826	03.908	04.867	86.743	-0.307±0.095	PdBI
2013 June 12.721	12.828	12.775	86.743	-0.043±0.073	PdBI
2013 June 04.730	04.801	04.765	36.0	1.6±0.9	RT-22
2013 June 05.703	05.732	05.717	36.0	1.9±1.2	RT-22
2013 June 05.710	05.785	05.747	36.0	2.6±0.9	RT-22
sGRB 140606A					
2014 June 14.039	14.099	14.069	86.743	0.331±0.187	PdBI
2014 June 15.039	15.099	15.069	86.743	-0.592±0.214	PdBI
sGRB 140622A					
2014 June 26.050	26.108	0.079	86.243	-0.376±0.123	PdBI
sGRB 140903A					
2014 Sep 05.617	05.705	02.661	86.743	0.120±0.130	PdBI

MAPPING software distributed by the Grenoble GILDAS group. Flux calibration includes a correction for atmospheric decorrelation which has been determined with a UV plane point source fit to the phase calibration quasar 1156+295. The carbon star MWC349 was used as the primary flux calibrator due to its well-known millimetre spectral properties (see e.g. Schwarz 1978). The burst location was also followed-up using the RT-22 radio telescope of CrAO (Crimea) at 36 GHz and the data reduced using the standard software routines (Villata et al., 2006) and used modulated radiometers in combination with the registration regime 'ON-ON' for collecting data from the telescope (Nesterov, Volvach, and Strepka, 2000). The upper limits based on these observations are also given in Table 4.2. As a part of the present analysis, upper limits (1-σ) based on IRAM Plateau de Bure Interferometer observations of sGRB 140606A, sGRB 140622A and sGRB 140903A using the carbon star MWC349 as the primary flux calibrator are also tabulated in Table 4.2.

Observations at mm-wavelengths are very important as they suffer negligible absorption or interstellar scintillation effects, so sGRBs at high redshifts

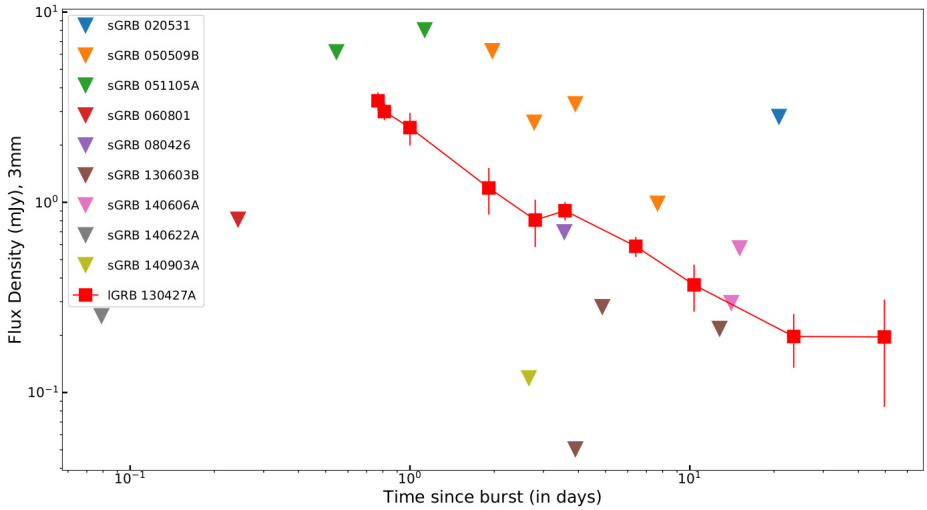

FIGURE 4.3: Comparison of the 3-mm afterglow light curve of nearby lGRB 130427A (Perley et al., 2014) to the present set of mm-wavelength upper-limits (1-σ) of 4 sGRBs (from Table 4.2) along with another set of upper-limits of 5 sGRBs placed at a common redshift of z = 0.34.

or highly-extinguished bursts could be observed. It is expected that emission at mm-wavelengths is normally above the self-absorption frequency and lies around the peak of the GRB synchrotron spectrum, allowing to probe for possible reverse shock emission at early epochs and to constrain afterglow models observed recently in case of many lGRBs (de Ugarte Postigo et al., 2012a; Perley et al., 2014).

In Figure 4.3, observed mm-wavelength upper-limits of four sGRBs presented in Table 4.2 were plotted along with previous observations of another 5 sGRBs (namely sGRB 020531, sGRB 050509B, sGRB 051105A, sGRB 060801 and sGRB 080426) and were compared with the afterglow light curve of a well-known nearby and bright lGRB 130427A observed at 3-mm (Perley et al., 2014). It is clear from Figure 4.3 that using PdBI, we have been able to observe 9 sGRBs so far but none was detected at mm-wavelengths in contrast with lGRBs which have been detected in many cases constraining various physical models (de Ugarte Postigo et al., 2012a; Perley et al., 2014). Out of these nine sGRBs, only sGRB 130603B (Fong et al., 2014) and sGRB 140903A (Troja et al., 2016) were detected at VLA radio frequencies so far. However, as discussed further in this work, the observed 3-mm PdBI 1-σ upper limits for these two bursts are consistent with those predicted by the forward shock afterglow models. The

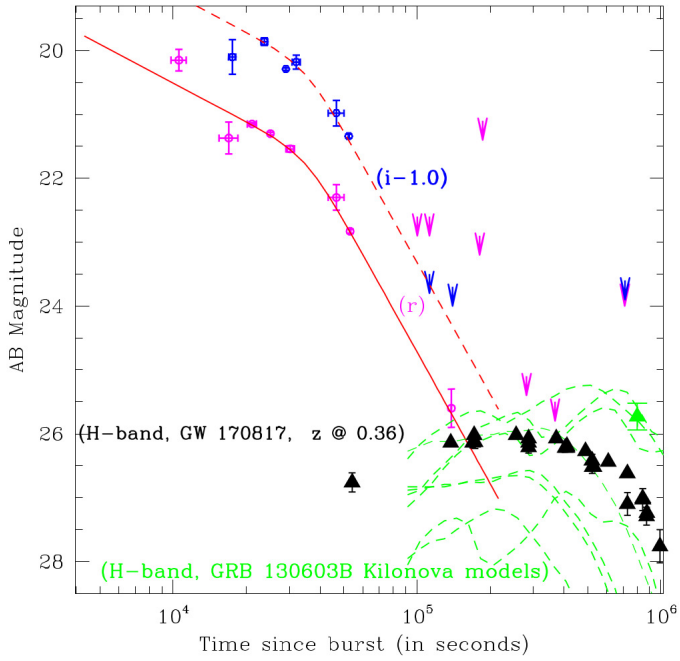

FIGURE 4.4: Afterglow optical r (pink) and i (blue) band light-curves of the sGRB 130603B. The solid red curves are the best-fit broken power-law model to the r-band light curves as described above. The red dashed line is the model over-plotted on the i-band light curve to guide eyes. The green triangle in the right bottom corner is the single point detection of the underlying 'kilonova' detection as described in Tanvir et al., (2013). The green dashed lines are the H-band 'kilonova' models at the redshift of $\sim$ 0.36 as taken from Tanaka et al., (2014). The black triangles are the H-band light curve (at redshift z = 0.36) of the electromagnetic counterpart of the recently discovered GW170817 (sGRB 170817A/AT 2017gfo) for comparisons as compiled in Villar et al., (2017a).

gamma-ray fluence and observed X-ray flux values for these nine sGRBs are similar to those observed in other sGRBs. Non-detections of these nine sGRBs at 3-mm in the last decade using PdBI and other mm-wavelength facilities globally are helpful to constrain underlying physics behind these energetic sources and demand for more sensitive and deeper follow-up observations.

Properties of sGRB 130603B

Afterglow light-curves and comparison to models

Figure 4.4 shows the r and i band light curves of the sGRB 130603B afterglow including data from the present analysis and those published in the literature (Berger, Fong, and Chornock, 2013; Cucchiara et al., 2013; Tanvir et al., 2013; de Ugarte Postigo et al., 2014). To plot the light curves along with those published in the literature, the data were scaled to respective AB magnitudes in SDSS r and i bands (see Figure 4.4). The R_c band data taken at $\sim$ 0.122d comprise the earliest reported ground-based detection and the remaining data fill the temporal gap in the light curve for this interesting short-duration burst. From the present analysis, the number of new data points both in r and i bands are four each spread up to $\sim$ 2.3 d post-burst. Careful image-subtraction and calibration of the afterglow data $<$ 0.23 d post-burst indicate possible deviations from smooth power-law behaviour during the first few hours.

To determine the temporal flux decay slopes and the break time, we fitted an empirical function representing a broken power-law, $F_\nu = A[(t/t_b)^{s\alpha_1} + (t/t_b)^{s\alpha_2}]^{-1/s}$ to the r band combined light curve. The quantities α_1 and α_2 are asymptotic power-law flux decay slopes at early and late times with $\alpha_1 < \alpha_2$. The parameter $s > 0$ controls the sharpness of the break and t_b is the break time. The best fit of this broken power-law function to the r band data including the very first data point taken at $\sim$ 0.122d gives : $\alpha_1 = 0.81 \pm 0.14$; $\alpha_2 = 2.75 \pm 0.28$ and $t_b = 0.41 \pm 0.04$ with $\tilde{\chi}^2/dof = 2.22$ for a value of the smoothing parameter $s = 4$. The values of t_b and α_2 are similar to those derived by Fong et al., (2014). Although the data from *Swift*/XRT is consistent with a break occurring around 0.3 d, the later XMM-Newton observations suggest no turnover at X-ray frequencies and a continuing power-law instead (this 'X-ray excess' is also discussed by Fong et al., (2014)). The present analysis also helped to constrain the value of α_1 using a single band light curve and found to be shallower in comparison to that derived by Fong et al., (2014).

The present data set has also been used to constrain the spectral energy distribution (SED) of the afterglow. The RATIR data taken simultaneously at $\sim$0.52 d post-burst (see Table 4.1), require an optical-NIR spectral index $\beta_{opt} \sim$ 0.7 once corrected for Galactic and considerable host extinction, similar to those

measured by de Ugarte Postigo et al., (2014) at ∼0.35 d and by Fong et al., (2014) at ∼ 0.6d post-burst. The optical-NIR spectral index, together with the published value of the XRT spectral index $\beta_X = 1.2 \pm 0.1$ are consistent with $\Delta\beta = \beta_X - \beta_{opt}$ = 0.5, as expected in the case of a slow-cooling synchrotron spectrum (Sari, Piran, and Narayan, 1998) where the optical and XRT frequencies lie in two different spectral regimes.

Additionally, the derived values of the temporal slope α_1 and the spectral slope β_{opt} above are consistent with the closure relation $\beta = 3\alpha/2$ in the case of adiabatic deceleration in the interstellar medium *ISM* afterglow model for the spectral regime $\nu_m < \nu < \nu_c$, where ν_m is the break frequency corresponding to the minimum electron energy and ν_c is the cooling break frequency. The temporal flux decay index $\alpha_2 = 2.75 \pm 0.28$, the break-time $t_b = 0.41 \pm 0.04$ d and estimated slopes of the SEDs using the optical-NIR and XRT data are broadly consistent with the scenario described by Rhoads, (1999) where the edge of the relativistic outflow causes a steepening (jet-break) in the observed light curve by t^{-p} (Sari, Piran, and Halpern, 1999), where p is the electron energy index. Also, for the observed XRT frequencies which lie above ν_c, the temporal and spectral indices are consistent with the predictions made by the *ISM* model in case of the adiabatic deceleration for the data up to one day post-burst (de Ugarte Postigo et al., 2014; Fong et al., 2014).

Present afterglow data has made it possible to construct a single band afterglow light curve and do the temporal fitting to derive parameters like temporal indices and jet-break time. The optical afterglow data in r and i bands from the present analysis has allowed us to construct a better-sampled light curve of the sGRB 130603B and to constrain the value of the pre jet-break temporal decay index α_1 for the first time using data from a single band. This overall analysis supports the scenario that the observed steepening in the optical light curves is a jet-break as predicted theoretically by Sari, Piran, and Halpern, (1999) and Rhoads, (1999). However, the observed X-ray excess emission (Fong et al., 2014) for epochs > 1 d is not supported by the afterglow model.

Afterglow SED at the epoch of mm observations

Based on the present analysis and using the afterglow data in X-ray, r, i bands and the results published by de Ugarte Postigo et al., (2014) and Fong et

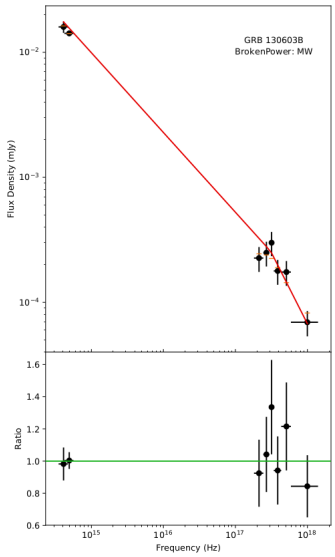

FIGURE 4.5: X-ray and optical SED of sGRB 130603B at the epoch of first millimetre observations, i.e. 0.22 d after the burst. We plot the best-fitting absorption and extinction corrected spectral model (solid red lines, broken power-law model), as well as the host galaxy absorbed and extinguished spectral model (orange dash lines) and the data (black circles) using the method described in Schady et al., (2010).

al., (2014), an afterglow SED was constructed for the epoch of our earliest millimetre observations, i.e. 0.22 d after the burst (see Figure 4.5). We first built a time-sliced X-ray spectrum from the Leicester XRT webpages [1], extracting data in the range 10 ks - 18 ks after the trigger. This tool provides the appropriate spectral and response files that are compatible for use with the spectral fitting package XSPEC. The source spectral file was normalized so that it has the same count rate as a single epoch spectrum measured at 0.22 d (see Schady et al., (2010) for details). For the optical data, we created appropriate spectral and response files for each filter. The flux values at 0.22 d for each spectral file were determined from an extrapolation/interpolation of the data between 10 ks and 30 ks by fitting a power-law and fixing the slope as 0.81. This is the decay index found for the first segment of the broken power-law fit to the r-band data. The optical errors were estimated by taking the average error of the data between 10 and 30 ks and adding a 5 per cent systematic error in quadrature.

The SEDs were fitted using XSPEC, following the procedure outlined in

[1] http://www.swift.ac.uk/xrt_spectra/

Schady et al., (2010) and Schady et al., (2007). We fit two different models, a power-law and broken power-law, which include Galactic and host galaxy absorption and extinction components (phabs, zphabs and zdust). The best-fit results obtained using the procedure mentioned above are plotted in Figure 4.5 which supports a broken power-law model with the Milky Way (MW) type of host extinction. Values of the best-fit broken power-law model and MW type of host extinction are consistent with those derived by de Ugarte Postigo et al., (2014). Assuming ν_m around mm-wavelengths, 86.7 GHz upper limits of the sGRB 130603B at 0.22 d post-burst (see Table 4.2) are also consistent with the extrapolated modelled flux values.

Broad-band modelling of sGRB 130603B afterglow

The multi-band afterglow data of sGRB 130603B discussed above along with those published in Fong et al., (2014) were used to fit a numerical-simulation-based model to constrain physical parameters of the jetted emission as described in Zhang et al., (2015). The numerical modelling (Zhang et al., 2015) calculates the flux density at any frequency and observer time. The Monte Carlo method is used to determine the best parameter values (i.e., with the smallest χ^2 value) utilizing the MultiNest algorithm from Feroz, Hobson, and Bridges, (2009). The optical-NIR data were corrected for the Galactic and host extinction values as constrained in Fong et al., (2014). The XRT data was also corrected for absorption effects. Based on the literature, it was decided to utilize the data 1000 s after the burst for the modelling to avoid possible prompt emission effects at early epochs as described in Zhang et al., (2015).

Using the model and initial guess values, following set of parameter values were determined: the blast wave total energy $E_{\rm iso,53}$ (in the units of 10^{53} ergs), the ambient number density n, the electron energy density fraction ϵ_e, the magnetic field energy density fraction ϵ_B, the electron energy index p and values of jet opening angle θ_{jet} and the observed angle θ_{obs}. The best-fit light curves obtained at different wavelengths are plotted in Figure 4.6, the Monte Carlo parameter distributions are plotted in Figure 4.7 and the resulting best-fit parameters and their uncertainties are listed in Table 4.3. A cross-check using an updated version of the *scalefit* package (van Eerten and MacFadyen, 2012; Ryan et al., 2015), produces a similar jet opening angle and inferred energy.

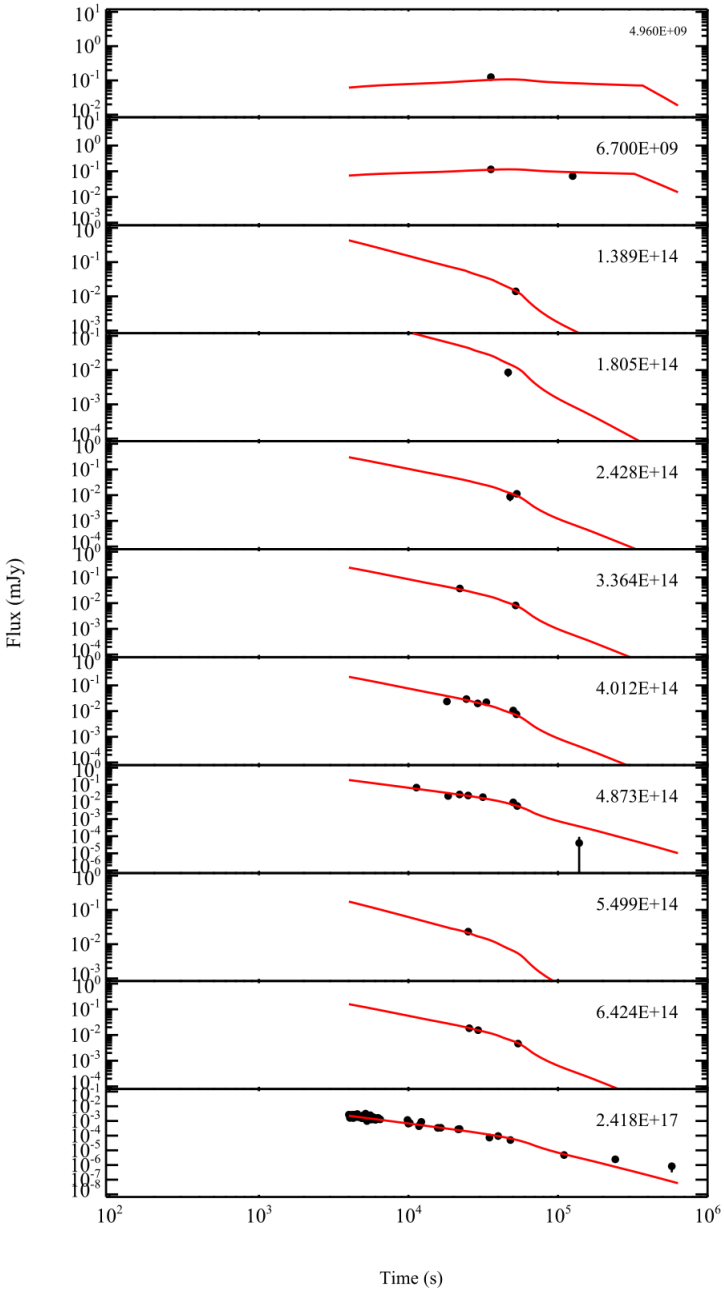

FIGURE 4.6: The best fit modelled multi-band light curves determined from the numerical simulations as described above (Zhang et al., 2015). The corresponding frequency is marked on the right corner in each panel in a unit of Hz. The x-axis is the time since the trigger in units of seconds. The observed flux density of each instrument is on the y-axis in units of mJy. All data were corrected for MW and host galaxy absorption and extinction effects before modelling. Red solid lines represent the modelled light curves.

TABLE 4.3: Best fit parameters of the numerical simulation (Zhang et al., 2015) to the multi-wavelength afterglow data of sGRB 130603B.

Parameters	Value (-/+)
p	$2.31^{-0.01}_{+0.04}$
$\log n$	$-2.36^{-0.01}_{+0.05}$
$\log \epsilon_e$	$-1.14^{-0.02}_{+0.01}$
$\log \epsilon_B$	$-1.47^{-0.11}_{+0.03}$
$\log \mathrm{E}_{\mathrm{iso},53}$	$-1.15^{-0.01}_{+0.05}$
θ_{jet}	$0.055^{-0.001}_{+0.001}$
$\theta_{obs}/\theta_{jet}$	$0.014^{-0.06}_{+0.017}$

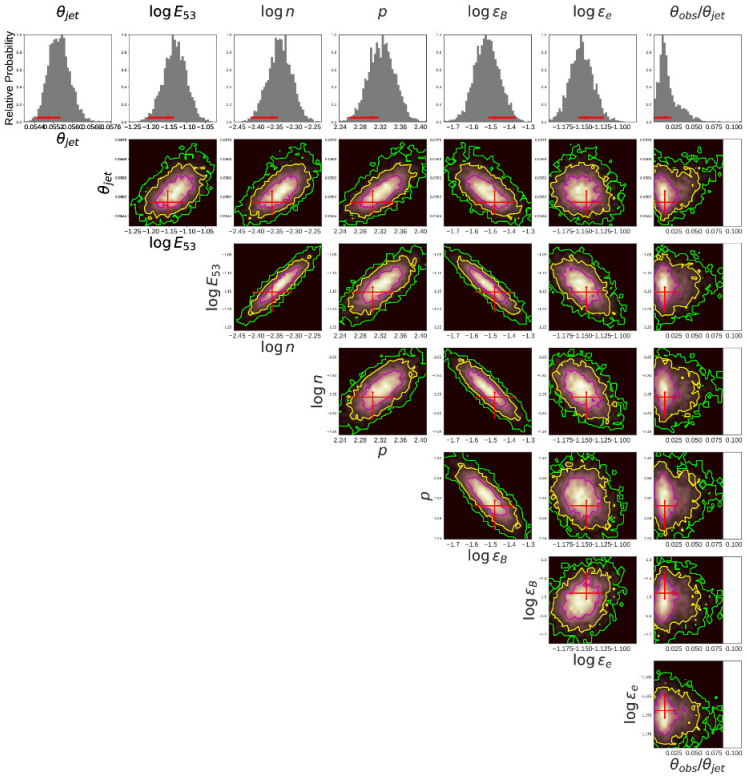

FIGURE 4.7: Triangle plot of the Monte Carlo fitting to our simulation-based model as described above (Zhang et al., 2015). It shows the posterior distribution and the correlation between the parameters.

Using the new data set discussed in this work, derived values of the physical parameters using present modelling method (Table 4.3) are constrained better than those reported by Fong et al., (2014). The derived value of observed jet opening angle, θ_{obs} is $\sim$ 3.2 degrees. This value of θ_{jet} gives rise to the beaming corrected $E_{iso,53}$ is $\sim 1.4 \times 10^{49}$ erg. It is also clear from the present modelling that the best-fit model was unable to reproduce the very late time X-ray emission observed in the case of sGRB 130603B as noticed by using Chandra observations Fong et al., (2014). It is also noted that values of the isotropic-equivalent gamma-ray energy E_{iso} and the blast wave energy $E_{iso,\gamma}$ are comparable, which in turn indicates the GRB radiative efficiency η_γ to be $\sim$ 23 per cent (with an uncertainty of $\sim$ 4 per cent), one of the highest among the known sample of sGRBs (Lloyd-Ronning and Zhang, 2004; Wang et al., 2015).

sGRB 130603B and 'kilonovae' connection

The 'kilonova' or 'macronova' events are electromagnetic transients powered by the radioactive decay of r-process elements synthesized in dynamical ejecta, and in the accretion disk winds during compact binary mergers where at least one component is a neutron star (Li and Paczyński, 1998; Kulkarni, 2005; Rosswog, 2005). Compact binary mergers are also expected to be sources of gravitational waves (Metzger and Berger, 2012; Tanaka and Hotokezaka, 2013; Nissanke, Kasliwal, and Georgieva, 2013; Siegel and Ciolfi, 2016a; Abbott et al., 2017b; Abbott et al., 2017c). For 'kilonovae', ejection of radioactive material during the merging process of the compact binaries could lead to an excess emission at optical-infrared or ultra-violet frequencies. The brightness, duration and spectrum of such emission is a function of the opacity, velocity, ejecta mass and viewing angle (Metzger et al., 2010; Barnes and Kasen, 2013; Piran, Nakar, and Rosswog, 2013; Rosswog et al., 2014; Tanaka et al., 2014; Mooley et al., 2018; Radice et al., 2018). In turn, the opacity depends crucially on the neutron richness of the ejecta, which determines how far any r-process nucleosynthesis proceeds. The high mass lanthanides, in particular, create heavy line blanketing which is expected to block out light in the optical bands largely. Recently, hydrodynamical modelling of such processes (Metzger and Fernández, 2014; Kasen, Fernández, and Metzger, 2015) has predicted a brief early blue emission component produced in the outer lanthanide-free ejecta and a

rather longer infrared transient produced in the inner lanthanide-blanketed regions at later epochs (Bulla et al., 2019). Using their disk-wind model for a case with a non-spinning black-hole (Kasen, Fernández, and Metzger, 2015), the optical bump observed in the case of sGRB 080503 (Perley et al., 2009) was interpreted in terms of an underlying 'kilonova' emission for an assumed redshift of z=0.25. Their (Kasen, Fernández, and Metzger, 2015) models were, however, unable to explain the observed infrared excess in sGRB 130603B which required higher accretion disk mass and perhaps a rapidly spinning black hole (Fan et al., 2013; Tanaka et al., 2014; Just et al., 2015). In this section, we attempt to place some constraints on the possible blue component of associated 'kilonova' based on the observed prompt emission and afterglow observations in bluer wavelengths for sGRB 130603B and their comparison with theoretical models.

It has been proposed by Barkov and Pozanenko, (2011) that one should observe extended prompt emission in the case of sGRBs initiating Blandford-Znajek (BZ) jets (Blandford and Znajek, 1977) due to large accretion disk mass and high accretion rate. However, in the case of sGRB 130603B, EE was not detected (see Figure 4.1). The absence of observable EE may indicate either that the observer is located off-axis with respect to the narrow BZ-jet, or that the accretion disk mass is small. In general, accretion disk mass should correlate with the ejected mass and the presence of EE could be an indicator of the emerging 'kilonovae' in sGRBs. Indeed, the plateau phase in X-ray emission observed in sGRB 130603B cannot be explained by a BZ-jet model (Kisaka and Ioka, 2015) if we assume a small accretion disk mass. The absence of the EE and the presence of a plateau phase could be explained by a low accretion rate which has still initiated BZ jet but with moderate bulk relativistic gamma-factor. Alternatively, the magnetar model could explain the plateau phase of sGRB 130603B and 'kilonovae' features (Fan et al., 2013; Metzger and Piro, 2014). Observing EE during the burst phase, along with the presence/absence of an early time X-ray plateau during afterglow phase for a larger sample of sGRBs, would allow discriminating among the possible progenitors as a sub-class of compact-binary mergers producing magnetars (Zhang and Mészáros, 2001; Rowlinson et al., 2013; Siegel and Ciolfi, 2016a; Siegel and Ciolfi, 2016b) but would also allow predicting some of them as potential candidates like GW170817.

In addition to the analysis described above, using published early time afterglow data of sGRB 130603B in *Swift*-UVOT u and Gemini g' bands around

$\sim$ 1.5 d post-burst (de Ugarte Postigo et al., 2014), we attempt to constrain the possible early time blue emission contributing to the underlying 'kilonova'. The observed limiting magnitude in $u >$ 22.3 mag and g' > 25.7 mag place limits on the corresponding luminosities of $L_u < 3.5 \times 10^{27}$ erg/s/Hz and $L_{g'} < 0.3 \times 10^{27}$ erg/s/Hz respectively. Using the transformation equations (2) & (3) given in Tanaka, (2016) (also see equations (7) & (8) in Fernández and Metzger 2016), we tried to constrain the parameter called ejected mass M_{ej}. However, these limiting values of luminosities in the two bands are not sufficiently deep to constrain values of the ejected mass meaningfully ($> 1.5\ M_{\odot}$) for the bluer component of 'kilonova' at the given epoch for the assumed values of the standard parameters. Considering the $WIND$ models of 'kilonovae' with rather lower opacity and expansion velocities (Tanaka, 2016; Kasen, Fernández, and Metzger, 2015; Metzger and Fernández, 2014), constraints for the ejected mass M_{ej} are even weaker i.e. $M_{ej} >$ a few $M_{\odot}$ which is un-physical. We caution that the placed limits on M_{ej} could be shallower if there were some contribution from the afterglow at the epoch of observations, which is certainly plausible. It is also worth mentioning that some of the parameters in the 'kilonovae' models like the range spin of the neutron star, f-parameter, neutron richness have not been well-constrained so far (Metzger et al., 2010; Kasen, Fernández, and Metzger, 2015), causing large uncertainty when predicting the possible emission at UV, optical or IR frequencies. On the other hand, in the case of observed underluminous and nearby event sGRB 170817A/GW170817, lanthanide-poor observed blue-components were successfully modelled using a three-component 'kilonova' model (Villar et al., 2017a; Villar et al., 2017b) with a more realistic value of $M_{ej} \sim 0.016\ M_{\odot}$. So, present constrain on M_{ej} in case of sGRB 130603B indicate that either blue-component 'kilonova' emission was absent/weaker in comparison to the observed blue-component in case of GW170817. These constraints further indicate that it could be possible to get a range of blue component of 'kilonovae' emission due to possible effects caused by a range of the dynamical ejecta, life-time and spin of the promptly formed magnetar/Black Hole, viewing angle effects etc. in case of some of the sGRBs. Early time deeper observations at bluer wavelengths for many such events at various distances are required to determine the range of properties like brightness, duration and possible diversity among these events.

Host galaxy SED modelling of sGRB 130603B

Information about the host galaxy, such as the characteristic age of the dominant stellar population and the average internal extinction, were obtained by analyzing its broad-band SED (Table 4.4) using stellar population synthesis models. The host galaxy of GRB 130603B is a perturbed spiral galaxy as seen in a high-resolution HST image (Tanvir et al., 2013) due to interaction with another galaxy. We combined our observational data in filters $B, g, r, R_C, i, z, J, H, K_s$ obtained with GTC, CAHA, and DOT telescopes (see Table 4.1) and combined them with ultra-violet data in $uvw2, uvm2, uvw1, U$ bands from de Ugarte Postigo et al., (2014) to construct the broad-band SED of the host galaxy. Taking into account a Galactic reddening along the line of sight of $E(B-V) = 0.02$ mag, and fixing the redshift of $z = 0.356$, we fitted the host SED using LE PHARE software package (Arnouts et al., 1999; Ilbert et al., 2006). We used the PEGASE2 population synthesis models library (Fioc and Rocca-Volmerange, 1997) to obtain the best-fitted SED and the main physical parameters of the galaxy: type, age, mass, star-formation rate (SFR) etc. We tried different reddening laws: Milky Way (Seaton, 1979), LMC (Fitzpatrick, 1986), SMC (Prevot et al., 1984), and the reddening law for starburst galaxies (Calzetti et al., 2000; Massarotti et al., 2001).

According to the best fit, the host is a type Sd galaxy with absolute magnitude in rest-frame $M_B = -20.9$, moderate bulk extinction of $E(B-V) = 0.2$, and Milky Way dust extinction law. It is about 0.7 Gyr years old, has a mass of $1.1 \times 10^{10} M_\odot$ and a low star-formation rate of SFR $\sim 6 M_\odot$yr. All the parameters are listed in Table 4.4. The reduced χ^2, galaxy morphological type, bulk extinction, absolute rest-frame B magnitude, age, mass, star formation rate, and specific star formation rate (SSFR) per unit galaxy stellar mass are listed for all 4 tested extinction laws. Figure 4.8 represents the best model corresponding to the Milky Way extinction law.

These results confirm the previous host galaxy studies (Cucchiara et al., 2013; de Ugarte Postigo et al., 2014; Chrimes et al., 2018) by independent observations and modelling, and adding a new piece of information about the extinction law inside the host galaxy. Our SED modelling results also constrain that SFR and mass of the host galaxy of sGRB 130603B are typical to those observed in case of other short bursts as shown in Figure 4.22. However, the resulting SFR is 5 times higher than that obtained by Chrimes et al., (2018) using

TABLE 4.4: GRB 130603B host galaxy properties derived from the SED fitting using stellar population synthesis models.

Fitted parameters	Starburst model	Milky Way model	LMC model	SMC model
χ^2/DOF	12.0/11	11.1/11	11.7/11	12.2/11
Type	Sbc	Sd	Sd	Sc
$E(B-V)$, mag	0.05	0.20	0.20	0.00
M_B, mag	$-20.05^{+0.07}_{-0.07}$	$-20.86^{+0.07}_{-0.07}$	$-20.06^{+0.07}_{-0.07}$	$-20.83^{+0.07}_{-0.07}$
Age, Gyr	$0.58^{+0.60}_{-0.42}$	$0.72^{+0.84}_{-0.55}$	$3.75^{+0.80}_{-2.25}$	$7.50^{+0.44}_{-5.82}$
Mass, $(\times 10^{10})$M$_{odot}$	$1.4^{+0.4}_{-0.1}$	$1.1^{+0.2}_{-0.7}$	$0.2^{+1.1}_{-0.1}$	$1.5^{+1.2}_{-0.9}$
SFR, M$_\odot$/yr	$8.3^{+16.8}_{-4.6}$	$5.9^{+11.9}_{-1.8}$	$7.6^{+16.4}_{-3.7}$	$8.3^{+17.2}_{-4.3}$
SSFR, $(\times 10^{-10})$yr^{-1}	$4.6^{+15.3}_{-2.1}$	$5.3^{10.8}_{-1.0}$	$5.3^{+19.5}_{-1.1}$	$2.1^{+25.3}_{-3.7}$

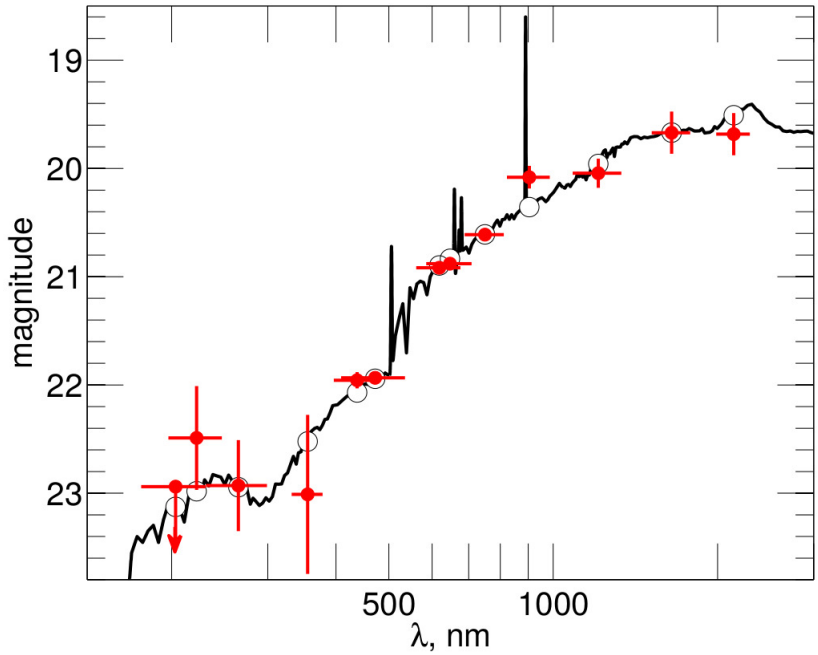

FIGURE 4.8: SED of the sGRB 130603B host galaxy fitted by the LE PHARE with fixed redshift $z = 0.356$. Filled red circles depict respectively the data points in the filters $uvw2, uvm2, uvw1, U$, taken from de Ugarte Postigo et al., (2014), and $B, g, r, R_C, i, z, J, H, K_s$ from the original observations. Data points in B and R_C bands were obtained using the 4K×4K CCD Imager (Pandey et al., 2018) mounted at the axial port of the recently commissioned 3.6m DOT at Nainital India (Kumar et al., 2018). Open circles represent model magnitudes for each filter.

different population synthesis libraries.

Multi-wavelength observations of another 8 sGRBs

During 2012-2015, a total of 45 sGRBs were localized by several space missions. Only 23/45 of these sGRBs were seen by *Swift*-XRT. Out of those 23, only 9 were detected at optical bands, and, for 7 such events have determined their redshifts. In this section, details of the prompt emission and multi-band observations to detect optical afterglow and host-galaxy of eight events (sGRB 121226A, sGRB 131224A, sGRB 140606A, sGRB 140622A, sGRB 140903A, sGRB 140930B, sGRB 141212A and sGRB 151228A) besides sGRB 130603B are discussed. Out of these eight sGRBs, three events, namely sGRB 131224A, sGRB 140606A and sGRB 151228A, were not detected by *Swift*-XRT. However, sGRB 140606A and sGRB 151228A were seen by *Fermi*-GBM continuous Time-Tagged Event (TTE) data. Out of the eight sGRBs from the present sample during 2012-2015, late time follow-up observations using 10.4 m GTC and 8.0 m Gemini-N could be obtained for 4 *Swift*-XRT localized bursts, i.e. for sGRB 121226A, sGRB 140622A, sGRB 140930B and sGRB 141212A, useful to constrain late-time afterglow emission, placing limits on possible 'kilonovae' emission and host galaxy.

The *INTEGRAL* SPI-ACS having a stable background (see Bisnovatyi-Kogan and Pozanenko 2011 and Minaev, Pozanenko, and Loznikov 2010 for details) is particularly useful in the search for EE after the prompt emission phase of sGRBs. As a part of the present analysis, prompt emission *INTEGRAL* SPI-ACS observations of sGRB 121226A, sGRB 130603B, sGRB 140606A, sGRB 140930B, sGRB 141212A and sGRB 151228A were analyzed and compared with other contemporaneous observations with the *Swift*-BAT and *Fermi*-GBM, when available. The analysis of the sub-set of these events do not show any signature of extended emission except sGRB 121226A and their spectral and temporal properties do not differ from those seen by *Swift*-BAT. Out of the eight sGRBs, for sGRB 140606A and sGRB 151228A, the characteristic photon peak energy $E_{\rm peak}$ could be determined using the prompt emission *Fermi*-GBM data. These two sGRBs, along with others discussed with presumed redshift values, allowed us to construct the Amati diagram along with published lGRBs (see Figure 4.9). Based on this diagram, the nature of these four bursts (namely sGRB 140606A,

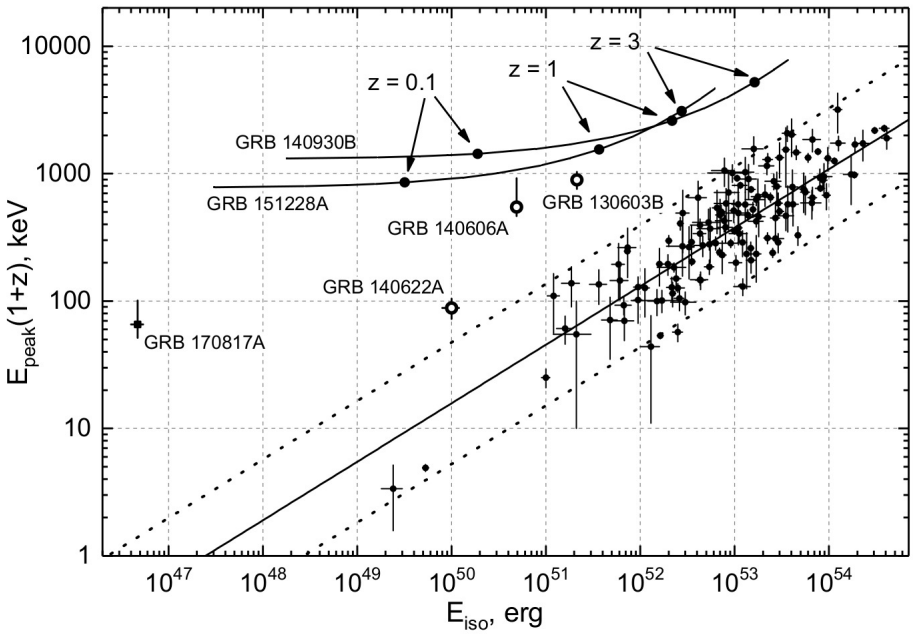

FIGURE 4.9: Amati diagram - a relation between equivalent isotropic energy emitted in the gamma-ray E_{iso} versus characteristic photon peak energy $E_{peak}(1+z)$ in the rest frame (Amati et al., 2008). The solid straight line indicates a power-law fit to the dependences for the long bursts; the dashed lines bound the 2σ correlation region. The trajectories of sGRB 140930B and sGRB 151228A are plotted as a function of the presumed redshift z. Open circles indicate short bursts (sGRB 140606A, sGRB 140622A and sGRB 130603B) with measured values of E_{peak} and redshift. Parameters of sGRB 170817A/GW170817 are also over-plotted for comparisons.

sGRB 140622A, sGRB 140930B and sGRB 151228A) are clearly categorized as short bursts.

Follow-up observations of these eight sGRBs suggest that the afterglows of these events were faint and were located either next to a bright star or embedded within the host galaxy, making the photometry complicated at the epoch of observations. Photometric results regarding the afterglow or host galaxies observed by the 10.4 m GTC and other ground-based telescopes as a part of the present analysis are tabulated in Table 4.6. Our optical-NIR observations indicate that for sGRB 141212A, the observed host galaxy was relatively bright and had star formation activity. Deeper 10.4 m GTC observations of the sGRB 140622A reveal that the burst could belong to a group of host-less bursts

(Tunnicliffe et al., 2014). Follow-up optical observations of sGRB 140903A constrain any underlying 'kilonovae' emission down to a limiting magnitude of R $>$ 22 mag at 10 d after the burst. Our early to late time afterglow observations of sGRB 140930B using 4.2 m William Herschel Telescope (WHT) and 8.0 m Gemini-N observations along with those observed by *Swift*-XRT are able to constrain the decaying nature of the burst and late time 10.4 m GTC observations place a deeper upper limit of $r \sim 24.8$ mag for any possible host galaxy. A summary of the observed prompt emission and afterglow properties of all the nine sGRBs are also listed in Table 4.7.

sGRB 121226A

Swift discovered sGRB 121226A (trigger=544027) on 2012 Dec. 26 at 19:09:43 UT (Krimm et al., 2012) which had a duration of T_{90} = 1.00$\pm$0.20s and a hard spectrum, i.e. energy fluence ratio 50-100 keV/25-50 keV = 1.4, classified as a short-hard burst (Baumgartner et al., 2012). The light curve of the burst in *Swift*-BAT data has a complex structure with negligible spectral lag, which is also in good agreement with the phenomenology of short-hard bursts. The light curve of the burst in the energy range of 100-350 keV has a feature of $\sim$2s duration at approximately 25s after the trigger with a statistical significance of 3σ. This feature was also found in the light curve obtained by SPI-ACS *INTEGRAL* ($>$ 100 keV) at a significance of 2.5σ. The off-axis angle of the SPI-ACS detector is 58 degrees and the detector has no in-flight IBAS trigger at the time of sGRB 121226A. Taking into account simultaneous detection of the *Swift*-BAT and *INTEGRAL* SPI-ACS of the feature 25s after the burst onset, we can classify it as EE. The corresponding fluence of EE component in SPI-ACS is $S_{EE} \sim 2.4 \times 10^{-7}$ erg cm^{-2} in the (75, 1000) keV range.

Starting at $\sim$ 36 s, 62.8 s and 104 s after the burst, respectively, the 0.6 m BOOTES-4/MET robotic telescope at the Lijiang Astronomical Observatory (China), 1.0m Zadko robotic telescope located at the observatory at Gingin, Australia and *Swift*-UVOT responded automatically to the trigger and did not find any optical afterglow down to a limiting magnitude of 19-20 mag (Guziy et al., 2012; Klotz et al., 2012; Breeveld and Krimm, 2012). Ground-based optical follow-up observations taken with 1.04m ST at ARIES Nainital $\sim$ 2 hrs (Bhatt and Pandey, 2012) to 11.5 hrs (Xu et al., 2012) after the burst did not detect any optical source

at the XRT location (Littlejohns et al., 2012). However, 10.4 m GTC multi-band observations taken 10.2–10.8 hrs post-burst (Castro-Tirado et al., 2012b) show a faint optical source consistent with the XRT position. The finding chart locating the XRT error circle is shown in Figure 4.10 based on the data taken by the 10.4 m GTC. Magnitudes of the optical source detected by the 10.4 m GTC in the r, i, z bands are reported in Table 4.6. Observations at the same location using the 3.6 m TNG $\sim$ 15.4 d after the burst also detect an object (Malesani et al., 2013) which did not appear to have faded in comparison to the detection in the r band taken much earlier by the 10.4 m GTC. However, the $(r - i)$ and $(z - r)$ colours of the 10.4 m GTC data is similar to those of other optical afterglows, though with large photometric errors. Our follow-up observations by the 10.4 m GTC taken around 53 d post-burst in i ($>$ 24.5 mag) and z ($>$ 23.8 mag) bands place deep limits for any possible host galaxy or possible underlying 'kilonova' emission in the observed bands. However, the 10.4 m GTC multi-band data from the present analysis together with those observed by Malesani et al., (2013) do not firmly establish afterglow decay nature of the optical source coincident with the *Swift*-XRT (Littlejohns et al., 2012) and VLA (Fong, Zauderer, and Berger, 2012) detections. Considering that the optical source is not the host galaxy, the flatter behaviour of the source between 0.5 d to 15.4 d post-burst has a luminosity of $L_r < 1.2 \times 10^{27}$ erg/s/Hz for an assumed redshift z $\sim$ 0.5. This luminosity corresponds to 5 times brighter than the rest-frame luminosity of any possible GW170817 like 'kilonova' at similar epochs and indicates the inferred value of luminosity to be afterglow dominated as seen in some cases of the sGRBs (Rossi et al., 2020). It is also notable that the *Swift*-XRT spectral analysis favours a higher Galactic absorption column density towards the burst direction (Littlejohns et al., 2012) having a steeper photon index. Further deeper observations would be required to look for any possible blue dwarf galaxy within the XRT error circle.

sGRB 131224A

sGRB 131224A was discovered on 2013 Dec. 24 at 16:54:37 UT by the Imager on Board the *INTEGRAL* Satellite (IBIS/ISGRI) with a fluence in the energy range 20- 200 keV of about $\sim 3 \times 10^{-8}$ erg cm^{-2}s^{-1} and duration of $T_{90} \sim$ 0.8s (Mereghetti et al., 2013). The burst position is 2.7 degrees off-axis and was also

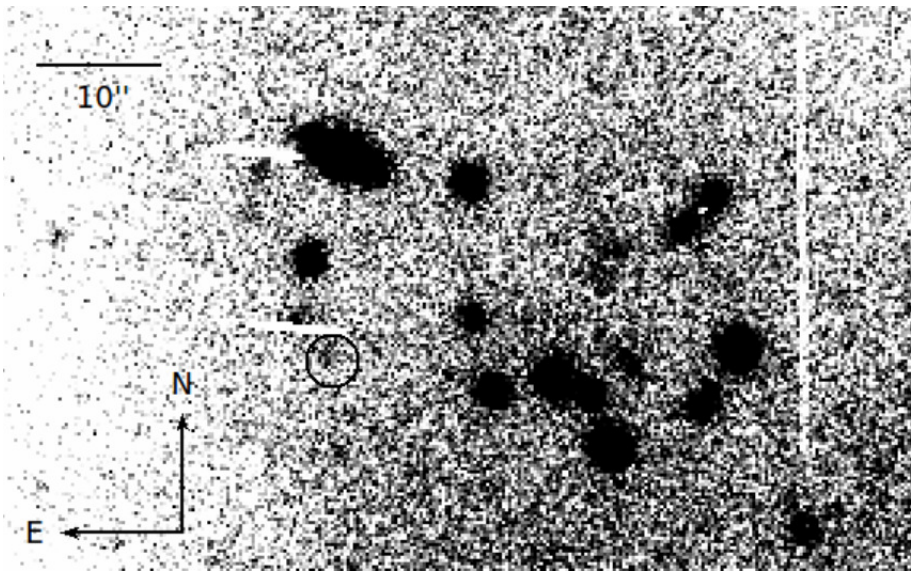

FIGURE 4.10: Finding chart of sGRB 121226A in the stacked frame of r band data obtained by the 10.4 m GTC telescope. The optical afterglow candidate within the XRT error box reported in Castro-Tirado et al., (2012b) is circled in the chart.

found by the Joint European X-Ray Monitor (JEM-X), X-ray telescope onboard *INTEGRAL*. The refined coordinates are: RA(J2000)= 296.821 deg, Dec(J2000)= +31.663 deg with an uncertainty of 1 arcmin (90 per cent c.l.). The burst is located (in projection) in the Galactic plane. The spectral lag between the light curves in energy ranges 3-35 keV and 20-200 keV is negligible. The burst consists of a single FRED pulse in the 3-35 keV energy range. The emission is visible up to 4s after the trigger and nearly symmetric in the hard IBIS/ISGRI channels as derived in this analysis (see Figure 4.11). Further, we analyzed *Fermi*/GBM data and found that sGRB 131224A was within the field of view but didn't trigger *Fermi*/GBM. In the temporal analysis, we found nothing significant in the *Fermi* daily Time-Tagged Event (TTE) data.

Optical observations of the *INTEGRAL* error-box by the MASTER-II robotic telescope starting $\sim$ 39 s after the burst trigger do not reveal any counterpart down to a limiting magnitude of $\sim$15.5 mag (Gorbovskoy et al., 2013a). *Swift*-XRT and UVOT observations starting around 2.9 hrs after the burst do not reveal any X-ray counterpart down to a limiting flux of $\sim 1.4 \times 10^{-13}\mathrm{erg\ cm^{-2}s^{-1}}$ (Gompertz, Page, and de Pasquale, 2013) or to a limiting magnitude of $\sim$ 21.1 mag in the UVOT u-band (Breeveld and de Pasquale, 2013), consistent with

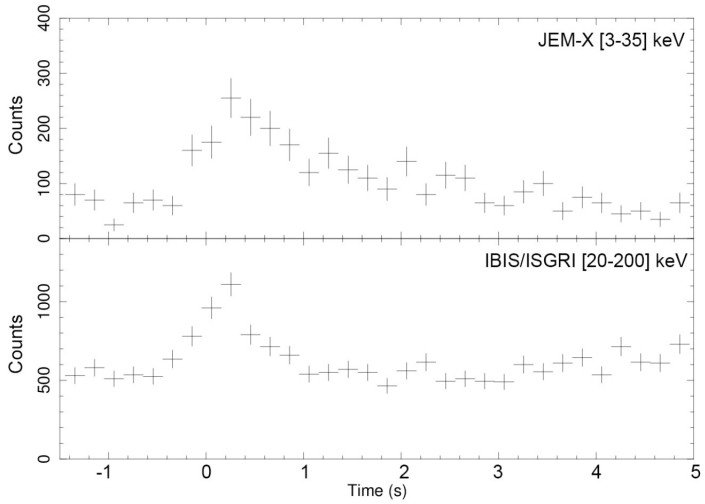

FIGURE 4.11: Light curve of sGRB 131224A obtained by JEM-X (top) and IBIS/ISGRI (bottom) on-board the *INTEGRAL* observatory with a time resolution of 0.2 sec.

those seen in the case of other sGRBs.

It could also be discussed whether the event 131224A genuinely is a GRB event. The burst energy and morphology are very similar to type-I X-ray bursts which are thermonuclear flashes on the surfaces of weakly magnetic accreting neutron stars in low-mass X-ray binaries (LMXBs, for reviews see e.g. (Lewin, van Paradijs, and Taam, 1995; Bildsten, 2000)). The burst is unusually soft for a short GRB and is not detected above 70 keV. The duration of the event in the soft (3-20 keV) energy band is 10s longer than in the hard (20-70 keV) energy band. The burst came from the direction of the Galactic plane, where the greatest number of known LMXBs are located. If the event is a type-I X-ray burst and taking into account no detection of any persistent X-ray emission in the follow-up XRT observation, then this source is a new member of the rare class of X-ray bursters with very low ($< 10^{35}$ erg/s) luminosity, the so-called 'burst-only' sources (see e.g. Cornelisse et al., (2004) and references therein).

Deeper observations of this burst were performed under our program using the 10.4 m GTC starting 1.11 d and around 7 d after the burst in i and z filters. Within the JEM-X *INTEGRAL* error-box, no new fading source was revealed down to a limiting magnitude of $\sim$ 23.6 mag in i band. The photometric results based on our analysis of the GTC data are tabulated in Table 4.6.

sGRB 140606A

Swift discovered sGRB 140606A (trigger=600951) on 2014 June 06 at 10:58:13 UT which had a duration of T_{90} = 0.34±0.09 s (Stroh et al., 2014; Cummings et al., 2014a). The time-averaged spectrum from T-0.04 to T+0.35 is best fitted by a simple power-law model. The burst is not visible in the soft energy channel (15-25 keV) and has negligible spectral lag. This confirms the short nature of the burst. *Fermi*/GBM data of the sGRB 140606A show that the burst was seen within the field of view but didn't trigger *Fermi*/GBM. However, significant gamma-ray emission in the *Fermi* Daily continuous Time-Tagged Event (TTE) data archive. We fit the spectrum of NaI n4 between T0-0.04 and T0+0.8s and found that the cutoff-PL model is the best fit to the data. The low-energy photon index = $0.82^{+1.34}_{-0.97}$ and E_{peak} = 185.13^{+126}_{-28} keV. The corresponding GBM flux is $\sim 6.0 \times 10^{-7}$ erg cm^{-2} s^{-1} in 1-10^4 keV. The spectral fitting plot with the cutoff-PL model is shown in Figure 4.12(left panel). The burst was detected by IBAS in SPI-ACS *INTEGRAL* (off-axis angle is 40 deg) as a 0.25 s single pulse and we do not detect EE (for details of SPI-ACS data analysis see, Minaev, Pozanenko, and Loznikov, (2010)). At a time scale of 50s, the upper limit on EE activity in SPI-ACS for sGRB 140606A is $\sim$ 7000 counts i.e. fluence $S_{EE} \sim (7.0 \times 10^{-7}$ erg cm^{-2}) at the 3σ significance level in the (75, 1000) keV range.

No X-ray counterpart of this burst observed by XRT due to an observing anomaly (Burrows and Kennea, 2014). *Swift* UVOT observations, starting $\sim$ 68 sec after the BAT trigger, do not detect any new optical source within the error circle (Marshall and Stroh, 2014) down to a limiting magnitude of $\sim$ 20 mag. Further optical observations by Xu et al., (2014a) also do not find any new optical source within the BAT error circle. Optical observations using the Abastumani AS-32 telescope starting 0.332 d after the burst do not find any optical afterglow down to a limiting magnitude of $\sim$ 21.7 mag in clear filter as reported by Volnova et al., (2014).

The field of sGRB 140606A was observed in B, V and Rc bands with the 6 m BTA/Scorpio-I (SAO RAS, Russia) on the night of June, 7 2014. The observations started 10 hrs after the trigger (Moskvitin et al., 2014b). The first BTA image covers 100 per cent of the BAT refined error circle. In the stacked R-band image, we detected a few hundred objects down to the limiting magnitude $R \sim 24.1$ mag (total exposure of 150 seconds). The stacked image combined

from all obtained frames (total exposure of 480 seconds) covers 14.7 square minutes, 82 per cent of the BAT circle with a limiting magnitude of $R \sim 26$ mag. The field was also observed with the 10.4 m GTC/Osiris (ORM, Spain) on Feb. 26 2015, almost 9 months after the burst. The stacked image combined from $5 \times 60 + 10$ seconds frames in r' band covers 13.2 square minutes, 73 per cent of the BAT circle. We detected a few hundred faint objects down to the same limiting magnitude, $R \sim 26$ mag. The brightest galaxies in the BAT circle are USNO 1275-0258796 and 1275-0258743 with magnitudes of $R \approx 18$. Due to the large number of objects in the BAT circle, we can not suggest a single candidate for the host galaxy or any possible flaring activity by an active galaxy in the observed error circle. As a part of the present analysis, mm-wavelength observations using the IRAM Plateau de Bure Interferometer for the full BAT error circle do not result any detection down to a limiting flux of 0.33±0.19 mJy around 4-15 d post-burst. The details of the mm observations of the sGRB 140606A taken at 86.74 GHz are tabulated in Table 4.2.

A blue object within the sGRB 140606A BAT error box at coordinates RA= $13^h27^m07.9^s$, Dec=+37°37′10.8″ (J2000, 1 arcmin error) with magnitude R =20.60 ±0.04 mag was found to be a quasar at z = 1.96 (see Figure 4.12, right panel). The expected chance of finding a quasar within the BTA field of view is ∼ 0.08 (following the QSO surface number from (Koo and Kron, 1982)) but the lack of variability between the initial BTA frame and the late-time GTC image does not support their relationship. As mentioned above, due to the lack of full coverage of the BAT error circle, the chance coincidence of the QSO gamma-ray flaring with the observed sGRB 140606A can not be established.

sGRB 140622A

Swift discovered sGRB 140622A (trigger=602278) on 2014 June 22 at 09:36:04 UT with a duration of T_{90} = 0.13±0.04 s (D'Elia et al., 2014a; Sakamoto et al., 2014a). The mask-weighted light curve shows a weak single FRED peak with a soft spectrum, which is best fitted by a black-body with kT = 11.6±1.8 keV which is not typical for the class of short bursts (Sakamoto et al., 2014a). The quickly fading X-ray light curve (temporal decay index 7.1±0.9 and mostly taken in photon counting mode) does, however, appear consistent with a short burst model, and does not appear to be similar to the light curves of SGRs or

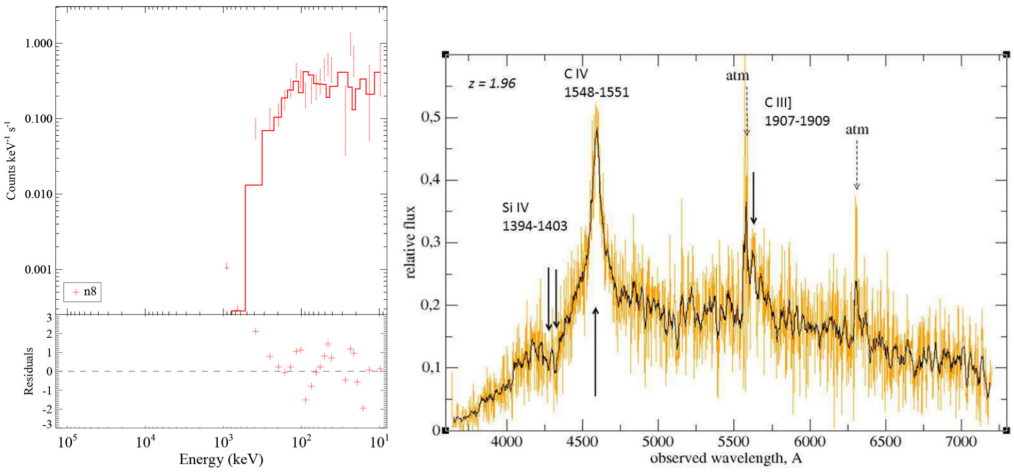

FIGURE 4.12: The best fit model of the prompt emission spectra of the *Fermi*/GBM (left panel) data of sGRB 140606A. The 6.0 m BTA (+SCORPIO) spectrum (4×900s) taken on 07 June 2014 of the new QSO (RA=$13^h27^m07.9^s$, Dec=+37°37′10.8″ J2000) discovered within the sGRB 140606A BAT error box showing the typical QSO emission lines at a redshift z = 1.96 ± 0.1 (right panel).

other Galactic sources (Burrows et al., 2014). The burst was not detected by *INTEGRAL* most probably due to the soft spectrum. The SPI-ACS *INTEGRAL* off-axis is 125 degrees. The early optical observations by 0.25m TAROT (Klotz et al., 2014) ∼ 23.2 s post-burst, by *Swift* UVOT ∼ 97 s post-burst (Marshall and D'Elia, 2014) and by 0.76 m KAIT ∼ 198 s post-burst (Zheng et al., 2014) do not reveal any optical source down to a limiting magnitude of ∼ 18, 21 and 19 mag respectively. However, optical observations taken by the TSHAO Zeiss-1000 (East) telescope starting 0.475 d after the burst in R_c filter with an exposure time of 60×60s+5×240s marginally detect a source at RA(J2000)=$21^h08^m41.69^s$, Dec(J2000)=-14°25′08.7″ (± 0.22″) at a magnitude of 22.5±0.3 mag. In the light of other non-detection to deeper limits from the data taken before and after the epoch of observations by TSHAO Zeiss-1000 (East), it seems that this marginal detection could be a false one. So, an upper limit of ∼ 22.5 mag is reported in Table 4.6. The 2.2m GROND observations taken ∼252 s after the burst do not reveal any optical counterpart within the XRT error-box down to a limiting magnitude of ∼ 24.3 mag. However, they do detect an optical source just outside the XRT error circle (Tanga, Delvaux, and Greiner, 2014) at a measured redshift of z ∼ 0.959 using VLT observations (Hartoog et al., 2014). At this redshift, the host distance from the XRT error circle would be around 21 kpc which could

easily rule out the suspected galaxy as a potential host for sGRB 140622A. The XRT error-box was also observed by the RATIR camera at the 1.5m telescope starting $\sim$ 1.2 min after the burst in several filters and no counterpart could be detected to deeper limits (Butler et al., 2014). As a part of the present analysis, mm-wavelength observations using the IRAM Plateau de Bure Interferometer for the full BAT error circle do not result any detection down to a limiting flux of -0.37$\pm$0.12 mJy within a few hours post-burst. The details of mm observations of the sGRB 140622A taken at 86.74 GHz are tabulated in Table 4.2.

So, to search for the potential host galaxy/counterpart, we triggered our proposal on the 10.4 m GTC. The analysis of the GTC r-band data (6$\times$100+5$\times$2 s) reveals that there is no optical counterpart down to a limiting magnitude of $\sim$ 25.8 mag at around 0.78 d post-burst. So, it is clear from the above observations that the host galaxy of this burst is fainter than $\sim$ 25.8 mag. It is worth mentioning that no detection of any host galaxy down to a deep limit of $r \sim$ 25.8 mag indicates sGRB 140622A to be a candidate belonging to the sub-set of other host-less events (Berger, 2010; Tunnicliffe et al., 2014). The *Swift*-BAT fluence in the 15–150 keV range is 2.7$\pm$0.5$\times10^{-08}$ erg cm^{-2} along with a $<$ 0.3 micro-Jansky limit at optical frequencies place a very crude limit for this burst as a possible high redshift one (Berger, 2010). Early epoch deeper observational limits at optical wavelengths and along with unusual *Swift*-BAT and XRT spectra (Sakamoto et al., 2014a; Burrows et al., 2014) also indicate the peculiar nature of this burst. The finding chart locating the XRT error-circle is shown in Figure 4.13 based on the data taken by the 10.4 m GTC.

sGRB 140903A

Swift- BAT triggered on a possible GRB on 2014 Sep. 03 at 15:00:30 UT. Due to a TDRSS telemetry gap, the XRT localization was performed $\sim$ 2.5 hrs post-burst and ultimately the burst was found to be a duration of T_{90} = 0.30$\pm$0.03s (Cummings et al., 2014c; Palmer et al., 2014a). The BAT and XRT data indicated a soft burst spectrum and an excess column density was observed (de Pasquale, Maselli, and Cummings, 2014), not very common in the case of sGRBs. The time-averaged spectrum from T-0.01 to T+0.35s was best fitted by a simple power-law model. The power-law index of the time-averaged spectrum is 1.99$\pm$0.12. Extended emission was not found (Sakamoto et al., 2014b; Serino et al., 2014) in

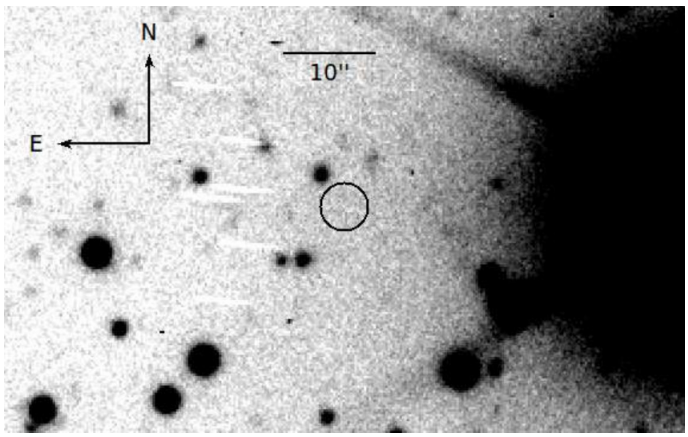

FIGURE 4.13: Finding chart of sGRB 140622A in the stacked frame of r band observed by the 10.4 m GTC telescope. The black circle is the XRT error box, having no sign of the optical afterglow down to a limiting magnitude of $\sim$ 25.8 mag $\sim$ 0.78 d after the burst.

the prompt emission light curve of this burst and the mask-weighted light curve shows a single FRED peak. The SPI-ACS *INTEGRAL* detector was switched off at the time of the burst. The spectral-lag analysis was performed by Sakamoto et al., (2014b) which found that: the spectral lag for the 50-100 keV to 100-350 keV bands is 16$\pm$7ms, and 21$\pm$ 7 ms for the 15-25 keV to 50-100 keV bands. According to Sakamoto et al., (2014b) these lag values indicate that GRB 140903A belongs to the long GRB population. This interpretation contradicts results obtained for individual pulses of BATSE bursts by Hakkila and Preece, (2014). According to Hakkila and Preece, (2014), short and long bursts show the same spectral evolution behaviour if the spectral lag analysis is performed for individual pulses of bursts instead of analyzing the whole burst structure. Similar results were also noted by Minaev et al., (2014) in their analysis of several other *INTEGRAL* bursts. sGRB 140903A is single-pulsed and belongs to the bottom-left region of the lag duration correlation constructed for individual pulses of BATSE bursts (Figure 3 in Hakkila and Preece, (2014)), which means that this burst belongs to the short GRB population. A low E_{iso} value (0.04×10^{51} erg, see below) is also more common for short bursts than for long ones. Troja et al., (2016) have shown that the burst has negligible lag and other prompt emission properties are very typical of those in case of other sGRBs. It was also noticed that this burst is located within 2.5 arcmin of the centre of the galaxy cluster NSC J155202+273349 at a photometric redshift of $\sim$ 0.295 (Fox and Cummings,

2014; Gal et al., 2003). However, Troja et al., (2016) have established that the burst was not associated with the galaxy cluster.

The optical afterglow of this sGRB was discovered by the 4.3m Discovery Channel Telescope (DCT) within the XRT error circle around 12 hrs after the burst (Capone et al., 2014; Troja et al., 2016). The optical afterglow candidate was also seen in further follow-up observations (Cenko and Perley, 2014; Dichiara, Guidorzi, and Japelj, 2014; Xu et al., 2014b). Fruchter, (2014) noticed that the candidate optical afterglow was present in archival images of the Pan-STARRS survey and was later suspected to be the host galaxy candidate. Troja et al., (2016) measured the redshift of the afterglow as ~ 0.351 using the Gemini-N 8.0 m telescope equipped with the Gemini Multi-Object Spectrographs (GMOS) camera. The fading behaviour of the optical afterglow candidate was established in further observations by Levan et al., (2014) and Cenko and Perley, (2014). The radio afterglow of the burst was also observed by JVLA at 6 GHz (Fong et al., 2014; Troja et al., 2016) and by GMRT at 1390 MHz (Nayana and Chandra, 2014). However, mm-wavelength observations using the IRAM Plateau de Bure Interferometer at the XRT location do not result any detection down to a limiting flux of 0.12 ± 0.13 mJy within a few days post-burst. The afterglow modelling of the multi-band data by Troja et al., (2016) indicates that our mm-wavelength IRAM observations were shallower in comparison to detected signals at the level of a few micro Jy at JVLA and GMRT frequencies. The details of our mm observations of the sGRB 140903A taken at 86.74 GHz are tabulated in Table 4.2. Spectroscopy of the afterglow was also performed using the 10.4 m GTC and the redshift value determined was ~ 0.351 (Troja et al., 2016) consistent with that reported by Cucchiara et al., (2014). Using the measured redshift of this burst (Troja et al., 2016) and the γ-ray fluence by Palmer et al., (2014a), the isotropic equivalent gamma-ray energy is $E_{iso} \sim 0.04 \times 10^{51}$ erg (20 to 10^4 keV, rest-frame).

The ISON-Kislovodsk SANTEL-400A optical telescope also started observations ~ 0.141 d after the burst and did not see any afterglow down to a limiting magnitude of ~ 18.6 mag (Pozanenko et al., 2014). To search further for the optical afterglow or for any possible 'kilonova' emission for this nearby sGRB, we observed the field of GRB 140903A with the 1.5 m AZT-22 telescope of Maidanak astronomical observatory on 2014 Sep. 4, 6, 7, and 13, taking 12-15 images of 60 s exposure in the R-filter. The position of the optical source is in the wing

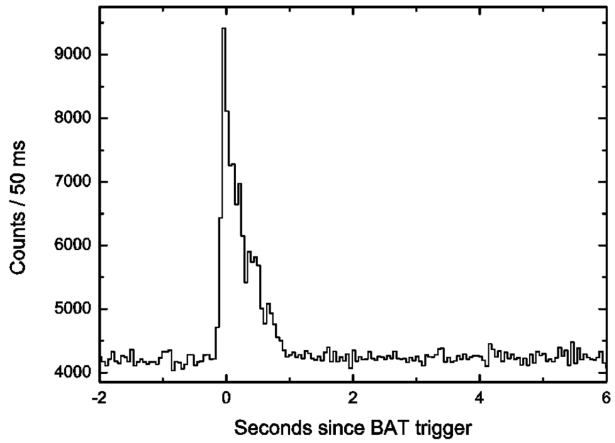

FIGURE 4.14: Light curve of sGRB 140930B obtained by SPI-ACS *INTEGRAL* in the energy range 0.1-10 MeV with 50 ms time bins as a part of the present study. On the x-axis, the time since the BAT trigger is shown. On the y-axis, counts per 50 ms are presented.

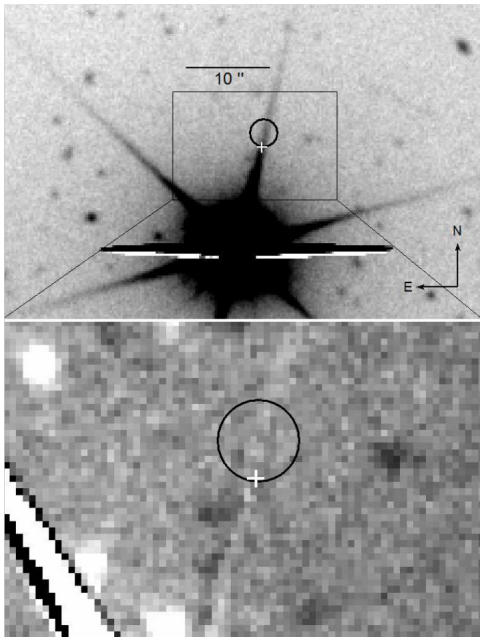

FIGURE 4.15: Finding chart of sGRB 140930B in the stacked frame of r band observed by the 10.4 m GTC telescope. The XRT error box shown in a black circle is overlapped with one of the spikes of the nearby bright star. In the bottom panel, the zoomed portion (inset) is shown after applying image subtraction and the '+' sign marks the position of the afterglow reported by Tanvir, Levan, and Fraser, (2014)

.

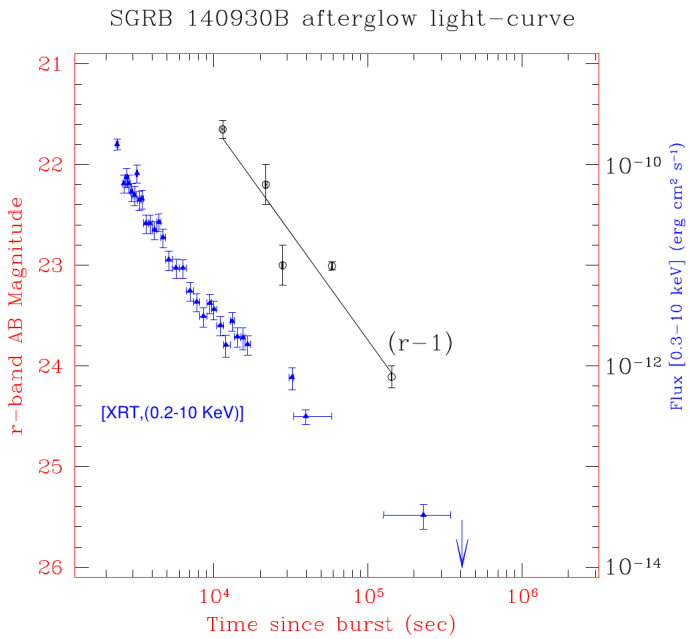

FIGURE 4.16: sGRB 140930B optical r band afterglow light-curve. The solid black curve is the best-fit power-law model to the r-band light curve. The two r band data points around 2×10^4 s (Fong, Calkins, and Berger, 2014) and 3×10^4 s (Graham et al., 2014) post-burst are from GCN circular archive, considered while fitting the power-law to derive the temporal decay index. For comparison, *Swift* XRT light curves are also plotted in blue colour.

of a bright star SDSS J155202.58+273611.7 (R = 12.9 mag). The limiting magnitude for every epoch far away from the bright star was obtained using nearby SDSS stars. To find a possible afterglow, we subtracted the combined image obtained on Sep. 13, 2014 from that of Sep. 4, 2014. At the position of the afterglow in the residual image, we do not find any source implying an equivalent upper limit variability of the source less than 0.5 magnitudes (3σ) between the two epochs. This is in agreement with observations by Xu et al., (2014b) and confirms the absence of an afterglow signature 30 hrs after the trigger. Based on those observations, we can also exclude the possibility of an underlying 'kilonova' brighter than R $\sim$ 22.0 (3σ) at 10 d associated with sGRB 140903A. The corresponding limiting luminosity for the given redshift, $L_R < 6.5 \times 10^{27}$ erg/s/Hz, seems afterglow dominated and brighter by a factor of 6 than any GW170817 like associated 'kilonova' at similar epochs (Rossi et al., 2020).

sGRB 140930B

Swift detected sGRB 140930B (trigger=614094) on 2014 Sep. 30 at 19:41:42 UT with a duration of T_{90} = 0.84±0.12s (de Pasquale et al., 2014; Baumgartner et al., 2014). The burst was also observed by *Konus*-Wind with the light curve having a complex multi-pulsed structure with a duration of $\sim$ 1.0 s and the emission was seen up to $\sim$ 10 MeV (Golenetskii et al., 2014b). The time-averaged spectrum of the burst (measured by *Konus*-Wind from T0 to T0+8.448s) had a best fit in the 20 keV - 15 MeV range by a power-law with exponential cut-off model with E_{peak} = 1302^{+2009}_{-459} keV and total fluence of $8.1^{+5.1}_{-2.5}$ $\times 10^{-6}$ erg cm^{-2} (Golenetskii et al., 2014b). Since the redshift of the sGRB 140930B is unknown, the trajectory of sGRB 140930B on the Amati diagram as a function of z (Figure 4.9, see also Minaev et al., (2012)) can be constructed using the fluence and E_{peak}(1+z) estimates. It follows from Figure 4.9 that the trajectory does not cross the correlation region and lies above those drawn for lGRBs, which may suggest that sGRB 140930B belongs to the class of short bursts. The higher E_{peak} value confirms that the burst is spectrally hard. Overall a FRED light curve with three pulses after the main peak is visible in SPI-ACS *INTEGRAL* (Figure 4.14). The SPI-ACS *INTEGRAL* off-axis is 67 degrees. There is no EE in either BAT (Baumgartner et al., 2014) or SPI-ACS *INTEGRAL* light curves. At a time scale of 50 s, the upper limit on EE activity in SPI-ACS for sGRB 140930B is $\sim$ 7300 counts i.e. $S_{EE} \sim (7.3 \times 10^{-7}$ erg cm^{-2}) at the 3σ significance level in the (75, 1000) keV range. *Fermi*-/GBM could not observe the burst as the satellite was passing in its South Atlantic Anomaly.

Early time optical observations using *Swift*-UVOT (Breeveld and de Pasquale, 2014), MASTER-II (Gorbovskoy et al., 2014b) and 1.23m CAHA (Gorosabel, Hellmich, and Mottola, 2014) do not reveal any optical afterglow down to a limiting magnitude of R $\sim$ 21.1 mag. UAFO ORI-65 and ISON-Kislovodsk SANTEL-400A telescopes started observations around 0.025 and 0.029 d after the burst and did not see any afterglow down to a limiting magnitude of $\sim$ 16.1 mag and 20.4 mag respectively (Polyakov et al., 2014). However, starting $\sim$ 3 hrs after the burst, the 4.2 m WHT found an optical source (Tanvir, Levan, and Fraser, 2014) that decayed in later images obtained by the 6.5m MMT (Fong, Calkins, and Berger, 2014) and the 2.2m GROND (Graham et al., 2014) telescopes. The spectroscopic observations using Gemini-south were reported by

Cenko et al., (2014) and the afterglow candidate was also observed in J and K_s bands using Keck-MOSFIRE (Perley and Jencson, 2014).

We started to observe the field of GRB 140930B on Oct. 3, 2014 at 22:58:33 UT, i.e. $\sim$ 3.1 d after the trigger taking 13 frames with an exposure of 60 seconds in the r filter under mean FWHM of 0.8 arcsec using the 10.4 m GTC. The refined position of the optical and infrared afterglow is strongly affected by a spike from nearby bright star S1 (J002523.61+241727.0, $r \sim 13.1$ mag). All bright stars in the frames from GTC have six symmetrical spikes from a secondary mirror mount. We found the central position of the S1 star and then we rotated the combined image around this position 60 degrees clockwise, to use a rotated image as a template for the subtraction of the spike contaminating the position of the afterglow. In the resulting image, we do not find any source at the position of the optical afterglow down to a limiting magnitude of $r \sim 24.5$ mag. The finding chart locating the XRT error circle is shown in Figure 4.15 based on the late time data taken by the 10.4 m GTC. At the epoch of our GTC observations, the limiting value of afterglow luminosity would be $L_r < 1.3 \times 10^{27}$ erg/s/Hz for an assumed redshift of z $\sim$ 0.5. This value is nearly similar to the expected luminosity of GW170817 like 'kilonova' at similar epochs (Rossi et al., 2020).

Also, the optical afterglow observed by the 4.2m WHT/ACAM and Gemini North/GMOS-N (Tanvir, Levan, and Fraser, 2014). The photometric results based on our multi-band observations are reported in Table 4.6. The r band photometry from the present study along with those given in the GCN (Fong, Calkins, and Berger, 2014; Graham et al., 2014) were used to produce the afterglow light curve as shown in Figure 4.16. The temporal flux decay index using the r band light curve was derived as $\alpha_o = 0.85 \pm 0.26$ during 0.13 to 1.65 d after the burst. The contemporaneous *Swift*-XRT light curve decay index is $\alpha_X = 1.6 \pm 0.1$ where the X-ray spectral index $\beta_X = -0.71 \pm 0.15$. Assuming the cooling break frequency ν_c lying between those two observed bands, the closure relations in case of the *ISM* afterglow model (Sari, Piran, and Narayan, 1998) are broadly consistent with the observed values of temporal decay at optical bands, whereas the temporal decay index at X-rays is steeper than the expected model predictions. The 10.4 m GTC was further triggered to search for any possible host galaxy on 10th Dec. 2018 and a total of 30 images of 120s each were acquired (see Table 4.6) in r-band. In the stacked image, we do not see any object down to a limiting magnitude of $\sim$ 24.8 mag at the location of the afterglow

after accounting for the possible effects of the nearby bright star. So, it is concluded that the host galaxy of the sGRB 140930B would be fainter than $r \sim 24.8$ mag.

sGRB 141212A

sGRB 141212A was discovered on 2014 Dec. 12 at 12:14:01 UT by the *Swift*-BAT (Ukwatta et al., 2014). The BAT light curve shows a single spike with a duration $\sim$ 0.1 sec in the energy range (25–350) keV. In the soft energy channel 15–25 keV, a second pulse is clearly visible with a duration of 0.1s at 0.3s after the trigger. The duration parameter T_{90} in the 15–350 keV energy range is 0.30$\pm$0.08s (Palmer et al., 2014b). The time-averaged spectrum from T+0.00 to T+0.34s is best fitted by a simple power-law model with a power-law index of 1.61$\pm$0.23. The fluence in the 15–150 keV band is 7.2$\pm$1.2$\times 10^{-08}$ erg cm^{-2} (Palmer et al., 2014b). GRB 141212A was also found in *INTEGRAL* SPI-ACS data (there was no IBAS trigger) as a single pulse with a duration of 0.15 sec and statistical significance of 7.3 σ (Figure 4.17). The second soft pulse is not visible in SPI-ACS which is sensitive above $\sim$ 80 keV. At a time scale of 50s, the upper limit on EE activity in SPI-ACS for sGRB 141212A is $\sim$ 7300 counts i.e. $S_{EE} \sim (7.3 \times 10^{-7}$ erg cm^{-2}) at the 3σ significance level in the (75, 1000) keV range. Ground-based MITSuME (Fujiwara et al., 2014), MASTER network of telescopes (Gres et al., 2014) and UVOT on-board *Swift* did not find any new optical source within the XRT error-box in the images taken around 31s, 46s and 72s after the BAT trigger respectively down to a limiting magnitude of V $\sim$ 19 mag.

We started observation of the sGRB 141212A with the 1.5 m AZT-33-IK telescope at Mondy observatory on Dec. 12 2014 at 12:36:10.7650 UT, i.e. 22 minutes after the trigger. We also observed it later with the same telescope on Dec. 14 and Dec. 18. We also observed the field with the 0.4m telescope at Khureltogot observatory and 1.0m telescope at Tien Shan observatory (see Table 4.6 for the complete log of observations). The host galaxy suggested by Malesani et al., (2014) was also detected from our observations using 1.0 – 1.5m telescopes. We did not find any evidence for the optical afterglow signature in our observations taken in R filter. A deeper photometric data were taken using the 8.0 m Gemini-N/GMOS-N under program GN-2014B-Q-10 in i band and the bright

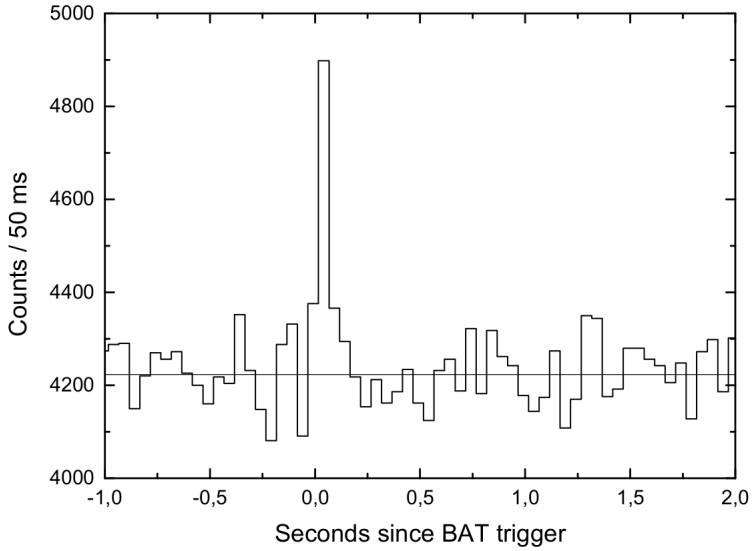

FIGURE 4.17: Light curve of sGRB 141212A from *INTEGRAL* SPI-ACS data in the energy range 0.1-10 MeV with 50 ms time resolution. The X-axis is the time since the BAT trigger, and the Y-axis is counts in 50 ms time bins. The thin horizontal line represents the background level.

host galaxy candidate was clearly detected in the data taken at the two epochs as listed in Table 4.6. Using this data, the possibility of any point source in the vicinity of the host galaxy candidate (Malesani et al., 2014) is ruled out up to a limiting magnitude of $i \sim 26$ mag (3-σ) at 0.68 d post-burst. This deep limiting value translates to a luminosity of $L_i < 5 \times 10^{26}$ erg/s/Hz (a factor of 3 deeper than the rest-frame luminosity of GW170817 like 'kilonova' at contemporaneous epochs), further implies that at the epoch of our observations in i band, any associated GW170817 like 'kilonova' with the burst would have been detected as seen in a few cases of sGRBs in Rossi et al., (2020).

Furthermore, multi-band photometry with the 10.4 m GTC in gri-filters was performed at late epochs, i.e. around 427.3 d post-burst, to investigate properties of the host galaxy (see Table 4.6). The finding chart with the XRT error circle superimposed on the data taken by the 10.4 m GTC is shown in Figure 4.18. The observed flux of the host galaxy of sGRB 141212A obtained by the 10.4 m GTC in different filters (see Table 4.6) and the suggested redshift of the burst $z = 0.596$ (Chornock, Fong, and Fox, 2014) allowed us to model the SED of the host galaxy. We also added upper limits in filters u and b from *Swift*-UVOT data (Oates and Ukwatta, 2014). To build the SED of the host galaxy of sGRB

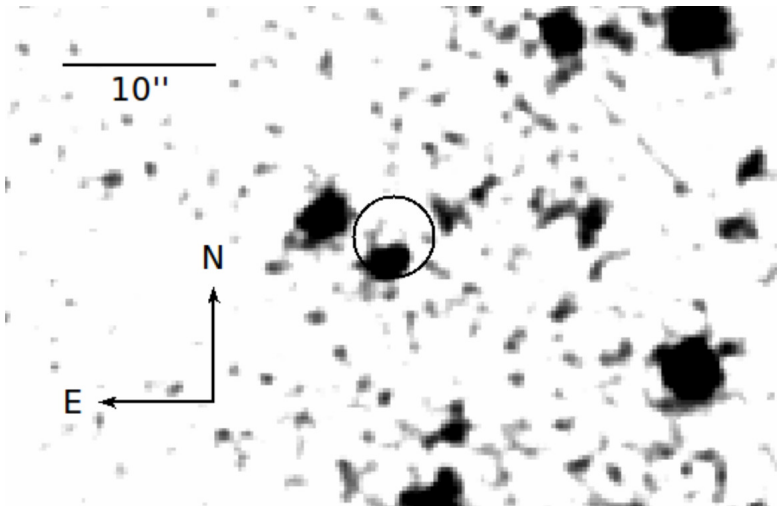

FIGURE 4.18: Finding chart of sGRB 141212A in the stacked frame of r band data obtained with the 10.4 m GTC telescope. The XRT error box is shown as a black circle. The bright host galaxy is also visible within the XRT error circle.

141212A and to estimate parameters, we used the LE PHARE software package (Arnouts et al., 1999; Ilbert et al., 2006) with fixed redshift. We used the PEGASE2 population synthesis models library to obtain the best-fit SED, the mass, the galaxy age and star formation rate. We tested four different reddening laws: the Milky Way extinction law by Seaton, (1979), LMC (Fitzpatrick, 1986), SMC (Prevot et al., 1984), and the reddening law for starburst galaxies (Calzetti et al., 2000; Massarotti et al., 2001). The reduced χ^2, galaxy morphological type, bulk extinction, absolute rest-frame B magnitude, age, mass, star formation rate, and specific star formation rate (SSFR) per unit galaxy stellar mass are listed in the Table 4.5 for all 4 tested extinction laws. Figure 4.19 represents the best model corresponding to the Milky Way extinction law.

The best fit shows that the host is a galaxy of elliptic type with $M_B = -19.9$ mag and a moderate linear size along the major axis about 13 kpc. The major axis is oriented 45 degrees North-West. Age of the host galaxy is ~ 2 Gyr, and the average internal extinction in the galaxy is rather high, $E(B-V) = 0.50$ mag. The host galaxy has a mass of $\sim 9 \times 10^9 M_\odot$, and a high star formation rate of SFR $\sim 50 M_\odot$/yr. All obtained parameters are in good agreement with previous studies by Chrimes et al., (2018) except for SFR which is two orders higher in our results.

TABLE 4.5: sGRB 141212A host galaxy properties derived from the SED fitting.

Fitted parameters	Starburst model	Milky Way model	LMC model	SMC model
χ^2/DOF	2.8/3	2.7/3	2.8/3	5.9/3
Type	E	E	E	S0
$E(B-V)$, mag	0.50	0.50	0.50	0.00
M_B, mag	-19.9	-19.9	-19.9	-19.7
Age, Gyr	$2.65^{+2.50}_{-0.11}$	$2.23^{+1.70}_{-0.09}$	$2.05^{+3.44}_{-0.13}$	$3.10^{+0.09}_{-0.25}$
Mass, $(\times 10^{10})M_\odot$	$1.0^{+5.4}_{-0.7}$	$0.9^{+3.7}_{-0.6}$	$0.9^{+8.5}_{-0.7}$	$1.4^{+12.6}_{-0.8}$
SFR, $M_\odot$/yr	87^{+343}_{-70}	48^{+147}_{-41}	49^{+155}_{-36}	$4.2^{+85.5}_{-1.5}$
SSFR, $(\times 10^{-10})$yr^{-1}	88^{+270}_{-65}	55^{+173}_{-46}	56^{+215}_{-49}	$2.9^{+73.6}_{-0.4}$

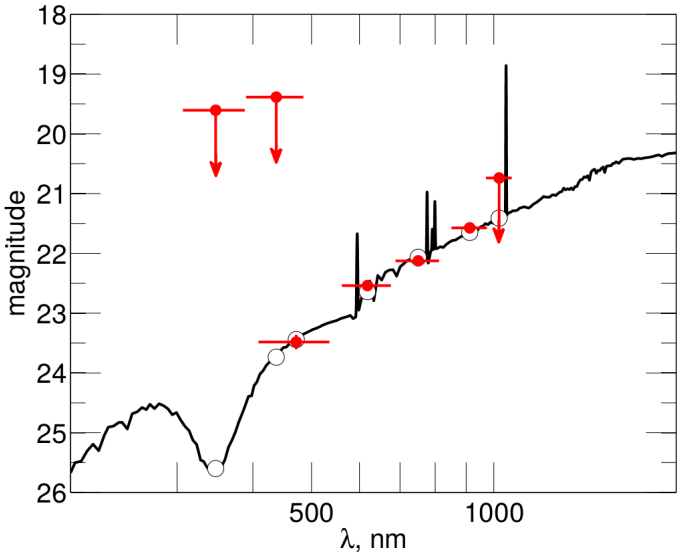

FIGURE 4.19: The SED (line) of the host galaxy of sGRB 141212A fitted by the LE PHARE with fixed redshift $z = 0.596$. Filled red circles depict respectively the data points in the *Swift*/UVOT filters u, b, taken from Oates and Ukwatta, (2014), g, r, i from original observations (see Table 4.6), and z, y from Chrimes et al., (2018, , Table A1). Open circles represent model magnitudes for each filter. All magnitudes are in the AB system.

sGRB 151228A

sGRB 151228A (trigger=668543) was discovered by *Swift* on 2015 Dec. 28 at 03:05:12 UT with a duration of T_{90} = 0.27±0.01s (Ukwatta et al., 2015; Barthelmy et al., 2015). The burst was also detected by *Fermi*-GBM (Bissaldi, Zhang, and Veres, 2015), but there was no *Swift*-XRT localization (Page and Ukwatta, 2015) due to an observing constraint. The burst was also detected by *INTEGRAL* SPI-ACS and triggered its IBAS system. The SPI-ACS light curve of sGRB 151228A is presented in Figure 4.20 (left panel) and shows two overlapping pulses with a total duration of about $\sim$ 0.3 sec. At a time scale of 50s, the upper limit on EE activity in SPI-ACS for sGRB 151228A is $\sim$ 7700 counts i.e. $S_{EE} \sim (7.7 \times 10^{-7}$ erg cm^{-2}) at the 3σ significance level in the (75, 1000) keV range. *Fermi*-GBM data was fitted for the time-averaged spectrum using the NaI n4 data and it was found that the cutoff-PL model was the best fit. The low-energy photon index = 0.72±0.84 and E_{peak} = $261.18^{+164.94}_{-58.28}$ keV, much lower than reported in Bissaldi, Zhang, and Veres, (2015). The corresponding GBM flux is $(1.4^{+1.39}_{-0.61})$ $\times 10^{-6}$ erg cm^{-2} s^{-1} in 1-10^4 keV. The light curve of *Fermi*-GBM also have two overlapping pulses with a total duration of about $\sim$ 0.4 sec. The spectral fitting plot with the cutoff-PL model is shown in Figure 4.20 (right panel). As estimated in the case of sGRB 140930B, we constructed the trajectory for sGRB 151228A on the Amati diagram (see Figure 4.9), because the redshift z for sGRB 151228A was unknown. The trajectory lies above the main correlation at any z, which may suggest that sGRB 151228A belongs to the class of the short bursts. Since the burst does not fall into the $E_{peak}(1+z)/E_{iso}$ correlation region at any z, the redshift and E_{iso} of this burst cannot be estimated.

Early optical searches within the BAT error circle do not find any new optical source down to a limiting magnitude of $\sim$17 mag using the 0.60m T60 telescope (TUBITAK National Observatory, Antalya - Turkey) starting 90 sec after the burst (Sonbas et al., 2015). The 10.4 m GTC was triggered around $\sim$ 1.143 d after the burst and covered the full error box in i filter with a total exposure time of 5×60 sec. The GTC observations cover the full BAT error circle, except for a 9.4″ gap between chips in the CCD camera (the gap covers $\sim$ 7.4 per cent of the total error box). The BAT error circle was again observed by the 10.4 m GTC in i filter around 69 d after the burst with a total exposure of 7×75 sec. Due to different limiting magnitude, FWHM and inadequate flat-fielding for the whole

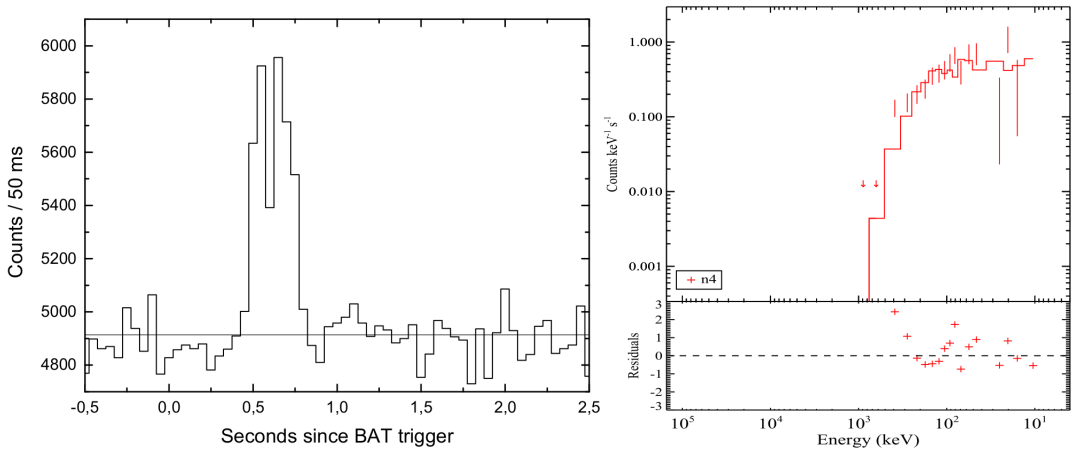

FIGURE 4.20: Light curve of sGRB 151228A from *INTEGRAL* SPI-ACS in the energy range 0.1-10 MeV with 50 ms time resolution. The X-axis is the time since the BAT trigger, and the Y-axis is counts in 50 ms time bins (left panel). The thin horizontal line represents the background level. The best fit model of the prompt emission spectra of the *Fermi*-GBM (right panel) data of sGRB 151228A in counts.

FOV of the CCD camera, we could not use the image subtraction method to search for the source at the first epoch. Instead, we performed a catalogue extraction at S/N = 3 for each epoch. We did not find any new object at the first epoch down to a limiting magnitude of >23.7 mag comparing with the second epoch (limiting magnitude for the second epoch was 24.8 mag). The results of our photometry and values of the limiting magnitude for sGRB 151228A are reported in Table 4.6.

GW170817 and the sample of sGRBs

On 17 Aug. 2017, 12:41:04.82 UT, the LIGO and Virgo interferometers detected a transient GW signal from a source named GW170817 (Abbott et al., 2017b). The *Fermi*-GBM triggered and located a short burst named sGRB 170817A (von Kienlin, Meegan, and Goldstein, 2017) about 1.7 s after the GW signal spatially consistent with the GW event (Connaughton et al., 2017). The error region was later followed-up extensively at lower frequencies to search for the underlying 'kilonova' signature (Coulter et al., 2017; Pian et al., 2017; Covino et al., 2017; Tanvir et al., 2017; Evans et al., 2017; Smartt et al., 2017; Cowperthwaite et al., 2017; Troja et al., 2017b). Discovery of this GW event called

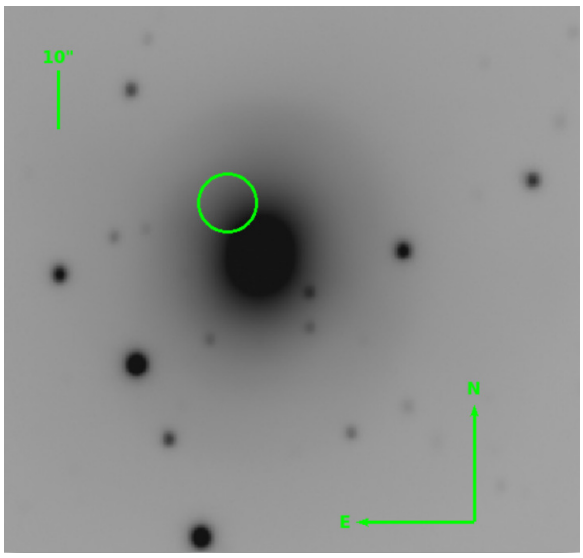

FIGURE 4.21: Finding chart of GW170817 (circle) in the stacked frame of i-band data obtained by the 10.4 m GTC telescope obtained $\sim$ 154.7 d post-burst.

GW170817/AT 2017gfo/SSS17a associated with the very nearby (host galaxy NGC 4993 at $\sim$ 40 Mpc) sGRB 170817A and the underlying bright 'kilonova' provides strong evidence favouring compact binary mergers as the progenitors for at least some of these events (Abbott et al., 2017b; Abbott et al., 2017c, and references therein).

The T_{90} duration of GW170817 connected sGRB 170817A was 0.5$\pm$0.1 s (70-300 keV) having multiple emission episodes and had a relatively soft spectrum with $E_{peak} = 65^{+35}_{-14}$ keV (Goldstein et al., 2017; Pozanenko et al., 2018). The burst was also detected by SPI-ACS on-board *INTEGRAL* (Savchenko et al., 2017) and morphology of the γ-ray light-curve is similar to that seen in the case of presently discussed sGRB 140930B, i.e. having multiple episodes of emissions and belong to a pattern-II class of bursts (Lu et al., 2017), suggesting a diverse set of progenitors and central engines (Dichiara et al., 2013). sGRB 170817A turned out to be the weakest detected sGRB having a soft spectrum with a thermal tail and was under-luminous by a factor of $\sim$ 1000 in comparison to known sGRBs. So, observed properties like a harder pulse with multiple episodes of emissions and a softer tail emission in the spectra have attracted significant attention in an effort to understand the nature of the event in terms of various physical models (Granot, Guetta, and Gill, 2017; Granot et al., 2018; Gottlieb, Nakar, and Piran, 2018; Pozanenko et al., 2018; Zhang et al., 2018a). Except for

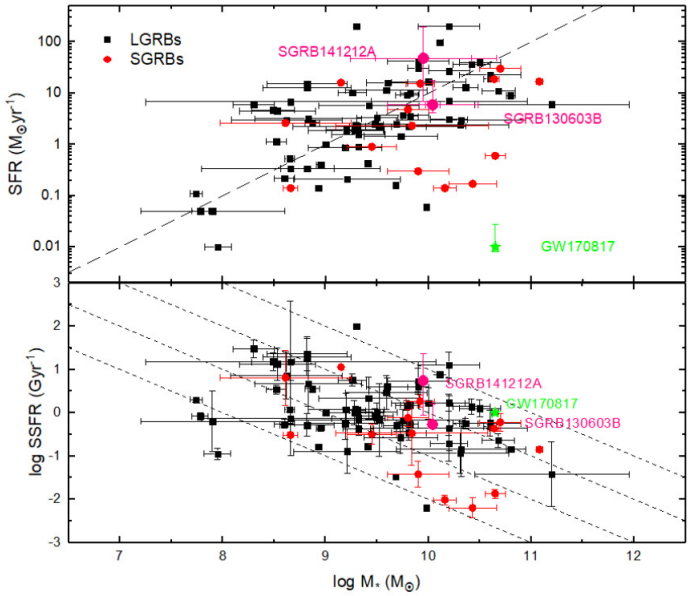

FIGURE 4.22: Plot of star formation rate versus stellar mass (top panel) and specific star formation rate versus stellar mass (bottom panel) for the known set of host galaxies of lGRBs and sGRBs. The dashed line marks a constant SFR of 1 Gyr^{-1} (top panel). The dashed lines mark the constant specific SFR of 0.1, 1, 10 and 100 Gyr^{-1} from left to right (bottom panel). The modelled values of star formation rates and mass of the hosts of sGRB 130603B and sGRB 141212A are plotted as pink circles. Corresponding values for the GW170817 are plotted as the green star.

resemblance with the duration T_{90}, all other observed prompt emission properties of the sGRB 170817A like the morphology of the γ-ray light-curve, E_{peak}, E_{iso} etc. were outliers with the known set of sGRBs including those discussed above as described in Figure 4.9.

sGRB 170817A counterparts at UV-optical-NIR frequencies are distinct to those expected for GRB afterglows (Piran, 1999) and predominantly follow physical mechanisms suggested for underlying 'kilonova' emission (Pian et al., 2017; Tanvir et al., 2017; Troja et al., 2017b) consistent with a compact binary merger origin for this event. However, contrary to red 'Kilonova' associated with the sGRB 130603B, sGRB 170817A UV-optical-NIR emission was explained well in terms of r-processed three-component sub-relativistic accretion disk powered

'kilonova' model (Villar et al., 2017b; Villar et al., 2017a). In Figure 4.4, the H-band light curve of the GW170817 counterpart (redshifted at z = 0.36) is compared along with 'kilonova' detection and models for the sGRB 130603B (Tanvir et al., 2013; Tanaka et al., 2014). The H-band redshifted light curve of the GW170817 counterpart is fainter in comparison to the corresponding *HST* detection of the 'kilonova' associated with the sGRB 130603B and exhibits distinct nature of the overall temporal decay.

Early time non-detection by the *Swift*-XRT until 9 d post-burst for sGRB 170817A compared to other known cases of X-ray detected sGRBs (Fong et al., 2017), places a constraint on the underlying emission mechanisms and supports a non-afterglow origin for the observed emission at lower frequencies. Using a deeper data-set of other bursts Gompertz et al., (2018) have concluded that not all sGRBs are associated with 'kilonovae' and share a diverse range of observed brightness. No detection of GW170817 like 'kilonova' for a good number of well-studied sGRBs to a deeper limit also indicates a diverse set of progenitors for some of the bursts (Gompertz et al., 2018; Rossi et al., 2020).

GW170817/sGRB 170817A was also observed using the 10.4 m GTC in i-band starting around 05:47:40 UT on 2018 Jan. 19 for a total exposure time of one hour (120s$\times$30). The images were stacked and processed as per standard techniques. A 3-σ upper limit of the stacked image is $i \sim 25$ mag whereas at the location of the optical transient (see Figure 4.21 and Table 4.6), a rather shallow value of $i \sim 23.5$ mag was estimated due to contamination of the host. The second epoch of the 10.4 m GTC observations of the host galaxy NGC 4993 were taken on 2019 Feb. 6 around 5:10:00 UT in i-band (120s$\times$30), and a deeper limit of $i \sim 24$ mag was estimated at the location of the GW170817 after image subtraction. This observed limiting magnitude ($\sim$ 154.7 d post-burst) at the location of the optical transient is in agreement with the extrapolated at contemporaneous epochs by Margutti et al., (2018) and thus supports a non-thermal origin of the emission at the epoch of our observations. On the other hand, detections of the sGRB 170817A/GW170817/AT 2017gfo/SSS17a at X-ray (Troja et al., 2017b) and VLA radio frequencies (Alexander et al., 2017) $\sim$9 d to 160 d post-burst exhibit rising light curves at both X-ray and radio frequencies and are broadly consistent with non-thermal collimated emission viewed off-axis or structured outflow (Granot et al., 2002; Granot, Guetta, and Gill, 2017; Evans

et al., 2017; Fong et al., 2017; Haggard et al., 2017; Hallinan et al., 2017; Margutti et al., 2017; Smartt et al., 2017; Troja et al., 2017b; Lazzati et al., 2018). However, Xie, Zrake, and MacFadyen, (2018) and Lyman et al., (2018) have found that the late time multi-band data of sGRB 170817A is well explained by both narrow and wide engine mild-relativistic models, though, early time non-detection at X-ray frequencies disfavours the wide engine model. So, it is clear that none of the models have been able to reproduce the full set of multi-band data for this nearby event.

The host galaxy SED modelling of sGRB 130603B and sGRB 141212A from the present sample of bursts indicate that their respective hosts are young and bluer with moderate values of star formation activity. However, in the case of sGRB 170817A, the host galaxy NGC 4993 is an old elliptical galaxy with little star formation activity and the projected offset of the burst location is rather closer to what has been seen in other cases of sGRBs (Fong et al., 2017; Levan et al., 2017). Figure 4.22 shows the distribution of star formation rates versus stellar mass (top panel) and specific star formation rates versus stellar mass (bottom panel) for the known set of host galaxies of lGRBs and sGRBs (Savaglio, Glazebrook, and Le Borgne, 2009) and GW170817 (Blanchard et al., 2017). In Figure 4.22, corresponding values for the sGRB 170817A/GW170817 clearly indicate that the star formation rate for sGRB 170817A/GW170817 host galaxy is well below from those seen in the case of the normal population of GRBs. Overall properties of the GRB 170817A/GW170817 and their comparison with other sGRBs indicate that we need multi-wavelength observations of a significantly larger number of nearby events to explore the full diversity of 'kilonovae' and their association with sGRBs.

Conclusions

In this chapter, we have analyzed and reported prompt emission data of nine short bursts, including sGRB 130603B as observed by *Swift*, *INTEGRAL* and *Fermi* satellites. The SPI-ACS *INTEGRAL* prompt emission observations of sGRB 130603B, sGRB 140930B, sGRB 141212A and sGRB 151228A in the energy range 0.1-10 MeV do not show any EE which is in agreement with those seen in the case of *Swift* observations with the exception of sGRB 121226A which shown

TABLE 4.6: Summary of the optical photometric observations of the afterglows of the eight sGRBs (2012-2015) and their host galaxies (h) using ground-based optical telescopes. Observations of GW170817 using the 10.4 m GTC are also appended to this table. The values of the magnitudes are in the AB system (limiting magnitudes are 3σ) and no extinction corrections have been applied.

t-t0 mid(d)	exp(s)	Afterglow/ Host galaxy	pass-band	Telescopes
		sGRB 121226A		
0.0042	5×19	>19	clear	0.6 m BOOTES-4 MET
0.0833	300×4	>18.8	I_c	1.04 m ST ARIES
0.0833	300×6	>19.5	R_c	1.04 m ST ARIES
0.432	75×2	23.65±0.37	z	10.4 m GTC
0.441	85×5	24.03±0.32	i	10.4 m GTC
0.451	70×8	24.30±0.30	r	10.4 m GTC
53.25	50×31	>23.79	z	10.4 m GTC
53.27	70×12	>24.47	i	10.4 m GTC
		sGRB 131224A		
1.111	30×1	>18.3	r	10.4 m GTC
1.113	60×3	>19.5	i	10.4 m GTC
1.116	75×3	>24.3	z	10.4 m GTC
7.099	5×4+10×1	>23.6	i	10.4 m GTC
7.105	20×4+10×1	>22.8	z	10.4 m GTC
		sGRB 140606A		
0.3315	3600	>21.7	clear	Abastumani AS-32
0.4292	4×30+3×120	>26.0	R_c	6.0 m BTA
0.3857	120+30	>24.2	V	6.0 m BTA
0.3893	120	>24.4	B	6.0 m BTA
271.642	60×5	>25.36	r	10.4 m GTC
		sGRB 140622A		
0.0687	4320	>23.64	r	1.5 m RATIR
0.0687	4320	>23.49	i	1.5 m RATIR
0.0687	1836	>19.41	Z	1.5 m RATIR
0.0687	1836	>18.73	Y	1.5 m RATIR
0.4752	4800	>22.5	R	TShAO Ziess-1000
0.781	100×6+5×2	>25.8	r	10.4 m GTC
		sGRB 140903A		
0.1406	100	>18.6	clear	ISON-Kislovodsk SANTEL-400A
1.0648	720	>22.0	R	Maidanak AZT-22
3.0072	900	>22.0	R	Maidanak AZT-22
4.0090	900	>22.0	R	Maidanak AZT-22
10.0500	720	>22.0	R	Maidanak AZT-22
		sGRB 140930B		
0.0291	3600	>20.4	clear	ISON-Kislovodsk, SANTEL-400A
0.0145	1200	>19.5	clear	ISON-Kislovodsk, SANTEL-400A
0.0309	2000	>19.6	clear	ISON-Krasnodar, Astrosib
0.0249	415	>16.1	clear	UAFO ORI-65
0.133	300×5	22.65±0.09	r	WHT 4.2 m/ACAM
0.153	300×5	22.61±0.06	i	WHT 4.2 m/ACAM
0.172	400×2	23.17±0.12	g	WHT 4.2 m/ACAM
0.677	150×9	24.01±0.04	r	Gemini North/GMOS-N
1.656	150×9	25.11±0.11	r	Gemini North/GMOS-N
3.141	60×13	>24.5	r	10.4 m GTC
1535.5	90×34	>24.75	r	10.4 m GTC
		sGRB 141212A		
0.0189	60×10	>22.2	R	Mondy AZT33-IK
0.0363	60×60	22.73±0.26 (h)	R	Mondy AZT33-IK
0.0783	120×30	22.75±0.28 (h)	R	Mondy AZT33-IK
0.0573	60×60+120×30	22.71±0.19 (h)	R	Mondy AZT33-IK
0.0242	60×5	>18.5	clear	Khureltogot ORI-40
0.0641	60×74	>19.9	clear	Khureltogot ORI-40
0.6814	180×5	22.13±0.04 (h)	i	Gemini North/GMOS-N
1.1563	300×13	22.63±0.18 (h)	R	TShAO Ziess-1000
1.7461	180×5	22.23±0.04 (h)	i	Gemini North/GMOS-N
2.0544	120×57	22.76±0.33 (h)	R	Mondy AZT33-IK
6.0676	120×85	22.86±0.16 (h)	R	Mondy AZT33-IK
427.375	5×3+120×11	23.86±0.08 (h)	g	10.4 m GTC
427.385	120×7	22.80±0.06 (h)	r	10.4 m GTC
427.403	90×6	22.32± 0.05 (h)	i	10.4 m GTC
		sGRB 151228A		
0.0011	60×3+20×2	>17.5	R	0.6 m T60
1.1429	5×60	>23.7	i	10.4 m GTC
69.0036	7×75	>24.8	i	10.4 m GTC
		sGRB 170817A/GW170817		
154.7	120×30	>24.0	i	10.4 m GTC
536.8	120×10	>24.0	i	10.4 m GTC

TABLE 4.7: Summary of the prompt emission and afterglow properties of the 9 sGRBs discussed in this work. The symbols used in the table have their usual meanings as discussed above.

sGRB	Redshift	T_{90}	E_{iso} [a]	E_{peak}	Early first observation				Afterglow detection	Host galaxy	Comments
		sec	erg	keV	t-t0,mid(s)	Magnitude	Pass-band	Telescope			
121226A	–	1.00 ± 0.20^{a}	–	–	93	>17.5	R	Zadko[a]	+	>24.6(r)	EE
130603B	0.3564 ± 0.0002^{a}	0.18 ± 0.02^{b}	$(2.1\pm0.2)\times10^{51\,b}$	660 ± 100^{a}	137	>19.6	$white$	UVOT[b]	+	$22.13\pm0.05(r)$	KN
131224A	–	0.8^{c}	–	–	44	>15.5	$white$	MASTER II[c]	–	>23.6(i)	not a GRB
140606A	1.96 ± 0.1	0.34 ± 0.09^{d}	4.9×10^{50}	$185.13^{+126\,d}_{-28}$	143	>21.1	$white$	UVOT[d]	–	>25.3(r)	
140622A	0.959^{b}	0.13 ± 0.04^{e}	$(1.0\pm0.2)\times10^{50}$	44 ± 8^{b}	106	>17.5	R	TAROT[e]	–	>25.8(r)	
140903A	0.351^{c}	0.30 ± 0.03^{f}	$(6.0\pm0.3)\times10^{49\,c}$	–	152	>20.0	$white$	UVOT[f]	+	$20.58\pm0.09(r')^{a}$	
140930B	–	0.84 ± 0.12^{g}	–	$1302^{+2009\,c}_{-495}$	44	>16.0	$white$	MASTER II[g]	+	> 25.1(r)	
141212A	0.596^{d}	0.30 ± 0.08^{h}	$(6.7\pm1.1)\times10^{49}$	–	51	>16.8	$white$	MASTER II[h]	–	$22.80\pm0.06(r)$	
151228A	–	0.27 ± 0.01^{i}	–	$261.18^{+164.94\,d}_{-58.28}$	95	>17.5	R	T60	–	>24.8(i)	

References

Redshift: [a] *Xu et al. (2012),* [b] *Hartoog et al. (2014),* [c] *Cucchiara et al. (2014),* [d] *Chornock et al. (2014)*

T_{90}: [a] *Baumgartner et al. (2012),* [b] *Barthelmy et al. (2013),* [c] *Mereghetti et al. (2013),* [d] *Cummings et al. (2014),* [e] *Sakamoto et al. (2014)*

E_{iso}: [a] *for GRB 130603B and GRB 140622A in the range 1-10000 keV, for other GRBs in the range 15-150 keV,* [b] *Frederiks et al. (2013),* [c] *Troja et al. (2016)*
[f] *Palmer et al. (2014),* [g] *Baumgartner et al. (2014),* [h] *Palmer et al. (2014b),* [i] *Barthelmy et al. (2015)*

E_{peak}: [a] *Golenetskii et al. (2013),* [b] *Sakamoto et al. (2014),* [c] *Golenetskii et al. (2014),* [d] *Present analysis*

Early first observation: [a] *Klotz et al. (2012),* [b] *Melandri et al. (2013),* [c] *Gorbovskoy et al. (2013),* [d] *Marshall and Stroh (2014),* [e] *Klotz et al. (2014)*
[f] *Breeveld and Cummings (2014),* [g] *Gorbovskoy et al. (2014),* [h] *Gres et al. (2014)*

Host galaxy: [a] *Troja et al. (2016)*

the EE component. Using *Fermi*-GBM data, E_{peak} values were determined for sGRB 140606A, sGRB 151228A and Amati diagram was constructed to establish the nature of the five sGRBs from the present sample. Also, analysis of the *INTEGRAL*/JEM-X observations indicates that sGRB 131224A may not be of a cosmological origin as discussed above.

Multi-wavelength afterglow observations for sGRB 130603B include the earliest ground-based optical detection and millimetre observations complementary to those published in the literature. Our r and i-bands data together with those previously published have helped to produce a well-sampled r band light curve, made it possible to estimate the value of pre-jet break temporal index $\alpha_1 = 0.81 \pm 0.14$ robustly. The derived values of pre- and post-jet break temporal flux decay indices along with the X-ray and optical-NIR spectral indices support the *ISM* afterglow model with cooling frequency ν_c between optical and X-ray frequencies. Derived values of the jet-break time, electron energy index were used to model the afterglow data of sGRB 130603B using numerical simulation-based Monte Carlo model as described in Zhang et al., (2015). Except at very early times ($<$ 1000s) and very late time ($>$ 100000s), largely the multi-band data of sGRB 130603B are explained in terms of the forward shock fireball model. The derived values of microphysical parameters of the burst are better constrained than those reported in Fong et al., (2014). The observed mm and cm-wavelength upper limits for sGRB 130603B are also consistent with forward-shock model predictions.

Using the reported values of photometric upper limits in bluer bands (i.e. *Swift*-UVOT u and Gemini-N g' bands at $\sim$ 1.5 d after the burst), we attempted to constrain the possible blue-component of 'kilonova' emission in case of sGRB 130603B. Accordingly, the values of the ejected mass were calculated as proposed by Kasen, Fernández, and Metzger, (2015) and Metzger et al., (2010) for the possible blue emission. However, the shallower observed limits at early epochs in *Swift*-UVOT u and Gemini-N g' bands do not provide any meaningful constraint for the blue component of 'kilonova' emission for sGRB 130603B but indicate that some of the sGRBs may not have the predicted blue-component. Deep afterglow observations of a further 8 sGRBs using the 10.4 m GTC and other telescopes reveal the nature of the decay and the complex environments of some of the sGRBs not well-studied so far. In the case of sGRB 140930B, our early to late time afterglow observations using the 4.2 m WHT and the 8.0 m

Gemini-N along with those observed by *Swift*-XRT are able to constrain the decaying nature of the burst and the late time GTC observations places a deeper upper limit of $r \sim 24.8$mag for any possible host galaxy. Whereas, in the case of sGRB 140622A, our optical observations using the 10.4 m GTC puts a deep limit of ∼25.6 mag for any afterglow or a host galaxy within the XRT error-box. These deep observations by the 10.4 m GTC also indicate that sGRB 140622A could belong to the category of known host-less bursts.

Observed limiting flux values at mm and cm-wavelengths for a set of 9 sGRBs using PdBI and their comparison with published light-curve of lGRB 130427A at 3-mm place constraints on the possible underlying physical mechanisms and demand for much deeper observations at these wavelengths.

Deeper optical-NIR follow-up observations of 4 *Swift*-XRT localized bursts sGRB 121226A, sGRB 140903A, sGRB 140930B and sGRB 141212A using 10.4 m GTC, Gemini-N 8.0 m and Maidanak AZT-22 1.5m up to a few days post-burst constrain for any 'kilonova' such as the one associated with the GW170817. Using prescription given in Rossi et al., (2020), a comparison of the rest-frame luminosity of 'kilonova' associated with GW170817 indicates that for sGRB 141212A, any such event would have been detected at the epoch of our Gemini-N 8.0 m observations. However, in cases of sGRB 121226A, sGRB 130603B, sGRB 140903A and sGRB 140930B, the derived luminosity values were found to be dominated by the afterglow, i.e. brighter than the 'kilonova' associated with the GW170817.

Upper limit derived using the late time (154.7 d post-burst) 10.4 m GTC observations ($i \sim 23.5$ mag) of the GW170817 is in agreement with the non-thermal origin of the emission as seen at other wavelengths. Comparison of prompt emission and properties of the host galaxy of the GW170817 discussed in the present work point towards diverse properties of associated 'kilonovae' and in turn points towards possibly diverse classes of compact binary mergers producing normal sGRBs and those with associated 'kilonovae'.

Optical-NIR photometry of the host galaxy of sGRB 130603B was independently modelled using *LePHARE* software. The modelling results support the Milky-way Galaxy model with a moderate value of the star formation activity in the host galaxy. We also conclude that the SFR and mass of the host galaxy are typical of those seen in the case of other GRBs. The host galaxy modelling of the sGRB 141212A indicates that the host is a MW type of Sc galaxy with a

moderate value of star formation.

Our observations and analysis of the 8 sGRBs and sGRB 170817A/GW170817 (Table 4.6 and 4.7) demand for systematically deeper and more prompt multi-wavelength observations of many of these events to detect the afterglow or to constrain the possible associated 'kilonovae', host galaxies and their properties in more detail. In the future, $JWST$ and other upcoming ground-based optical-NIR facilities like TMT and E-ELT will facilitate the study of sGRBs and GW events with unprecedented sensitivity.

Chapter 5

Conclusions and prospects for the future

This PhD thesis has focused on several typical gamma-ray burst events, belonging to both long- and short-duration categories, including multi-wavelength data gathered by our observational programs, complemented by open data available as well as by the published literature. These multi-wavelength observations include data gathered by space missions such as *Swift*, *Fermi*, *INTEGRAL* and *Spitzer*, and ground-based facilities ranging from moderate- to large-size instruments that include telescopes networks (MASTER, BOOTES) and single telescopes (1.5 m OSN, 2.2 m CAHA, 6.0 m BTA and 10.4 m GTC in the NIR/Optical) and the 30 m IRAM antenna and NOEMA (in radio) which altogether cover a significant part of the electromagnetic spectrum (radio, infrared, optical, X-rays and γ-rays). Combined with information from other astrophysical multi-messenger detectors, such as the ones detecting gravitational waves (LIGO, Virgo), GRB events will provide clues to better understand the underlying physics (jet structure, origin of the very high-energy photons, binary mergers, etc.) and their host galaxies (metallicities, star-formation rates, etc.)

Regarding the chapter devoted to GRB 140629A, our dataset spanned from several seconds up to 4 days after the trigger. The spectroscopy confirmed this event being at a redshift z = 2.276. From the X-rays and optical bands light curves, an achromatic jet break was found at $\sim$ 0.4 d. This scene supported a narrow uniform jet with an opening angle of 6.7$\circ$ in a dense environment following the numerical simulations based on multi-wavelength data. The afterglow temporal and spectral analysis also supported the scenario of a blast wave jet with a long-lasting central engine expanding into a uniform medium

in the slow cooling regime. After correcting for the jet effect, the energy released by this burst was consistent with the empirical correlations of both Amati and Ghirlanda. The jet break was a clear signature of the collimated outflow following the prompt emission, which helped to constrain the opening angle and provided the real estimation of the released energy following the GRB. As a geometric effect, due to the interaction between the burst and the circumburst medium, an achromatic, steepening temporal break is expected to show up, which indeed was the case for GRB 140629A. There are still a few GRBs that did not show this behaviour in the corresponding afterglow light curves or display chromatic breaks between different bands. The absence of achromatic breaks poses new challenges for the jet scenario in GRBs, especially for the short-duration GRBs population. Hence, taking late-time observations in different bands for better studying GRB afterglows is essential to clarify this problem. Another problem hinted in this particular burst (GRB 140629A) was regarding the observed polarization, which showed GRB 140629A as a weakly polarized event, according to the MASTER observation. Recently, constraints on the magnetic field properties of a supermassive black hole such as the one in the centre of the M87 giant galaxy, as observed by the Event Horizon Telescope (EHT), has provided insight into the black hole magnetic fields nature (Event Horizon Telescope Collaboration et al., 2021). In the much smaller BHs formed during the GRB events, values of polarization are also important to be measured. In the case of GRB 140629A, it is a weakly polarized event while an average $\sim$ 10 per cent polarization, either linear or circular, was measured during the afterglow phase in several cases (Gorbovskoy et al., 2016). In general, as the prompt emission is only lasting tens of seconds, it is difficult to measure optical polarization using ground-based follow-up telescopes, with the exception of fast-reacting robotic telescopes responding to incoming long-duration GRB, as it was the case for GRB 160625B (Troja et al., 2017a). X-ray polarization can be detected from space-borne instruments such as Polar attached to the *Tiangong-2* station, an instrument well suited for detecting the prompt emission, which shows low or zero polarization result in the time-integrated analysis for some events (albeit this could be an artificial result of summing over the changing polarization signal and the true moderate polarization be washed out)(Kole et al., 2020). Hence the combination of data provided by ground-based fast reaction telescopes and next-generation missions, such as Polar-2 and the *LargE*

Area burst Polarimeter (LEAP, proposed to be deployed on the *ISS* in 2025), is expected to provide more precise observation on GRBs to find out the similarities between massive BHs and stellar BHs, with the later being proposed as the central engine for most long-duration GRBs. It can also be used to distinguish the models dealing with the presence of the magnetic field, such as the Internal-Collision-Induced Magnetic Reconnection and Turbulence (ICMART) model, which predicts a decaying linear polarization degree during the prompt emission whose maximum value can reach as high as 60 per cent at early times (Zhang and Yan, 2011; Kole et al., 2020).

Regarding the chapter devoted to GRB 190829A, this is one of the very few events in which released photons at TeV energies were detected. In this case, it was H.E.S.S. the ground-based facility which detected the high-energy source dubbed TeV J0258-089, for which we used the 10.4m GTC to determine its redshift ($z = 0.0785$), making of it one of the nearest GRBs ever detected. Its prompt emission consisted of two episodes separated by a $\sim$ 40 s gap and its spectral evolution at late times exceeded the synchrotron limit, posing a challenge to the proposed progenitor models. Using the 10.4 m GTC to monitor the GRB 190829A light curve, we found a late-time bump in the i-band light curve peaking at $\sim$ 20 d post burst. The observed spectral evolution from 0.32 to 4.09 d after the trigger was a signature of the transition from the expected afterglow light curve to the emergence of an underlying supernova. At $\sim$ 4.09 d, the observed spectrum closely resembled that of GRB 980425/SN 1998bw. Besides, the associated SN (dubbed SN 2019oyw) light curve could be well described by the radioactive decay of Ni, which is typically seen in SNe Ic-BL (showing broad lines). Regarding the comparison with other afterglow + SN light curves, the late time bump and a spectral softening during the 'SN phase' appeared in the X-ray data for both in GRB 190829A and GRB 180728A, the latter being an event which shared a similar prompt behaviour. For the time being, there are 6 GRBs for which VHE emission has been recorded: GRB 190114C, GRB 180720B, GRB 201015A, GRB 201216C, GRB 160821B and GRB 190829A (MAGIC Collaboration et al., 2019b; Abdalla et al., 2019; MAGIC Collaboration et al., 2019a; de Naurois and H. E. S. S. Collaboration, 2019; Acciari et al., 2021; Blanch et al., 2020a; Blanch et al., 2020b). In the long-duration burst GRB 201015A, the SN association and a late-time X-ray bump were also reported (Gompertz et al., 2020) therefore increasing the sample of such events displaying a VHE

detection, a SN association and a late X-ray bump. Regarding the late X-ray bump only, a survey in the current GRB/SN databases should be done in order to explore the connection to the optical supernova bump, which could be related to the GRB origin. Although other VHE GRBs did not show underlying SNe, a much larger sample is needed in the future in order to draw further conclusions.

In the chapter devoted to short-duration GRBs, a multi-wavelength analysis is employed for the kilonova related event, GRB 130603B. We also studied other eight short-duration bursts observed during 2012-2015. The data from *INTEGRAL*, *Swift* and *Fermi* were used to search for the precursor and extended emission components in the prompt emission phase, but only GRB 121226A showed extended emission activity as seen by *Swift*-BAT although at a bit lower significance in the *INTEGRAL*/SPI-ACS data. All the events had a negligible spectral lag, as expected from short-duration events. The duration, T_{90}, which is essential for the bimodal classification of GRBs (albeit there are some exceptions, such as GRB 060614 and GRB 060124 (Della Valle et al., 2006a; Romano et al., 2006).) was found to be energy-dependent. There are more scientific satellites that have been designed for GRB studies, such as *AstroSat*, *HXMT* and *GECAM*, so a detailed time-domain analysis based on the different energy bins from those instruments or a higher time resolution facility, such as ASIM aboard the *ISS*, can shed light in some GRB fields, in particular regarding internal energy dissipation process.

The GRB 130603B optical afterglow observations collected as part of our ToO program, were used together with other data published elsewhere in order to build a complementary small short-duration GRBs database covering from radio and optical to γ-rays. For GRB 130603B, the temporal and spectral data supported the existence of a jet break at $\sim$ 0.4 d post-trigger, and the spectral index difference between optical-NIR and X-rays was found to be consistent with the value predicted in the slow-cooling synchrotron spectrum, where the optical and X-ray frequencies lie in two different spectral regimes. The broadband data modelling provided a better constraint on microphysical parameters with this particular event being better explained by the forward shock fireball model and a jet with a half-opening angle of $\sim$3.2 deg, which implies the released energy of $\sim 1.4 \times 10^{49}$ erg indicating a high radiation efficiency of $\sim$ 23 per cent. Our photometric upper limits in bluer bands and late-time deeper

optical-NIR observation were used to constrain the 'kilonova'-related component in GRB 130603B (and in the short-duration GRB sample). However, the observed limiting magnitudes in $u-$, $g-$bands were not deep enough to set any constrain on the blue emission from the underlying 'kilonova'. Only GRB 141212A has a deeper limiting magnitude than the expected one for GW 170817 in rest-frame at contemporaneous epochs (Rossi et al., 2020), which indicates their detectability if this case would be similar. However, the derived luminosity values in other bursts are higher than the expected 'kilonova' component associated with GW 170817, which are still afterglow dominated. Therefore, systematically deeper and more prompt multi-wavelength observations of the short-duration GRB sample in the future will be essential in order to detect the afterglow and constrain the possible associated 'kilonova' component, which should be one of the topics of my future research.

Finally, I want to emphasize the powerfulness of The Burst Optical Observer and Transient Exploring System (BOOTES) network (Castro-Tirado et al., 1999a) as a worldwide robotic telescope network managed by the group I joined at the Instituto de Astrofísica de Andalucía (IAA-CSIC). It consists of 5 stations in Spain, New Zealand, China and México and another two (in South Africa and Chile) which shall become operational in 2022. Each station is equipped with a 0.6 m Ritchey-Chretien telescope with an EMCCD attached to it and an all-sky camera (dubbed Compact All-Sky Automated Network Developed for Research in Astronomy, CASANDRA). The main goal is the continuous monitoring from both hemispheres for astronomical transients, such as GRBs, Fast Radio Bursts (FRBs), Tidal Disruption Event (TDEs), neutrino alerts, etc. And since GW detectors such as LIGO and Virgo became operational in 2015, we also started to observe the sky and followed up any incoming alert in order to find the electromagnetic counterpart at optical wavelength. Nowadays, LIGO and Virgo have already conducted three scientific observing runs. These are O1 (2015 Sep. 12 to 2016 Jan. 19), O2 (2016 Nov. 30 to 2017 Aug. 25) and O3 (2019 Apr. 1 to 2020 Mar. 27), where the time gaps in between were devoted for upgrading and commissioning the improved instrumentation. During O1, the BOOTES-3 all-sky camera gathered the only existing image simultaneously to the first direct detection of astrophysical GW signal, GW150914 (Abbott et al., 2016b), although no optical counterpart was found down to a limiting magnitude of 5 (Abbott et al., 2016a). During the O2 period, the BOOTES-5 60cm

telescope imaged 15 galaxies which were selected by the cross-correlation of the GLADE catalogue of nearby galaxies and the GW170817 localization probability map as given on Aug 18.21UT (Abbott et al., 2017c). The optical counterpart (SSS17a) was found by some other team in the outskirts of its host galaxy, NGC 4993, which we also imaged, finding it with a magnitude r=18.20±0.45 in the stacked image, which is consistent with other contemporaneous measurements (Zhang et al., 2018a). This was the only detection with a Spanish facility (BOOTES-5) of the first electromagnetic counterpart even found. And during the O3 run, 72 GW triggers were issued, ending up with 54 confirmed (i.e. real) events. The BOOTES network has responded to all incoming alerts, with more than 80 per cent of those events being followed up either by tiled observations (to cover the larger error areas with a mosaic of images) or imaging the "probably-related galaxies" in order to search for transient blue objects (such as SSS17a) in the galaxy outskirts. Although no electromagnetic counterparts were found during the entire O3 period, the limits imposed were important. Thus, for the time being, there is still only one case for which an EM counterpart was found, GRB 170817 (Abbott et al., 2017b). With the improvement on the instruments sensitivity and the future GW detectors, such as the India GW detector, the future error regions to be determined during the O4 period (starting in mid-2022) more accurate positions will become available, and we expect some of them to become within reach of the BOOTES network. One important remark that deserves further attention is the case of GRB 160821B, the only short-duration burst with VHE detection (Acciari et al., 2021), which also showed a related kilonova (Troja et al., 2019) although no GW was reported (due to the lack of operational GW detectors at the precise GRB time). In the forthcoming O4 run (expected by mid-2022), we indeed expect more short-duration GRBs to be related to GW alerts, as it was the case for GRB 170817A. I hope to continue chasing them with the complete BOOTES network by then.

Bibliography

Abbott, B. P. et al. (2016a). "Localization and Broadband Follow-up of the Gravitational-wave Transient GW150914". In: *Astrophysical Journal Letters* 826.1, L13, p. L13.

Abbott, B. P. et al. (2016b). "Observation of Gravitational Waves from a Binary Black Hole Merger". In: *Physical Review Letters* 116.6, 061102, p. 061102.

Abbott, B. P. et al. (2017a). "Gravitational Waves and Gamma-Rays from a Binary Neutron Star Merger: GW170817 and GRB 170817A". In: *Astrophysical Journal Letters* 848.2, L13, p. L13.

Abbott, B. P. et al. (2017b). "GW170817: Observation of Gravitational Waves from a Binary Neutron Star Inspiral". In: *Physical Review Letters* 119.16, 161101, p. 161101.

Abbott, B. P. et al. (2017c). "Multi-messenger Observations of a Binary Neutron Star Merger". In: *Astrophysical Journal Letters* 848.2, L12, p. L12.

Abdalla, H. et al. (2019). "A very-high-energy component deep in the γ-ray burst afterglow". In: *Nature* 575.7783, pp. 464–467.

Abdo, A. A. et al. (2009a). "Fermi Observations of GRB 090902B: A Distinct Spectral Component in the Prompt and Delayed Emission". In: *Astrophysical Journal Letters* 706.1, pp. L138–L144.

Abdo, A. A. et al. (2009b). "Fermi Observations of High-Energy Gamma-Ray Emission from GRB 080916C". In: *Science* 323.5922, p. 1688.

Acciari, V. A. et al. (2021). "MAGIC Observations of the Nearby Short Gamma-Ray Burst GRB 160821B". In: *Astrophysical Journal* 908.1, 90, p. 90.

Ackermann, M. et al. (2010). "Fermi Observations of GRB 090510: A Short-Hard Gamma-ray Burst with an Additional, Hard Power-law Component from 10 keV TO GeV Energies". In: *Astrophysical Journal* 716.2, pp. 1178–1190.

Ackermann, M. et al. (2011). "Detection of a Spectral Break in the Extra Hard Component of GRB 090926A". In: *Astrophysical Journal* 729.2, 114, p. 114.

Ackermann, M. et al. (2014). "Fermi-LAT Observations of the Gamma-Ray Burst GRB 130427A". In: *Science* 343.6166, pp. 42–47.

Afanasiev, V. L. and A. V. Moiseev (2005). "The SCORPIO Universal Focal Reducer of the 6-m Telescope". In: *Astronomy Letters* 31.3, pp. 194–204.

Ahn, Seh-Won et al. (2005). "Fabrication of a 50 nm half-pitch wire grid polarizer using nanoimprint lithography". In: *Nanotechnology* 16.9, p. 1874.

Akaike, H. (1974). "A New Look at the Statistical Model Identification". In: *IEEE Transactions on Automatic Control* 19, pp. 716–723.

Akerlof, Carl et al. (2000). "Prompt Optical Observations of Gamma-Ray Bursts". In: *Astrophysical Journal Letters* 532.1, pp. L25–L28.

Alam, Shadab et al. (2015). "The Eleventh and Twelfth Data Releases of the Sloan Digital Sky Survey: Final Data from SDSS-III". In: *Astrophysical Journal Supplement* 219.1, 12, p. 12.

Alard, C. and Robert H. Lupton (1998). "A Method for Optimal Image Subtraction". In: *Astrophysical Journal* 503.1, pp. 325–331.

Albert, A. et al. (2017). "Search for High-energy Neutrinos from Binary Neutron Star Merger GW170817 with ANTARES, IceCube, and the Pierre Auger Observatory". In: *Astrophysical Journal Letters* 850.2, L35, p. L35.

Alexander, K. D. et al. (2017). "The Electromagnetic Counterpart of the Binary Neutron Star Merger LIGO/Virgo GW170817. VI. Radio Constraints on a Relativistic Jet and Predictions for Late-time Emission from the Kilonova Ejecta". In: *Astrophysical Journal Letters* 848.2, L21, p. L21.

Amati, L., F. Frontera, and C. Guidorzi (2009). "Extremely energetic Fermi gamma-ray bursts obey spectral energy correlations". In: *Astronomy and Astrophysics* 508.1, pp. 173–180.

Amati, L. et al. (2002). "Intrinsic spectra and energetics of BeppoSAX Gamma-Ray Bursts with known redshifts". In: *Astronomy and Astrophysics* 390, pp. 81–89.

Amati, L. et al. (2018). "The THESEUS space mission concept: science case, design and expected performances". In: *Advances in Space Research* 62.1, pp. 191–244.

Amati, Lorenzo (2006). "The $E_{p,i}$-E_{iso} correlation in gamma-ray bursts: updated observational status, re-analysis and main implications". In: *Monthly Notices of the RAS* 372.1, pp. 233–245.

Amati, Lorenzo and Massimo Della Valle (2013). "Measuring Cosmological Parameters with Gamma Ray Bursts". In: *International Journal of Modern Physics D* 22.14, 1330028, p. 1330028.

Amati, Lorenzo et al. (2008). "Measuring the cosmological parameters with the $E_{p,i}$-E_{iso} correlation of gamma-ray bursts". In: *Monthly Notices of the RAS* 391.2, pp. 577–584.

Anderson, G. E. et al. (2014). "Probing the bright radio flare and afterglow of GRB 130427A with the Arcminute Microkelvin Imager". In: *Monthly Notices of the RAS* 440.3, pp. 2059–2065.

Aptekar, R. L. et al. (1995). "Konus-W Gamma-Ray Burst Experiment for the GGS Wind Spacecraft". In: *Space Science Reviews* 71.1-4, pp. 265–272.

Arnaud, K. A. (1996). "XSPEC: The First Ten Years". In: *Astronomical Data Analysis Software and Systems V*. Ed. by George H. Jacoby and Jeannette Barnes. Vol. 101. Astronomical Society of the Pacific Conference Series, p. 17.

Arnouts, S. et al. (1999). "Measuring and modelling the redshift evolution of clustering: the Hubble Deep Field North". In: *Monthly Notices of the RAS* 310.2, pp. 540–556.

Atwood, W. B. et al. (2009). "The Large Area Telescope on the Fermi Gamma-Ray Space Telescope Mission". In: *Astrophysical Journal* 697.2, pp. 1071–1102.

Axelsson, M. et al. (2012). "GRB110721A: An Extreme Peak Energy and Signatures of the Photosphere". In: *Astrophysical Journal Letters* 757.2, L31, p. L31.

Band, D. et al. (1993). "BATSE Observations of Gamma-Ray Burst Spectra. I. Spectral Diversity". In: *Astrophysical Journal* 413, p. 281.

Barkov, Maxim V. and Alexei S. Pozanenko (2011). "Model of the extended emission of short gamma-ray bursts". In: *Monthly Notices of the RAS* 417.3, pp. 2161–2165.

Barnes, Jennifer and Daniel Kasen (2013). "Effect of a High Opacity on the Light Curves of Radioactively Powered Transients from Compact Object Mergers". In: *Astrophysical Journal* 775.1, 18, p. 18.

Barthelmy, S. (2008). "GCN and VOEvent: A status report". In: *Astronomische Nachrichten* 329.3, p. 340.

Barthelmy, S. D. et al. (1995). "BACODINE, the Real-Time BATSE Gamma-Ray Burst Coordinates Distribution Network". In: *Astrophysics and Space Science* 231.1-2, pp. 235–238.

Barthelmy, S. D. et al. (1998a). "Current Status and New Developments with the GRB Coordinates Network (GCN)". In: *American Astronomical Society Meeting Abstracts #192*. Vol. 192. American Astronomical Society Meeting Abstracts, p. 43.11.

Barthelmy, S. D. et al. (1998b). "The GRB coordinates network (GCN): A status report". In: *Gamma-Ray Bursts, 4th Hunstville Symposium*. Ed. by Charles A. Meegan, Robert D. Preece, and Thomas M. Koshut. Vol. 428. American Institute of Physics Conference Series, pp. 99–103.

Barthelmy, S. D. et al. (2013). "GRB 130603B: Swift-BAT refined analysis." In: *GRB Coordinates Network* 14741, p. 1.

Barthelmy, S. D. et al. (2015). "GRB 151228A: Swift-BAT refined analysis." In: *GRB Coordinates Network* 18754, p. 1.

Barthelmy, Scott D. et al. (2005). "The Burst Alert Telescope (BAT) on the SWIFT Midex Mission". In: *Space Science Reviews* 120.3-4, pp. 143–164.

Baumgartner, W. H. et al. (2012). "GRB 121226A, Swift-BAT refined analysis." In: *GRB Coordinates Network* 14111, p. 1.

Baumgartner, W. H. et al. (2014). "GRB 140930B Swift-BAT refined analysis." In: *GRB Coordinates Network* 16870, p. 1.

Beloborodov, Andrei M. (2002). "Prompt Emission and Early Afterglows of Gamma-Ray Bursts". In: *arXiv e-prints*, astro-ph/0201321, astro–ph/0201321.

Beloborodov, Andrei M., Boris E. Stern, and Roland Svensson (2000). "Power Density Spectra of Gamma-Ray Bursts". In: *Astrophysical Journal* 535.1, pp. 158–166.

Berger, E. (2010). "A Short Gamma-ray Burst "No-host" Problem? Investigating Large Progenitor Offsets for Short GRBs with Optical Afterglows". In: *Astrophysical Journal* 722.2, pp. 1946–1961.

Berger, E., W. Fong, and R. Chornock (2013). "An r-process Kilonova Associated with the Short-hard GRB 130603B". In: *Astrophysical Journal Letters* 774.2, L23, p. L23.

Berger, E. et al. (2002). "The Faint Optical Afterglow and Host Galaxy of GRB 020124: Implications for the Nature of Dark Gamma-Ray Bursts". In: *Astrophysical Journal* 581.2, pp. 981–987.

Berger, Edo (2014). "Short-Duration Gamma-Ray Bursts". In: *Annual Review of Astron and Astrophys* 52, pp. 43–105.

Beuermann, K. et al. (1999). "VLT observations of GRB 990510 and its environment". In: *Astronomy and Astrophysics* 352, pp. L26–L30.

Bhatt, V. K. and S. B. Pandey (2012). "GRB 121226A: optical observations." In: *GRB Coordinates Network* 14109, p. 1.

Bianco, F. B. et al. (2014). "Multi-color Optical and Near-infrared Light Curves of 64 Stripped-envelope Core-Collapse Supernovae". In: *Astrophysical Journal Supplement* 213.2, 19, p. 19.

Biehl, Daniel et al. (2017). "Astrophysical neutrino production diagnostics with the Glashow resonance". In: *Journal of Cosmology and Astroparticle Physics* 2017.1, 033, p. 033.

Bildsten, Lars (2000). "Theory and observations of Type I X-Ray bursts from neutron stars". In: *Cosmic Explosions: Tenth AstroPhysics Conference*. Ed. by Stephen S. Holt and William W. Zhang. Vol. 522. American Institute of Physics Conference Series, pp. 359–369.

Bisnovatyi-Kogan, G. S. and A. S. Pozanenko (2011). "About the measurements of the hard X-ray background". In: *Astrophysics and Space Science* 332.1, pp. 57–63.

Bissaldi, E., B. Zhang, and P. Veres (2015). "GRB 151228A: Fermi GBM observation." In: *GRB Coordinates Network* 18736, p. 1.

Blanch, O. et al. (2020a). "GRB 201216C: MAGIC detection in very high energy gamma rays". In: *GRB Coordinates Network* 29075, p. 1.

Blanch, O. et al. (2020b). "MAGIC observations of GRB 201015A: hint of very high energy gamma-ray signal". In: *GRB Coordinates Network* 28659, p. 1.

Blanchard, P. K. et al. (2017). "The Electromagnetic Counterpart of the Binary Neutron Star Merger LIGO/Virgo GW170817. VII. Properties of the Host Galaxy and Constraints on the Merger Timescale". In: *Astrophysical Journal Letters* 848.2, L22, p. L22.

Blanchard, Peter K., Edo Berger, and Wen-fai Fong (2016). "The Offset and Host Light Distributions of Long Gamma-Ray Bursts: A New View From HST Observations of Swift Bursts". In: *Astrophysical Journal* 817.2, 144, p. 144.

Blandford, R. D. and C. F. McKee (1976). "Fluid dynamics of relativistic blast waves". In: *Physics of Fluids* 19, pp. 1130–1138.

Blandford, R. D. and R. L. Znajek (1977). "Electromagnetic extraction of energy from Kerr black holes." In: *Monthly Notices of the RAS* 179, pp. 433–456.

Bloom, J. S., S. G. Djorgovski, and S. R. Kulkarni (2001). "The Redshift and the Ordinary Host Galaxy of GRB 970228". In: *Astrophysical Journal* 554.2, pp. 678–683.

Bloom, J. S., D. A. Frail, and S. R. Kulkarni (2003). "Gamma-Ray Burst Energetics and the Gamma-Ray Burst Hubble Diagram: Promises and Limitations". In: *Astrophysical Journal* 594.2, pp. 674–683.

Bloom, J. S., S. R. Kulkarni, and S. G. Djorgovski (2002). "The Observed Offset Distribution of Gamma-Ray Bursts from Their Host Galaxies: A Robust Clue to the Nature of the Progenitors". In: *Astronomical Journal* 123.3, pp. 1111–1148.

Bloom, J. S. et al. (1998). "The Host Galaxy of GRB 970508". In: *Astrophysical Journal Letters* 507.1, pp. L25–L28.

Boella, G. et al. (1997). "BeppoSAX, the wide band mission for X-ray astronomy". In: *Astronomy and Astrophysics Supplement* 122, pp. 299–307.

Bolmer, J., J. Greiner, and T. W. Chen (2019). "GRB190829A: GROND detection of the accompanying SN". In: *GRB Coordinates Network* 25651, p. 1.

Breeveld, A. A. and M. de Pasquale (2013). "GRB 131224A: Swift/UVOT upper limits." In: *GRB Coordinates Network* 15615, p. 1.

— (2014). "GRB 140930B: Swift/UVOT Upper Limits." In: *GRB Coordinates Network* 16869, p. 1.

Breeveld, A. A. and H. A. Krimm (2012). "GRB 121226A: Swift/UVOT upper limits." In: *GRB Coordinates Network* 14113, p. 1.

Breeveld, A. A. and A. Y. Lien (2014). "GRB 140629A: Swift/UVOT Detection." In: *GRB Coordinates Network* 16494, p. 1.

Briggs, M. S. et al. (1999). "Observations of GRB 990123 by the Compton Gamma Ray Observatory". In: *Astrophysical Journal* 524.1, pp. 82–91.

Bromberg, Omer et al. (2013). "Short versus Long and Collapsars versus Non-collapsars: A Quantitative Classification of Gamma-Ray Bursts". In: *Astrophysical Journal* 764.2, 179, p. 179.

Bruzual, G. and S. Charlot (2003). "Stellar population synthesis at the resolution of 2003". In: *Monthly Notices of the RAS* 344.4, pp. 1000–1028.

Bufano, Filomena et al. (2012). "The Highly Energetic Expansion of SN 2010bh Associated with GRB 100316D". In: *Astrophysical Journal* 753.1, 67, p. 67.

Bulla, M. et al. (2019). "The origin of polarization in kilonovae and the case of the gravitational-wave counterpart AT 2017gfo". In: *Nature Astronomy* 3, pp. 99–106.

Burdanov, A. Y., V. V. Krushinsky, and A. A. Popov (2014). "Astrokit-an efficient program for high-precision differential CCD photometry and search for variable stars". In: *Astrophysical Bulletin* 69.3, pp. 368–376.

Burrows, D. N. and J. A. Kennea (2014). "Swift XRT status update." In: *GRB Coordinates Network* 16356, p. 1.

Burrows, D. N. et al. (2011). "Relativistic jet activity from the tidal disruption of a star by a massive black hole". In: *Nature* 476.7361, pp. 421–424.

Burrows, D. N. et al. (2014). "GRB 140622A: Swift-XRT refined Analysis." In: *GRB Coordinates Network* 16439, p. 1.

Burrows, David N. et al. (2005). "The Swift X-Ray Telescope". In: *Space Science Reviews* 120.3-4, pp. 165–195.

Burrows, David N. et al. (2006). "Jet Breaks in Short Gamma-Ray Bursts. II. The Collimated Afterglow of GRB 051221A". In: *Astrophysical Journal* 653.1, pp. 468–473.

Burrows, David N. et al. (2008). "The Swift X-Ray Telescope: Status and Performance". In: *arXiv e-prints*, arXiv:0803.1844, arXiv:0803.1844.

Butler, N. et al. (2014). "GRB 140622A: RATIR Optical and NIR Observations." In: *GRB Coordinates Network* 16436, p. 1.

Calzetti, Daniela et al. (2000). "The Dust Content and Opacity of Actively Star-forming Galaxies". In: *Astrophysical Journal* 533.2, pp. 682–695.

Campana, S. et al. (2006). "The association of GRB 060218 with a supernova and the evolution of the shock wave". In: *Nature* 442.7106, pp. 1008–1010.

Campana, S. et al. (2011). "The unusual gamma-ray burst GRB 101225A explained as a minor body falling onto a neutron star". In: *Nature* 480.7375, pp. 69–71.

Cano, Z. et al. (2011). "XRF 100316D/SN 2010bh and the Nature of Gamma-Ray Burst Supernovae". In: *Astrophysical Journal* 740.1, 41, p. 41.

Cano, Z. et al. (2014). "A trio of gamma-ray burst supernovae:. GRB 120729A, GRB 130215A/SN 2013ez, and GRB 130831A/SN 2013fu". In: *Astronomy and Astrophysics* 568, A19, A19.

Cano, Zach (2013). "A new method for estimating the bolometric properties of Ibc supernovae". In: *Monthly Notices of the RAS* 434.2, pp. 1098–1116.

Cano, Zach et al. (2017). "The Observer's Guide to the Gamma-Ray Burst Supernova Connection". In: *Advances in Astronomy* 2017, 8929054, p. 8929054.

Capone, J. et al. (2014). "GRB140903A: Discovery Channel Telescope Optical Detection." In: *GRB Coordinates Network* 16769, p. 1.

Castro-Tirado, A. J. and J. Gorosabel (1999). "Optical observations of GRB afterglows: GRB 970508 and GRB 980326 revisited". In: 138, pp. 449–450.

Castro-Tirado, A. J. et al. (1994). "WATCH Observations of Gamma-Ray Bursts During 1990-1992". In: *Gamma-Ray Bursts*. Ed. by Gerald J. Fishman. Vol. 307. American Institute of Physics Conference Series, p. 17.

Castro-Tirado, A. J. et al. (1999a). "The Burst Observer and Optical Transient Exploring System (BOOTES)". In: *Astronomy and Astrophysics Supplement* 138, pp. 583–585.

Castro-Tirado, A. J. et al. (2005). "<ASTROBJ>GRB 050509b</ASTROBJ>: the elusive optical/nIR/mm afterglow of a short-duration GRB". In: *Astronomy and Astrophysics* 439.2, pp. L15–L18.

Castro-Tirado, A. J. et al. (2007). "The dark nature of <ASTROBJ>GRB 051022</ASTROBJ> and its host galaxy". In: *Astronomy and Astrophysics* 475.1, pp. 101–107.

Castro-Tirado, A. J. et al. (2012a). "Building the BOOTES world-wide Network of Robotic telescopes". In: *Astronomical Society of India Conference Series*. Vol. 7. Astronomical Society of India Conference Series, pp. 313–320.

Castro-Tirado, A. J. et al. (2012b). "GRB 121226A: 10.4m GTC optical observations." In: *GRB Coordinates Network* 14114, p. 1.

Castro-Tirado, Alberto J. et al. (1999b). "Decay of the GRB 990123 Optical Afterglow: Implications for the Fireball Model". In: *Science* 283, p. 2069.

Cenko, S. B. and D. A. Perley (2014). "GRB 140903A: P60 Optical Observations." In: *GRB Coordinates Network* 16770, p. 1.

Cenko, S. B. et al. (2014). "GRB 140930B: Gemini South Spectroscopy." In: *GRB Coordinates Network* 16873, p. 1.

Cepa, Jordi et al. (2000). "OSIRIS tunable imager and spectrograph". In: *Optical and IR Telescope Instrumentation and Detectors*. Ed. by Masanori Iye and Alan F. Moorwood. Vol. 4008. Society of Photo-Optical Instrumentation Engineers (SPIE) Conference Series, pp. 623–631.

Chand, Vikas et al. (2020). "Peculiar Prompt Emission and Afterglow in the H.E.S.S.-detected GRB 190829A". In: *Astrophysical Journal* 898.1, 42, p. 42.

Chandra, Poonam and et al. (2019). "GRB 190829A: Detection of radio afterglow with the uGMRT". In: *GRB Coordinates Network* 25627, p. 1.

Chandra, Poonam and Dale A. Frail (2012). "A Radio-selected Sample of Gamma-Ray Burst Afterglows". In: *Astrophysical Journal* 746.2, 156, p. 156.

Chary, R., E. E. Becklin, and L. Armus (2002). "Are Starburst Galaxies the Hosts of Gamma-Ray Bursts?" In: *Astrophysical Journal* 566.1, pp. 229–238.

Chary, R., E. Berger, and L. Cowie (2007). "Spitzer Observations of Gamma-Ray Burst Host Galaxies: A Unique Window into High-Redshift Chemical Evolution and Star Formation". In: *Astrophysical Journal* 671.1, pp. 272–277.

Cheng, K. S. and T. Lu (2001). "Gamma-Ray Bursts: Afterglows and Central Engines". In: *Chinese Journal of Astronomy and Astrophysics* 1, pp. 1–20.

Chernenko, A. (2011). "On the Intrinsic Simplicity of Spectral Variability of GRBs". In: *Acta Polytechnica* 51.2, p. 61.

Chevalier, Roger A. and Zhi-Yun Li (1999). "Gamma-Ray Burst Environments and Progenitors". In: *Astrophysical Journal Letters* 520.1, pp. L29–L32.

Chornock, R., W. Fong, and D. B. Fox (2014). "GRB 141212A: Gemini-N spectroscopy and photometry." In: *GRB Coordinates Network* 17177, p. 1.

Chornock, Ryan et al. (2010). "Spectroscopic Discovery of the Broad-Lined Type Ic Supernova 2010bh Associated with the Low-Redshift GRB 100316D". In: *arXiv e-prints*, arXiv:1004.2262, arXiv:1004.2262.

Chrimes, Ashley A. et al. (2018). "Investigating a population of infrared-bright gamma-ray burst host galaxies". In: *Monthly Notices of the RAS* 478.1, pp. 2–27.

Christensen, L., J. Hjorth, and J. Gorosabel (2004). "UV star-formation rates of GRB host galaxies". In: *Astronomy and Astrophysics* 425, pp. 913–926.

Ciardi, Benedetta and Abraham Loeb (2000). "Expected Number and Flux Distribution of Gamma-Ray Burst Afterglows with High Redshifts". In: *Astrophysical Journal* 540.2, pp. 687–696.

Connaughton, V. et al. (2017). "LIGO/Virgo G298048: Fermi GBM trigger 170817.529 and LIGO single IFO trigger". In: *GRB Coordinates Network* 21506, p. 1.

Coppin, Paul, Krijn D. de Vries, and Nick van Eijndhoven (2020). "Identification of gamma-ray burst precursors in Fermi-GBM bursts". In: *Physical Review D* 102.10, 103014, p. 103014.

Cornelisse, R. et al. (2004). "Burst-only sources: probing type I X-ray bursters at low persistent luminosities". In: *Nuclear Physics B Proceedings Supplements* 132, pp. 518–523.

Costa, E. et al. (1997). "Discovery of an X-ray afterglow associated with the γ-ray burst of 28 February 1997". In: *Nature* 387.6635, pp. 783–785.

Coulter, D. A. et al. (2017). "LIGO/Virgo G298048: Potential optical counterpart discovered by Swope telescope". In: *GRB Coordinates Network* 21529, p. 1.

Covino, S. et al. (2004). "Polarization of Gamma-Ray Burst Optical and Near-Infrared Afterglows". In: *Gamma-Ray Bursts in the Afterglow Era*. Ed. by Marco Feroci et al. Vol. 312. Astronomical Society of the Pacific Conference Series, p. 169.

Covino, S. et al. (2017). "The unpolarized macronova associated with the gravitational wave event GW 170817". In: *Nature Astronomy* 1, pp. 791–794.

Covino, Stefano et al. (1999). "GRB 990510: linearly polarized radiation from a fireball". In: *Astronomy and Astrophysics* 348, pp. L1–L4.

Cowperthwaite, P. S. et al. (2017). "The Electromagnetic Counterpart of the Binary Neutron Star Merger LIGO/Virgo GW170817. II. UV, Optical, and Near-infrared Light Curves and Comparison to Kilonova Models". In: *Astrophysical Journal Letters* 848.2, L17, p. L17.

Cucchiara, A., D. Perley, and S. B. Cenko (2013). "GRB 130603B: Gemini observations." In: *GRB Coordinates Network* 14748, p. 1.

Cucchiara, A. et al. (2011). "A Photometric Redshift of z $\sim$9.4 for GRB 090429B". In: *Astrophysical Journal* 736.1, 7, p. 7.

Cucchiara, A. et al. (2013). "Gemini Spectroscopy of the Short-hard Gamma-Ray Burst GRB 130603B Afterglow and Host Galaxy". In: *Astrophysical Journal* 777.2, 94, p. 94.

Cucchiara, A. et al. (2014). "GRB 140903A: tentative spectroscopic redshift." In: *GRB Coordinates Network* 16774, p. 1.

Cummings, J. R. et al. (2014a). "GRB 140606A: Swift-BAT refined analysis." In: *GRB Coordinates Network* 16354, p. 1.

Cummings, J. R. et al. (2014b). "GRB 140629A: Swift-BAT refined analysis." In: *GRB Coordinates Network* 16481, p. 1.

Cummings, J. R. et al. (2014c). "GRB 140903A: Swift detection of a possible burst." In: *GRB Coordinates Network* 16763, p. 1.

Daddi, E. et al. (2007). "Multiwavelength Study of Massive Galaxies at z$\sim$2. I. Star Formation and Galaxy Growth". In: *Astrophysical Journal* 670.1, pp. 156–172.

Dai, Z. G. and T. Lu (1998). "Gamma-ray burst afterglows and evolution of post-burst fireballs with energy injection from strongly magnetic millisecond pulsars". In: *Astronomy and Astrophysics* 333, pp. L87–L90.

Dai, Zigao, Frédéric Daigne, and Peter Mészáros (2017). "The Theory of Gamma-Ray Bursts". In: *Space Science Reviews* 212.1-2, pp. 409–427.

Daigne, F. and R. Mochkovitch (1998). "Gamma-ray bursts from internal shocks in a relativistic wind: temporal and spectral properties". In: *Monthly Notices of the RAS* 296.2, pp. 275–286.

Dainotti, Maria, Roberta Del Vecchio, and Mariusz Tarnopolski (2016). "Gamma Ray Burst Prompt correlations". In: *arXiv e-prints*, arXiv:1612.00618, arXiv:1612.00618.

Dar, Arnon (2006). "Fireball and Cannonball Models of Gamma-Ray Bursts Confront Observations". In: *Chinese Journal of Astronomy and Astrophysics Supplement* 6.S1, pp. 301–314.

D'Avanzo, P. et al. (2014a). "A complete sample of bright Swift short gamma-ray bursts". In: *Monthly Notices of the RAS* 442.3, pp. 2342–2356.

D'Avanzo, P. et al. (2014b). "GRB 140629A: TNG redshift confirmation." In: *GRB Coordinates Network* 16493, p. 1.

Davies, Melvyn B. et al. (2007). "Progenitors of Long Gamma-Ray Bursts". In: *Gamma-Ray Bursts: Prospects for GLAST*. Ed. by Magnus Axelsson and Felix Ryde. Vol. 906. American Institute of Physics Conference Series, pp. 69–78.

de Naurois, M. and H. E. S. S. Collaboration (2019). "GRB190829A: Detection of VHE gamma-ray emission with H.E.S.S." In: *GRB Coordinates Network* 25566, p. 1.

de Pasquale, M., A. Maselli, and J. R. Cummings (2014). "GRB 140903A: Swift-XRT refined Analysis." In: *GRB Coordinates Network* 16767, p. 1.

de Pasquale, M. et al. (2014). "GRB 140930B: Swift detection of a short burst." In: *GRB Coordinates Network* 16857, p. 1.

De Pasquale, M. et al. (2016). "The 80 Ms follow-up of the X-ray afterglow of GRB 130427A challenges the standard forward shock model". In: *Monthly Notices of the RAS* 462.1, pp. 1111–1122.

de Ugarte Postigo, A. et al. (2012a). "Pre-ALMA observations of GRBs in the mm/submm range". In: *Astronomy and Astrophysics* 538, A44, A44.

de Ugarte Postigo, A. et al. (2012b). "The distribution of equivalent widths in long GRB afterglow spectra". In: *Astronomy and Astrophysics* 548, A11, A11.

de Ugarte Postigo, A. et al. (2013). "GRB 130603B: afterglow detection from NOT." In: *GRB Coordinates Network* 14743, p. 1.

de Ugarte Postigo, A. et al. (2014). "Spectroscopy of the short-hard GRB 130603B. The host galaxy and environment of a compact object merger". In: *Astronomy and Astrophysics* 563, A62, A62.

de Ugarte Postigo, A. et al. (2019). "GRB 190829A: GTC confirmation of an associated Type Ic-BL Supernova". In: *GRB Coordinates Network* 25677, p. 1.

Dean, A. J. et al. (2003). "The Modelling of Background Noise in Astronomical Gamma Ray Telescopes". In: *Space Science Reviews* 105.1, pp. 285–376.

D'Elia, V. et al. (2014a). "GRB 140622A: Swift detection of a short burst." In: *GRB Coordinates Network* 16433, p. 1.

D'Elia, V. et al. (2014b). "VLT/X-shooter spectroscopy of the GRB 120327A afterglow". In: *Astronomy and Astrophysics* 564, A38, A38.

D'Elia, V. et al. (2015). "SN 2013dx associated with GRB 130702A: a detailed photometric and spectroscopic monitoring and a study of the environment". In: *Astronomy and Astrophysics* 577, A116, A116.

Della Valle, M. et al. (2006a). "An enigmatic long-lasting γ-ray burst not accompanied by a bright supernova". In: *Nature* 444.7122, pp. 1050–1052.

Della Valle, M. et al. (2006b). "Hypernova Signatures in the Late Rebrightening of GRB 050525A". In: *Astrophysical Journal Letters* 642.2, pp. L103–L106.

Desai, D., B. D. Metzger, and F. Foucart (2019). "Imprints of r-process heating on fall-back accretion: distinguishing black hole-neutron star from double neutron star mergers". In: *Monthly Notices of the RAS* 485.3, pp. 4404–4412.

Dessart, Luc et al. (2017). "Radiative-transfer models for explosions from rotating and non-rotating single WC stars. Implications for SN 1998bw and LGRB/SNe". In: *Astronomy and Astrophysics* 603, A51, A51.

Di Sciascio, Giuseppe (2019). "Ground-based Gamma-Ray Astronomy: an Introduction". In: *Journal of Physics Conference Series*. Vol. 1263. Journal of Physics Conference Series, p. 012003.

Dichiara, S., C. Guidorzi, and J. Japelj (2014). "GRB 140903A: FTN observations." In: *GRB Coordinates Network* 16781, p. 1.

Dichiara, S. et al. (2013). "A Search for Pulsations in Short Gamma-Ray Bursts to Constrain their Progenitors". In: *Astrophysical Journal* 777.2, 132, p. 132.

Dichiara, S. et al. (2019). "GRB 190829A: Swift detection of a burst consistent with a galaxy at z=0.08". In: *GRB Coordinates Network* 25552, p. 1.

Eichler, David et al. (1989). "Nucleosynthesis, neutrino bursts and γ-rays from coalescing neutron stars". In: *Nature* 340.6229, pp. 126–128.

Evans, P. A. et al. (2009). "Methods and results of an automatic analysis of a complete sample of Swift-XRT observations of GRBs". In: *Monthly Notices of the RAS* 397.3, pp. 1177–1201.

Evans, P. A. et al. (2014). "GRB 140629A: Enhanced Swift-XRT position." In: *GRB Coordinates Network* 16479, p. 1.

Evans, P. A. et al. (2017). "Swift and NuSTAR observations of GW170817: Detection of a blue kilonova". In: *Science* 358.6370, pp. 1565–1570.

Evans, P. A. et al. (2019). "GRB 190829A: Enhanced Swift-XRT position". In: *GRB Coordinates Network* 25567, p. 1.

Event Horizon Telescope Collaboration et al. (2021). "First M87 Event Horizon Telescope Results. VII. Polarization of the Ring". In: *Astrophysical Journal Letters* 910.1, L12, p. L12.

Everett, Mark E. and Steve B. Howell (2001). "A Technique for Ultrahigh-Precision CCD Photometry". In: *Publications of the ASP* 113.789, pp. 1428–1435.

Fan, Yi-Zhong et al. (2013). "A Supramassive Magnetar Central Engine for GRB 130603B". In: *Astrophysical Journal Letters* 779.2, L25, p. L25.

Fermi GBM Team (2019). "GRB 190829A: Fermi GBM Final Real-time Localization". In: *GRB Coordinates Network* 25551, p. 1.

Fernández, Rodrigo and Brian D. Metzger (2016). "Electromagnetic Signatures of Neutron Star Mergers in the Advanced LIGO Era". In: *Annual Review of Nuclear and Particle Science* 66.1, pp. 23–45.

Feroz, F., M. P. Hobson, and M. Bridges (2009). "MULTINEST: an efficient and robust Bayesian inference tool for cosmology and particle physics". In: *Monthly Notices of the RAS* 398.4, pp. 1601–1614.

Fioc, M. and B. Rocca-Volmerange (1997). "PEGASE: a UV to NIR spectral evolution model of galaxies. Application to the calibration of bright galaxy counts." In: *Astronomy and Astrophysics* 500, pp. 507–519.

Fishman, G. J. (1999). "Observed properties of gamma-ray bursts". In: *Astronomy and Astrophysics Supplement* 138, pp. 395–398.

Fishman, Gerald J. et al. (1994). "The First BATSE Gamma-Ray Burst Catalog". In: *Astrophysical Journal Supplement* 92, p. 229.

Fitzpatrick, Edward L. (1986). "An average interstellar extinction curve for the Large Magellanic Cloud." In: *Astronomical Journal* 92, pp. 1068–1073.

Foley, R. J. et al. (2013). "GRB 130603B: Magellan redshift confirmation." In: *GRB Coordinates Network* 14745, p. 1.

Fong, W., E. Berger, and D. B. Fox (2010). "Hubble Space Telescope Observations of Short Gamma-Ray Burst Host Galaxies: Morphologies, Offsets, and Local Environments". In: *Astrophysical Journal* 708.1, pp. 9–25.

Fong, W., M. Calkins, and E. Berger (2014). "GRB 140930B: MMT confirmation of the optical afterglow." In: *GRB Coordinates Network* 16863, p. 1.

Fong, W., B. A. Zauderer, and E. Berger (2012). "GRB 121226A: 5.8 GHz VLA observations." In: *GRB Coordinates Network* 14126, p. 1.

Fong, W. et al. (2012). "A Jet Break in the X-Ray Light Curve of Short GRB 111020A: Implications for Energetics and Rates". In: *Astrophysical Journal* 756.2, 189, p. 189.

Fong, W. et al. (2013). "Demographics of the Galaxies Hosting Short-duration Gamma-Ray Bursts". In: *Astrophysical Journal* 769.1, 56, p. 56.

Fong, W. et al. (2014). "Short GRB 130603B: Discovery of a Jet Break in the Optical and Radio Afterglows, and a Mysterious Late-time X-Ray Excess". In: *Astrophysical Journal* 780.2, 118, p. 118.

Fong, W. et al. (2016). "The Afterglow and Early-type Host Galaxy of the Short GRB 150101B at z = 0.1343". In: *Astrophysical Journal* 833.2, 151, p. 151.

Fong, W. et al. (2017). "The Electromagnetic Counterpart of the Binary Neutron Star Merger LIGO/Virgo GW170817. VIII. A Comparison to Cosmological Short-duration Gamma-Ray Bursts". In: *Astrophysical Journal Letters* 848.2, L23, p. L23.

Fox, D. B. and J. R. Cummings (2014). "GRB 140903A: Coincident galaxy cluster in archival images." In: *GRB Coordinates Network* 16766, p. 1.

Fox, D. B. et al. (2005). "The afterglow of GRB 050709 and the nature of the short-hard γ-ray bursts". In: *Nature* 437.7060, pp. 845–850.

Fraija, N. et al. (2020). "On the origin of the multi-GeV photons from the closest burst with intermediate luminosity: GRB 190829A". In: *arXiv e-prints*, arXiv:2003.11252, arXiv:2003.11252.

Frail, D. A. et al. (1997). "The radio afterglow from the γ-ray burst of 8 May 1997". In: *Nature* 389.6648, pp. 261–263.

Frail, D. A. et al. (2001). "Beaming in Gamma-Ray Bursts: Evidence for a Standard Energy Reservoir". In: *Astrophysical Journal Letters* 562.1, pp. L55–L58.

Frail, Dale A. (2003). "The Radio Afterglows of Gamma-Ray Bursts". In: *arXiv e-prints*, astro-ph/0309557, astro–ph/0309557.

Friedman, Andrew S. and Joshua S. Bloom (2005). "Toward a More Standardized Candle Using Gamma-Ray Burst Energetics and Spectra". In: *Astrophysical Journal* 627.1, pp. 1–25.

Frontera, F. et al. (2009). "The Gamma-Ray Burst Catalog Obtained with the Gamma-Ray Burst Monitor Aboard BeppoSAX". In: *Astrophysical Journal Supplement* 180.1, pp. 192–223.

Fruchter, A. S. (2014). "GRB 140903A: Pan STARRS images of the field." In: *GRB Coordinates Network* 16776, p. 1.

Fruchter, A. S. et al. (2006). "Long γ-ray bursts and core-collapse supernovae have different environments". In: *Nature* 441.7092, pp. 463–468.

Fujiwara, T. et al. (2014). "GRB 141212A: MITSuME Akeno upper limits." In: *GRB Coordinates Network* 17160, p. 1.

Fynbo, J. P. U. et al. (2009). "Low-resolution Spectroscopy of Gamma-ray Burst Optical Afterglows: Biases in the Swift Sample and Characterization of the Absorbers". In: *Astrophysical Journal Supplement* 185.2, pp. 526–573.

Fynbo, Johan P. U. et al. (2006). "No supernovae associated with two long-duration γ-ray bursts". In: *Nature* 444.7122, pp. 1047–1049.

Fynbo, Johan P. U. et al. (2008). "Reconciling the Metallicity Distributions of Gamma-Ray Burst, Damped Lyα, and Lyman Break Galaxies at z $\approx$ 3". In: *Astrophysical Journal* 683.1, pp. 321–328.

Gal, R. R. et al. (2003). "The Northern Sky Optical Cluster Survey. II. An Objective Cluster Catalog for 5800 Square Degrees". In: *Astronomical Journal* 125.4, pp. 2064–2084.

Galama, T. J. et al. (1998). "An unusual supernova in the error box of the γ-ray burst of 25 April 1998". In: *Nature* 395.6703, pp. 670–672.

Galama, T. J. et al. (1999). "On the possible association of SN 1998bw and GRB 980425". In: *Astronomy and Astrophysics Supplement* 138, pp. 465–466.

Gao, He et al. (2013). "A complete reference of the analytical synchrotron external shock models of gamma-ray bursts". In: *New Astronomy Review* 57.6, pp. 141–190.

Gehrels, N., E. Chipman, and D. A. Kniffen (1993). "The Compton Gamma Ray Observatory." In: *Astronomy and Astrophysics Supplement* 97, pp. 5–12.

Gehrels, N., E. Ramirez-Ruiz, and D. B. Fox (2009). "Gamma-Ray Bursts in the Swift Era". In: *Annual Review of Astron and Astrophys* 47.1, pp. 567–617.

Gehrels, N. et al. (2004). "The Swift Gamma-Ray Burst Mission". In: *Astrophysical Journal* 611.2, pp. 1005–1020.

Gehrels, N. et al. (2005). "A short γ-ray burst apparently associated with an elliptical galaxy at redshift z = 0.225". In: *Nature* 437.7060, pp. 851–854.

Gehrels, N. et al. (2006). "A new γ-ray burst classification scheme from GRB060614". In: *Nature* 444.7122, pp. 1044–1046.

Georgy, C. et al. (2009). "The different progenitors of type Ib, Ic SNe, and of GRB". In: *Astronomy and Astrophysics* 502.2, pp. 611–622.

Ghirlanda, G., L. Nava, and G. Ghisellini (2010). "Spectral-luminosity relation within individual Fermi gamma rays bursts". In: *Astronomy and Astrophysics* 511, A43, A43.

Ghirlanda, G. et al. (2007). "Confirming the γ-ray burst spectral-energy correlations in the era of multiple time breaks". In: *Astronomy and Astrophysics* 466.1, pp. 127–136.

Ghirlanda, Giancarlo, Gabriele Ghisellini, and Davide Lazzati (2004). "The Collimation-corrected Gamma-Ray Burst Energies Correlate with the Peak Energy of Their νF_ν Spectrum". In: *Astrophysical Journal* 616.1, pp. 331–338.

Gibson, S. L. et al. (2017). "Fallback accretion on to a newborn magnetar: short GRBs with extended emission". In: *Monthly Notices of the RAS* 470.4, pp. 4925–4940.

Goldstein, A. et al. (2017). "An Ordinary Short Gamma-Ray Burst with Extraordinary Implications: Fermi-GBM Detection of GRB 170817A". In: *Astrophysical Journal Letters* 848.2, L14, p. L14.

Golenetskii, S. et al. (2013). "Konus-wind observation of GRB 130603B." In: *GRB Coordinates Network* 14771, p. 1.

Golenetskii, S. et al. (2014a). "Konus-Wind observation of GRB 140629A." In: *GRB Coordinates Network* 16495, p. 1.

Golenetskii, S. et al. (2014b). "Konus-Wind observation of GRB 140930B." In: *GRB Coordinates Network* 16868, p. 1.

Gompertz, B. et al. (2020). "GRB 201015A: Late X-ray Detections with Chandra". In: *GRB Coordinates Network* 28822, p. 1.

Gompertz, B. P., A. S. Fruchter, and A. Pe'er (2018). "The Environments of the Most Energetic Gamma-Ray Bursts". In: *Astrophysical Journal* 866.2, 162, p. 162.

Gompertz, B. P., K. L. Page, and M. de Pasquale (2013). "GRB 131224A: Swift-XRT observation." In: *GRB Coordinates Network* 15610, p. 1.

Gompertz, B. P. et al. (2018). "The Diversity of Kilonova Emission in Short Gamma-Ray Bursts". In: *Astrophysical Journal* 860.1, 62, p. 62.

Gorbovskoy, E. et al. (2013a). "GRB 131224A: MASTER-net early optical observations." In: *GRB Coordinates Network* 15608, p. 1.

Gorbovskoy, E. et al. (2014a). "GRB 140629A: MASTER optical observations." In: *GRB Coordinates Network* 16507, p. 1.

Gorbovskoy, E. et al. (2014b). "GRB 140930B: MASTER early possible OT detection." In: *GRB Coordinates Network* 16875, p. 1.

Gorbovskoy, E. S. et al. (2012). "Prompt, early and afterglow optical observations of five γ-ray bursts: GRB 100901A, GRB 100902A, GRB 100905A, GRB 100906A and GRB 101020A". In: *Monthly Notices of the RAS* 421.3, pp. 1874–1890.

Gorbovskoy, E. S. et al. (2013b). "The MASTER-II network of robotic optical telescopes. First results". In: *Astronomy Reports* 57.4, pp. 233–286.

Gorbovskoy, E. S. et al. (2016). "Early polarization observations of the optical emission of gamma-ray bursts: GRB 150301B and GRB 150413A". In: *Monthly Notices of the RAS* 455.3, pp. 3312–3318.

Gorosabel, J., S. Hellmich, and S. Mottola (2014). "GRB 140930B: 1.23m CAHA optical observations." In: *GRB Coordinates Network* 16860, p. 1.

Gorosabel, J. et al. (1998). "An optical study of the GRB 970111 field beginning 19 hours after the gamma-ray burst". In: *Astronomy and Astrophysics* 339, pp. 719–728.

Gottlieb, Ore, Ehud Nakar, and Tsvi Piran (2018). "The cocoon emission - an electromagnetic counterpart to gravitational waves from neutron star mergers". In: *Monthly Notices of the RAS* 473.1, pp. 576–584.

Gou, L. J. et al. (2004). "Detectability of Long Gamma-Ray Burst Afterglows from Very High Redshifts". In: *Astrophysical Journal* 604.2, pp. 508–520.

Graham, J. et al. (2014). "GRB 140930B: GROND observations." In: *GRB Coordinates Network* 16872, p. 1.

Granot, J. (2007). "The Structure and Dynamics of GRB Jets". In: *Revista Mexicana de Astronomia y Astrofisica, vol. 27*. Vol. 27. Revista Mexicana de Astronomia y Astrofisica Conference Series, pp. 140–165.

Granot, Jonathan, Dafne Guetta, and Ramandeep Gill (2017). "Lessons from the Short GRB 170817A: The First Gravitational-wave Detection of a Binary Neutron Star Merger". In: *Astrophysical Journal Letters* 850.2, L24, p. L24.

Granot, Jonathan and Enrico Ramirez-Ruiz (2010). "Jets and Gamma-Ray Burst Unification Schemes". In: *arXiv e-prints*, arXiv:1012.5101, arXiv:1012.5101.

Granot, Jonathan, Enrico Ramirez-Ruiz, and Rosalba Perna (2005). "Afterglow Observations Shed New Light on the Nature of X-Ray Flashes". In: *Astrophysical Journal* 630.2, pp. 1003–1014.

Granot, Jonathan et al. (2002). "Off-Axis Afterglow Emission from Jetted Gamma-Ray Bursts". In: *Astrophysical Journal Letters* 570.2, pp. L61–L64.

Granot, Jonathan et al. (2018). "Off-axis emission of short GRB jets from double neutron star mergers and GRB 170817A". In: *Monthly Notices of the RAS* 481.2, pp. 1597–1608.

Greiner, J. et al. (2015a). "Gamma-Ray Bursts Trace UV Metrics of Star Formation over $3 < z < 5$". In: *Astrophysical Journal* 809.1, 76, p. 76.

Greiner, Jochen et al. (2015b). "A very luminous magnetar-powered supernova associated with an ultra-long γ-ray burst". In: *Nature* 523.7559, pp. 189–192.

Gres, O. et al. (2014). "GRB 141212A: MASTER early optical observations." In: *GRB Coordinates Network* 17162, p. 1.

Groot, P. J. et al. (1998). "A Search for Optical Afterglow from GRB 970828". In: *Astrophysical Journal Letters* 493.1, pp. L27–L30.

Guilloteau, S. et al. (1992). "The IRAM interferometer on Plateau de Bure." In: *Astronomy and Astrophysics* 262, p. 624.

Guziy, S. et al. (2005). "The search for the host galaxy of the gamma-ray burst GRB 000214". In: *Astronomy and Astrophysics* 441.3, pp. 975–979.

Guziy, S. et al. (2012). "GRB 121226A: BOOTES-4/MET optical observations." In: *GRB Coordinates Network* 14106, p. 1.

Haggard, Daryl et al. (2017). "A Deep Chandra X-Ray Study of Neutron Star Coalescence GW170817". In: *Astrophysical Journal Letters* 848.2, L25, p. L25.

Hakkila, Jon and Robert D. Preece (2014). "Gamma-Ray Burst Pulse Shapes: Evidence for Embedded Shock Signatures?" In: *Astrophysical Journal* 783.2, 88, p. 88.

Hallinan, G. et al. (2017). "A radio counterpart to a neutron star merger". In: *Science* 358.6370, pp. 1579–1583.

Harry, Gregory M. and LIGO Scientific Collaboration (2010). "Advanced LIGO: the next generation of gravitational wave detectors". In: *Classical and Quantum Gravity* 27.8, 084006, p. 084006.

Hartoog, O. E. et al. (2014). "GRB 140622A: VLT/X-shooter redshift." In: *GRB Coordinates Network* 16437, p. 1.

Hirata, K. et al. (1987). "Observation of a neutrino burst from the supernova SN1987A". In: *Physical Review Letters* 58.14, pp. 1490–1493.

Hjorth, Jens and Joshua S. Bloom (2012). "The Gamma-Ray Burst - Supernova Connection". In: *Chapter 9 in "Gamma-Ray Bursts*, pp. 169–190.

Hjorth, Jens et al. (2003). "A very energetic supernova associated with the γ-ray burst of 29 March 2003". In: *Nature* 423.6942, pp. 847–850.

Hogg, David W. et al. (2002). "The K correction". In: *arXiv e-prints*, astro-ph/0210394, astro–ph/0210394.

Horváth, I. (1998). "A Third Class of Gamma-Ray Bursts?" In: *Astrophysical Journal* 508.2, pp. 757–759.

Hotokezaka, Kenta et al. (2013). "Progenitor Models of the Electromagnetic Transient Associated with the Short Gamma Ray Burst 130603B". In: *Astrophysical Journal Letters* 778.1, L16, p. L16.

Hu, You-Dong et al. (2014). "Internal Energy Dissipation of Gamma-Ray Bursts Observed with Swift: Precursors, Prompt Gamma-Rays, Extended Emission, and Late X-Ray Flares". In: *Astrophysical Journal* 789.2, 145, p. 145.

Huang, K. Y. et al. (2007). "Multicolor Shallow Decay and Chromatic Breaks in the GRB 050319 Optical Afterglow". In: *Astrophysical Journal Letters* 654.1, pp. L25–L28.

Hulse, R. A. and J. H. Taylor (1975). "Discovery of a pulsar in a binary system." In: *Astrophysical Journal Letters* 195, pp. L51–L53.

Hurley, K. et al. (1994). "Detection of a γ-ray burst of very long duration and very high energy". In: *Nature* 372.6507, pp. 652–654.

Hurley, K. et al. (2003). "The Current Performance of the Third Interplanetary Network". In: *Gamma-Ray Burst and Afterglow Astronomy 2001: A Workshop Celebrating the First Year of the HETE Mission*. Ed. by G. R. Ricker and R. K. Vanderspek. Vol. 662. American Institute of Physics Conference Series, pp. 473–476.

Hurley, K. et al. (2013). "The Interplanetary Network Supplement to the Fermi GBM Catalog of Cosmic Gamma-Ray Bursts". In: *Astrophysical Journal Supplement* 207.2, 39, p. 39.

Hurley, K. et al. (2016). "The Interplanetary Network Response to LIGO GW150914". In: *Astrophysical Journal Letters* 829.1, L12, p. L12.

IceCube Collaboration et al. (2018a). "Multimessenger observations of a flaring blazar coincident with high-energy neutrino IceCube-170922A". In: *Science* 361.6398, eaat1378, eaat1378.

IceCube Collaboration et al. (2018b). "Neutrino emission from the direction of the blazar TXS 0506+056 prior to the IceCube-170922A alert". In: *Science* 361.6398, pp. 147–151.

Ilbert, O. et al. (2006). "Accurate photometric redshifts for the CFHT legacy survey calibrated using the VIMOS VLT deep survey". In: *Astronomy and Astrophysics* 457.3, pp. 841–856.

Izzo, L. et al. (2018). "GRB 180728A: discovery of the associated supernova." In: *GRB Coordinates Network* 23142, p. 1.

Izzo, L. et al. (2019). "Signatures of a jet cocoon in early spectra of a supernova associated with a γ-ray burst". In: *Nature* 565.7739, pp. 324–327.

Jarosik, N. et al. (2011). "Seven-year Wilkinson Microwave Anisotropy Probe (WMAP) Observations: Sky Maps, Systematic Errors, and Basic Results". In: *Astrophysical Journal Supplement* 192.2, 14, p. 14.

Jin, Zhi-Ping et al. (2016). "The Macronova in GRB 050709 and the GRB-macronova connection". In: *Nature Communications* 7, 12898, p. 12898.

Jóhannesson, Gudlaugur, Gunnlaugur Björnsson, and Einar H. Gudmundsson (2006). "Afterglow Light Curves and Broken Power Laws: A Statistical Study". In: *Astrophysical Journal Letters* 640.1, pp. L5–L8.

Just, O. et al. (2015). "Comprehensive nucleosynthesis analysis for ejecta of compact binary mergers". In: *Monthly Notices of the RAS* 448.1, pp. 541–567.

Kalberla, P. M. W. et al. (2005). "The Leiden/Argentine/Bonn (LAB) Survey of Galactic HI. Final data release of the combined LDS and IAR surveys with improved stray-radiation corrections". In: *Astronomy and Astrophysics* 440.2, pp. 775–782.

Kaneko, Yuki et al. (2006). "The Complete Spectral Catalog of Bright BATSE Gamma-Ray Bursts". In: *Astrophysical Journal Supplement* 166.1, pp. 298–340.

Kann, D. A. et al. (2011). "The Afterglows of Swift-era Gamma-Ray Bursts. II. Type I GRB versus Type II GRB Optical Afterglows". In: *Astrophysical Journal* 734.2, 96, p. 96.

Karle, Albrecht and IceCube Collaboration (2009). "IceCube: Construction status and first results". In: *Nuclear Instruments and Methods in Physics Research A* 604.1-2, S46–S52.

Kasen, Daniel, Rodrigo Fernández, and Brian D. Metzger (2015). "Kilonova light curves from the disc wind outflows of compact object mergers". In: *Monthly Notices of the RAS* 450.2, pp. 1777–1786.

Kasliwal, Mansi M. et al. (2017). "Infrared Emission from Kilonovae: The Case of the Nearby Short Hard Burst GRB 160821B". In: *Astrophysical Journal Letters* 843.2, L34, p. L34.

Kennicutt Robert C., Jr. (1998). "The Global Schmidt Law in Star-forming Galaxies". In: *Astrophysical Journal* 498.2, pp. 541–552.

Kisaka, Shota and Kunihito Ioka (2015). "Long-lasting Black Hole Jets in Short Gamma-Ray Bursts". In: *Astrophysical Journal Letters* 804.1, L16, p. L16.

Klebesadel, Ray W., Ian B. Strong, and Roy A. Olson (1973). "Observations of Gamma-Ray Bursts of Cosmic Origin". In: *Astrophysical Journal Letters* 182, p. L85.

Klose, S. et al. (2004). "Probing a Gamma-Ray Burst Progenitor at a Redshift of z = 2: A Comprehensive Observing Campaign of the Afterglow of GRB 030226". In: *Astronomical Journal* 128.5, pp. 1942–1954.

Klotz, A. et al. (2008). "Early emission of rising optical afterglows: the case of GRB 060904B and GRB 070420". In: *Astronomy and Astrophysics* 483.3, pp. 847–855.

Klotz, A. et al. (2012). "GRB 121226A: zadko observatory - gingin optical observations." In: *GRB Coordinates Network* 14107, p. 1.

Klotz, A. et al. (2014). "GRB 140622A: TAROT La Silla observatory optical observations." In: *GRB Coordinates Network* 16468, p. 1.

Kobayashi, Shiho, Tsvi Piran, and Re'em Sari (1997). "Can Internal Shocks Produce the Variability in Gamma-Ray Bursts?" In: *Astrophysical Journal* 490, p. 92.

Kobayashi, Shiho and Bing Zhang (2007). "The Onset of Gamma-Ray Burst Afterglow". In: *Astrophysical Journal* 655.2, pp. 973–979.

Kocevski, Daniel and Nathaniel Butler (2008). "Gamma-Ray Burst Energetics in the Swift Era". In: *Astrophysical Journal* 680.1, pp. 531–538.

Kole, M. et al. (2020). "The POLAR gamma-ray burst polarization catalog". In: *Astronomy and Astrophysics* 644, A124, A124.

Koo, D. C. and R. G. Kron (1982). "QSO counts - A complete survey of stellar objects to B = 23". In: *Astronomy and Astrophysics* 105.1, pp. 107–119.

Kornilov, Victor G. et al. (2012). "Robotic optical telescopes global network MASTER II. Equipment, structure, algorithms". In: *Experimental Astronomy* 33.1, pp. 173–196.

Kouveliotou, Chryssa et al. (1993). "Identification of Two Classes of Gamma-Ray Bursts". In: *Astrophysical Journal Letters* 413, p. L101.

Krimm, H. A. et al. (2012). "GRB 121226A: Swift detection of a burst." In: *GRB Coordinates Network* 14105, p. 1.

Krühler, T. et al. (2011). "The SEDs and host galaxies of the dustiest GRB afterglows". In: *Astronomy and Astrophysics* 534, A108, A108.

Kulkarni, S. R. (2005). "Modeling Supernova-like Explosions Associated with Gamma-ray Bursts with Short Durations". In: *arXiv e-prints*, astro-ph/0510256, astro–ph/0510256.

Kumar, Amit et al. (2020). "SN 2010kd: Photometric and Spectroscopic Analysis of a Slow-decaying Superluminous Supernova". In: *Astrophysical Journal* 892.1, 28, p. 28.

Kumar, Brijesh et al. (2018). "3.6-m Devasthal Optical Telescope Project: Completion and first results". In: *Bulletin de la Societe Royale des Sciences de Liege* 87, pp. 29–41.

Kumar, Pawan and Tsvi Piran (2000). "Some Observational Consequences of Gamma-Ray Burst Shock Models". In: *Astrophysical Journal* 532.1, pp. 286–293.

Kumar, Pawan and Bing Zhang (2015). "The physics of gamma-ray bursts & relativistic jets". In: *Physics Reports* 561, pp. 1–109.

Kuulkers, E. et al. (2000). "GRB 990510: On the Possibility of a Beamed X-Ray Afterglow". In: *Astrophysical Journal* 538.2, pp. 638–644.

Lamb, D. Q. (1995). "The Distance Scale to Gamma-Ray Bursts". In: *Publications of the ASP* 107, p. 1152.

Lamb, Gavin P. and Shiho Kobayashi (2018). "GRB 170817A as a jet counterpart to gravitational wave triggerGW 170817". In: *Monthly Notices of the RAS* 478.1, pp. 733–740.

Lan, Lin et al. (2018). "Characteristics of Two-episode Emission Patterns in Fermi Long Gamma-Ray Bursts". In: *Astrophysical Journal* 862.2, 155, p. 155.

Laskar, T. et al. (2019). "GRB 190829A: ATCA cm-band detection". In: *GRB Coordinates Network* 25676, p. 1.

Laskar, Tanmoy et al. (2016). "A Reverse Shock in GRB 160509A". In: *Astrophysical Journal* 833.1, 88, p. 88.

Lasker, Barry M. et al. (2008). "The Second-Generation Guide Star Catalog: Description and Properties". In: *Astronomical Journal* 136.2, pp. 735–766.

Lattimer, J. M. and D. N. Schramm (1974). "Black-Hole-Neutron-Star Collisions". In: *Astrophysical Journal Letters* 192, p. L145.

Lazzati, Davide et al. (2018). "Late Time Afterglow Observations Reveal a Collimated Relativistic Jet in the Ejecta of the Binary Neutron Star Merger GW170817". In: *Physical Review Letters* 120.24, 241103, p. 241103.

Le Floc'h, Emeric et al. (2006). "Probing Cosmic Star Formation Using Long Gamma-Ray Bursts: New Constraints from the Spitzer Space Telescope". In: *Astrophysical Journal* 642.2, pp. 636–652.

Lee, William H. and Enrico Ramirez-Ruiz (2007). "The progenitors of short gamma-ray bursts". In: *New Journal of Physics* 9.1, p. 17.

Leibler, C. N. and E. Berger (2010). "The Stellar Ages and Masses of Short Gamma-ray Burst Host Galaxies: Investigating the Progenitor Delay Time Distribution and the Role of Mass and Star Formation in the Short Gamma-ray Burst Rate". In: *Astrophysical Journal* 725.1, pp. 1202–1214.

Lesage, S. et al. (2019). "GRB 190829A: Fermi GBM detection". In: *GRB Coordinates Network* 25575, p. 1.

Levan, A. J. et al. (2014). "GRB 140903A: Possible optical variability." In: *GRB Coordinates Network* 16784, p. 1.

Levan, A. J. et al. (2017). "The Environment of the Binary Neutron Star Merger GW170817". In: *Astrophysical Journal Letters* 848.2, L28, p. L28.

Lewin, W. H. G., J. van Paradijs, and R. E. Taam (1995). "X-ray bursts." In: *X-ray Binaries*, pp. 175–232.

Li, Li-Xin and Bohdan Paczyński (1998). "Transient Events from Neutron Star Mergers". In: *Astrophysical Journal Letters* 507.1, pp. L59–L62.

Li, Liang et al. (2012). "A Comprehensive Study of Gamma-Ray Burst Optical Emission. I. Flares and Early Shallow-decay Component". In: *Astrophysical Journal* 758.1, 27, p. 27.

Li, Yanguo et al. (2020). "The GECAM and its payload". In: *Scientia Sinica Physica, Mechanica & Astronomica* 50.12, p. 129508.

Li, Ye, Bing Zhang, and Hou-Jun Lü (2016). "A Comparative Study of Long and Short GRBs. I. Overlapping Properties". In: *Astrophysical Journal Supplement* 227.1, 7, p. 7.

Liang, E. W. et al. (2006). "Testing the Curvature Effect and Internal Origin of Gamma-Ray Burst Prompt Emissions and X-Ray Flares with Swift Data". In: *Astrophysical Journal* 646.1, pp. 351–357.

Liang, En-Wei, Bin-Bin Zhang, and Bing Zhang (2007). "A Comprehensive Analysis of Swift XRT Data. II. Diverse Physical Origins of the Shallow Decay Segment". In: *Astrophysical Journal* 670.1, pp. 565–583.

Liang, En-Wei et al. (2008). "A Comprehensive Analysis of Swift XRT Data. III. Jet Break Candidates in X-Ray and Optical Afterglow Light Curves". In: *Astrophysical Journal* 675.1, pp. 528–552.

Liang, En-Wei et al. (2010). "Constraining Gamma-ray Burst Initial Lorentz Factor with the Afterglow Onset Feature and Discovery of a Tight Γ_0-E $_{\gamma,iso}$ Correlation". In: *Astrophysical Journal* 725.2, pp. 2209–2224.

Liang, Enwei and Bing Zhang (2005). "Model-independent Multivariable Gamma-Ray Burst Luminosity Indicator and Its Possible Cosmological Implications". In: *Astrophysical Journal* 633.2, pp. 611–623.

Liddle, Andrew R. (2007). "Information criteria for astrophysical model selection". In: *Monthly Notices of the RAS* 377.1, pp. L74–L78.

Lien, A. Y. et al. (2014). "GRB 140629A: Swift detection of a burst with an optical counterpart." In: *GRB Coordinates Network* 16477, p. 1.

Lien, A. Y. et al. (2019). "GRB 190829A, Swift-BAT refined analysis". In: *GRB Coordinates Network* 25579, p. 1.

Lien, Amy et al. (2016). "The Third Swift Burst Alert Telescope Gamma-Ray Burst Catalog". In: *Astrophysical Journal* 829.1, 7, p. 7.

Lin, Huan et al. (1996). "The Luminosity Function of Galaxies in the Las Campanas Redshift Survey". In: *Astrophysical Journal* 464, p. 60.

Lipunov, V. et al. (2019a). "GRB 190829A: MASTER confirmation of GROND SN". In: *GRB Coordinates Network* 25652, p. 1.

Lipunov, V. et al. (2019b). "MASTER Transient Discovery Report for 2019-08-29". In: *Transient Name Server Discovery Report* 2019-1657, p. 1.

Lipunov, V. M. et al. (2004). "MASTER: The Mobile Astronomical System of Telescope-Robots". In: *Astronomische Nachrichten* 325.6, pp. 580–582.

Lipunov, Vladimir et al. (2010). "Master Robotic Net". In: *Advances in Astronomy* 2010, 349171, p. 349171.

Littlejohns, O. M. et al. (2012). "GRB 121226A: Swift-XRT refined analysis." In: *GRB Coordinates Network* 14112, p. 1.

Littlejohns, O. M. et al. (2015). "A detailed study of the optical attenuation of gamma-ray bursts in the Swift era". In: *Monthly Notices of the RAS* 449.3, pp. 2919–2936.

Lloyd, Nicole M., Vahé Petrosian, and Robert S. Mallozzi (2000). "Cosmological versus Intrinsic: The Correlation between Intensity and the Peak of the νF_ν Spectrum of Gamma-Ray Bursts". In: *Astrophysical Journal* 534.1, pp. 227–238.

Lloyd-Ronning, Nicole M. and Bing Zhang (2004). "On the Kinetic Energy and Radiative Efficiency of Gamma-Ray Bursts". In: *Astrophysical Journal* 613.1, pp. 477–483.

Loeb, Abraham (2016). "Electromagnetic Counterparts to Black Hole Mergers Detected by LIGO". In: *Astrophysical Journal Letters* 819.2, L21, p. L21.

Lorenz, E. and R. Wagner (2012). "Very-high energy gamma-ray astronomy. A 23-year success story in high-energy astroparticle physics". In: *European Physical Journal H* 37.3, pp. 459–513.

Lü, Jing et al. (2012). "Lorentz-factor-Isotropic-luminosity/Energy Correlations of Gamma-Ray Bursts and Their Interpretation". In: *Astrophysical Journal* 751.1, 49, p. 49.

Lu, Rui-Jing et al. (2012). "A Comprehensive Analysis of Fermi Gamma-Ray Burst Data. II. E $_p$ Evolution Patterns and Implications for the Observed Spectrum-Luminosity Relations". In: *Astrophysical Journal* 756.2, 112, p. 112.

Lu, Rui-Jing et al. (2017). "{Fermi}/GBM Short Gamma-ray Burst Catalog and Case Study for GRB 170817A/GW 170817". In: *arXiv e-prints*, arXiv:1710.06979, arXiv:1710.06979.

Lyman, J. D. et al. (2016). "Bolometric light curves and explosion parameters of 38 stripped-envelope core-collapse supernovae". In: *Monthly Notices of the RAS* 457.1, pp. 328–350.

Lyman, J. D. et al. (2018). "The optical afterglow of the short gamma-ray burst associated with GW170817". In: *Nature Astronomy* 2, pp. 751–754.

Lyons, N. et al. (2010). "Can X-ray emission powered by a spinning-down magnetar explain some gamma-ray burst light-curve features?" In: *Monthly Notices of the RAS* 402.2, pp. 705–712.

MAGIC Collaboration et al. (2019a). "Observation of inverse Compton emission from a long γ-ray burst". In: *Nature* 575.7783, pp. 459–463.

MAGIC Collaboration et al. (2019b). "Teraelectronvolt emission from the γ-ray burst GRB 190114C". In: *Nature* 575.7783, pp. 455–458.

Malesani, D. et al. (2004). "SN 2003lw and GRB 031203: A Bright Supernova for a Faint Gamma-Ray Burst". In: *Astrophysical Journal Letters* 609.1, pp. L5–L8.

Malesani, D. et al. (2013). "Short GRB 121226A: TNG observation of the host galaxy." In: *GRB Coordinates Network* 14139, p. 1.

Malesani, D. et al. (2014). "GRB 141212A: extended object within the XRT error circle." In: *GRB Coordinates Network* 17170, p. 1.

Margutti, R. et al. (2017). "The Electromagnetic Counterpart of the Binary Neutron Star Merger LIGO/Virgo GW170817. V. Rising X-Ray Emission from an Off-axis Jet". In: *Astrophysical Journal Letters* 848.2, L20, p. L20.

Margutti, R. et al. (2018). "The Binary Neutron Star Event LIGO/Virgo GW170817 160 Days after Merger: Synchrotron Emission across the Electromagnetic Spectrum". In: *Astrophysical Journal Letters* 856.1, L18, p. L18.

Marshall, F. E. and V. D'Elia (2014). "GRB 140622A: Swift/UVOT Upper Limits." In: *GRB Coordinates Network* 16446, p. 1.

Marshall, F. E. and M. C. Stroh (2014). "GRB 140606A: Swift/UVOT Upper Limits." In: *GRB Coordinates Network* 16358, p. 1.

Massarotti, M. et al. (2001). "New insights on the accuracy of photometric redshift measurements". In: *Astronomy and Astrophysics* 380, pp. 425–434.

Maxham, Amanda and Bing Zhang (2009). "Modeling Gamma-Ray Burst X-Ray Flares Within the Internal Shock Model". In: *Astrophysical Journal* 707.2, pp. 1623–1633.

Mazets, E. P. et al. (1981). "Catalog of cosmic gamma-ray bursts from the KONUS experiment data". In: *Astrophysics and Space Science* 80.1, pp. 3–83.

McConnell, Mark L. (2017). "High energy polarimetry of prompt GRB emission". In: *New Astronomy Review* 76, pp. 1–21.

Meegan, C. A. et al. (1992). "Spatial distribution of γ-ray bursts observed by BATSE". In: *Nature* 355.6356, pp. 143–145.

Meegan, Charles et al. (2009). "The Fermi Gamma-ray Burst Monitor". In: *Astrophysical Journal* 702.1, pp. 791–804.

Melandri, A. et al. (2013). "GRB 130603B: Swift detection of a bright short burst." In: *GRB Coordinates Network* 14735, p. 1.

Mereghetti, S. et al. (2013). "GRB 131224A: a short GRB detected by INTEGRAL." In: *GRB Coordinates Network* 15607, p. 1.

Mészáros, P. (2006). "Gamma-ray bursts". In: *Reports on Progress in Physics* 69.8, pp. 2259–2321.

Mészáros, P. and M. J. Rees (1997). "Optical and Long-Wavelength Afterglow from Gamma-Ray Bursts". In: *Astrophysical Journal* 476.1, pp. 232–237.

Metzger, B. D. and E. Berger (2012). "What is the Most Promising Electromagnetic Counterpart of a Neutron Star Binary Merger?" In: *Astrophysical Journal* 746.1, 48, p. 48.

Metzger, B. D., A. L. Piro, and E. Quataert (2008). "Time-dependent models of accretion discs formed from compact object mergers". In: *Monthly Notices of the RAS* 390.2, pp. 781–797.

Metzger, B. D. et al. (2010). "Electromagnetic counterparts of compact object mergers powered by the radioactive decay of r-process nuclei". In: *Monthly Notices of the RAS* 406.4, pp. 2650–2662.

Metzger, Brian D. and Rodrigo Fernández (2014). "Red or blue? A potential kilonova imprint of the delay until black hole formation following a neutron star merger". In: *Monthly Notices of the RAS* 441.4, pp. 3444–3453.

Metzger, Brian D. and Anthony L. Piro (2014). "Optical and X-ray emission from stable millisecond magnetars formed from the merger of binary neutron stars". In: *Monthly Notices of the RAS* 439.4, pp. 3916–3930.

Metzger, M. R. et al. (1997). "Spectral constraints on the redshift of the optical counterpart to the γ-ray burst of 8 May 1997". In: *Nature* 387.6636, pp. 878–880.

Minaev, P. Y. and A. S. Pozanenko (2020). "The $E_{p,I}$-E_{iso} correlation: type I gamma-ray bursts and the new classification method". In: *Monthly Notices of the RAS* 492.2, pp. 1919–1936.

Minaev, P. Yu. and A. S. Pozanenko (2017). "Precursors of short gamma-ray bursts in the SPI-ACS/INTEGRAL experiment." In: *Astronomy Letters* 43.1, pp. 1–20.

Minaev, P. Yu., A. S. Pozanenko, and V. M. Loznikov (2010). "Extended emission from short gamma-ray bursts detected with SPI-ACS/INTEGRAL". In: *Astronomy Letters* 36.10, pp. 707–720.

Minaev, P. Yu. et al. (2012). "GRB 070912—A gamma-ray burst recorded from the direction to the galactic center". In: *Astronomy Letters* 38.10, pp. 613–628.

Minaev, P. Yu. et al. (2014). "Catalog of short gamma-ray transients detected in the SPI/INTEGRAL experiment". In: *Astronomy Letters* 40.5, pp. 235–267.

Minaev, Pavel, Alexei Pozanenko, and Sergei Molkov (2018). "Precursors of short gamma-ray bursts detected by the INTEGRAL observatory". In: *International Journal of Modern Physics D* 27.10, 1844013, p. 1844013.

Mirabal, N. et al. (2006). "GRB 060218/SN 2006aj: A Gamma-Ray Burst and Prompt Supernova at z = 0.0335". In: *Astrophysical Journal Letters* 643.2, pp. L99–L102.

Molinari, E. et al. (2007). "REM observations of GRB 060418 and GRB 060607A: the onset of the afterglow and the initial fireball Lorentz factor determination". In: *Astronomy and Astrophysics* 469.1, pp. L13–L16.

Monet, David G. et al. (2003). "The USNO-B Catalog". In: *Astronomical Journal* 125.2, pp. 984–993.

Mooley, K. P. et al. (2018). "A mildly relativistic wide-angle outflow in the neutron-star merger event GW170817". In: *Nature* 554.7691, pp. 207–210.

Moskvitin, A. et al. (2014a). "GRB 140629A: BTA redshift." In: *GRB Coordinates Network* 16489, p. 1.

Moskvitin, A. S. et al. (2014b). "GRB 140606A: BTA and OSN optical observations." In: *GRB Coordinates Network* 16411, p. 1.

Murakami, T. et al. (1989). "The gamma-ray burst detector system on board Ginga." In: *Publications of the ASJ* 41, pp. 405–426.

Murakami, T. et al. (1991). "A γ-ray burst preceded by X-ray activity". In: *Nature* 350.6319, pp. 592–594.

Nakagawa, Y. E. and Hete-2 Collaboration (2009). "HETE-2 highlights". In: *Frontier Objects in Astrophysics and Particle Physics*. Ed. by F. Giovannelli and G. Mannocchi, p. 315.

Nakamura, Takayoshi et al. (2001). "Light Curve and Spectral Models for the Hypernova SN 1998BW Associated with GRB 980425". In: *Astrophysical Journal* 550.2, pp. 991–999.

Nakar, Ehud (2007). "Short-hard gamma-ray bursts". In: *Physics Reports* 442.1-6, pp. 166–236.

Nakar, Ehud and Jonathan Granot (2007). "Smooth light curves from a bumpy ride: relativistic blast wave encounters a density jump". In: *Monthly Notices of the RAS* 380.4, pp. 1744–1760.

Narayan, Ramesh, Bohdan Paczynski, and Tsvi Piran (1992). "Gamma-Ray Bursts as the Death Throes of Massive Binary Stars". In: *Astrophysical Journal Letters* 395, p. L83.

Nava, L. et al. (2012). "A complete sample of bright Swift long gamma-ray bursts: testing the spectral-energy correlations". In: *Monthly Notices of the RAS* 421.2, pp. 1256–1264.

Nayana, A. J. and P. Chandra (2014). "Possible radio detection of GRB 140903A with the GMRT." In: *GRB Coordinates Network* 16815, p. 1.

Nemmen, R. S. et al. (2012). "A Universal Scaling for the Energetics of Relativistic Jets from Black Hole Systems". In: *Science* 338.6113, p. 1445.

Nesterov, N. S., A. E. Volvach, and I. D. Strepka (2000). "Observations of Extragalactic Radio Sources at 36 GHz". In: *Astronomy Letters* 26, pp. 204–207.

Netzer, Hagai (2015). "Revisiting the Unified Model of Active Galactic Nuclei". In: *Annual Review of Astron and Astrophys* 53, pp. 365–408.

Nicuesa Guelbenzu, A. et al. (2012). "Multi-color observations of short GRB afterglows: 20 events observed between 2007 and 2010". In: *Astronomy and Astrophysics* 548, A101, A101.

Nissanke, Samaya, Mansi Kasliwal, and Alexandra Georgieva (2013). "Identifying Elusive Electromagnetic Counterparts to Gravitational Wave Mergers: An End-to-end Simulation". In: *Astrophysical Journal* 767.2, 124, p. 124.

Norris, J. et al. (2013). "GRB 130603B: Swift-BAT spectral lag analysis." In: *GRB Coordinates Network* 14746, p. 1.

Norris, J. P. and J. T. Bonnell (2006). "Short Gamma-Ray Bursts with Extended Emission". In: *Astrophysical Journal* 643.1, pp. 266–275.

Norris, J. P., G. F. Marani, and J. T. Bonnell (2000). "Connection between Energy-dependent Lags and Peak Luminosity in Gamma-Ray Bursts". In: *Astrophysical Journal* 534.1, pp. 248–257.

Norris, J. P. et al. (1986). "Spectral Evolution of Pulse Structures in Gamma-Ray Bursts". In: *Astrophysical Journal* 301, p. 213.

Noterdaeme, P. et al. (2012). "Discovery of a compact gas-rich damped Lyman-α galaxy at z = 2.2: evidence of a starburst-driven outflow". In: *Astronomy and Astrophysics* 540, A63, A63.

Oates, S. R. and T. N. Ukwatta (2014). "GRB 141212A: Swift/UVOT Upper Limits." In: *GRB Coordinates Network* 17180, p. 1.

Oates, S. R. et al. (2007). "The two-component afterglow of Swift GRB 050802". In: *Monthly Notices of the RAS* 380.1, pp. 270–280.

Oates, S. R. et al. (2009). "A statistical study of gamma-ray burst afterglows measured by the Swift Ultraviolet Optical Telescope". In: *Monthly Notices of the RAS* 395.1, pp. 490–503.

Osborne, J. P. et al. (2014). "GRB 140629A: Swift-XRT refined Analysis." In: *GRB Coordinates Network* 16490, p. 1.

Paciesas, William S. et al. (1999). "The Fourth BATSE Gamma-Ray Burst Catalog (Revised)". In: *Astrophysical Journal Supplement* 122.2, pp. 465–495.

Paczynski, B. (1986). "Gamma-ray bursters at cosmological distances". In: *Astrophysical Journal Letters* 308, pp. L43–L46.

Paczynski, Bohdan (1995). "How Far Away Are Gamma-Ray Bursters?" In: *Publications of the ASP* 107, p. 1167.

Page, K. L. and T. N. Ukwatta (2015). "GRB 151228A: Correction to GCN 18770." In: *GRB Coordinates Network* 18772, p. 1.

Palmer, D. M. et al. (2014a). "GRB 140903A: Swift-BAT refined analysis." In: *GRB Coordinates Network* 16768, p. 1.

— (2014b). "GRB 141212A: Swift-BAT refined analysis." In: *GRB Coordinates Network* 17175, p. 1.

Panaitescu, A. (2007). "Jet breaks in the X-ray light-curves of Swift gamma-ray burst afterglows". In: *Monthly Notices of the RAS* 380.1, pp. 374–380.

Panaitescu, A. and P. Kumar (2001). "Fundamental Physical Parameters of Collimated Gamma-Ray Burst Afterglows". In: *Astrophysical Journal Letters* 560.1, pp. L49–L53.

Panaitescu, A. and P. Mészáros (1999). "Dynamical Evolution, Light Curves, and Spectra of Spherical and Collimated Gamma-Ray Burst Remnants". In: *Astrophysical Journal* 526.2, pp. 707–715.

Panaitescu, A. et al. (2006). "Evidence for chromatic X-ray light-curve breaks in Swift gamma-ray burst afterglows and their theoretical implications". In: *Monthly Notices of the RAS* 369.4, pp. 2059–2064.

Pandey, S. B. (2013). "Core-Collapse Supernovae and Gamma-Ray Bursts in TMT Era". In: *Journal of Astrophysics and Astronomy* 34.2, pp. 157–173.

Pandey, Shashi Bhushan et al. (2018). "First-light instrument for the 3.6-m Devasthal Optical Telescope: 4Kx4K CCD Imager". In: *Bulletin de la Societe Royale des Sciences de Liege* 87, pp. 42–57.

Park, I. H. et al. (2018). "UFFO/ Lomonosov: The Payload for the Observation of Early Photons from Gamma Ray Bursts". In: *Space Science Reviews* 214.1, 14, p. 14.

Patat, Ferdinando et al. (2001). "The Metamorphosis of SN 1998bw". In: *Astrophysical Journal* 555.2, pp. 900–917.

Pe'er, Asaf (2015). "Physics of Gamma-Ray Bursts Prompt Emission". In: *Advances in Astronomy* 2015, 907321, p. 907321.

Pe'er, Asaf and Felix Ryde (2011). "A Theory of Multicolor Blackbody Emission from Relativistically Expanding Plasmas". In: *Astrophysical Journal* 732.1, 49, p. 49.

Pei, Yichuan C. (1992). "Interstellar Dust from the Milky Way to the Magellanic Clouds". In: *Astrophysical Journal* 395, p. 130.

Pélangeon, A. et al. (2008). "Intrinsic properties of a complete sample of HETE-2 gamma-ray bursts. A measure of the GRB rate in the Local Universe". In: *Astronomy and Astrophysics* 491.1, pp. 157–171.

Perley, D. A. and A. M. Cockeram (2019). "GRB 190829A: Flattening of optical light curve from continued Liverpool Telescope photometry". In: *GRB Coordinates Network* 25623, p. 1.

Perley, D. A. and J. Jencson (2014). "GRB 140930B: Keck NIR imaging." In: *GRB Coordinates Network* 16867, p. 1.

Perley, D. A. et al. (2009). "GRB 080503: Implications of a Naked Short Gamma-Ray Burst Dominated by Extended Emission". In: *Astrophysical Journal* 696.2, pp. 1871–1885.

Perley, D. A. et al. (2014). "The Afterglow of GRB 130427A from 1 to 10^{16} GHz". In: *Astrophysical Journal* 781.1, 37, p. 37.

Perley, D. A. et al. (2016a). "The Swift Gamma-Ray Burst Host Galaxy Legacy Survey. I. Sample Selection and Redshift Distribution". In: *Astrophysical Journal* 817.1, 7, p. 7.

Perley, D. A. et al. (2016b). "The Swift GRB Host Galaxy Legacy Survey. II. Rest-frame Near-IR Luminosity Distribution and Evidence for a Near-solar Metallicity Threshold". In: *Astrophysical Journal* 817.1, 8, p. 8.

Pian, E. et al. (2006). "An optical supernova associated with the X-ray flash XRF 060218". In: *Nature* 442.7106, pp. 1011–1013.

Pian, E. et al. (2017). "Spectroscopic identification of r-process nucleosynthesis in a double neutron-star merger". In: *Nature* 551.7678, pp. 67–70.

Piran, T. (1999). "Gamma-ray bursts and the fireball model". In: *Physics Reports* 314.6, pp. 575–667.

Piran, Tsvi (2004). "The physics of gamma-ray bursts". In: *Reviews of Modern Physics* 76.4, pp. 1143–1210.

Piran, Tsvi, Ehud Nakar, and Stephan Rosswog (2013). "The electromagnetic signals of compact binary mergers". In: *Monthly Notices of the RAS* 430.3, pp. 2121–2136.

Polyakov, K. et al. (2014). "GRB 140930B: ISON-Kislovodsk observations." In: *GRB Coordinates Network* 16862, p. 1.

Poole, T. S. et al. (2008). "Photometric calibration of the Swift ultraviolet/optical telescope". In: *Monthly Notices of the RAS* 383.2, pp. 627–645.

Pozanenko, A. et al. (2014). "GRB 140903A: ISON-Kislovodsk observations." In: *GRB Coordinates Network* 16779, p. 1.

Pozanenko, A. S. et al. (2018). "GRB 170817A Associated with GW170817: Multi-frequency Observations and Modeling of Prompt Gamma-Ray Emission". In: *Astrophysical Journal Letters* 852.2, L30, p. L30.

Prevot, M. L. et al. (1984). "The typical interstellar extinction in the Small Magellanic Cloud." In: *Astronomy and Astrophysics* 132, pp. 389–392.

Prochaska, Jason X. et al. (2008). "A Survey for N V Absorption at $z \approx z_{GRB}$ in GRB Afterglow Spectra: Clues to Gas Near the Progenitor Star". In: *Astrophysical Journal* 685.1, pp. 344–353.

Qin, Ying et al. (2013). "A Comprehensive Analysis of Fermi Gamma-Ray Burst Data. III. Energy-dependent T_{90} Distributions of GBM GRBs and Instrumental Selection Effect on Duration Classification". In: *Astrophysical Journal* 763.1, 15, p. 15.

Quimby, Robert M. et al. (2018). "Spectra of Hydrogen-poor Superluminous Supernovae from the Palomar Transient Factory". In: *Astrophysical Journal* 855.1, 2, p. 2.

Racusin, J. L. et al. (2009). "Jet Breaks and Energetics of Swift Gamma-Ray Burst X-Ray Afterglows". In: *Astrophysical Journal* 698.1, pp. 43–74.

Racusin, J. L. et al. (2011). "Fermi and Swift Gamma-ray Burst Afterglow Population Studies". In: *Astrophysical Journal* 738.2, 138, p. 138.

Radice, David et al. (2018). "Binary Neutron Star Mergers: Mass Ejection, Electromagnetic Counterparts, and Nucleosynthesis". In: *Astrophysical Journal* 869.2, 130, p. 130.

Rau, A. et al. (2005). "The 1st INTEGRAL SPI-ACS gamma-ray burst catalogue". In: *Astronomy and Astrophysics* 438.3, pp. 1175–1183.

Rees, M. J. and P. Meszaros (1994). "Unsteady Outflow Models for Cosmological Gamma-Ray Bursts". In: *Astrophysical Journal Letters* 430, p. L93.

Rees, M. J. and P. Mészáros (1998). "Refreshed Shocks and Afterglow Longevity in Gamma-Ray Bursts". In: *Astrophysical Journal Letters* 496.1, pp. L1–L4.

Rhoads, James E. (1997). "How to Tell a Jet from a Balloon: A Proposed Test for Beaming in Gamma-Ray Bursts". In: *Astrophysical Journal Letters* 487.1, pp. L1–L4.

— (1999). "The Dynamics and Light Curves of Beamed Gamma-Ray Burst Afterglows". In: *Astrophysical Journal* 525.2, pp. 737–749.

Rhodes, L. et al. (2020). "Radio afterglows of very high-energy gamma-ray bursts 190829A and 180720B". In: *Monthly Notices of the RAS* 496.3, pp. 3326–3335.

Ricci, Fulvio and Alain Brillet (1997). "A Review of Gravitational Wave Detectors". In: *Annual Review of Nuclear and Particle Science* 47, pp. 111–156.

Ricker, G. R. et al. (2003). "The High Energy Transient Explorer (HETE): Mission and Science Overview". In: *Gamma-Ray Burst and Afterglow Astronomy 2001: A Workshop Celebrating the First Year of the HETE Mission*. Ed. by G. R. Ricker and R. K. Vanderspek. Vol. 662. American Institute of Physics Conference Series, pp. 3–16.

Robertson, Brant E. and Richard S. Ellis (2012). "Connecting the Gamma Ray Burst Rate and the Cosmic Star Formation History: Implications for Reionization and Galaxy Evolution". In: *Astrophysical Journal* 744.2, 95, p. 95.

Rodney, Steven A. et al. (2015). "Two SNe Ia at Redshift ∼2: Improved Classification and Redshift Determination with Medium-band Infrared Imaging". In: *Astronomical Journal* 150.5, 156, p. 156.

Romano, P. et al. (2006). "Panchromatic study of GRB 060124: from precursor to afterglow". In: *Astronomy and Astrophysics* 456.3, pp. 917–927.

Roming, Peter W. A. et al. (2005). "The Swift Ultra-Violet/Optical Telescope". In: *Space Science Reviews* 120.3-4, pp. 95–142.

Rossi, A. et al. (2020). "A comparison between short GRB afterglows and kilonova AT2017gfo: shedding light on kilonovae properties". In: *Monthly Notices of the RAS* 493.3, pp. 3379–3397.

Rossi, Elena M. et al. (2004). "The polarization of afterglow emission reveals γ-ray bursts jet structure". In: *Monthly Notices of the RAS* 354.1, pp. 86–100.

Rosswog, S. (2005). "Mergers of Neutron Star-Black Hole Binaries with Small Mass Ratios: Nucleosynthesis, Gamma-Ray Bursts, and Electromagnetic Transients". In: *Astrophysical Journal* 634.2, pp. 1202–1213.

Rosswog, S. et al. (2014). "The long-term evolution of neutron star merger remnants - I. The impact of r-process nucleosynthesis". In: *Monthly Notices of the RAS* 439.1, pp. 744–756.

Rowlinson, A. et al. (2013). "Signatures of magnetar central engines in short GRB light curves". In: *Monthly Notices of the RAS* 430.2, pp. 1061–1087.

Rueda, J. A. et al. (2020). "Magnetic Fields and Afterglows of BdHNe: Inferences from GRB 130427A, GRB 160509A, GRB 160625B, GRB 180728A, and GRB 190114C". In: *Astrophysical Journal* 893.2, 148, p. 148.

Ruffini, R. et al. (2016). "On the Classification of GRBs and Their Occurrence Rates". In: *Astrophysical Journal* 832.2, 136, p. 136.

Ruffini, Remo et al. (2001). "On a Possible Gamma-Ray Burst-Supernova Time Sequence". In: *Astrophysical Journal Letters* 555.2, pp. L117–L120.

Ryan, Geoffrey et al. (2015). "Gamma-Ray Bursts are Observed Off-axis". In: *Astrophysical Journal* 799.1, 3, p. 3.

Ryde, Felix (2005). "Is Thermal Emission in Gamma-Ray Bursts Ubiquitous?" In: *Astrophysical Journal Letters* 625.2, pp. L95–L98.

Sahu, Kailash C. et al. (1997). "The optical counterpart to γ-ray burst GRB970228 observed using the Hubble Space Telescope". In: *Nature* 387.6632, pp. 476–478.

Sahu, Sarira and Carlos E. López Fortín (2020). "Origin of Sub-TeV Afterglow Emission from Gamma-Ray Bursts GRB 190114C and GRB 180720B". In: *Astrophysical Journal Letters* 895.2, L41, p. L41.

Sakamoto, T. et al. (2014a). "GRB 140622A: An unusual short event, Swift-BAT refined analysis." In: *GRB Coordinates Network* 16438, p. 1.

Sakamoto, T. et al. (2014b). "GRB 140903A: Swift-BAT Spectral lag analysis." In: *GRB Coordinates Network* 16771, p. 1.

Salvaterra, R. et al. (2009). "GRB090423 at a redshift of z∼8.1". In: *Nature* 461.7268, pp. 1258–1260.

Salvaterra, R. et al. (2010). "On the offset of short gamma-ray bursts". In: *Monthly Notices of the RAS* 406.2, pp. 1248–1252.

Sanchez-Ramirez, R. et al. (2013). "GRB 130603B: optical follow-up and independent GTC redshift determination and afterglow spectrum." In: *GRB Coordinates Network* 14747, p. 1.

Sánchez-Ramírez, R. et al. (2016). "The evolution of neutral gas in damped Lyman α systems from the XQ-100 survey". In: *Monthly Notices of the RAS* 456.4, pp. 4488–4505.

Sánchez-Ramírez, R. et al. (2017). "GRB 110715A: the peculiar multiwavelength evolution of the first afterglow detected by ALMA". In: *Monthly Notices of the RAS* 464.4, pp. 4624–4640.

Sari, Re'em and Peter Mészáros (2000). "Impulsive and Varying Injection in Gamma-Ray Burst Afterglows". In: *Astrophysical Journal Letters* 535.1, pp. L33–L37.

Sari, Re'em and Tsvi Piran (1997). "Cosmological gamma-ray bursts: internal versus external shocks". In: *Monthly Notices of the RAS* 287.1, pp. 110–116.

— (1999). "Predictions for the Very Early Afterglow and the Optical Flash". In: *Astrophysical Journal* 520.2, pp. 641–649.

Sari, Re'em, Tsvi Piran, and J. P. Halpern (1999). "Jets in Gamma-Ray Bursts". In: *Astrophysical Journal Letters* 519.1, pp. L17–L20.

Sari, Re'em, Tsvi Piran, and Ramesh Narayan (1998). "Spectra and Light Curves of Gamma-Ray Burst Afterglows". In: *Astrophysical Journal Letters* 497.1, pp. L17–L20.

Savaglio, S., K. Glazebrook, and D. Le Borgne (2006). "GRB Host Studies (GHostS)". In: *Gamma-Ray Bursts in the Swift Era*. Ed. by S. S. Holt, N. Gehrels, and J. A.

Nousek. Vol. 836. American Institute of Physics Conference Series, pp. 540–545.

— (2009). "The Galaxy Population Hosting Gamma-Ray Bursts". In: *Astrophysical Journal* 691.1, pp. 182–211.

Savchenko, V. et al. (2017). "INTEGRAL Detection of the First Prompt Gamma-Ray Signal Coincident with the Gravitational-wave Event GW170817". In: *Astrophysical Journal Letters* 848.2, L15, p. L15.

Scargle, Jeffrey D. (1998). "Studies in Astronomical Time Series Analysis. V. Bayesian Blocks, a New Method to Analyze Structure in Photon Counting Data". In: *Astrophysical Journal* 504.1, pp. 405–418.

Schady, P. et al. (2007). "Dust and gas in the local environments of gamma-ray bursts". In: *Monthly Notices of the RAS* 377.1, pp. 273–284.

Schady, P. et al. (2010). "Dust and metal column densities in gamma-ray burst host galaxies". In: *Monthly Notices of the RAS* 401.4, pp. 2773–2792.

Schlafly, Edward F. and Douglas P. Finkbeiner (2011). "Measuring Reddening with Sloan Digital Sky Survey Stellar Spectra and Recalibrating SFD". In: *Astrophysical Journal* 737.2, 103, p. 103.

Schlegel, David J., Douglas P. Finkbeiner, and Marc Davis (1998). "Maps of Dust Infrared Emission for Use in Estimation of Reddening and Cosmic Microwave Background Radiation Foregrounds". In: *Astrophysical Journal* 500.2, pp. 525–553.

Schulze, S. et al. (2011). "The circumburst density profile around GRB progenitors: a statistical study". In: *Astronomy and Astrophysics* 526, A23, A23.

Schutz, B. F. (1999). "Gravitational wave astronomy". In: *Classical and Quantum Gravity* 16.12A, A131–A156.

Schwarz, U. J. (1978). "Mathematical-statistical Description of the Iterative Beam Removing Technique (Method CLEAN)". In: *Astronomy and Astrophysics* 65, p. 345.

Seaton, M. J. (1979). "Interstellar extinction in the UV." In: *Monthly Notices of the RAS* 187, p. 73.

Selsing, J. et al. (2018). "GRB 180728A: classification of the associated SN 2018fip." In: *GRB Coordinates Network* 23181, p. 1.

Serino, M. et al. (2014). "GRB 140903A: MAXI/GSC upper limit." In: *GRB Coordinates Network* 16778, p. 1.

Serkowski, K., D. S. Mathewson, and V. L. Ford (1975). "Wavelength dependence of interstellar polarization and ratio of total to selective extinction." In: *Astrophysical Journal* 196, pp. 261–290.

Shibata, Masaru and Keisuke Taniguchi (2011). "Coalescence of Black Hole-Neutron Star Binaries". In: *Living Reviews in Relativity* 14.1, 6, p. 6.

Shirasaki, Yuji et al. (2003). "Design and Performance of the Wide-Field X-Ray Monitor on Board the High-Energy Transient Explorer 2". In: *Publications of the ASJ* 55, pp. 1033–1049.

Siegel, Daniel M. and Riccardo Ciolfi (2016a). "Electromagnetic Emission from Long-lived Binary Neutron Star Merger Remnants. I. Formulation of the Problem". In: *Astrophysical Journal* 819.1, 14, p. 14.

— (2016b). "Electromagnetic Emission from Long-lived Binary Neutron Star Merger Remnants. II. Lightcurves and Spectra". In: *Astrophysical Journal* 819.1, 15, p. 15.

Smartt, S. J. et al. (2017). "A kilonova as the electromagnetic counterpart to a gravitational-wave source". In: *Nature* 551.7678, pp. 75–79.

Sonbas, E. et al. (2015). "GRB 151228A: T60 observations." In: *GRB Coordinates Network* 18746, p. 1.

Stanek, K. Z. et al. (2003). "Spectroscopic Discovery of the Supernova 2003dh Associated with GRB 030329". In: *Astrophysical Journal Letters* 591.1, pp. L17–L20.

Stroh, M. C. et al. (2014). "GRB 140606A: Swift detection of a short hard burst." In: *GRB Coordinates Network* 16353, p. 1.

Strong, I. B. and R. W. Klebesadel (1976). "Cosmic gamma-ray bursts." In: *Scientific American* 235, pp. 66–70.

Svinkin, D. et al. (2020). "Improved IPN error box for GRB 200415A (consistent with the Sculptor Galaxy)". In: *GRB Coordinates Network* 27595, p. 1.

Tanaka, Masaomi (2016). "Kilonova/Macronova Emission from Compact Binary Mergers". In: *Advances in Astronomy* 2016, 634197, p. 634197.

Tanaka, Masaomi and Kenta Hotokezaka (2013). "Radiative Transfer Simulations of Neutron Star Merger Ejecta". In: *Astrophysical Journal* 775.2, 113, p. 113.

Tanaka, Masaomi et al. (2014). "Radioactively Powered Emission from Black Hole-Neutron Star Mergers". In: *Astrophysical Journal* 780.1, 31, p. 31.

Tang, Chen-Han et al. (2019). "Statistical Study of Gamma-Ray Bursts with a Plateau Phase in the X-Ray Afterglow". In: *Astrophysical Journal Supplement* 245.1, 1, p. 1.

Tanga, M., C. Delvaux, and J. Greiner (2014). "GRB 140422A: GROND Upper limits." In: *GRB Coordinates Network* 16435, p. 1.

Tanvir, N. R., A. J. Levan, and M. Fraser (2014). "GRB 140930B: WHT detection of candidate afterglow." In: *GRB Coordinates Network* 16861, p. 1.

Tanvir, N. R. et al. (2013). "A 'kilonova' associated with the short-duration γ-ray burst GRB 130603B". In: *Nature* 500.7464, pp. 547–549.

Tanvir, N. R. et al. (2017). "The Emergence of a Lanthanide-rich Kilonova Following the Merger of Two Neutron Stars". In: *Astrophysical Journal Letters* 848.2, L27, p. L27.

Terreran, G. et al. (2019). "GRB190829A: Keck LRIS spectroscopic confirmation of the accompanying supernova". In: *GRB Coordinates Network* 25664, p. 1.

Thöne, C. C. et al. (2011). "The unusual γ-ray burst GRB 101225A from a helium star/neutron star merger at redshift 0.33". In: *Nature* 480.7375, pp. 72–74.

Thöne, C. C. et al. (2013). "GRB 100219A with X-shooter - abundances in a galaxy at z =4.7". In: *Monthly Notices of the RAS* 428.4, pp. 3590–3606.

Tody, Doug (1993). "IRAF in the Nineties". In: *Astronomical Data Analysis Software and Systems II*. Ed. by R. J. Hanisch, R. J. V. Brissenden, and J. Barnes. Vol. 52. Astronomical Society of the Pacific Conference Series, p. 173.

Toy, Vicki L. et al. (2016). "Exploring Damped Lyα System Host Galaxies Using Gamma-Ray Bursts". In: *Astrophysical Journal* 832.2, 175, p. 175.

Troja, E., S. Rosswog, and N. Gehrels (2010). "Precursors of Short Gamma-ray Bursts". In: *Astrophysical Journal* 723.2, pp. 1711–1717.

Troja, E. et al. (2007). "Swift Observations of GRB 070110: An Extraordinary X-Ray Afterglow Powered by the Central Engine". In: *Astrophysical Journal* 665.1, pp. 599–607.

Troja, E. et al. (2008). "Different progenitors of short hard gamma-ray bursts". In: *Monthly Notices of the RAS* 385.1, pp. L10–L14.

Troja, E. et al. (2016). "An Achromatic Break in the Afterglow of the Short GRB 140903A: Evidence for a Narrow Jet". In: *Astrophysical Journal* 827.2, 102, p. 102.

Troja, E. et al. (2017a). "Significant and variable linear polarization during the prompt optical flash of GRB 160625B." In: *Nature* 547, pp. 425–427.

Troja, E. et al. (2017b). "The X-ray counterpart to the gravitational-wave event GW170817". In: *Nature* 551.7678, pp. 71–74.

Troja, E. et al. (2018). "A luminous blue kilonova and an off-axis jet from a compact binary merger at z = 0.1341". In: *Nature Communications* 9, 4089, p. 4089.

Troja, E. et al. (2019). "The afterglow and kilonova of the short GRB 160821B". In: *Monthly Notices of the RAS* 489.2, pp. 2104–2116.

Tsvetkova, A. et al. (2019). "Konus-Wind observation of GRB 190829A". In: *GRB Coordinates Network* 25660, p. 1.

Tunnicliffe, R. L. et al. (2014). "On the nature of the 'hostless' short GRBs". In: *Monthly Notices of the RAS* 437.2, pp. 1495–1510.

Ukwatta, T. N. et al. (2014). "GRB 141212A: Swift detection of a short burst." In: *GRB Coordinates Network* 17158, p. 1.

Ukwatta, T. N. et al. (2015). "GRB 151228A: Swift detection of a short burst." In: *GRB Coordinates Network* 18731, p. 1.

Usov, V. V. (1992). "Millisecond pulsars with extremely strong magnetic fields as a cosmological source of γ-ray bursts". In: *Nature* 357.6378, pp. 472–474.

Valeev, A. F. et al. (2019). "GRB 190829A: 10.4m GTC spectroscopy". In: *GRB Coordinates Network* 25565, p. 1.

van Eerten, Hendrik and Andrew MacFadyen (2013). "Gamma-Ray Burst Afterglow Light Curves from a Lorentz-boosted Simulation Frame and the Shape of the Jet Break". In: *Astrophysical Journal* 767.2, 141, p. 141.

van Eerten, Hendrik, Alexander van der Horst, and Andrew MacFadyen (2012). "Gamma-Ray Burst Afterglow Broadband Fitting Based Directly on Hydrodynamics Simulations". In: *Astrophysical Journal* 749.1, 44, p. 44.

van Eerten, Hendrik J. and Andrew I. MacFadyen (2012). "Gamma-Ray Burst Afterglow Scaling Relations for the Full Blast Wave Evolution". In: *Astrophysical Journal Letters* 747.2, L30, p. L30.

van Paradijs, J. et al. (1997). "Transient optical emission from the error box of the γ-ray burst of 28 February 1997". In: *Nature* 386.6626, pp. 686–689.

Viganò, D. and S. Mereghetti (2009). "Calibration of the INTEGRAL SPI Anti Coincidence Shield with Gamma Ray Bursts observations". In: *The Extreme Sky: Sampling the Universe above 10 keV*, p. 49.

Villar, V. A. et al. (2017a). "The Combined Ultraviolet, Optical, and Near-infrared Light Curves of the Kilonova Associated with the Binary Neutron Star Merger

GW170817: Unified Data Set, Analytic Models, and Physical Implications". In: *Astrophysical Journal Letters* 851.1, L21, p. L21.

Villar, V. Ashley et al. (2017b). "Theoretical Models of Optical Transients. I. A Broad Exploration of the Duration-Luminosity Phase Space". In: *Astrophysical Journal* 849.1, 70, p. 70.

Villata, M. et al. (2006). "The unprecedented optical outburst of the quasar <ASTROBJ>3C 454.3</ASTROBJ>. The WEBT campaign of 2004-2005". In: *Astronomy and Astrophysics* 453.3, pp. 817–822.

Volnova, A. et al. (2014). "GRB 140606A: AAO optical upper limit." In: *GRB Coordinates Network* 16371, p. 1.

Volnova, A. et al. (2019). "GRB 190829A observations in CrAO, photometry of the SN". In: *GRB Coordinates Network* 25682, p. 1.

von Kienlin, A., C. Meegan, and A. Goldstein (2017). "GRB 170817A: Fermi GBM detection." In: *GRB Coordinates Network* 21520, p. 1.

von Kienlin, A. et al. (2020). "The Fourth Fermi-GBM Gamma-Ray Burst Catalog: A Decade of Data". In: *Astrophysical Journal* 893.1, 46, p. 46.

von Kienlin, Andreas et al. (2004). "The GLAST burst monitor". In: *UV and Gamma-Ray Space Telescope Systems*. Ed. by Günther Hasinger and Martin J. L. Turner. Vol. 5488. Society of Photo-Optical Instrumentation Engineers (SPIE) Conference Series, pp. 763–770.

Vreeswijk, P. M. et al. (2013). "Time-dependent excitation and ionization modelling of absorption-line variability due to GRB 080310". In: *Astronomy and Astrophysics* 549, A22, A22.

Walker, Katharine C., Bradley E. Schaefer, and E. E. Fenimore (2000). "Gamma-Ray Bursts Have Millisecond Variability". In: *Astrophysical Journal* 537.1, pp. 264–269.

Wang, Xiang-Gao et al. (2015). "How Bad or Good Are the External Forward Shock Afterglow Models of Gamma-Ray Bursts?" In: *Astrophysical Journal Supplement* 219.1, 9, p. 9.

Wang, Xiang-Gao et al. (2018). "Gamma-Ray Burst Jet Breaks Revisited". In: *Astrophysical Journal* 859.2, 160, p. 160.

Wang, Y. et al. (2019). "Two Predictions of Supernova: GRB 130427A/SN 2013cq and GRB 180728A/SN 2018fip". In: *Astrophysical Journal* 874.1, 39, p. 39.

Wheeler, J. Craig, V. Johnson, and A. Clocchiatti (2015). "Analysis of late-time light curves of Type IIb, Ib and Ic supernovae". In: *Monthly Notices of the RAS* 450.2, pp. 1295–1307.

Wiersema, K. et al. (2014). "Circular polarization in the optical afterglow of GRB 121024A". In: *Nature* 509.7499, pp. 201–204.

Wijers, R. A. M. J. and T. J. Galama (1999). "Physical Parameters of GRB 970508 and GRB 971214 from Their Afterglow Synchrotron Emission". In: *Astrophysical Journal* 523.1, pp. 177–186.

Winkler, C. et al. (2003). "The INTEGRAL mission". In: *Astronomy and Astrophysics* 411, pp. L1–L6.

Wolfe, A. M. et al. (1986). "Damped Lyman-Alpha Absorption by Disk Galaxies with Large Redshifts. I. The Lick Survey". In: *Astrophysical Journal Supplement* 61, p. 249.

Wolfe, Arthur M., Eric Gawiser, and Jason X. Prochaska (2005). "Damped Ly α Systems". In: *Annual Review of Astron and Astrophys* 43.1, pp. 861–918.

Woosley, S. E. (1993). "Gamma-Ray Bursts from Stellar Mass Accretion Disks around Black Holes". In: *Astrophysical Journal* 405, p. 273.

Woosley, S. E. and J. S. Bloom (2006). "The Supernova Gamma-Ray Burst Connection". In: *Annual Review of Astron and Astrophys* 44.1, pp. 507–556.

Xie, Xiaoyi, Jonathan Zrake, and Andrew MacFadyen (2018). "Numerical Simulations of the Jet Dynamics and Synchrotron Radiation of Binary Neutron Star Merger Event GW170817/GRB 170817A". In: *Astrophysical Journal* 863.1, 58, p. 58.

Xin, Li-Ping et al. (2018). "Photometric and Spectroscopic Observations of GRB 140629A". In: *Astrophysical Journal* 860.1, 8, p. 8.

Xu, D. et al. (2012). "GRB 121226A: NOT optical upper limit." In: *GRB Coordinates Network* 14110, p. 1.

Xu, D. et al. (2013). "GRB 130603B: VLT/X-shooter redshift confirmation." In: *GRB Coordinates Network* 14757, p. 1.

Xu, D. et al. (2014a). "GRB 140606A: Nanshan optical upper limit." In: *GRB Coordinates Network* 16359, p. 1.

Xu, D. et al. (2014b). "GRB 140903A: NOT optical and NIR observations." In: *GRB Coordinates Network* 16783, p. 1.

Yang, Bin et al. (2015). "A possible macronova in the late afterglow of the long-short burst GRB 060614". In: *Nature Communications* 6, 7323, p. 7323.

Yi, S. X. et al. (2014). "X-Ray Afterglow Plateaus of Long Gamma-Ray Bursts: Further Evidence for Millisecond Magnetars". In: *arXiv e-prints*, arXiv:1401.1601, arXiv:1401.1601.

Yonetoku, D. et al. (2004). "Gamma-Ray Burst Formation Rate Inferred from the Spectral Peak Energy-Peak Luminosity Relation". In: *Astrophysical Journal* 609.2, pp. 935–951.

Yu, Shun-jing et al. (2020). "SVOM: a Joint Gamma-ray Burst Detection Mission". In: *Chinese Astronomy and Astrophysics* 44.2, pp. 269–282.

Yüksel, Hasan et al. (2008). "Revealing the High-Redshift Star Formation Rate with Gamma-Ray Bursts". In: *Astrophysical Journal Letters* 683.1, p. L5.

Yurkov, V. et al. (2014). "GRB 140629A: MASTER OT detection." In: *GRB Coordinates Network* 16478, p. 1.

Zauderer, B. A. et al. (2011). "Birth of a relativistic outflow in the unusual γ-ray transient Swift J164449.3+573451". In: *Nature* 476.7361, pp. 425–428.

Zhang, B. B. et al. (2018a). "A peculiar low-luminosity short gamma-ray burst from a double neutron star merger progenitor". In: *Nature Communications* 9, 447, p. 447.

Zhang, B. B. et al. (2018b). "Transition from fireball to Poynting-flux-dominated outflow in the three-episode GRB 160625B". In: *Nature Astronomy* 2, pp. 69–75.

Zhang, Bin-Bin, En-Wei Liang, and Bing Zhang (2007). "A Comprehensive Analysis of Swift XRT Data. I. Apparent Spectral Evolution of Gamma-Ray Burst X-Ray Tails". In: *Astrophysical Journal* 666.2, pp. 1002–1011.

Zhang, Bin-Bin et al. (2011). "A Comprehensive Analysis of Fermi Gamma-ray Burst Data. I. Spectral Components and the Possible Physical Origins of LAT/GBM GRBs". In: *Astrophysical Journal* 730.2, 141, p. 141.

Zhang, Bin-Bin et al. (2014). "How Long does a Burst Burst?" In: *Astrophysical Journal* 787.1, 66, p. 66.

Zhang, Bin-Bin et al. (2015). "An Analysis of Chandra Deep Follow-up Gamma-Ray Bursts: Implications for Off-axis Jets". In: *Astrophysical Journal* 806.1, 15, p. 15.

Zhang, Bing (2019). "Extreme emission seen from γ-ray bursts". In: *Nature* 575.7783, pp. 448–449.

Zhang, Bing, Shiho Kobayashi, and Peter Mészáros (2003). "Gamma-Ray Burst Early Optical Afterglows: Implications for the Initial Lorentz Factor and the Central Engine". In: *Astrophysical Journal* 595.2, pp. 950–954.

Zhang, Bing, Hou-Jun Lü, and En-Wei Liang (2016). "GRB Observational Properties". In: *Space Science Reviews* 202.1-4, pp. 3–32.

Zhang, Bing and Peter Mészáros (2001). "Gamma-Ray Burst Afterglow with Continuous Energy Injection: Signature of a Highly Magnetized Millisecond Pulsar". In: *Astrophysical Journal Letters* 552.1, pp. L35–L38.

— (2002a). "Gamma-Ray Burst Beaming: A Universal Configuration with a Standard Energy Reservoir?" In: *Astrophysical Journal* 571.2, pp. 876–879.

— (2002b). "Gamma-Ray Bursts with Continuous Energy Injection and Their Afterglow Signature". In: *Astrophysical Journal* 566.2, pp. 712–722.

— (2004). "Gamma-Ray Bursts: progress, problems & prospects". In: *International Journal of Modern Physics A* 19.15, pp. 2385–2472.

Zhang, Bing and Huirong Yan (2011). "The Internal-collision-induced Magnetic Reconnection and Turbulence (ICMART) Model of Gamma-ray Bursts". In: *Astrophysical Journal* 726.2, 90, p. 90.

Zhang, Bing et al. (2006). "Physical Processes Shaping Gamma-Ray Burst X-Ray Afterglow Light Curves: Theoretical Implications from the Swift X-Ray Telescope Observations". In: *Astrophysical Journal* 642.1, pp. 354–370.

Zhang, Bing et al. (2009). "Discerning the Physical Origins of Cosmological Gamma-ray Bursts Based on Multiple Observational Criteria: The Cases of z = 6.7 GRB 080913, z = 8.2 GRB 090423, and Some Short/Hard GRBs". In: *Astrophysical Journal* 703.2, pp. 1696–1724.

Zhang, Weiqun and Andrew I. MacFadyen (2006). "RAM: A Relativistic Adaptive Mesh Refinement Hydrodynamics Code". In: *Astrophysical Journal Supplement* 164.1, pp. 255–279.

Zheng, W. et al. (2014). "GRB 140622A: KAIT Optical Upper Limit." In: *GRB Coordinates Network* 16441, p. 1.

Publications

Articles published in peer-reviewed Journals:

1. B.-B. Zhang, Z.-K. Liu, Z.-K. Peng, Y. Li, H.-J. Lyu, et al. include **Hu**, **Y**.-**D**.; A Peculiarly Short-duration Gamma-Ray Burst from Massive Star Core Collapse, 2021, Nature Astronomy, In press.

2. Rahul Gupta, S. R. Oates, S. B. Pandey, A. J. Castro-Tirado, Jagdish C. Joshi, et al. include **Hu**, **Y**.-**D**.; GRB 140102A: Prompt emission spectral evolution and optical reverse shock emission, 2021, Monthly Notices of the Royal Astronomical Society, Submitted.

3. **Hu**, **Y**.-**D**., Castro-Tirado, A. J., Kumar, A., Gupta, R., Valeev, A. F., et al. 10.4m GTC observations of the nearby VHE-detected GRB 190829A/SN 2019oyw, 2021, Astronomy and Astrophysics, 646, A50.

4. Lin, L., Zhang, C. F., Wang, P., Gao, H., Guan, X., et al. include **Hu**, **Y**.-**D**.; No pulsed radio emission during a bursting phase of a Galactic magnetar, 2020, Nature, 587, 65.

5. Ackley, K., Amati, L., Barbieri, C., Bauer, F. E., Benetti, S., et al. include **Hu**, **Y**.-**D**.; Observational constraints on the optical and near-infrared emission from the neutron star-black hole binary merger candidate S190814bv, 2020, Astronomy and Astrophysics, 643,.

6. Anand, Shreya, Coughlin, Michael W., Kasliwal, Mansi M., Bulla, Mattia, Ahumada, Tomás, et al. include **Hu**, **Y**.-**D**.; Optical follow-up of the neutron star-black hole mergers S200105ae and S200115j, 2021, Nature Astronomy, 5,.

7. Kasliwal, Mansi M., Anand, Shreya, Ahumada, Tomas, Stein, Robert, Sagues Carracedo, Ana, et al. include **Hu**, **Y**.-**D**.; Kilonova Luminosity Function Constraints based on Zwicky Transient Facility Searches for 13 Neutron Star Mergers, 2020, The Astrophysical Journal, 905, 145.

8. Andreoni, Igor, Goldstein, Daniel A., Kasliwal, Mansi M., Nugent, Peter E., Zhou, Rongpu, et al. include **Hu**, **Y**.-**D**.; GROWTH on S190814bv: Deep Synoptic Limits on the Optical/Near-infrared Counterpart to a Neutron Star-Black Hole Merger, 2020, The Astrophysical Journal, 890,.

9. **Hu**, **Y**.-**D**., Oates, S. R., Lipunov, V. M., Zhang, B. -B., Castro-Tirado, A. J., et al. Multiwavelength observations of GRB 140629A. A long burst with an achromatic jet break in the optical and X-ray afterglow, 2019, Astronomy and Astrophysics, 632,.

10. MAGIC Collaboration, Acciari, V. A., Ansoldi, S., Antonelli, L. A., Engels, A. Arbet, Baack, et al. include **Hu**, **Y**.-**D**.; Observation of inverse Compton emission from a long γ-ray burst, 2019, Nature, 575, 463.

11. Troja, E., Castro-Tirado, A. J., Becerra González, J., **Hu**, **Y**.-**D**., Ryan, G. S., et al. The afterglow and kilonova of the short GRB 160821B, 2019, Monthly Notices of the Royal Astronomical Society, 489, 2116.

12. Pandey, S. B., **Hu**, **Y**.-**D**., Castro-Tirado, Ao J., Pozanenko, A. S., Sánchez-Ramírez, R., et al. A multiwavelength analysis of a collection of short-duration GRBs observed between 2012 and 2015, 2019, Monthly Notices of the Royal Astronomical Society, 485, 5318.

13. Melandri, A., Rossi, A., Benetti, S., D'Elia, V., Piranomonte, S., et al. include **Hu**, **Y**.-**D**.; Unveiling the enigma of ATLAS17aeu, 2019, Astronomy and Astrophysics, 621,.

14. Zhang, B. -B., Zhang, B., Castro-Tirado, A. J., Dai, Z. G., Tam, P. -H. T., et al. include **Hu**, **Y**.-**D**.; Transition from fireball to Poynting-flux-dominated outflow in the three-episode GRB 160625B, 2018, Nature Astronomy, 2, 75.

15. Sadovnichy, V. A., Panasyuk, M. I., Svertilov, S. I., Lipunov, V. M., Bogomolov, V. V., et al. include **Hu**, **Y**.-**D**.; Prompt and Follow-up Multi-wavelength Observations of the GRB 161017A, 2018, The Astrophysical Journal, 861,.

16. Zhang, B. -B., Zhang, B., Sun, H., Lei, W. -H., Gao, H., et al. include **Hu**, **Y**.-**D**.; A peculiar low-luminosity short gamma-ray burst from a double neutron star merger progenitor, 2018, Nature Communications, 9,.

17. Abbott, B. P., Abbott, R., Abbott, T. D., Acernese, F., Ackley, K., et al. include **Hu**, **Y**.-**D**.; Multi-messenger Observations of a Binary Neutron Star Merger, 2017, The Astrophysical Journal, 848,.

18. Sánchez-Ramírez, R., Hancock, P. J., Jóhannesson, G., Murphy, Tara, de Ugarte Postigo, A., et al. include **Hu**, **Y**.-**D**.; GRB 110715A: the peculiar multi-wavelength evolution of the first afterglow detected by ALMA, 2017, Monthly Notices of the Royal Astronomical Society, 464, 4640.

19. Abbott, B. P., Abbott, R., Abbott, T. D., Abernathy, M. R., Acernese, F., et al. include **Hu**, **Y**.-**D**.; Supplement: "Localization and Broadband Follow-up of the Gravitational-wave Transient GW150914" (2016, ApJL, 826, L13), 2016, The Astrophysical Journal Supplement Series, 225,.

20. Abbott, B. P., Abbott, R., Abbott, T. D., Abernathy, M. R., Acernese, F., et al. include **Hu**, **Y**.-**D**.; Localization and Broadband Follow-up of the

Gravitational-wave Transient GW150914, 2016, The Astrophysical Journal, 826,.

Articles published in Conference Proceedings:

1. **Hu**, **Y**.-**D**., X. Y. Li, A. J. Castro-Tirado, E. J. Fernandez-Garciá, A. Castellon, et al. BOOTES network in gravitational wave era. Sixth Workshop on Robotic Autonomous Observatories (2019), RevMexAA(SC), In press.

2. A. F. Valeev, A. J. Castro-Tirado, **Hu**, **Y**.-**D**., V. V. Sokolov, I. Agudo, et al. Optical spectroscopy of candidates in the LIGO/VIRGO binary merger error boxes. Sixth Workshop on Robotic Autonomous Observatories (2019), RevMexAA(SC), In press.

3. Castro-Tirado, Alberto J., **Hu**, **Y**.-**D**., Zhang, Binbin, & Sokolov, Vladimir Electromagnetic Counterparts to Gravitational Waves and the case of GRB 17081 7A, 2019, The Multi-Messenger Astronomy: Gamma-Ray Bursts, Search for Electromagnetic Counterparts to Neutrino Events and Gravitational Waves, 47.

4. Acosta-Pulido, J. A., Agudo, I., Alberdi, A., Alcolea, J., Alfaro, E. J., et al. include **Hu**, **Y**.-**D**.; The Spanish Square Kilometre Array White Book, 2015, arXiv e-prints,.

GCN Circulars and Astronomer's Telegrams:

1. **Hu**, **Y**.-**D**., Fernandez-Garcia, E., Castro-Tirado, A. J., et al. (2021), GRB 210411C: BOOTES-4/MET optical upper limit, GRB Coordinates Network, 29803,

2. **Hu**, **Y**.-**D**., Fernandez-Garcia, E., Castro-Tirado, A. J., et al. (2021), GRB 210406A: 10.4m GTC follow-up observation, GRB Coordinates Network, 29799,

3. **Hu**, **Y**.-**D**., Fernandez-Garcia, E., Castro-Tirado, A. J., et al. (2021), GRB 210406A: BOOTES-4/MET optical upper limit, GRB Coordinates Network, 29768,

4. **Hu**, **Y**.-**D**., Fernandez-Garcia, E., Castro-Tirado, A. J., et al. (2021), GRB 210402A: BOOTES-network early optical upper limit, GRB Coordinates Network, 29755,

5. **Hu**, **Y**.-**D**., Fernandez-Garcia, E., Caballero-Garcia, A. J. C.-T. M. D., et al. (2021), GRB210222B: BOOTES-1 optical afterglow detection, GRB Coordinates Network, 29546,

6. **Hu**, **Y**.-**D**., Fernandez-Garcia, E., Castro-Tirado, A. J., et al. (2021), GRB 210212A: BOOTES-4/MET optical upper limit, GRB Coordinates Network, 29494,

7. **Hu**, **Y**.-**D**., Fernandez-Garcia, E., Castro-Tirado, A. J., et al. (2021), GRB 210209A: BOOTES-4/MET optical upper limit, GRB Coordinates Network, 29460,

8. **Hu**, **Y**.-**D**., Fernandez-Garcia, E., Castro-Tirado, A. J., et al. (2021), GRB 210208A: BOOTES-2/TELMA optical upper limit, GRB Coordinates Network, 29439,

9. **Hu**, **Y**.-**D**., Fernandez-Garcia, E., Castro-Tirado, A. J., et al. (2021), GRB 210205A: BOOTES-4/MET optical upper limit, GRB Coordinates Network, 29400,

10. **Hu**, **Y**.-**D**., Fernandez-Garcia, E., Castro-Tirado, A. J., et al. (2021), ZTF21aaeyldq: 2.2m CAHA BVRI optical observations, GRB Coordinates Network, 29312,

11. **Hu**, **Y**.-**D**., Fernandez-Garcia, E., Castro-Tirado, A. J., et al. (2021), GRB 210104B: BOOTES network optical upper limit, GRB Coordinates Network, 29249,

12. **Hu**, **Y**.-**D**., Fernandez-Garcia, E., Castro-Tirado, A. J., et al. (2021), GRB 210104A: BOOTES-4/MET early optical afterglow detection, GRB Coordinates Network, 29236,

13. **Hu**, **Y**.-**D**., Fernandez-Garcia, E., Castro, M. A., et al. (2020), GRB 201223A: BOOTES-4/MET early optical observation, GRB Coordinates Network, 29160,

14. **Hu**, **Y**.-**D**., Castro-Tirado, A. J., Kumar, A., et al. (2020), VizieR Online Data Catalog: GRB 190829A/SN 2019oyw spectra (Hu+, 2021), VizieR Online Data Catalog,

15. **Hu**, **Y**.-**D**., Fernandez-Garcia, E., Castro-Tirado, A. J., et al. (2020), GRB 201029A: BOOTES-1 optical upper limit, GRB Coordinates Network, 28807,

16. **Hu**, **Y**.-**D**., Aceituno, F. J., Castro-Tirado, A. J., Fernandez-Garcia, E., & a larger Collaboration (2020), GRB 201027A: 1.5m OSN optical upper limit, GRB Coordinates Network, 28794,

17. Fernandez-Garcia, E., **Hu**, **Y**.-**D**., Castro-Tirado, A. J., et al. (2020), GRB 201024A: BOOTES-2/TELMA early optical observation and 1.5m OSN follow-up, GRB Coordinates Network, 28763,

18. **Hu**, **Y**.-**D**., Fernandez-Garcia, E., Castro-Tirado, A. J., et al. (2020), GRB 201015A: BOOTES-1 early optical afterglow detection, GRB Coordinates Network, 28645,

19. **Hu**, **Y**.-**D**., Fernandez-Garcia, E., Castro-Tirado, A. J., et al. (2020), GRB 201014A: BOOTES-1 and -2 early optical upper limits, GRB Coordinates Network, 28630,

20. **Hu**, **Y**.-**D**., Sota, A., Castro-Tirado, A. J., et al. (2020), SGR 1830-0645 / GRB 201010A: 1.5m OSN optical upper limit, GRB Coordinates Network, 28601,

21. **Hu**, **Y**.-**D**., Fernandez-Garcia, E., Castro-Tirado, A. J., et al. (2020), GRB 200809B: BOOTES-3/YA optical upper limit, GRB Coordinates Network, 28242,

22. **Hu**, **Y**.-**D**., Fernandez-Garcia, E., Castro-Tirado, A. J., et al. (2020), GRB 200801C: BOOTES-1 and BOOTES-2 optical limits, GRB Coordinates Network, 28189,

23. **Hu**, **Y**.-**D**., Fernandez-Garcia, E., Castro-Tirado, A. J., et al. (2020), GRB200729A: BOOTES-1 optical upper limit, GRB Coordinates Network, 28167,

24. **Hu**, **Y**.-**D**., Fernandez-Garcia, E., Castro-Tirado, A. J., et al. (2020), GRB200716C: BOOTES-1 optical afterglow detection, GRB Coordinates Network, 28126,

25. **Hu**, **Y**.-**D**., Fernandez-Garcia, E., Castro-Tirado, A. J., et al. (2020), GRB 200612A: BOOTES-3/YA optical upper limit, GRB Coordinates Network, 27919,

26. **Hu**, **Y**.-**D**., Fernandez-Garcia, E., Castro-Tirado, A. J., et al. (2020), GRB 200608A: BOOTES-3 and BOOTES-4 optical upper limit, GRB Coordinates Network, 27907,

27. **Hu**, **Y**.-**D**., Fernandez-Garcia, E., Castro-Tirado, A. J., et al. (2020), GRB 200529A: BOOTES-2/TELMA early optical upper limit, GRB Coordinates Network, 27853,

28. **Hu**, **Y**.-**D**., Fernandez-Garcia, E., Castro-Tirado, A. J., et al. (2020), GRB 200522A: BOOTES-3/YA optical upper limit, GRB Coordinates Network, 27784,

29. **Hu**, **Y**.-**D**., Fernandez-Garcia, E., Castro-Tirado, A. J., et al. (2020), GRB 200519A: BOOTES-3/YA optical counterpart observations, GRB Coordinates Network, 27760,

30. **Hu**, **Y**.-**D**., Fernandez-Garcia, E., Castro-Tirado, A. J., et al. (2020), Swift J1818.0-1607: BOOTES-3/YA optical upper limit, GRB Coordinates Network, 27749,

31. **Hu**, **Y**.-**D**., Fernandez-Garcia, E., Castro-Tirado, A. J., et al. (2020), SGR Swift J1818.0-1607: BOOTES-4/MET optical limit, GRB Coordinates Network, 27378,

32. **Hu**, **Y**.-**D**., Castro-Tirado, A. J., Fernandez-Garcia, E., et al. (2020), GRB 200306C: BOOTES-1 detection of the optical afterglow, GRB Coordinates Network, 27329,

33. Sota, A., Fernandez-Garcia, E., **Hu**, **Y**.-**D**., et al. (2020), GRB 200224A: BOOTES-1 and 1.5m OSN optical observations, GRB Coordinates Network, 27176,

34. **Hu**, **Y**.-**D**., Castro-Tirado, A. J., Valeev, A. F., et al. (2020), LIGO/Virgo S200213t: AT2020clw/ZTF20aanaoyz, AT2020crd/ZTF20aanakge and AT2020cly /ZTF20aanakes 10.4m GTC spectroscopy, GRB Coordinates Network, 27154,

35. Castro-Tirado, A. J., **Hu**, **Y**.-**D**., & Lombardi, G. (2020), LIGO/Virgo S200213t: AT2020ciz/ZTF20aamvnat, AT2020cjb/ZTF20aamvnth and 2020cjf /ZTF20aamvodd 10.4m GTC spectroscopy, GRB Coordinates Network, 27063,

36. Valeev, A. F., Lombardi, G., & et al. (2020), LIGO/Virgo S200213t: AT2020ciy /ZTF20aamvqxl, AT2020cjg/ZTF20aamvoxx and AT2020cje/ZTF20 aamvtip 10.4m GTC spectroscopy, GRB Coordinates Network, 27060,

37. Valeev, A. F., & Castro-Rodriguez, N. (2020), LIGO/Virgo S200114f: AT2020vr, AT2020vt, AT2020wa and AT2020wc 10.4m GTC spectroscopy, GRB Coordinates Network, 26764,

38. Castro-Tirado, A. J., & Font, J. (2020), LIGO/Virgo S200105ae: AT2020pq, AT2020ps and AT2020pv 10.4m GTC spectroscopy, GRB Coordinates Network, 26703,

39. Valeev, A. F., & Font, J. (2020), LIGO/Virgo S200105ae: AT2020pp and AT2020py 10.4m GTC spectroscopy, GRB Coordinates Network, 26702,

40. **Hu**, **Y**.-**D**., Caballero Garcia, M. D., Font, J., & a larger Collaboration (2020), LIGO/Virgo S200105ae: AT2020oo 10.4m GTC spectroscopy, GRB Coordinates Network, 26701,

41. Valeev, A. F., Castro-Rodriguez, N., & a larger Collaboration (2019), LIGO/Virgo S191213g: AT2019wxt 10.4m GTC further spectroscopy, GRB Coordinates Network, 26591,

42. **Hu**, **Y**.-**D**., Geier, S., & a larger Collaboration (2019), LIGO/Virgo S191205ah: AT2019wmy 10.4m GTC spectroscopy, GRB Coordinates Network, 26502,

43. Castro-Tirado, A. J., **Hu**, **Y**.-**D**., Valeev, A. F., et al. (2019), LIGO/Virgo S191213g: AT2019wnh, AT2019wnk and AT2019wrt 10.4m GTC spectroscopy, GRB Coordinates Network, 26492,

44. **Hu**, **Y**.-**D**., Valeev, A. F., Castro-Tirado, A. J., et al. (2019), LIGO/Virgo S191205ah: AT2019wix and AT2019wib 10.4m GTC spectroscopy, GRB Coordinates Network, 26422,

45. Valeev, A. F., **Hu**, **Y**.-**D**., Castro-Tirado, A. J., et al. (2019), LIGO/Virgo S191205ah: AT2019wkv, AT2019wid and AT2019wiy 10.4m GTC spectroscopy, GRB Coordinates Network, 26421,

46. Carrasco, I., **Hu**, **Y**.-**D**., Fernandez-Garcia, E., et al. (2019), GRB 191213A: BOOTES-5/JGT optical limit, GRB Coordinates Network, 26420,

47. **Hu**, **Y**.-**D**., Valeev, A. F., Castro-Tirado, A. J., et al. (2019), LIGO/Virgo S191205ah: AT2019wfa 10.4m GTC spectroscopy, GRB Coordinates Network, 26405,

48. Valeev, A. F., **Hu**, **Y**.-**D**., Castro-Tirado, A. J., et al. (2019), LIGO/Virgo S191205ah: MASTER OT 1.5m OSN imaging and 10.4m GTC spectroscopy, GRB Coordinates Network, 26382,

49. **Hu**, **Y**.-**D**., Fernandez-Garcia, E., Castro-Tirado, A. J., et al. (2019), GRB 191122A: BOOTES-4/MET optical limit, GRB Coordinates Network, 26273,

50. **Hu**, **Y**.-**D**., Fernandez-Garcia, E., Castro-Tirado, A. J., et al. (2019), GRB 191106A: BOOTES-4/MET optical limit, GRB Coordinates Network, 26179,

51. **Hu**, **Y**.-**D**., Fernandez-Garcia, E., Castro-Tirado, A. J., et al. (2019), GRB 191029A: BOOTES-4/MET optical limit, GRB Coordinates Network, 26092,

52. **Hu**, **Y**.-**D**., Fernandez-Garcia, E., Castro-Tirado, A. J., et al. (2019), GRB 191016A: early time BOOTES Network and follow-up 1.5m OSN optical observations, GRB Coordinates Network, 26017,

53. **Hu**, **Y**.-**D**., Fernandez-Garcia, E., Castro-Tirado, A. J., et al. (2019), GRB 190919B: BOOTES-5/JGT and BOOTES-3/YA optical observations, GRB Coordinates Network, 25798,

54. Valeev, A. F., **Hu**, **Y**.-**D**., Castro-Tirado, A. J., et al. (2019), LIGO/Virgo S190910h: AT2019pxi, AT2019pxj and AT2019pxn 10.4m GTC spectroscopy, GRB Coordinates Network, 25731,

55. **Hu**, **Y**.-**D**., Castro-Tirado, A. J., Valeev, A. F., et al. (2019), LIGO/Virgo S190814bv: AT2019odc and AT2019omt 10.4m GTC spectroscopy, GRB Coordinates Network, 25588,

56. Valeev, A. F., Castro-Tirado, A. J., **Hu**, **Y**.-**D**., et al. (2019), GRB 190829A: 10.4m GTC spectroscopy, GRB Coordinates Network, 25565,

57. Castro-Tirado, A. J., Valeev, A. F., **Hu**, **Y**.-**D**., et al. (2019), LIGO/Virgo S190814bv: AT2019nxe and AT2019obc 10.4m GTC spectroscopy, GRB Coordinates Network, 25543,

58. Valeev, A. F., **Hu**, **Y**.-**D**., Castro-Tirado, A. J., et al. (2019), Fermi GBM-190816: ZTF19abqanpy 10.4m GTC spectroscopy, GRB Coordinates Network, 25421,

59. **Hu**, **Y**.-**D**., Valeev, A. F., Sokolov, V. V., et al. (2019), LIGO/Virgo S190728q: AT2019lvw 10.4m GTC spectroscopy, GRB Coordinates Network, 25276,

60. Valeev, A. F., Castro-Tirado, A. J., **Hu**, **Y**.-**D**., et al. (2019), LIGO/Virgo S190728q: AT2019lzc 10.4m GTC spectroscopy, GRB Coordinates Network, 25261,

61. **Hu**, **Y**.-**D**., Li, X.-Y., Carrasco, I., et al. (2019), GRB 190613B: BOOTES-5/JGT early optical observations, GRB Coordinates Network, 24826,

62. **Hu**, **Y**.-**D**., Li, X.-Y., Fernandez-Garcia, E., et al. (2019), GRB 190604B: BOOTES-3 early optical limits, GRB Coordinates Network, 24750,

63. **Hu**, **Y**.-**D**., Li, X.-Y., Fernandez-Garcia, E., et al. (2019), GRB 190515B: BOOTES-4/MET and 2.2m CAHA optical limits., GRB Coordinates Network, 24567,

64. Castro-Tirado, A. J., Valeev, A. F., Sokolov, V. V., et al. (2019), LIGO/Virgo S190510g: AT2019ezb and AT2019far 10.4m GTC spectroscopy., GRB Coordinates Network, 24535,

65. Sanchez-Ramirez, R., Valeev, A. F., Sokolov, V. V., et al. (2019), LIGO/Virgo S190426c: Gaia19boq 0.6m BOOTES-5/JGT, 1.5m OSN and 10.4m GTC observations., GRB Coordinates Network, 24368,

66. **Hu**, **Y**.-**D**., Castro-Tirado, A. J., Valeev, A. F., et al. (2019), LIGO/Virgo S190426c: ZTF19aaslzjf, ZTF19aasmftm and ZTF19aasmddt 1.5m OSN and 10.4m GTC observations., GRB Coordinates Network, 24359,

67. **Hu**, **Y**.-**D**., Castro-Tirado, A. J., Li, X.-Y., et al. (2019), LIGO/Virgo S190425z: 1.5m OSN and 10.4m imaging of the UVOT source field., GRB Coordinates Network, 24324,

68. Valeev, A. F., Sokolov, V. V., Castro-Tirado, A. J., et al. (2019), LIGO/Virgo S190426c: DG19ytre and DG19kplb 1.5m OSN imaging and 10.4m GTC spectroscopy., GRB Coordinates Network, 24317,

69. **Hu**, **Y**.-**D**., Li, X.-Y., Fernandez-Garcia, E., et al. (2019), GRB 190427A: BOOTES-1 and BOOTES-5/JGT early follow-up observations., GRB Coordinates Network, 24272,

70. **Hu**, **Y**.-**D**., Li, X.-Y., Carrasco, I., et al. (2019), LIGO/Virgo S190425z: BOOTES-5/JGT observations of galaxies., GRB Coordinates Network, 24270,

71. Castro-Tirado, A. J., **Hu**, **Y**.-**D**., Li, X.-Y., et al. (2019), LIGO/Virgo S190425z: ZTF19aarzaod 1.5m OSN imaging and 10.4m GTC spectroscopy., GRB Coordinates Network, 24214,

72. Valeev, A. F., Sokolov, I. V., Sokolov, V. V., et al. (2019), LIGO/Virgo S190408an: MASTER OT J231043.63+470956.4 BOOTES-4 and 10.4m GTC follow-up observations., GRB Coordinates Network, 24092,

73. **Hu**, **Y**.-**D**., Li, X.-Y., Fernandez-Garcia, E., et al. (2019), GRB 190331B: BOOTES-3/YA optical observations., GRB Coordinates Network, 24043,

74. **Hu**, **Y**.-**D**., Li, X.-Y., Fernandez-Garcia, E., et al. (2019), GRB 190326A: 2.2m CAHA telescope optical limit., GRB Coordinates Network, 24023,

75. **Hu**, **Y**.-**D**., Li, X.-Y., Fernandez-Garcia, E., et al. (2019), GRB 190220B: BOOTES-4 optical observation., GRB Coordinates Network, 23916,

76. Perez Del Pulgar, C., **Hu**, **Y**.-**D**., Li, X.-Y., et al. (2019), GRB 190219A: BOOTES-1 optical limits., GRB Coordinates Network, 23904,

77. **Hu**, **Y**.-**D**., Li, X.-Y., Fernandez-Garcia, E., et al. (2019), GRB 190211A: BOOTES-4/MET optical afterglow confirmation., GRB Coordinates Network, 23886,

78. **Hu**, **Y**.-**D**., Li, X.-Y., Fernandez-Garcia, E., et al. (2019), GRB 190123A: BOOTES-4/MET optical limit., GRB Coordinates Network, 23772,

79. Castro-Tirado, A. J., **Hu**, **Y**.-**D**. Fernandez-Garcia, E., et al. (2019), GRB 190114C: refined redshift by the 10.4m GTC., GRB Coordinates Network, 23708,

80. Fernandez-Garcia, E., **Hu**, **Y**.-**D**., Li, X.-Y., et al. (2019), GRB 190114B: BOOTES-4/MET optical afterglow detection., GRB Coordinates Network, 23694,

81. Li, X.-Y., **Hu**, **Y**.-**D**., Carrasco, I., et al. (2019), GRB 190109B: BOOTES-5/JGT optical observations., GRB Coordinates Network, 23655,

82. **Hu**, **Y**.-**D**., Li, X.-Y., Fernandez-Garcia, E., et al. (2019), GRB 190106A: BOOTES-4/MET optical observations., GRB Coordinates Network, 23627,

83. **Hu**, **Y**.-**D**., Li, X.-Y., Fernandez-Garcia, E., et al. (2019), GRB 181231A: BOOTES-2/TELMA optical observations., GRB Coordinates Network, 23599,

84. **Hu**, **Y**.-**D**., Castro-Tirado, A. J., Li, X.-Y., et al. (2019), Swift J1728.9-3613: BOOTES-3/YA optical counterpart candidate observation, The Astronomer's Telegram, 12443,

85. **Hu**, **Y**.-**D**., Carrasco, I., Fernandez-Garcia, E., et al. (2018), GRB 181213A: BOOTES-5/JGT optical observations., GRB Coordinates Network, 23527,

86. **Hu**, **Y**.-**D**., Fernandez-Garcia, E., Ayala, A., et al. (2018), GRB 181203A: BOOTES-3/YA optical observations., GRB Coordinates Network, 23513,

87. Perez, C., Castellon, A., Carrasco, I., et al. (2018), GRB 180904A: BOOTES-2/TELMA early observations., GRB Coordinates Network, 23209,

88. **Hu**, **Y**.-**D**., Fernandez-Garcia, E., Tello, J. C., et al. (2018), GRB 180905A: BOOTES-3/YA optical observations., GRB Coordinates Network, 23208,

89. **Hu**, **Y**.-**D**., Sota, A., Casanova, V., & Castro-Tirado, A. J. (2018), GRB 180818B: 1.5m OSN optical afterglow candidate., GRB Coordinates Network, 23161,

90. Fernandez-Garcia, E., **Hu**, **Y**.-**D**., Tello, J. C., et al. (2018), GRB 180821A: BOOTES-3/YA optical observations., GRB Coordinates Network, 23159,

91. Carrasco, I., **Hu**, **Y**.-**D**. Fernandez-Garcia, E., et al. (2018), GRB 180812A: BOOTES-5/JGT optical afterglow detection., GRB Coordinates Network, 23130,

92. **Hu**, **Y**.-**D**., Aceituno, F. J., Tello, J. C., & Castro-Tirado, A. J. (2018), GRB 180805B: 1.5m OSN I-band observation., GRB Coordinates Network, 23088,

93. Carrasco, I., **Hu**, **Y**.-**D**. Fernandez-Garcia, E., et al. (2018), GRB 180721A: BOOTES-5/JGT optical observations., GRB Coordinates Network, 23018,

94. Perez, C., Castellon, A., Fernandez-Garcia, E., et al. (2018), GRB 180720C: BOOTES-2/TELMA optical observations., GRB Coordinates Network, 23016,

95. Carrasco, I., **Hu**, **Y**.-**D**. Fernandez-Garcia, E., et al. (2018), GRB 180709A: BOOTES-5/JGT optical observations., GRB Coordinates Network, 22939,

96. Sota, A., **Hu**, **Y**.-**D**. Tello, J. C., Carrasco, I., & Castro-Tirado, A. J. (2018), GRB 180418A: 1.5m OSN optical observations., GRB Coordinates Network, 22657,

97. Castro-Tirado, A. J., Tello, J. C., **Hu**, **Y**.-**D**. et al. (2017), LIGO/Virgo G298048: optical observations with BOOTES-5 at San Pedro Mártir, GRB Coordinates Network, 21624,

98. Feng, H. X., **Hu**, **Y**.-**D**., Xu, D., et al. (2017), GRB 170921A: Nanshan optical upper limit., GRB Coordinates Network, 21907,

99. Feng, H. X., Xu, D., Zhu, Z. P., et al. (2017), GRB 170903A: Nanshan optical upper limit., GRB Coordinates Network, 21795,

100. Tello, J. C., Castro-Tirado, A. J., Cunniffe, R., et al. (2017), GRB 170822A: BOOTES-5/JGT optical afterglow candidate., GRB Coordinates Network, 21642,

101. Castro-Tirado, A. J., Gonzalez-Rodriguez, A., **Hu**, **Y**.-**D**. et al. (2017), GRB 170728B: BOOTES-2/TELMA optical detection during the extended gamma-ray phase., GRB Coordinates Network, 21393,

102. Xu, D., Qin, Y., Zhao, Y., et al. (2017), GRB 170428A: Xinglong 2.16-m upper limit and host galaxy candidate., GRB Coordinates Network, 21048,

103. Xu, D., Qin, Y., **Hu**, **Y**.-**D**., et al. (2017), GRB 170202A: Xinglong 2.16m photometry and spectroscopic redshift., GRB Coordinates Network, 20588,

104. Castro-Tirado, A. J., Valeev, A. F., Sokolov, V. V., et al. (2016), GRB 161017A: GTC additional spectroscopy and refined redshift., GRB Coordinates Network, 20077,

105. **Hu**, **Y**.-**D**. Sota, A., & Castro-Tirado, A. J. (2016), GRB 160824A: 1.5m OSN I-band observation., GRB Coordinates Network, 19863,

106. Jeong, S., Park, I. H., **Hu**, **Y**.-**D**. Scarpa, R., & Castro-Tirado, A. J. (2016), GRB 160821B: GTC follow-up observation., GRB Coordinates Network, 19847,

107. Castro-Tirado, A. J., Valeev, A. F., Jeong, S., et al. (2016), GRB 160623A: afterglow spectroscopy by GTC and independent redshift determination., GRB Coordinates Network, 19710,

108. Castro-Tirado, A. J., Fatkhullin, T. A., Moskvitin, A. S., et al. (2016), GRB 160629A: BTA and GTC redshift., GRB Coordinates Network, 19632,

109. Tello, J. C., **Hu**, **Y**.-**D**. Castro-Tirado, A. J., & Oates, S. (2016), GRB 160601A: GTC observations confirming transient source decay., GRB Coordinates Network, 19491,

110. Xu, D., Han, Y.-H., **Hu**, **Y**.-**D**., Qing, Y., & Xin, L.-P. (2016), GRB 160131A: LCOGT-SSO optical observations., GRB Coordinates Network, 18957,

111. Xu, D., Han, Y.-H., **Hu**, **Y**.-**D**., & Qing, Y. (2016), GRB 160127A: LCOGT-Sutherland optical upper limit., GRB Coordinates Network, 18946,

112. Kruehler, T., Xu, D., **Hu**, **Y**.-**D**., Qing, Y., & Han, Y.-H. (2016), GRB 160117B: LCOGT-SSO optical observations., GRB Coordinates Network, 18878,

113. Han, Y., Kruehler, T., Xu, D., **Hu**, **Y**.-**D**. & Qing, Y. (2015), GRB 151210A: Optical afterglow candidate from LCOGT-Cerro Tololo., GRB Coordinates Network, 18679,

114. Xu, D., Malesani, D., Qin, Y., Han, Y.-H., & **Hu**, **Y**.-**D**. (2015), GRB 151127A: LCOGT-SSO optical upper limits., GRB Coordinates Network, 18644,

115. Xu, D., Qin, Y., **Hu**, **Y**.-**D**., et al. (2015), GRB 150910A: Nanshan optical observations., GRB Coordinates Network, 18269,

116. Sanchez-Ramirez, R., Gorosabel, J., Perez-Ramirez, D., et al. (2015), GRB 150818A: 10.4m GTC spectroscopy and host galaxy., GRB Coordinates Network, 18177,

117. Cunniffe, R., Jelinek, M., **Hu**, **Y**.-**D**. et al. (2015), GRB 150309A: BOOTES-1 and -2 upper limit., GRB Coordinates Network, 17554,